Determining the Mass Composition of Ultra-high Energy Cosmic Rays Using Air Shower Universality

Zur Erlangung des akademischen Grades eines

Doktors der Naturwissenschaften

an der Fakultät für Physik des
Karlsruher Instituts für Technologie (KIT)

genehmigte

Dissertation

von

M.Sc. Appl. Phys. Ariel Bridgeman
aus Aurora, Colorado

Tag der mündlichen Prüfung: 25. Mai 2018

Referent: Prof. Dr. Dr. h.c. Johannes Blümer

Korreferent: Prof. Dr. Ulrich Husemann

Betreuer: Dr. Markus Roth

24. August 2018

Abstract

Ultra-high energy cosmic rays are accelerated via the most energetic and powerful processes in the Universe. For over a hundred years, the study of these particles has elicited great interest. While our knowledge and theoretical models have vastly improved over the last century, the exact sites at which and physical mechanisms by which the acceleration of these charged nuclei occurs remain elusive. In order to elucidate their origins, it is critical for us to better understand the energy spectrum and mass composition of cosmic rays. By doing so, we can come to more fully understand the astrophysical conditions needed to accelerate them and the interactions by which they are affected by during their propagation to Earth. Human-made accelerators and low-energy cosmic ray experiments provide insight into proposed acceleration and propagation models. Nevertheless, the most energetic ultra-high energy cosmic rays have a flux of around 1 particle per km^2 per century at an energy of around 10^{20} eV. This energy is roughly a factor of one hundred more energetic than the center-of-mass energies attainable at the Large Hadron Collider (and over a factor of a thousand more energetic than the energies at which the charge and nuclear mass of a cosmic ray may be directly measured). While models from the Large Hadron Collider may be extrapolated to the highest energies, it is critical that large-scale detectors be used to measure the macroscopic properties of cosmic rays.

The Pierre Auger Observatory (Auger), located in the Argentine Province of Mendoza, is the largest ultra-high energy cosmic ray detector, extending over 3000 km^2. As an ultra-high energy cosmic ray traverses Earth's atmosphere, it will interact with the atmospheric nuclei to generate electromagnetic and hadronic cascades, which will continue to develop until the remaining energy of a constituent particle is too small for further particle generation. Thus, the Auger observatory uses the atmosphere as a calorimeter to measure the development of an air shower cascade. The fluorescence detector measures the fluorescence light induced by the interacting cascades (the longitudinal profile), and the surface detector samples the footprint of the shower at the ground level (the lateral distribution). The depth at which the cascade is fully developed may be determined from the longitudinal profile, which is used to infer the primary mass. Due to its sensitivity to ambient light, the duty cycle, however, of the fluorescence detector is limited to around 15 %, whereas the surface detector is active around 100 % of the time. Thus, in order to measure enough events to test astrophysical scenarios at the highest energy, the reconstruction of the surface detector must be augmented to be able to infer the primary mass, which is not directly accessible from the lateral distribution. This is possible with the air shower universality approach. Within this method, the unique timing and signal distributions of different particle components in the cosmic-ray-induced cascade are exploited to describe air showers as a function of their primary energy, mass, and geometry. The universality approach is easily extendable to other detector types and is of essential importance for the upgrade of Auger and future analyses.

The major focus of this work is to determine the mass composition derived with the universality approach. The results found are compatible with those found by the fluorescence detector and provide insight into the mass composition above $10^{19.5}$ eV. At the highest

energies, the mass composition determined using the universality approach trends towards a lighter composition, which is a promising signal for point-source anisotropy. To achieve these results, a new reconstruction procedure was developed which exhibits minimal dependence on the arrival direction, has an efficiency across all energies of more than 90 %, and fully includes correlations between the reconstructed physics observables. Reconstructed air shower simulations using contemporary hadronic interaction models were individually studied and compared. Similarities and differences between reconstructed simulations and data are highlighted throughout this work. The methods developed in this work are of great interest for the data analysis of the forthcoming upgrade to Auger (AugerPrime).

Acronyms

This is a list of acronyms used within this work sorted alphabetically according to the short version.

ADST	Advanced Data Summary Tree
AERA	Auger Engineering Radio Array
AGASA	Akeno Giant Air Shower Array
AMIGA	Auger Muon Detectors for the Infill Ground Array
Auger	Pierre Auger Observatory
CDAS	Central Data Acquisition System
CIC	Constant Intensity Cut
c.d.f.	cumulative distribution function
CLF	Central Laser Facility
CMB	Cosmic Microwave Background
CR	cosmic ray
EAS	extensive air shower
FADC	flash analog to digital converter
FD	Fluorescence Detector
FoV	field of view
GDAS	Global Data Assimilation System
GPS	Global Positioning System
GZK	Greisen–Zatsepin–Kuzmin
HEAT	High Elevation Auger Telescopes
HiRes	High Resolution Fly's Eye
ICRC	International Cosmic Ray Conference
IR	infrared
KASCADE	Karlsruhe Shower Core and Array Detector
KSETA	Karlsruhe School of Elementary Particle and Astroparticle Physics: Science and Technology
LDF	lateral distribution function

LHC	Large Hadron Collider
LL	Los Leones
LM	Los Morados
MAD	median absolute deviation
MD	Muon Detector
MoPS	multiplicity of positive steps
NKG	Nishimura-Kamata-Greisen
p.d.f.	probability density function
PE	photoelectron
PMT	photo-multiplier tube
RD	Radio Detector
SD	Surface Detector
SD-1500	SD array with 1500 m spacing
SD-750	SD array with 750 m spacing
SSD	Scintillator Surface Detector
TA	Telescope Array
ToT	time-over-threshold trigger
ToTd	time-over-threshold deconvoluted trigger
UHECR	ultra-high energy cosmic ray
VAOD	vertical aerosol optical depth
VCT	vertical centered through-going
VEM	vertical-equivalent muon
WCD	water-Cherenkov detector
XLF	Extreme Laser Facility

Contents

1 Introduction **1**
- 1.1 Cosmic rays . . . 1
  - 1.1.1 Historical overview . . . 1
  - 1.1.2 Extensive Air Showers . . . 3
  - 1.1.3 Macroscopic characteristics . . . 5
- 1.2 Pierre Auger Observatory . . . 10
  - 1.2.1 Surface Detector . . . 13
  - 1.2.2 Fluorescence Detector . . . 15
  - 1.2.3 Atmospheric monitoring . . . 16
  - 1.2.4 Muon Detector . . . 16
  - 1.2.5 Radio Detector . . . 17
  - 1.2.6 The Auger Upgrade . . . 17
  - 1.2.7 Selected results . . . 19

2 Reconstruction of SD events **23**
- 2.1 Event selection . . . 24
  - 2.1.1 Local station triggers . . . 24
  - 2.1.2 Central data station trigger . . . 25
  - 2.1.3 Physics event selection . . . 25
  - 2.1.4 Photomultiplier and other quality selections . . . 26
- 2.2 Fluctuations of the SD measurements . . . 26
  - 2.2.1 Shower-to-shower fluctuations . . . 26
  - 2.2.2 WCD sampling fluctuations . . . 26
- 2.3 Reconstruction . . . 27
  - 2.3.1 Shower geometry . . . 28
  - 2.3.2 Lateral distribution function and maximum-likelihood method . . . 28
- 2.4 Constant intensity cut method . . . 31
  - 2.4.1 Event selection criteria . . . 31
  - 2.4.2 Geomagnetic and weather corrections . . . 32
  - 2.4.3 Correction function for the signal estimator . . . 33
- 2.5 Energy calibration . . . 33
  - 2.5.1 Pertinent improvements to the FD reconstruction . . . 33
  - 2.5.2 Event selection criteria . . . 34
  - 2.5.3 Calibration procedure . . . 35

3 Air shower universality **37**
- 3.1 Methodology . . . 38
  - 3.1.1 Universality of the electromagnetic cascade . . . 38
  - 3.1.2 Universality for hadrons . . . 38
  - 3.1.3 Model of ground signals in WCDs . . . 42

3.1.4 Time model of signals in WCDs . . . 46
3.2 Reconstruction . . . 50
3.2.1 Constructing the likelihood function . . . 50
3.2.2 Example reconstructions . . . 55
3.2.3 Reconstruction methods . . . 57

4 Study of the constrained axis reconstruction 73
4.1 Comparison with the global method . . . 74
4.2 Event selection in simulations . . . 75
4.2.1 Identifying outliers . . . 75
4.2.2 Fiducial selection . . . 76
4.2.3 Resulting bias and resolution . . . 83
4.3 Event selection in data . . . 83
4.3.1 Fiducial selection . . . 83
4.3.2 Data-based corrections . . . 87

5 Mass composition 95
5.1 Event selection and systematic effects . . . 96
5.2 Moment-based analysis methods . . . 98
5.2.1 Average depth of the shower maximum . . . 98
5.2.2 Fluctuations of the depth of shower maximum . . . 103
5.2.3 Average relative muon content . . . 104
5.2.4 Estimation of the logarithmic mass . . . 104
5.3 Distribution-based analysis method . . . 107

6 Summary and conclusions 115

A General 123
A.1 Violin plots . . . 123
A.2 Angular resolution . . . 125

B Data sets 127
B.1 Data . . . 127
B.2 Monte Carlo air shower library . . . 132

C Tables of results 137
C.1 Parameterizations for the universality fiducial selections . . . 137
C.2 Parameterizations of the biases as functions of energy . . . 139
C.3 The mass composition of UHECRs . . . 141

D Analyses 143
D.1 Proposed change from likelihood to deviance function . . . 143
D.1.1 Constructing the deviance minimizing function . . . 143
D.1.2 In-depth comparative analysis to negative log-likelihood . . . 145
D.2 Saturation in a WCD . . . 152
D.3 Event selection for the global reconstruction . . . 159
D.4 Study of the iterative fit . . . 164
D.4.1 In simulations . . . 164
D.4.2 Calibration with golden hybrid data . . . 168
D.5 Addenda to the study of the constrained axis reconstruction . . . 179
D.5.1 Event selection . . . 179
D.5.2 Event selection in simulations . . . 181

D.5.3 Event selection in data 184
D.6 Global reconstruction with fixed axis 190
D.6.1 Using SD axis vs MC axis 190
D.6.2 Comparison to constrained axis fit 192
D.7 Addendum to mass composition 196
D.7.1 Event selection and systematics 196
D.7.2 Average depth of the shower maximum 196
D.7.3 Distribution-based analysis method 199

E Acknowledgments **201**

CHAPTER 1

Introduction

1.1 Cosmic rays

Cosmic rays (CRs) have been studied at various energies for over a century. These subatomic, charged nuclei not only elicit interest due to their high energy hadronic interactions but also because they provide insight into the evolution and structure of the universe. Arriving from galactic and extragalactic sources, CRs interact with Earth's atmosphere to yield extensive air showers. From the measurement of a cosmic ray-induced air shower, it is possible to reconstruct the energy of the bombarding primary particle. The energy spectrum of particles extends up to 10^{20} eV and follows a steep power law. On a macroscopic level, this kinetic energy is roughly equivalent to the speed of a tennis ball when served; when compared to the highest energy man-made experiment, the *Large Hadron Collider* (LHC), the highest energy CRs are over four orders of magnitude more energetic than the protons accelerated to ~7 TeV. Around an energy of 10^{16} eV, the rate of CR is 1 particle per m^2 per year, whereas the rate for *ultra-high energy cosmic rays* (UHECRs) is 1 particle per km^2 per century.

The composition of CRs ranges from hydrogen to uranium nuclei; the relative proportion of nuclei species changes as a function of energy. As the magnetic deflection of a nucleus is proportional to its charge, the lightest nuclei are deflected less by the galactic and extragalactic fields. However, at the highest energies, one must also take into account propagation effects –such as the interaction with the *Cosmic Microwave Background* (CMB).

Due to the deflection of charged nuclei, the arrival directions of CRs is observed as isotropic. However, at the highest energies where there is a lower rate of CRs and potentially an exhaustion of sources, it is generally believed that an underlying anisotropy will be present. Taking into account the charge-based deflections is essential for the identification of sources. Possible sources include shock fronts of supernova remnants, active galactic nuclei, and gamma-ray bursts.

1.1.1 Historical overview

Before the start of the 20^{th} century, Henri Becquerel discovered spontaneous radioactivity. Through further study of this phenomena, ionizing radiation was found present in the atmosphere of the Earth. The popular explanation was that the Earth itself was the source of the ionizing radiation. Motivated by the efforts of Domenico Pacini and other physicists to confirm or disprove this theory, Victor Hess measured the ionizing radiation as a function

of altitude using electroscopes in hot air balloons [1, 2]. His results showed that the level of radiation decreased up to around 1 km and then increased as he approached his terminal height of 5.3 km. He concluded that there were extraterrestrial sources of radiation. Upon further verification from other physicists, Hess' discovery of CRs led him to receive the Nobel Prize in 1936.

Follow-up experiments sought to establish the composition of CRs. In 1927, Jacob Clay found that the CR intensity varied with latitude — a phenomenon associated with the deflection of charged particles by the geomagnetic field [3]. Further studies established that the deflected primary CRs are almost always positively-charged particles, with the composition dominated by protons [4].

Through the various studies of CRs, it was noted by several physicists that separated detectors had near-simultaneous measurements more often than the expected accidental rate [4]. In 1937, Pierre Auger investigated this phenomenon and concluded that high-energy primary CRs interact with the nuclei of the air in the atmosphere to initiate cascades of secondary interactions [5]. In 1954, Walter Heitler formulated a first theoretical description of an extensive air shower [6, 7], which is discussed in Section 1.1.2.

To better study CRs, large detector arrays have been built since the mid-1940s. In the 1960s, the then largest CR detector was the array of the Massachusetts Institute of Technology's group at Volcano Ranch, New Mexico. Their 20 stations equipped with scintillator counters were the first to measure a particle at 10^{20} eV [8]. This milestone necessitated new and larger experiments to answer questions at the highest energies [9].

In 1966, Kenneth Greisen, Vadim Kuzmin, and Georgiy Zatsepin theorized the upper limit on the energy of cosmic rays coming from distant sources. Known as the *Greisen–Zatsepin–Kuzmin* (GZK) cut-off, this theory predicted that UHECRs would interact with photons of the CMB and lose a significant amount of their energy over great distances. Protons would lose energy via pion production, whereas heavier nuclei would lose energy via photo-disintegration. Using protons to establish their limits, they found that CRs with energies above 5×10^{19} eV would experience these interactions, leading to a suppression at the end of the energy spectrum. Thus, UHECRs that we measure must mostly originate within $\approx$ 100 Mpc of Earth with minimal contributions from sources further away [9, 10].

The Haverah Park experiment in North Yorkshire deployed the first array of *water-Cherenkov detectors* (WCDs); their 12 km^2 array measured UHECRs for about 20 years [11]. The first evidence for the flux suppression was found by the *High Resolution Fly's Eye* (HiRes) collaboration using fluorescence telescopes [12, 13]. The *Akeno Giant Air Shower Array* (AGASA), which used WCDs, could not confirm these findings [14]. To solve the contention, a greater number of events[1] and better detector techniques were needed, leading to the proposal and development of the *Pierre Auger Observatory* (Auger). Through more than 13 years of data collection, Auger has shown that the flux suppression exists, yet, as to whether this is due to the GZK cut-off or merely from the diminishing acceleration power of sources remains unclear[2]. This is further addressed in the following sections.

Throughout this time period, the study of cosmic rays led to the discovery of the positron, muon, charged pions, various hadrons and mesons, and the first so-called 'strange particles' [4]. CRs continue to provide insight into high-energy physics which cannot yet be probed by man-made accelerators.

[1] While AGASA and HiRes could measure events up to 10^{20} eV, the number of UHECRs in a year that could be observed at these sites was greatly limited. AGASA covered an area of 100 km^2. HiRes, due to its fluorescence telescopes, could only take data on clear, moonless nights. In contrast, the hybrid detector of the Pierre Auger Observatory has an area of 3000 km^2 of WCDs which are overlooked by fluorescence telescopes.

[2] The top-down models where UHECRs originate from the decay of massive particles originating from the early Universe are already strongly disfavored with the current upper limits of the photon and neutrino fluxes ([15] and references therein).

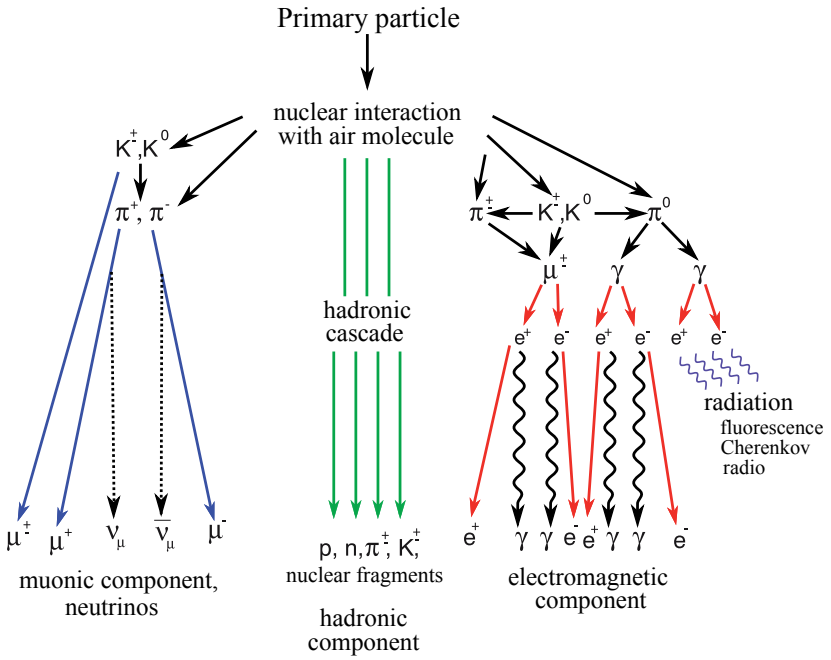

Figure 1.1: Illustration of the components of an EAS. The development of a cosmic ray air shower and the relative branching ratios are described in the text (adapted from [17]).

1.1.2 Extensive Air Showers

Arriving from galactic and extragalactic sources, CRs enter and interact with Earth's atmosphere to produce secondary particles. Provided that each secondary particle has sufficient energy, it too will interact with the atmospheric nuclei to yield further particles. This process continues to repeat, creating what is known as an *extensive air shower* (EAS).

In each of these interactions, roughly half of the original energy is distributed among the generated hadrons. Mostly, light mesons —such as pions (about 90 %) and kaons (about 10 %)— are created, whereas baryons are rarely produced [16]. Around a third of the pions created in the first interaction are neutral; these almost immediately decay into two high energy photons. In contrast, the charged pions and kaons have longer lifetimes and usually produce more particles in successive hadronic interactions with the atmospheric nuclei or decay into muons.

The development of an air shower may be described with three particle components (depicted in Fig. 1.1):

- Dominating at the start of an EAS, the **hadronic** component contains nuclear fragments and long-lived charged pions and kaons. For each hadronic generation, roughly a third of the energy is transferred to the electromagnetic component, feeding new electromagnetic sub-showers.

- Carrying 98 % of the shower's energy, the **electromagnetic** component is comprised of ($e^{\pm}$, γ). π^0-decays mostly feed this cascade.

- When the charged pions decay —generally near the end of the hadronic cascade, they decay into muons ($\mu^{\pm}$) and muon neutrinos. This gives rise to the **muonic** component, which propagates toward the ground with a low probability of interaction.

A brief discussion of these components based on the Heitler (or cascade) model follows [6, 7]. To note, in air shower universality, the components describing an EAS are defined

based on their unique signal and timing properties. A more detailed overview of the particle components used in the air shower universality analyses is given in Section 3.1.2.

1.1.2.1 Electromagnetic component

As portrayed in the rightmost cascade of Fig. 1.1, the development of the electromagnetic component may be described with two physical processes. In what is known as pair production, photons create e^+e^- pairs when interacting with a nucleus. In turn, the $e^\pm$ are decelerated when deflected by the magnetic field of a nucleus, and the lost kinetic energy is converted into a photon in the process known as bremsstrahlung. This interaction roughly occurs after one splitting length $\mathrm{d} = \ln(2)\lambda_r$, where $\lambda_r \approx 37\,\mathrm{g\,cm^{-2}}$ is the electromagnetic radiation length in air.

Extending this simplified description further, the Heitler model assumes that the particle number is doubled with each interaction and that the energy is shared equally among the particles. Thus, after n steps, the shower consists of 2^n particles. This process will continue until the energy of an individual particle drops below a critical energy (in air $E_c^e \approx 85\,\mathrm{MeV}$). Below this critical energy, electrons begin to lose more energy in collisions than in radiative processes and are thus absorbed by the atmosphere. A portion of this transferred energy is released in isotropically-emitted fluorescence light. See Section 1.2.2 for an overview of how Auger measures this light to recover/reconstruct macroscopic information of the primary CR.

Of course, this simplified model is not completely accurate. In most cases, an $e^\pm$ will not deposit exactly half of its energy into a single bremsstrahlung photon. Nevertheless, the simple model encapsulates the following facts:

- The total number of electromagnetic particles is proportional to the primary energy.
- The atmospheric depth of maximum shower development is logarithmically proportional to E_0.

The electromagnetic component may also be treated quantitatively using the cascade equations [7, 18].

1.1.2.2 Hadronic component

The hadronic component derives from the production of hadrons, nuclear deexcitation, and pion and muon decays. It is thus composed of soft processes with small momentum transfers, which cannot be calculated with quantum chromodynamics. It is, however, possible to extend the electromagnetic Heitler model to qualitatively describe the hadronic development of a proton-induced air shower. Through superposition, this model may be extended to describe heavier nuclei; the shower of a nucleus with atomic number A and total energy E is described as A showers induced by protons with energies E/A.

Like the electromagnetic cascade, the hadronic one continues to develop until the individual pions have less energy than the critical energy; this is where the decay length of the pion is less than the distance to the next interaction. This critical energy scales with atmospheric density, and typical values for air showers are 20 to 30 GeV. At this stage of development, as depicted in the leftmost cascade of Fig. 1.1, charged pions decay into muons and neutrinos. The number of generations to reach this energy is around four to seven for air showers [19]. Due to their difficult-to-observe nature, the neutrinos created in these reactions are part of the *invisible* energy and are estimated from simulations to contain about 5 % of the total energy.

Further knowledge of the hadronic component is gained with air shower simulations, which are based on the extrapolated cross-sections from proton-proton collisions at the LHC and fixed-target proton-nucleus experiments (e.g. CASTOR, NA61). The leading software for generating simulations of air showers is CORSIKA [20]. This program provides a structured interface in which low- (e.g up to around 100 GeV: FLUKA [21], GHEISHA [22]) and high-energy (e.g. QGSJET-II.04 [23], EPOS-LHC [24], and SIBYLL-2.3 [25]) hadronic interaction models are used to generate air showers induced by protons, nuclei, photons, or many other types of particles. The main difference between these hadronic interaction models is which chromodynamic theory is used for the extrapolation (e.g. Gribov-Regge theory, mini-jet models, etc.). As the LHC and other particle physics experiments are upgraded to accelerate particles to even higher energies, these models can be tested and tuned to provide results that will, ultimately, better agree with the measurements of UHECRs and describe the physical interactions and phenomena observed immediately after the Big Bang.

1.1.3 Macroscopic characteristics

The three main observables studied to determine the nature of cosmic rays are their energy spectrum, mass composition, and arrival directions. The chemical composition of air showers is useful for understanding the features in the energy spectrum, helping to discover the sources of CRs, and elucidating the origin of the flux suppression at the highest energies. As UHECRs are studied by observing the atmospheric showers they produce, their composition is thus inferred from measurements such as the depth of the shower maximum $X_{\max}$ and the number of muons N_μ generated by an EAS. With Auger, we are able to measure the $X_{\max}$ with fluorescence telescopes and the N_μ with ground-level WCD and underground muon counters, as discussed further in Section 1.2. The muon measurement also provides insight into hadronic interactions, which are currently extrapolated from data of the LHC.

1.1.3.1 Energy spectrum

As shown in Fig. 1.2, the cosmic ray energy spectrum extends over more than ten orders of magnitude in energy. It is well described by a steeply falling power law. Through the flux measurements made by the various experiments, four distinct spectral features became evident.

The first steepening of the spectrum —known as the **knee**— occurs at around 3×10^{15} eV . The *Karlsruhe Shower Core and Array Detector* (KASCADE) experiment has shown that this observation corresponds to a loss of light elements in the all-particle flux [26, 27]. Around 8×10^{16} eV, a less pronounced steepening of the spectrum is observed. Dubbed the **second knee**, this feature can be attributed to an extinguishing heavy component in the flux [28]. 'Knees' for intermediate masses are found through detailed analyses, yet the overall flux adds up such that these are not visible in the all-particle spectrum.

While the knees in the spectrum are understood as features of the flux of galactic CRs, the **ankle** at 5×10^{18} eV is a feature attributed to the transition of the galactic to the extragalactic component. Three scenarios are used to describe the ankle:

1. The **pair production dip** scenario, shown in Fig. 1.3a, claims that the flux of extragalactic protons is already dominant at energies below the ankle. However, this flux is suppressed due to e^+e^- pair-production processes with photons from the CMB [29]. In this scenario, the galactic flux of iron must quickly drop, and the proton fraction must be greater than 80 %.

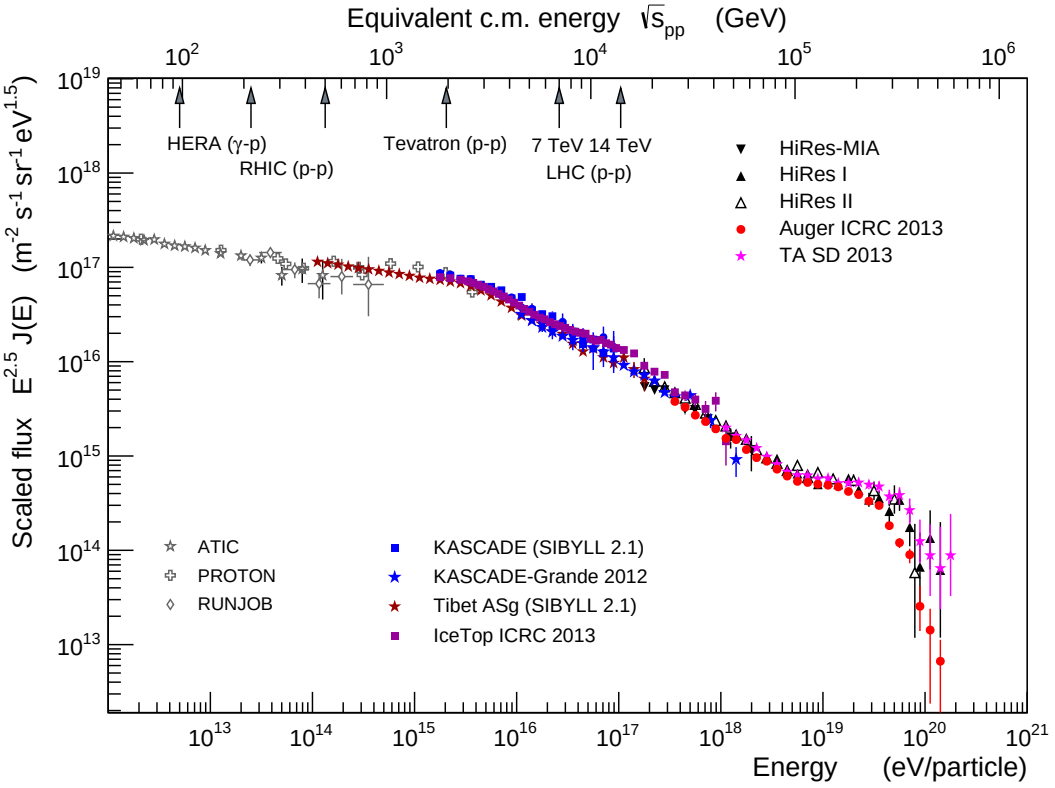

Figure 1.2: Measurements of the flux of CRs from various experiments. The flux is scaled by $E^{2.5}$ to better visualize spectral features, which are discussed further in the text [30].

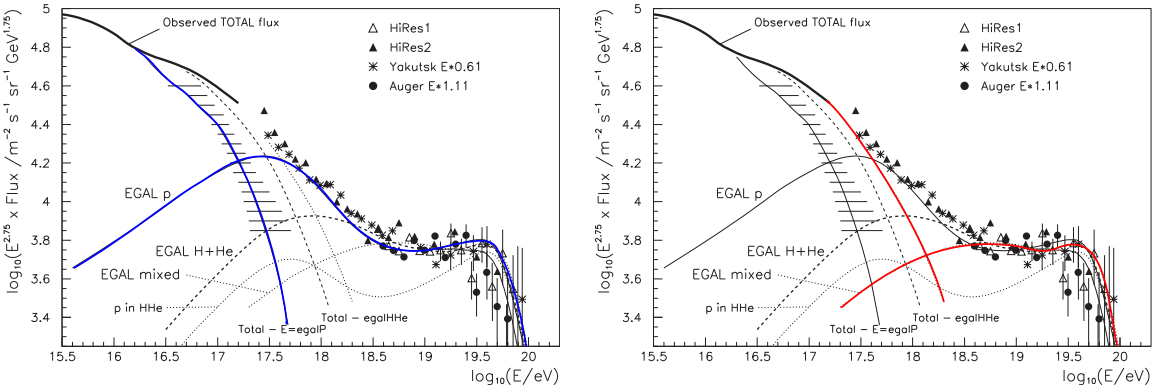

(a) **(b)**

Figure 1.3: Visualization of the (a) pair production dip [29] and (b) mixed composition [31] scenarios that describe the ankle feature.

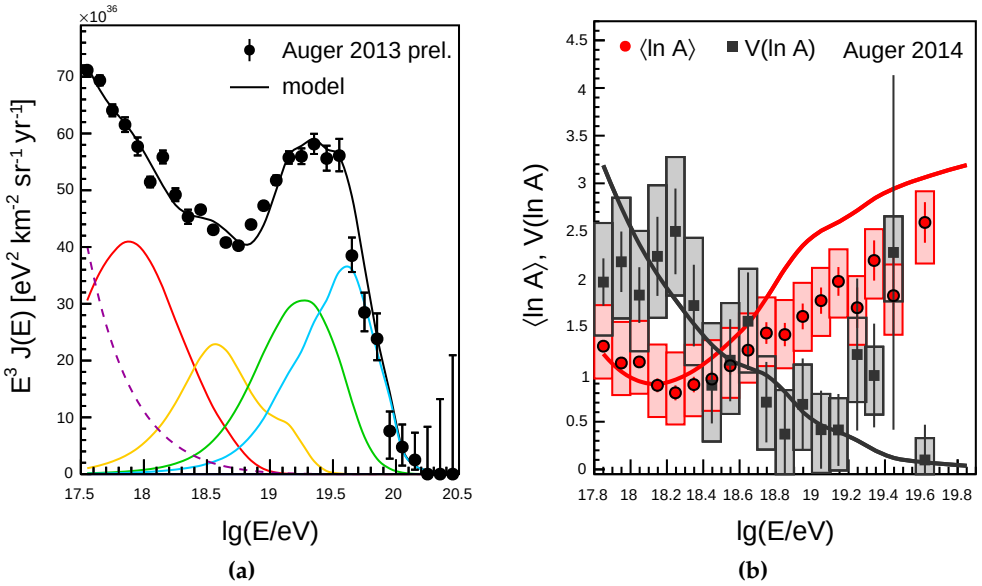

Figure 1.4: (a) Comparison of the predicted flux of UHECRs to a recent combined Auger spectrum. The flux is scaled with E^3; the best-fitting model using pure silicon (aqua) is shown. (b) Prediction of the average logarithmic mass and its fluctuations. A comparison to recent Auger results from [33] is given. Statistical uncertainties of the measurement are represented with error bars, while systematic uncertainties are depicted with boxes [32].

2. Depicted in Fig. 1.3b, the **mixed-composition** scenario predicts that the galactic component dominates before the ankle and that the transition to extragalactic particles occurs at the ankle [31].

3. A more recent model based upon the **photo-disintegration of UHECRs at the sources** offers an alternate explanation for the ankle as well as the flux suppression. At energies below the ankle, heavier injected nuclei are disintegrated at their sources as their escape times are larger than their interaction time; thus, the flux in this region is dominated by protons originating from higher energy nuclei. Above the ankle, an increasingly larger fraction of heavy nuclei can escape before interacting. Coupled with realistic assumption on the magnetic and photon fields of sources, this model is able to reproduce the spectrum and mass composition of UHECRs as measured with Auger as shown in Fig. 1.4. For more details on this model and the inherent assumptions, see [32].

As previously mentioned, the flux at the highest energies is suppressed above 3×10^{19} eV. In part, this suppression can be attributed to the GZK effect. As protons with energies above 5×10^{19} eV propagate, they interact with photons from the CMB leading to a Δ-resonance:

$$\gamma_{\mathrm{CMB}} + p \rightarrow \Delta^+ \rightarrow p + \pi^0\,,$$
$$\gamma_{\mathrm{CMB}} + p \rightarrow \Delta^+ \rightarrow n + \pi^+\,.$$

Around 20 % of the energy of the primary proton is lost with each interaction. Taking into account the mean free path of this interaction, extragalactic protons with energies above this threshold must originate from within $\approx$ 100 Mpc of Earth. In Fig. 1.10a, the energy loss as a function of distance is shown for protons. Heavier nuclei are affected by photo-disintegration processes, leading to similar energy losses. Nevertheless, the flux suppression might merely be experimental evidence of the maximum energy attainable

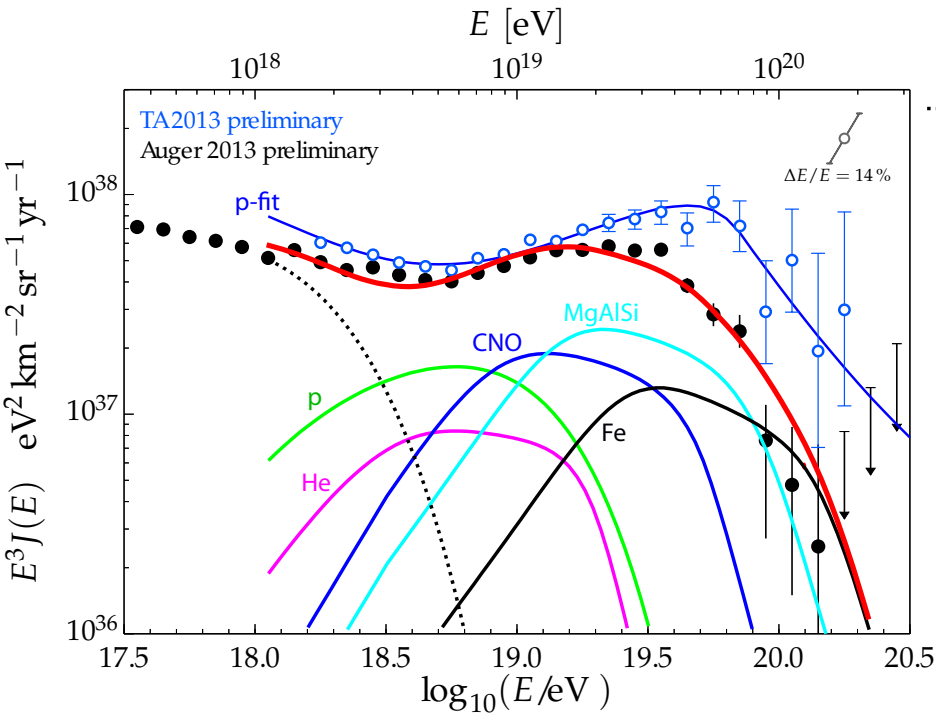

Figure 1.5: Measurements of the flux of UHECRs as published by TA and Auger [35, 36]. TA data is fit to a model of extragalactic proton sources (blue line). Auger data is compared to a model assuming (1) a maximum acceleration energy where the flux as a function of energy E is proportional to E^{-1} and (2) an enhanced galactic CR composition from [37]. An additional galactic components is plotted as a dotted black line [34].

by cosmic accelerators. As discussed in relation to the 'knees', we would, thus, expect charge-dependent cut-offs for the different extragalactic components. In Fig. 1.5, Auger data is described with such a charge-dependent mixed model, where the maximum energy is defined as $E_{\mathrm{max}} = Z \times 10^{18.7}\,\mathrm{eV}$. In contrast, *Telescope Array* (TA) data is fit to a pure proton model with the GZK suppression taken into account [34]. To elucidate the physical composition and the main propagation effect, further determination of the mass composition of UHECRs is necessary. Both, the current Auger results described in Section 1.2.7 and the results derived in Chapter 5 strongly disfavor a pure proton scenario at the highest energies.

1.1.3.2 Mass composition

While there are several empirical and physical observables associated with determining the mass composition, we will restrict our focus here to the depth of the shower maximum. As an EAS develops, sub-showers of particles are generated until the critical energy of an individual particle is reached. At this point, the interaction probability is less than the probability of the particle decaying, losing energy, or being absorbed by the atmosphere. After this stage of the shower development, an EAS diminishes. The point along the shower axis where the energy deposit is maximal is known as the depth of shower maximum X_{max}. Most of the energy of an air shower is carried by the electromagnetic component, which can be described as a function of traversed air density or grammage:

$$X = \int_z^\infty \rho(\vec{r}(z'))\,\mathrm{d}z' \,.$$

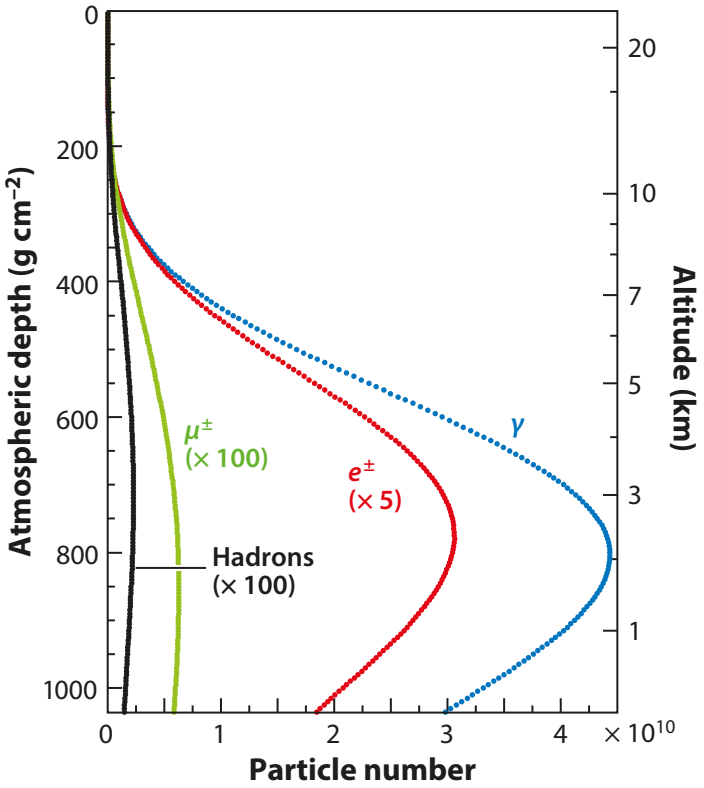

Figure 1.6: The longitudinal profiles of different particle components from a CORSIKA simulation of a proton-induced air shower with a primary energy of 10^{19} eV [38].

Extending the Heitler model presented in Section 1.1.2, it follows that the depth of maximum development of an iron shower with energy E will be higher in the atmosphere than the one of a proton shower with identical energy E. Thus, $X_{\max}$ is used to discriminate particles by their primary mass. A generalized superposition model describing the relationship of the mean $X_{\max}$ with respect to energy E and primary mass A is [39]:

$$\langle X_{\max} \rangle = X_0 + D \lg \left(\frac{E}{E_0 A} \right) + \xi \ln A + \delta \ln A \lg \left(\frac{E}{E_0} \right) ,$$

where X_0 is the mean depth of proton showers at an energy of E_0 and D is the elongation rate —the change of $\langle X_{\max} \rangle$ per decade in energy, and ξ and δ encapsulate deviations from the ideal superposition model. The dispersion of $X_{\max}$ is expected to be only influenced by shower-to-shower fluctuations:

$$\sigma^2(X_{\max}) = \sigma^2_{\text{sh}}(\ln A) . \tag{1.1}$$

The longitudinal profiles for the different particle components of a proton CORSIKA simulation are depicted in Fig. 1.6. The measured average depth of the shower maximum development $X_{\max}$ is shown in Fig. 1.7.

1.1.3.3 Arrival directions

In considering the energy spectrum shown in Fig. 1.2, we have discussed the transition from galactic to extragalactic sources. In the region of flux suppression, 1 particle per km^2 per century and an exhaustion of sources is expected. Possible sources of UHECRs are summarized in the Hillas plot in Fig. 1.8. For a given source with an accelerating system

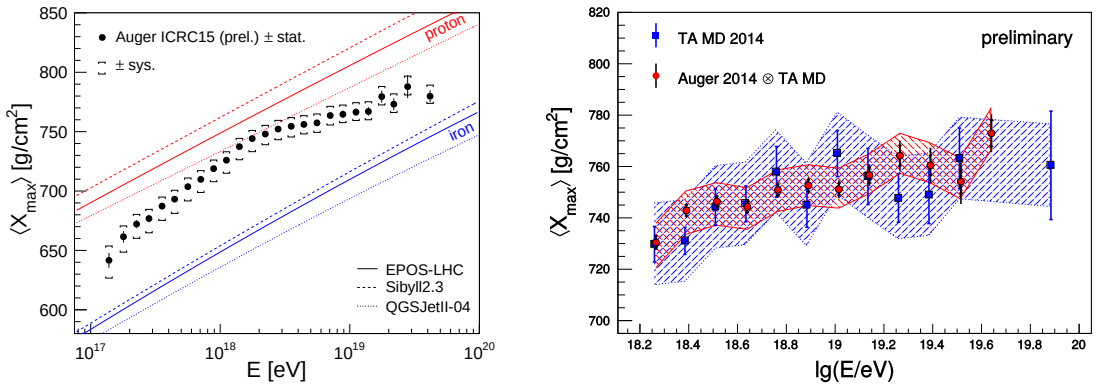

(a) **(b)**

Figure 1.7: The average depth of the shower maximum as a function of reconstructed primary energy. (a) Auger data and comparative models from different hadronic interaction models. While both Auger and TA use fluorescence detectors to measure $X_{\max}$, they account for biases and detector effects in a different manner. (b) When data from the Middle Drum detector of TA (TA-MD) is compared to Auger data folded with the TA acceptance, the compatibility of the measurements of the two experiments is seen [40].

of size R, the maximum energy a particle can attain is determined by its charge Z and the strength of the source's magnetic field B (roughly $E \approx Z\,B\,R$). The Hillas plot uses this formalism to categorize sources, which makes it apparent that only a few sources are able to accelerate particles up to the highest energies. For UHECRs, the most promising sources include active galactic nuclei and gamma ray bursts, whereas pulsars are a less likely (yet still possible) option.

The rather isotropic arrival directions of particles suggest a dominance of extragalactic sources due to the lack of hot spots, which a prevalence of galactic sources would cause. With the pervasiveness of extragalactic sources, the propagation effects as particles traverse the universe must be taken into account. Such effects primarily are determined by the deflections from magnetic fields, which are proportional to the charge Z of the particle, and the energy loss of particles with respect to their distance traversed —for protons, see Fig. 1.10a. Previous efforts have been made to use the arrival directions of particles to backtrack them to their sources, but many of these studies did not take into account charge-based magnetic deflections. In Fig. 1.9 the effect of charge on deflections is illustrated for proton and carbon simulations originating from the same sources. A distinct correlation between proton arrival directions and sources may be seen, whereas the magnetic deflection of the carbon signal (as observed via the arrival directions) has obscured the sources. With this in mind as well as taking into account the interactions of UHECR with the CMB, it is possible to compute the probability that a proton event measured with a given energy came from a source within a given distance, as shown in Fig. 1.10b. The GZK interaction begins to have a significant impact at an energy of 8×10^{19} eV, where there is only a 10 % probability that the cosmic ray traveled a distance greater than 100 Mpc.

1.2 Pierre Auger Observatory

Located in the Argentine Pampas near Malargüe, the *Pierre Auger Observatory* (Auger) [43] is the world's leading hybrid detector for measuring UHECRs. Due to the low particle flux observed at the highest energies, the *Surface Detector* (SD) of the observatory, which

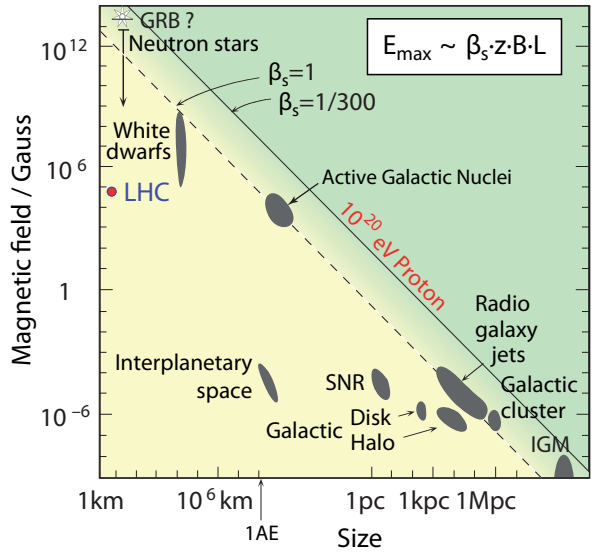

Figure 1.8: The Hillas plot illustrates possible candidate sources for UHECRs. The solid (dashed) diagonal represents the acceleration power required for a 10^{20} eV proton (iron nucleus) [31].

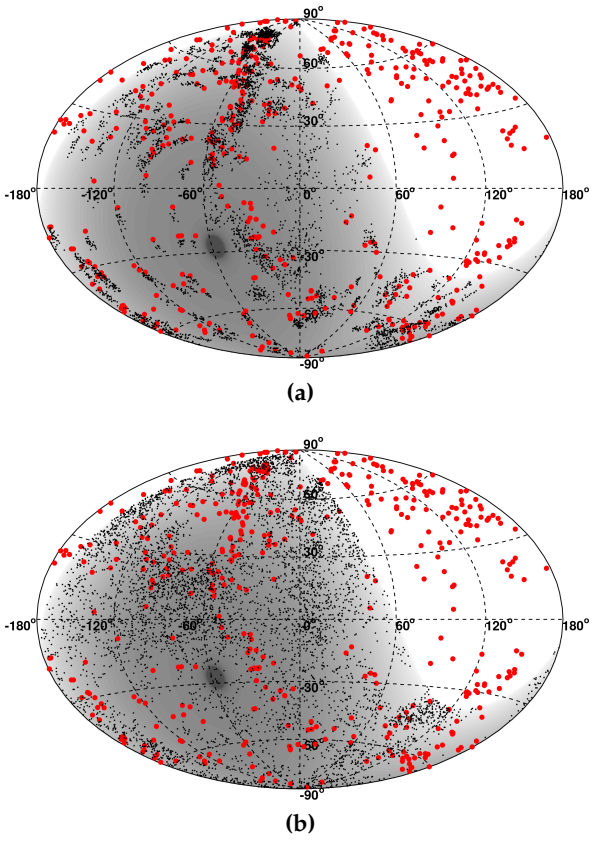

Figure 1.9: The arrival directions of simulated (a) proton- and (b) carbon-induced extensive air showers with initial energies of 10^{19} eV are depicted with black points; the initial sources for these simulations are indicated in red [41].

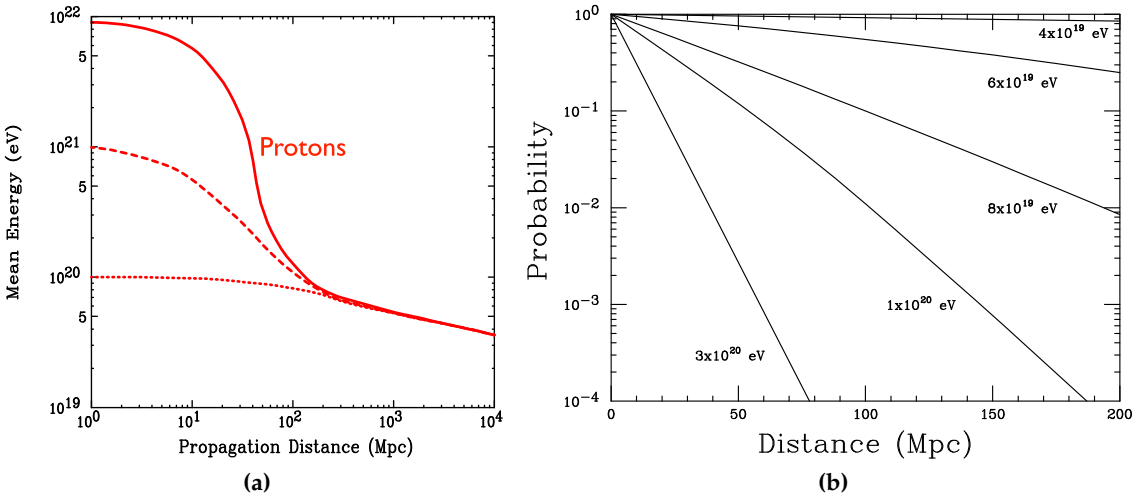

Figure 1.10: (a) Energy losses of protons due to the interaction with photons from the CMB. (b) The probability that an observed event with energy E originated from a source located at a distance larger than that indicated on the abscissa. A source spectrum proportional to $E^{-2.5}$ is used [42].

measures the secondary particles at the ground, covers more than 3000 km^2. Overlooking the SD, the *Fluorescence Detector* (FD) consists of 24 telescopes that observe the light created during the development of an EAS. These complementary measurements allow for the reconstruction of the properties of a primary CR with minimal use of simulations. The fluorescence telescopes measure the calorimetric energy deposited by an extensive air shower as it traverses the atmosphere —known as the longitudinal profile. The depth at which the energy deposited is maximal —X_{max}— is closely related to the primary mass. On average, proton-induced showers will develop deeper in the atmosphere, whereas iron-induced ones will develop earlier in the atmosphere[3]. In contrast, the SD detector measures the distribution of particles at ground. While the signal measured in each station is correlated with the energy and mass composition of the primary particle, the SD cannot directly determine the energy. Instead, its energy scale must be calibrated with the FD. The SD operates at a duty cycle of around 100 %, whereas the light-based detection used by the FD[4] is limited to clear, moonless nights which amounts to a duty cycle of around 15 %.

The location of the observatory is optimal: rain is rare, light pollution is minimal, and the atmosphere is relatively clear. Nevertheless, to account for seasonal and daily fluctuations, the atmosphere is monitored using lasers —located at the *Central Laser Facility* (CLF) and *Extreme Laser Facility* (XLF). In addition to the aforementioned detectors, there are a few extensions that have been added or are being currently deployed. Since the beginning of the measurement at the observatory in 2004, there have been several noteworthy discoveries; selected results relevant to this work are discussed in Section 1.2.7. A pictorial overview of the location of the detectors and supporting facilities for the Auger Observatory is given in Fig. 1.11.

[3] See Section 1.1.3.2 for more details.

[4] Furthermore, many of the events measured by the FD are removed by quality cuts prior to analysis. As discussed in more detail throughout this section and Section 2.5, the main quality cuts relate to the the change of the fluorescence yield as a function of temperature and pressure, as well as the limited field of view of each telescope. In contrast, the effects of weather on the SD energy have been found to be on the order of 0.5 % [44].

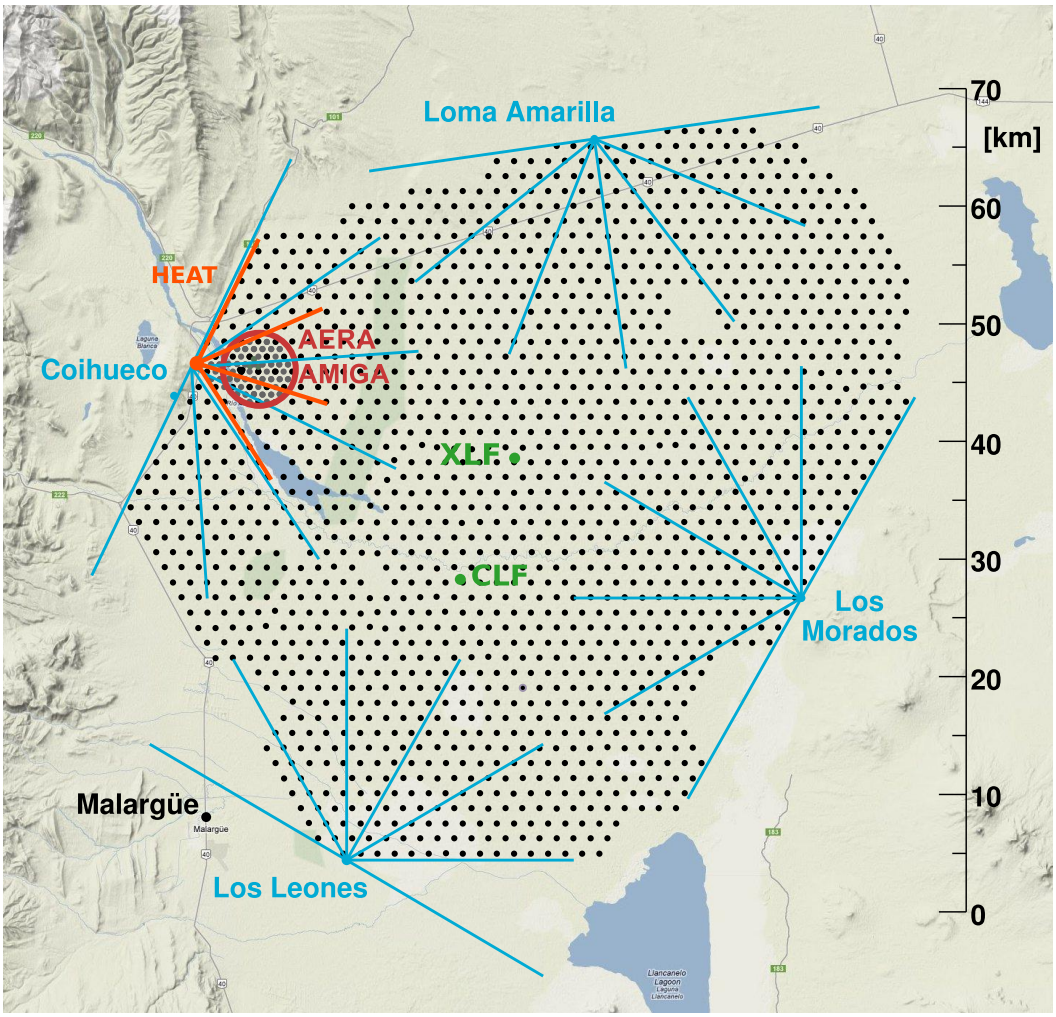

Figure 1.11: Overview of Auger. The location of each SD station is denoted with a dot. The FD buildings are located at Los Leones, Coihueco, Loma Amarilla, and Los Morados; the field of view of each telescope is demarked by the blue lines. Also shown are *High Elevation Auger Telescopes* (HEAT), *Auger Engineering Radio Array* (AERA), *Auger Muon Detectors for the Infill Ground Array* (AMIGA), and the essential facilities for atmospheric monitoring —*Central Laser Facility* (CLF) and *Extreme Laser Facility* (XLF). A denser array of SD WCDs (known colloquially as the *infill*) is located in the vicinity of HEAT, AERA, and AMIGA; it compliments the measurements of these detectors for energies above $10^{17.5}$ eV. Each aspect of the observatory is described further in this section (adapted from [45]).

1.2.1 Surface Detector

The standard SD is composed of more than 1600 WCDs that are tessellated across the observatory in triangular grids[5] with 1500 m spacing [46]. With this geometry, the threshold for full trigger efficiency is reached for primary energies above 3×10^{18} eV; further details of event selection and reconstruction are given in Chapter 2. Each WCD is 10 m^2, 1.2 m tall, filled with 12 tons of purified water, and lined with a reflective surface. Symmetrically distributed at 1.2 m from the center of the tank's inner lid are three nine-inch diameter, downward-facing *photo-multiplier tubes* (PMTs). Solar panels are installed on each WCD to power the PMTs and other electronics. A schematic of a WCD is given in Fig. 1.12a. For

[5]With the exception of stations on the border of the array, each station is surrounded by a hexagon of neighboring stations.

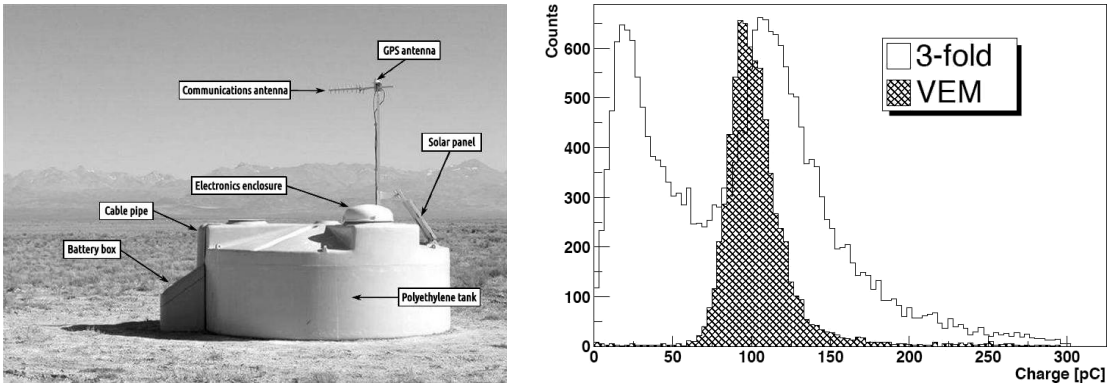

(a) (b)

Figure 1.12: (a) Schematic of a WCD [43]. (b) Average charge spectrum from WCDs used for the *vertical-equivalent muon* (VEM) calibration as detailed in the text [43].

studying lower-energy CRs, other tank spacings of 750 and 433 m have been added to the observatory. To differentiate between these configurations, they are designated by their spacing —e.g. *SD array with 1500 m spacing* (SD-1500).

As charged secondary particles from an EAS enter a WCD, some of them have a speed greater than the phase velocity of light in water. The interacting with such particles leads to the electrical polarization of the water, yielding light upon return to equilibrium. This light is scattered, reflected, and, lastly, collected by the PMTs. Within each PMT, there are two outputs which are relayed: an anode and dynode signal. The information from these coupled signals enables a higher dynamic range for the signal measurement and is motivated by the steep power-law-like drop of the particle density with increased distance to the shower core. The analog signals from the PMTs are filtered and digitized by two 10-bit, 40-MHz semi-flash analog-to-digital converters. Over time, we expect the signal response to change due to aging of the electronics and possible water contamination. To account for these differences and enable comparisons with Monte Carlo simulations, signals are continually calibrated in units of VEM[6], which corresponds to the signal induced from a *vertical centered through-going* (VCT) muon, prior to air shower analyses. Atmospheric muons pass through the SD at a rate of around 2500 Hz, providing a natural tool for calibrating the WCDs roughly every minute. While the SD cannot select VCT muons from the muon flux, vertically aligned plastic scintillators on the top and bottom of a test tank aided in the calibration procedure; histograms for the calibration are shown in Fig. 1.12b. The black-lined histogram shows the average charge spectrum when the three PMTs trigger in coincidence; the hatched histogram contains only vertical muons without coincidence required. The difference in the peaks of the two histograms can be attributed to the increase of light production as a muon's track length increases with inclination. The time-binned signals are converted by equating the histograms' peaks with an expression of integrated signal in units of VEM. Further details of the calibration are found in [47].

When the signal is very large, the electronics of a WCD hinder a proper measurement [48]. The semi-flash analog-to-digital converter has a 10-bit dynamic range. For the baseline offset, roughly 50 channels are used, which leaves more than 970 channels for the signal range. As a VEM corresponds to around 50 channels in the dynode and 1.6 channels in the anode, overflow of the readouts will occur at around 20 and 600 VEM respectively. Additionally, the PMTs respond non-linearly above 50 mA, which occurs around the onset

[6] vertical-equivalent muon

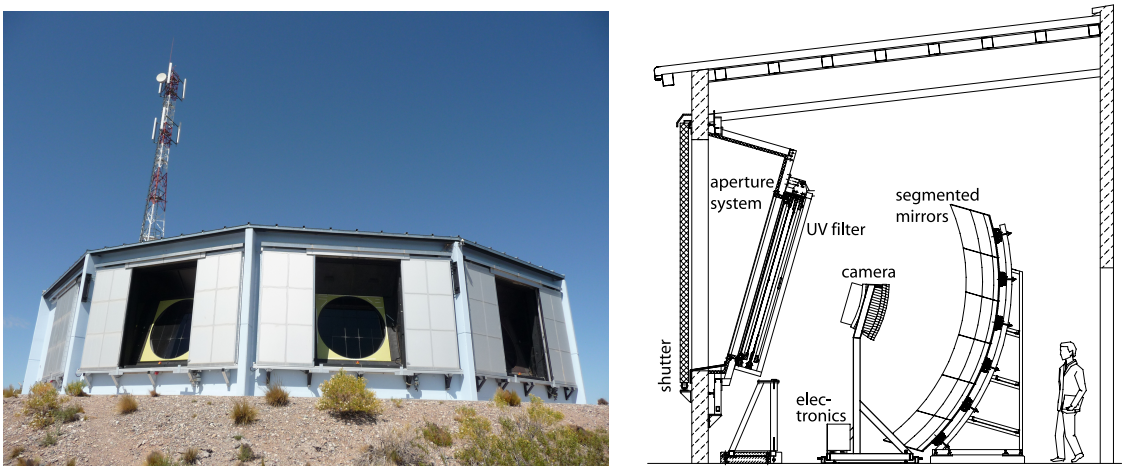

(a) (b)

Figure 1.13: (a) FD building at Los Leones [43]. (b) Schematic of an FD telescope [43].

of the overflow of the anode. Several methods have been developed to successfully recover these saturated signals to estimate the true signal [48–50].

1.2.2 Fluorescence Detector

The standard FD consists of 24 telescopes housed in four buildings surrounding the standard SD [51]. Each telescope covers a *field of view* (FoV) of $30^\circ \times 30^\circ$ in azimuth and elevation. With six telescopes in a building, this renders a joint FoV of 180° in azimuth for each site. For observing lower-energy primaries which produce shallower showers, three additional telescopes with an elevated FoV (maximum elevation of 29°) were added in an adjacent building at the Coihueco site. Just as the standard FD corresponds to the standard SD (SD-1500), the elevated telescopes, known as *High Elevation Auger Telescopes* (HEAT), overlook the SD-750[7] (full trigger efficiency at 3×10^{17} eV). An FD building (Los Leones) is shown in Fig. 1.13a.

As an EAS develops, secondary electromagnetic particles excite the nitrogen molecules of the atmosphere. In their return to their ground state, these nitrogen molecules isotropically emit fluorescence light with peaks in wavelength at 337 and 357 nm. In order for an FD telescope to observe this light, the fluorescence photons must pass through a circular diaphragm with a radius of 1.1 m that is covered by a filter glass window. This filter reduces the background light flux, improving the signal-to-noise ratio, and acts as a shield between the telescopes and the outside. The bombarding light is focused by a segmented spherical mirror of 13 m^2 with a 3400 mm radius of curvature onto the camera. The camera is composed of hexagonal PMTs arranged in a 22 x 20 grid. A Winston cone aids in directing light to the active cathode of a 45.5 mm-wide PMT. A schematic of an FD telescope is shown in Fig. 1.13b.

The light collected by the FD provides a calorimetric measurement of the longitudinal profile of an EAS. Essentially, the FD is directly observing the electromagnetic development of an air shower. Thus, in order to best reconstruct an air shower, it is critical to minimize or account for light reduction agents as much as possible. To this effect, the telescopes are in clean, climate-controlled rooms, and regular cleaning of the outside of the filter is performed. As it is a cleanroom, the inside apparatus is cleaned less frequently. Nevertheless, ongoing

[7] SD array with 750 m spacing

studies indicate that dust on the parts of the apparatus has an impact on the final energy scale of Auger —on the order of 10 % [52]. In addition, ambient conditions affect the measurements by scattering, attenuating, or competing with the fluorescence light: other light sources (i.e. the sun and moon), atmospheric pressure, humidity, temperature, aerosols, and cloud coverage. The atmospheric-related effects are monitored nightly and discussed in detail in Section 1.2.3. Thus, for optimal measurements, the FD is operated only on clear, moonless nights, yielding a duty cycle around 15 %. In the near future, however, the duty cycle will be increased to around 21 % [15]. Recent efforts found that an increase in the duty cycle is possible by operating the FD during times where the fraction of the moon in the sky is large. To protect the PMTs from deterioration from excessive anode current, the voltage supply will be reduced during these time periods.

1.2.3 Atmospheric monitoring

Atmospheric monitoring is critical for the calorimetric measurement of the FD, and it is moderately important for the measurements of the SD. Many of the atmospheric monitoring sites are shown in Fig. 1.11: the *Extreme Laser Facility* (XLF), *Central Laser Facility* (CLF), lidars, and *infrared* (IR) cloud cameras. Atmospheric variables —such as temperature, humidity, and pressure— directly influence the longitudinal development of air showers as well as the amount of fluorescence light emitted and scattered by molecules. Due to the effect of weather on the shower development, the secondary particle densities observed at the ground are also affected.

During the nights per lunar cycle that are dark enough to operate the FD, hourly measurements of the aerosol contamination are made using the XLF and CLF. Air temperature, pressure, wind speed, and humidity are recorded at ground level by weather stations at the CLF and FD buildings. Additionally, the *Global Data Assimilation System* (GDAS) provides valuable continuous information about atmospheric parameters [53]. Scanning the atmosphere outside the FoV of the FD, lidars measure the mean cloud cover and the lowest cloud height each hour [54]. IR cloud cameras complement the lidar data by providing 2D images of the whole FoV every five minutes. Overall, the amount of aerosols and cloud cover is estimated from the signature of back-scattered light; this light is collected with separate mirrors and PMTs at each FD site. As the laser shots are fired outside the FoV, the atmospheric monitoring usually does not interfere with FD measurements.

1.2.4 Muon Detector

Collectively known as the *Muon Detector* (MD), the *Auger Muon Detectors for the Infill Ground Array* (AMIGA) is an extension that directly measures the muonic content of air showers [55]. The muonic content of an EAS—like the depth of the shower maximum measured by the FD— is an event-level variable which is used to determine the primary mass composition. AMIGA operates in the energy region (10^{17} eV to 10^{19} eV) where the transition from galactic to extra-galactic sources is thought to occur. With sufficient data, the MD will elucidate the mass composition in this energy range. Additionally, recent results from Auger (Section 1.2.7) have indicated that the muonic content found in data is 20 % to 60 % greater than that estimated from simulations [56, 57]. While the upgrade to Auger (Section 1.2.6) will be able to help with this contention, its methods to do so will benefit from fine-tuning with the direct measurement of the muonic content by AMIGA.

As depicted in Fig. 1.14, the MD consists of plastic scintillators buried a few meters away from the WCDs of the SD-750. The first completed unit was deployed in 2014; deployment across the entire SD-750 is ongoing [59]. To study systematics and accuracies in counting, twin MD stations were deployed at two locations in the unitary hexagon. Each

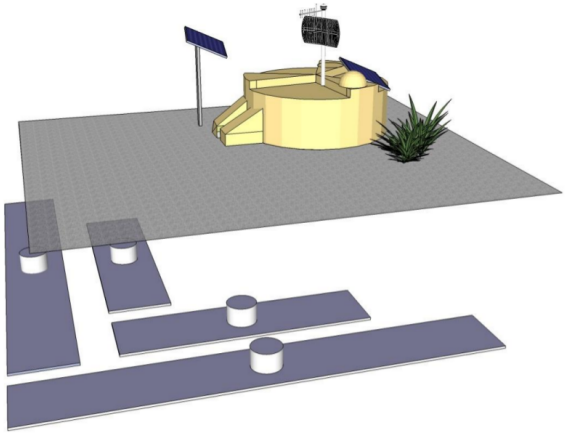

Figure 1.14: A WCD station of the SD-750 is shown with its surrounding muon counters [58].

MD station consists of two 5 m^2 and two 10 m^2 scintillator counters, which are buried 2.25 m underground. The soil shielding, amounting to approximately 540 g cm^{-2} of vertical mass, significantly attenuates contamination from electromagnetic particles. Each of the modules is comprised of 64 scintillation bars of 40 mm x 20 mm. As muons enter the detector, light is produced via scintillation; it is channeled via optical fibers to PMTs. Unlike the SD, the MD only returns the count of muons above a given threshold —not the signal or peak intensity. The threshold value for each of the 64 bars is individually monitored and set with a calibration algorithm. Thus, the count of muons minimally depends on the gain and fluctuations of the PMT, the impact position of the muon on the bar, and the light attenuation along the fiber length [60].

1.2.5 Radio Detector

Located within the SD-750, the *Auger Engineering Radio Array* (AERA) —the world's largest radio detector for CR showers—consists of 153 radio stations covering an area of 17 km^2. As an EAS develops, the charged particles are deflected in the Earth's magnetic field via the Lorentz force. These deflected particles emit coherent radiation in the MHz regime [61]. Askaryan emission —radio emission due to the time-varying net-charge excess of the shower— minimally contributes to the observed radio signal [62]. Like the FD, the *Radio Detector* (RD) directly observes the electromagnetic component of an EAS. Due to the size of the array and spacing between stations (at most 750 m), AERA measures above an energy threshold of 10^{17} eV. It is composed of 24 log-periodic dipole antennas (Fig. 1.15a) and 125 butterfly antennas (Fig. 1.15b) that operate in the frequency range from 30 MHz to 80 MHz.

So far, the significant achievements of AERA include: measuring the polarization of the geomagnetic and Askaryan emissions [64], determining the energy of cosmic rays with radio emissions [65], and synchronizing measurements on the nanosecond-level [66]. Some first multi-hybrid events exist and are currently studied. Recently, the LOFAR collaboration was able to reconstruct the energy and mass-sensitive variables —like the shower maximum— with their measured radio emissions [67]. Encouraged by these results as well as duty cycle of nearly 100 %, the RD is a promising candidate for the future measurement of UHECRs.

1.2.6 The Auger Upgrade

In Section 1.1, the current understanding of CR physics was discussed. However, CRs are several orders of magnitude more energetic than what we are able to generate at the LHC,

(a) (b)

Figure 1.15: (a) A log-periodic dipole antenna and (b) a butterfly antenna [63].

are quite rare (steeply falling flux $\propto E^{-2.5}$), and are measured indirectly from the extensive air showers that are produced when they interact with molecules in the atmosphere. As such, there are many open questions in the study of UHECRs. Foremost among these are:

- Which celestial objects are accelerating cosmic rays? How does this acceleration occur at the highest energies? In which energy range are CRs predominantly from galactic or extragalactic sources?
- What sort of interactions do the CRs partake in during propagation from their sources to Earth, which may alter their energies and, possibly, cause the disintegration of their nuclei?
- Which physical mechanism(s) leads to the suppression of the flux at the highest energies?

While many recent results indicate a strong preference for particular models to answer these questions, it is through the direct measurement of the mass composition that the validity of these models may be solidified. As the largest UHECR experiment in the world, the Auger observatory is undergoing an upgrade —known as *AugerPrime*— that seeks to augment the SD by affixing scintillators on top of each WCD station [15, 43, 68]. The differing responses of the two detectors measuring the same event[8] —coupled with the muonic content verification of the MD– will be used to drastically increase the sensitivity of the measurements to the primary composition such that these open questions can be addressed with much more detail and, maybe even, resolved with high statistical significance.

The basic unit for the *Scintillator Surface Detector* (SSD) consists of two modules of around $2\,\mathrm{m}^2$ of extruded plastic scintillator, which is divided into 12 bars that are 1.6 m long and coated with TiO_2 to improve the reflectivity. The light from scintillation is collected by wavelength-shifting fibers coupled to a single PMT. Since October 2016, more than 13

[8]The universality approach investigated in this work heralds the quality of the results which will be obtained with the upgrade. The implementation of universality in this work —with only the SD— is reliant upon the accuracy of simulations, which currently poorly describes the muonic content seen in data. With the additional measurement from the MD and scintillator, universality models and air shower simulations will be greatly improved. The obtained resolutions of the reconstructed observables will be small enough to perform high-level event separation of the primary mass composition.

Figure 1.16: A WCD station of the SD-750 is shown a scintillator on top. The capsules in the foreground are access hatches for the surrounding muon counters [68].

WCDs in the observatory have been outfitted with scintillators; the upgrade is anticipated to be completed sometime in 2020. To support the addition of the scintillator, new electronics have been added, which also facilitate a faster sampling rate of 120 MHz and support the to-be-installed small PMTs[9]. An upgraded station is shown in Fig. 1.16.

1.2.7 Selected results

This section contains an overview of recent results, which are pertinent to this work, obtained from data measured at Auger. For a complete list of physics results and technical reports of the last three years, see [33, 39, 53, 54, 56, 64, 70–103]. The measurement of the flux of UHECRs using ten years of data is shown in Fig. 1.17. The spectrum shows a flattening at an energy of $10^{18.7}$ eV; a feature denoted as the ankle. The flux suppression at the highest energies is established with a significance of more than $30\,\sigma$.

Of particular interest is the mass composition of cosmic rays. This is accessible via the central moments and distributions of mass-sensitive parameters. The first two central moments of the measured distribution of the depth of shower maximum is shown in Fig. 1.18 [104]. At the highest energies, the data trends to heavier elements; however, there are relatively few hybrid events there (due to the low duty cycle of the FD). Similarly, we can use the distributions of the shower maximum to investigate the mass composition, as seen in Fig. 1.19. Again, a trend towards heavier elements is present at the highest energies with intermediate elements favored over more massive elements like iron. The results and discussion are given in Chapter 5.

The number of muons is another mass-sensitive parameter. Unlike the shower maximum, the number of muons is not immediately measured by the FD or vertical events of the SD; although, future work with AMIGA and SSD should provide further insights. To derive the muonic content, different methods have been developed, including one from shower universality (discussed in Chapter 3). Regardless of the method chosen, a deficit of muons in simulations becomes apparent when comparing with Auger's data [56, 57].

[9] As discussed in Chapter 2 and Appendix D.2, the nine-inch PMTs used by Auger saturate when the core of an EAS lands close to a station. When this occurs, critical information is lost which would help to better constrain the reconstruction. In order to remedy this problem, a smaller PMT, which saturates at a much higher threshold. will be installed inside each tank.

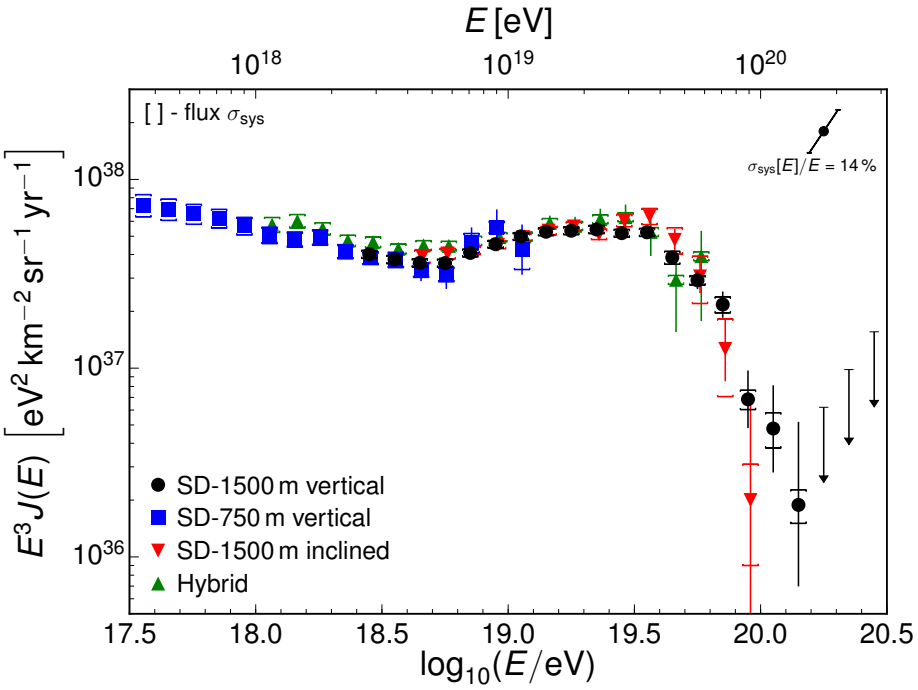

Figure 1.17: Results on the measurement of the flux of UHECRs from Auger data: SD-750, SD-1500, inclined events with zenith angles above 60° measured with the SD-1500, and hybrid events. The overall systematic uncertainty of the energy scale is 14 % [69].

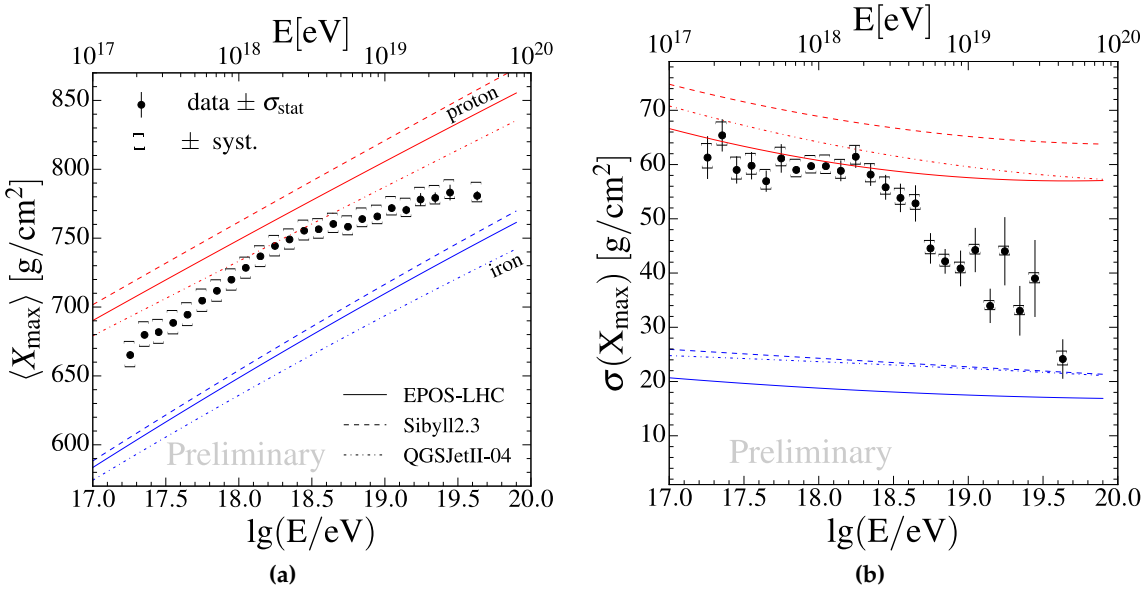

Figure 1.18: (a) The average X_{max} and (b) second central moment of X_{max} from hybrid events as functions of the primary energy. For comparison, model lines from current proton and iron air shower simulations are included [104].

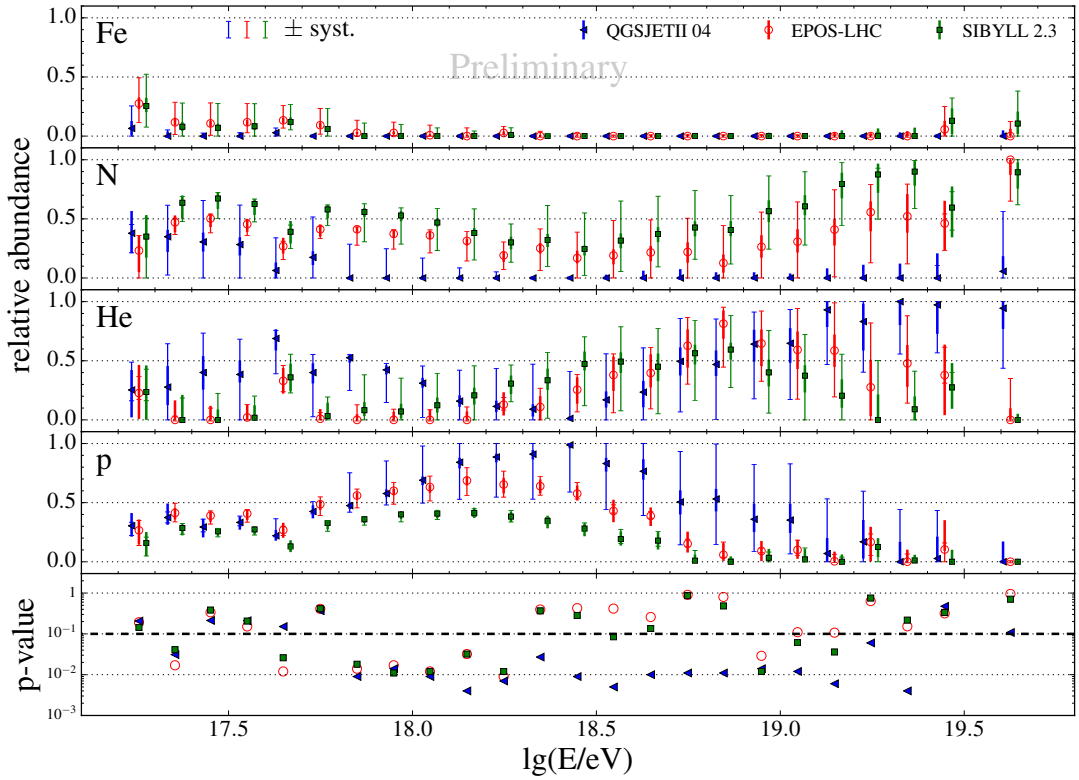

Figure 1.19: Fit of the $X_{\max}$ distribution measured by Auger FD as a function of primary energy to templates of four simulated nuclear fractions. While the relative fractions for a given nuclear species are different for the various interaction models, the general trend —in the evolution of the mass composition as a function of energy— from a lighter to a heavier composition is jointly observed. The p-values indicate the goodness of the fit to the simulated distributions; values exceeding 10^{-1} are considered relatively well fit [104]. For further information on this analysis, see a similar approach presented in Section 5.3.

Above a zenith angle of 60°, the electromagnetic component of an EAS has fully diminished –due to the (zenith-dependent) traversed atmosphere– before reaching the ground. Thus, the muonic content of air showers may be directly obtained from inclined air showers measured by the SD [56]. In Fig. 1.20a, the measured muons are shown with respect to predictions of two contemporary hadronic interaction models. The absolute reference of 1.0 corresponds to proton at 10^{19} eV and simulated with QGSJET-II.03. While the new interaction models predict more muons than the older ones, the data indicate an even larger relative number close to 2.0. The abundance of muons scales with

$$N_\mu \propto \left(\frac{E_0}{\zeta_c^\pi}\right)^\beta , \tag{1.2}$$

where ζ_c^π is the energy at which further particle $\pi^\pm$ ceases and β is $\approx 0.9 - 0.95$ (the value of which depends upon the chosen interaction model) [7]. The mismatch between the muon number in data and simulations could thus be attributed to the differing energy scale and/or muonic content of simulations. To answer this question, 411 events which were jointly measured by the Auger SD and FD were used [57]. With an energy of $10^{18.8}$ eV to $10^{19.2}$ eV, these events covered a zenith angle range of 0° to 60°, which enabled the selection of distinct zenith bins to accounts for the differing attenuations of the EAS components. The results are given in Fig. 1.20b. R_E is a scaling factor active on the entire ground particle distribution with respect to energy; R_{had} affects only the hadronic (muonic) component.

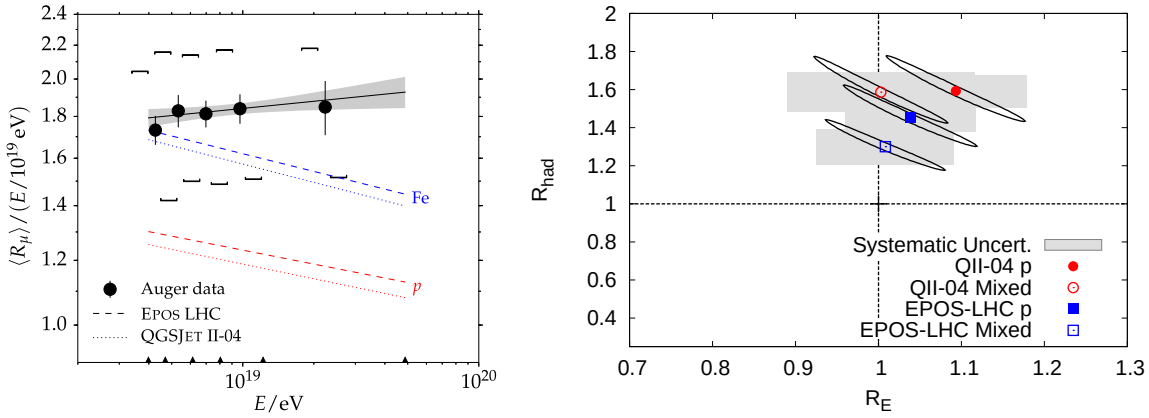

Figure 1.20: (a) Measurement of the relative muon content in inclined air showers [56]. (b) Rescaling of the energy factor R_E and hadronic energy R_{had} to match air shower measurements with recent simulations [57]. The muon numbers need to be rescaled to match data, whereas the energy is on a similar scale to data.

The statistical uncertainty ellipses reflect the strong anti-correlation between the energy and the number of muons. All hadronic models examined indicate that the number of muons in simulations is underestimated by an amount of 20 % to 60 %. Conversely, they show that the overall energy scale is correct, given a fixed, measured ground signal.

CHAPTER 2

Reconstruction of SD events

The *Pierre Auger Observatory* (Auger) (Section 1.2.1) uses a hybrid technique to detect air showers with the *Surface Detector* (SD) and *Fluorescence Detector* (FD). As the FD observes the longitudinal profile of the shower, it provides a calorimetric measurement of the energy of the incident primary. The energy measurement of the FD allows for a mostly simulation-independent way to calibrate the ground signals measured with the SD. The SD reconstruction of an *extensive air shower* (EAS) is performed independent of the FD. The universality approach employed in this work uses the data measured with the *SD array with 1500 m spacing* (SD-1500). Throughout this chapter the event selection and reconstruction method used for the SD-1500 are described.

The SD observes the lateral distribution of an EAS at ground level; an example *footprint* of an EAS is depicted in Fig. 2.1a. The *water-Cherenkov detectors* (WCDs) of the SD are configured in an array of tessellated equilateral triangles with a separation of 1500 m between each pair of stations. To select air shower signals, several hardware and software triggers (Section 2.1.1) are applied. The arrangement and timing of triggered stations are considered in concurrence to select physics events (Section 2.1.3). To ensure the proper functioning of an SD station and the availability of its PMTs, time-based quality cuts (Section 2.1.4) are also applied.

Reconstruction begins with the determination of the shower arrival direction and impact point on the ground (Section 2.3.1). The lateral distribution of station signals is fit with a *lateral distribution function* (LDF) (Section 2.3.2). The estimated signal of the LDF at a defined distance (1000 m) is chosen as the shower size estimator. This signal estimator is shown to be least sensitive to shower-to-shower fluctuations and to assumption on the exact shape of the LDF —including variations due to different primary masses. This shower size estimator is calibrated to the primary energy (Section 2.5) using golden hybrid data —data measured by both the FD and SD.

As discussed in Chapter 3, the universality reconstruction utilizes the distinct timing and signal information from the WCDs of the SD to recover the depth of shower maximum X_{max}, the relative muon content of an air shower R_{μ}, and other mass-sensitive variables which were previously inaccessible to the standard SD reconstruction [105–108]. The results stemming from the mass-sensitive variables are presented in Chapter 5. Both the standard SD and universality reconstruction are implemented in the $\overline{\mathrm{Off}}\underline{\mathrm{line}}$ software [109]. Developed within the Pierre Auger Collaboration, $\overline{\mathrm{Off}}\underline{\mathrm{line}}$ is an extensive framework to simulate the detector response and, subsequently, reconstruct air showers.

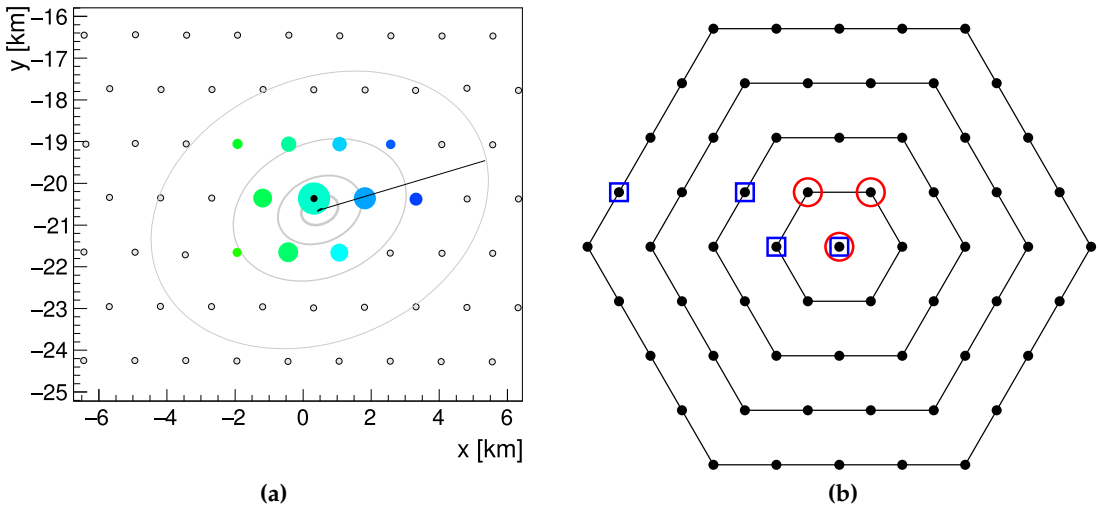

Figure 2.1: (a) The *footprint* of an event with an energy of 1.41×10^{19} eV and zenith angle of 50.6° (Event time: 26. February 2016, Sd Id: 36923464. This particular event is further shown and described in Fig. 2.5 and Fig. 2.3b. The overall size of each station is proportional to its total signal. The color of the stations denote their relative arrival times; stations triggering earliest are blue, whereas the later ones are green. The reconstructed arrival direction of the air shower is indicated with the solid black line (from Offline EventBrowser). (b) Example of an events' station configuration fulfilling the T4-3TOT condition (red) and the 4C1 condition (blue) [110].

2.1 Event selection

The SD trigger system has five levels —T1-T5. Each event must successively pass the triggers individual stations to the triggers characterizing multi-station events, physics events, and those defining quality selection.

2.1.1 Local station triggers

Cosmic-ray-induced air showers generate billions of particles. As such, we expect the three *photo-multipliers* (PMTs) in each triggered WCD to simultaneously measure a signal over a certain threshold. Through studies of the signal, the T1 hardware trigger —applied at each station— was developed; in the event that a given PMT is defective, a modification of the trigger is used so that the station may still be considered in the reconstruction. The criterion for this trigger is that either a coincidence of the three PMTs crosses the threshold value of 1.75 VEM (Thr1, threshold 1 trigger) or a coincidence in two PMTs with more than 12 FADC[1] bins above the 0.2 VEM threshold in a time range of 120 bins.

Next, the T2 requires signals to fulfill any of these criteria:

1. To pass the ***threshold trigger*** **(Thr2)**, the coincident signal must be above 3.2 VEM in all PMTs. This mainly triggers short muonic signals close to the core, which is relevant primarily for inclined showers.

2. The ***time-over-threshold trigger*** **(ToT)** requires signals in two PMTs with more than 13 time bins above 0.2 VEM and within a time window of 120 bins. Its purpose is to discriminate air shower signals from the mostly muonic background. This trigger is most relevant for vertical showers.

[1] flash analog to digital converter

3. Starting in June 2013, two new triggers were added to the stations to enhance the sensitivity to small signals. With the ***time-over-threshold deconvoluted trigger* (ToTd)**, the ToT is modified with a deconvolution of the exponential fall-off of peaks created by muons. This helps to better identify small muonic signals [111, 112]. The ***multiplicity of positive steps* (MoPS)** trigger was added in order to increase the sensitivity to small electromagnetic signals [113] (and references therein). This method looks for certain *steps* in consecutive time bins of a signal trace and is optimized to select small electromagnetic signals.

If a station meets one of the criteria, its information is sent to the *Central Data Acquisition System* (CDAS) for further scrutiny. To note, events with the new station triggers are not analyzed in this work.

2.1.2 Central data station trigger

At the CDAS, the T3 trigger is used to scrutinize the time coincidence of T2 triggers for the identification of stations belonging to a common event —such as an air shower. To minimize triggering on random occurrences, the time window in which coincidence may occur depends on the distance between the stations. Due to the tessellated triangular-geometry of the array, each station is directly surrounded by six others and, moving outwards, concentric hexagons of stations. Each concentric hexagon is known as a crown and contains stations that are the same distance away from the station with the largest signal —the *hottest* station. With this distinction, two different station patterns are used to fulfill this criterion (shown in Fig. 2.1b):

1. A **3-fold condition (T3-3ToT)** requires the coincidence of three neighboring stations with ToT triggers within the first two crowns of the hottest station (including this station). Vertical showers usually fulfill this criterion.

2. A **4-fold condition (4C1)** requires four coincident stations with Thr2 or ToT within four crowns of the hottest station. This condition is mainly relevant for very inclined showers.

The T3 trigger is optimized to be a good compromise between selection efficiency and purity. All events passing this trigger are recorded for later studies.

2.1.3 Physics event selection

With an efficiency of more than 99.99 %, the T4 physics trigger selects air showers and reject lightning, random coincidences, and events with accidentally triggered stations [50]. Seen as a stricter version of the T3, there are two allowed geometries as depicted in Fig. 2.1b: a compact alignment of at least three stations within the first two crowns (T4-3ToT) or a more loose alignment of at least four stations within the first four crowns (T4-4C2). The timing of the triggered stations must be compatible with a planar shower front moving at the speed of light. A variance of arrival times is taken into account to accommodate for the sampling fluctuations and uncertainties in the absolute GPS[2] times of individual stations. Stations with incompatible timing —most likely triggered from background muons— are rejected.

[2]Global Positioning System

2.1.4 Photomultiplier and other quality selections

Each station transfers its state of availability to the CDAS at a rate of 100 Hz. Stored separate from the event data, this station information is used during $\overline{\text{Off}}\underline{\text{line}}$ reconstructions to ensure that stations for an event were properly functioning at the time of said event.

In general, the signal of a station is defined as the mean of the signal of active PMTs. During this step, non-functioning PMTs are removed. The signal does not suffer from this, but the fluctuations of the measured signals increase with the removal of a PMT.

Further quality selections are used; as they are primarily applied after the reconstruction, these will be described in Section 2.4.1 and Section 2.5.2. One of the most basic selection criterion is known as the 6T5 cut, where the hottest tank must be surrounded by six functioning stations. To note, these stations need not trigger for the event. Other common variations of this criterion include the 5T5 and 4T5. In essence, these selections are to ensure: 1) consistency with the exposure[3] calculation and 2) proper reconstruction where the air shower core is enclosed in the array.

2.2 Fluctuations of the SD measurements

As with any scientific measurement, the observance of an EAS by the SD inherently includes the propagation of systematic and statistical uncertainties. To properly reconstruct air showers and estimate uncertainties, a proper study of these effects is required.

2.2.1 Shower-to-shower fluctuations

Due to the probabilistic nature of particle interactions, the development of an air shower is prone to statistical fluctuations. Namely, identical primary particles within identical atmospheric conditions will produce different air showers. Ultimately, this leads to variations in the observables of an air shower —such as the measured ground signals and depth of the shower maximum. While shower-to-shower fluctuations are unquantifiable at the station-level, the event-based shower size estimator has shower-to-shower fluctuations on the order of 10 % [114]. As all stations are subject to the same variation, shower-to-shower fluctuations need not be considered in the event reconstruction.

2.2.2 WCD sampling fluctuations

The signal measurement of the SD is affected by statistical and systematic variations due to changes in 1) the electronic set-up (for signal calibration), 2) the number of photoelectrons produced by particles that trigger the equivalent of a VEM, and 3) the zenith-dependence of the electromagnetic and muonic cascades. Due to their underlying Poissonian fluctuations from the counting of particles, these sampling fluctuations correspond to a relative uncertainty which decreases with increasing signal S and scales with $1/\sqrt{S}$. The overall uncertainty is estimated from the observed variations in the signal measurement of detectors separated by 11 m [113, 115]. Known as *doublets*, these detectors are located in the SD-750.

Additionally, the average signal uncertainty increases with zenith angle as $\propto \sec\theta$. As the zenith angle is increased, the fraction of muonic signal increases with respect to the total signal as shown in Fig. 3.3a. In Fig. 2.2, the uncertainty of the signal is shown as

[3] The exposure is the time-integrated aperture of the detector. As the Auger observatory consists of several components, the aperture at a given time is calculated as the stations available for data-taking of the experiment. The xT5 selections allow for the purely geometrical calculation of the aperture, without need for simulations. The other required ingredient for the exposure is an activity log of individual stations, which is saved every second.

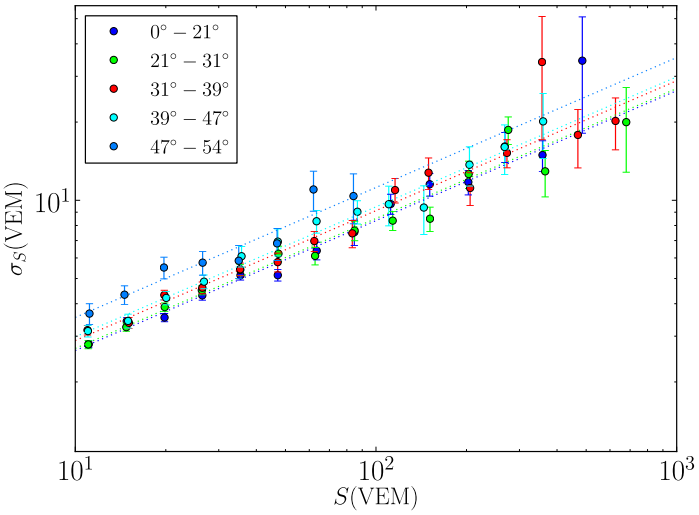

Figure 2.2: Using the measurement from doublet detectors in the SD-750, the uncertainty model for Auger WCDs was derived [115]. The dashed lines represent the model predictions.

a function of the signal in different zenith angle intervals. The signal uncertainty model takes into account the shower-to-shower fluctuations and contributions from the detector resolution [113]:

$$\sigma[S] = \sqrt{\sigma[\text{sh}]^2 \cdot S + \sigma[\text{det}]^2} \tag{2.1}$$

$$\sigma[\text{sh}] := f_S = 0.865\ (1 + 0.593\ (\sec\theta - 1.22)) \tag{2.2}$$

$$\sigma[\text{det}] := 0.023 \cdot S \tag{2.3}$$

where the factor for $\sigma[\text{det}]$ is derived from the calibration uncertainty. For Offline reconstructions, a heuristic Poisson factor is used to convert the signals into effective particle numbers (see Section 2.3.2):

$$p(f_S) = t + \frac{1-t}{\sqrt{f_S}}, \tag{2.4}$$

with $t := 1/\ (1 + e^z)$ and $z := 40\ (0.98 - f_S)$ (shown in Fig. 2.4b).

2.3 Reconstruction

The foundations of the SD reconstruction[4] are the fit of the shower geometry —which takes into account the timing of each station— and the lateral distribution function —which describes the radial dependence of the shower signal with respect to the shower core. As the shape of the LDF varies from shower to shower, an expected signal at a fixed radial distance —dependent on the tank spacing— is used. This estimator is robust as it minimizes the dependence of the LDF on the primary mass. Intrinsically, this method leads to a poor determination of the primary mass[5]. Yet, with this method, the SD is able to reconstruct the energy and arrival direction of the primary cosmic ray with good accuracy.

[4] An overview of the SD reconstruction is presented in this section; it is detailed in [110].

[5] To overcome these issues, a novel reconstruction method based on air shower universality was developed as described in Section 3.2.

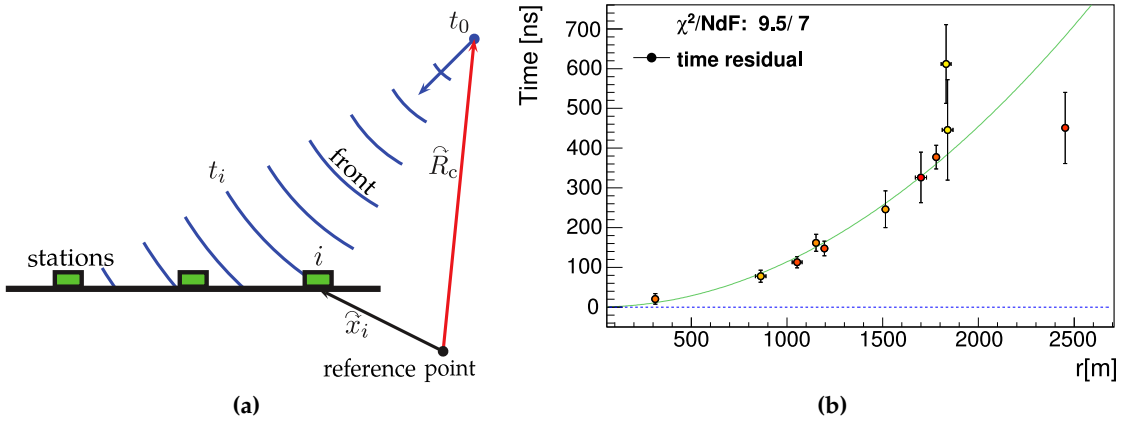

Figure 2.3: (a) Schematic of a spherical shower front propagating to the SD and ground [50]. (b) The arrival start times of the stations are fit to a curved shower front for the event described in Fig. 2.1a. The error bars represent the uncertainties from the time variance model, whereas the green shaded region is the uncertainty associated with the fit (from Offline EventBrowser).

2.3.1 Shower geometry

First, the arrival direction of the shower is estimated by fitting the start times t of the stations to a plane front moving at the speed of light c along the shower axis $\hat{a}$

$$\vec{x}(t) - \vec{b} = -c(t - t_0)\hat{a},$$

where the signal-weighted barycenter $\vec{b}$ is the spatial origin and the time origin t_0 is the weighted time average of the triggered stations.

If there are at least four triggered stations and a successful LDF fit, the shower front is fit with a more suitable spherical model. A visualization of the spherical shower front is shown in Fig. 2.3a, and an example of an event fit with a curved shower front is shown in Fig. 2.3b. The arrival direction is then described as function of the station trigger times t_i and positions $\vec{x}_i$:

$$c(t_i - t_0) = |\vec{R}_c - \vec{x}_i|\,, \tag{2.5}$$

where $\vec{R}_c$ and t_0 are the space and time coordinates of the virtual origin of the spherical shower front. To derive the shower axis $\vec{a}$, the apparent origin of the shower axis is described as:

$$\vec{R}_c = \vec{c} + R_c\vec{a},$$

where the radius of curvature R_c is the distance to the shower origin as measured from the impact point $\vec{c}$. The system of equations derived from Eq. (2.5) may be solved with a linear approximation followed by a non-linear optimization using MINUIT-2.

Due to the expansive development of an EAS, only the first particles to arrive are expected to originate close to the first interaction point. The particles arriving later will have an effective origin closer to the depth of the shower maximum. As will be discussed in Section 3.1.4, the effective origin of particles depends upon the particle components and their respective longitudinal developments.

2.3.2 Lateral distribution function and maximum-likelihood method

Following the estimation of the shower arrival direction, the impact point, arrival direction, and the lateral distribution are fit using a maximum-likelihood method. The likelihood

function takes into account the probabilities for non-saturated, non-triggered (silent), and saturated[6] stations. Most saturated signals may be recovered [48, 49, 116] as shown in Fig. 2.4a. The recovered spectrum extends that of the non-saturated stations so that it follows the power-law shape of the energy spectrum.

The signals measured in the lateral distribution of an air shower follow an inverse power-law with respect to the distance from the shower axis (in the detector plane) r:

$$S(r) = S_{r_{\text{opt}}} f_{\text{LDF}}(r),$$

where $f_{\text{LDF}}(r)$ is the lateral distribution function. The optimal distance r_{opt} is the distance at which the LDF is best constrained ($f_{\text{LDF}}(r_{\text{opt}}) = 1$); thus, it depends strongly on the station spacing. r_{opt} was estimated to be 1000 m for the SD-1500 and 450 m for the SD-750 array [50, 117, 118]. We distinguish the SD-750 and SD-1500 shower sizes as S_{450} and S_{1000}, respectively.

Many different functional LDF forms were tested to describe air shower signals on the ground. Nevertheless, the implemented choice in $\overline{\text{Off}}\underline{\text{line}}$[7] is a modified *Nishimura-Kamata-Greisen* (NKG) function [120, 121]:

$$S(r) = S_{r_{\text{opt}}} \left(\frac{r}{r_{\text{opt}}}\right)^{\beta} \left(\frac{r + r_1}{r_{\text{opt}} + r_1}\right)^{\beta+\gamma}, \tag{2.6}$$

where the distance r_1 and spectral index γ allow for more flexibility of the function far from the core than a regular NKG function. As already mentioned, this flexibility in the LDF is necessitated by the transition of dominance from the electromagnetic to the muonic cascade far from the core. As estimated from data, the best fit for r_1 is 700 m. An example of an LDF fit is depicted in Fig. 2.5.

The signals of the WCDs provide information about the PEs[8] produced by Cherenkov photons, yet the number and energy spectrum of secondary particles inducing the signal is not known and difficult to estimate. Thus, in order to construct the maximum-likelihood method, an effective conversion from VEM to the number of particles is used. Due to the transition from the dominance of the electromagnetic to the muonic cascade, the conversion depends on the zenith angle of the shower and is derived from the signal uncertainty model as shown in Section 2.2.2. Thus, with the Poisson factor p, we have the conversion:

$$n_{\text{eff}} = p\,(S/\text{VEM})\,, \tag{2.7}$$

where the factor p is estimated from the signal uncertainty model described in Eq. (2.4) and depicted in Fig. 2.4b.

With the conversion to particle numbers, the log-likelihood function $\ln \mathcal{L}$ for the LDF fit is constructed as follows:

$$\ell = \ln \mathcal{L} = \sum_{i}^{\text{non-sat.}} \ln f_{\text{P}}(n_i, \mu_i) + \sum_{i}^{\text{sat.}} \ln f_{\text{sat}}(n_i, \mu_i) + \sum_{i}^{\text{non-trig.}} \ln f_{\text{non-trig.}}(n_i, \mu_i)\,, \tag{2.8}$$

with the effective observed particle numbers n_i and their expectation values μ_i.

[6] As mentioned in Section 1.2.1, saturation of a PMT results from an overflow of the finite range of the FADC electronics, yielding a non-linear response.

[7] A better LDF, which also takes into account the shower asymmetry, was developed in [119], but it has not yet been implemented in $\overline{\text{Off}}\underline{\text{line}}$.

[8] photoelectrons

[8] Unsaturated stations are better known as non-saturated stations.

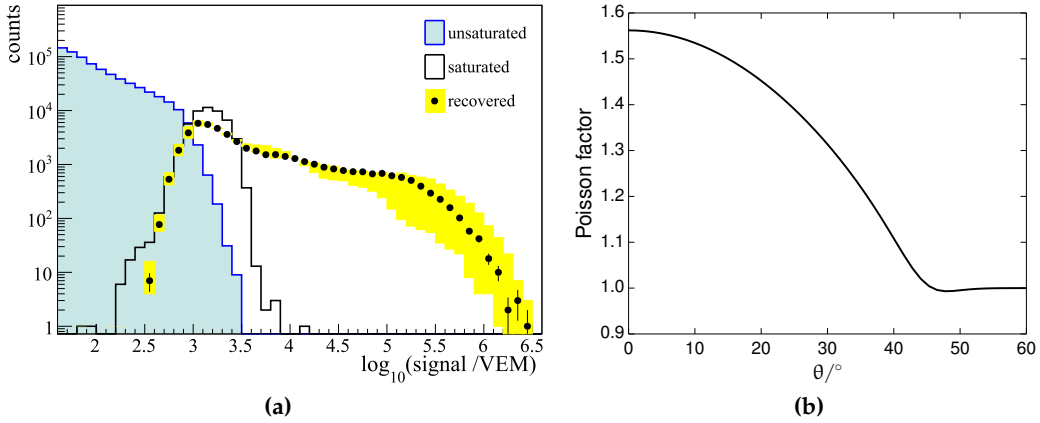

Figure 2.4: (a) After applying a 5T5 selection (defined in Section 2.1.4), the signal spectra of unsaturated[9] (blue histogram) and saturated (black histogram) signals are shown together with the recovered signals (black points) and their systematic uncertainty (yellow area) [48]. (b) To convert signals to effective particle numbers, the empirical Poisson factor —described in the text— is used. Here, it is shown as a function of zenith angle. At large zenith angles where muons are dominant, the factor approaches one as the signal of one VCT muon is on average 1 VEM. At smaller zenith angles where the electromagnetic component dominates, 1 VEM corresponds to around 20 particles [108].

The three contributions to the log-likelihood function are for:

1. **non-saturated signals**, which follow Poissonian statistics according to $f_p(n_i;\mu_i) = \mu_i^{n_i}\exp(-\mu_i)/n_i!$.

2. unrecovered **saturated signals**, which are treated as a lower limit in the likelihood. $\ln f_{\text{sat}}(n_i,\mu_i)$ is calculated by integrating a Gaussian p.d.f.[10] over all values $n \geq n_i$. If a saturated signal is successfully recovered, it is treated like a non-saturated signal.

3. **non-triggered stations**. It takes roughly 3 VEM to trigger a single station[11]. Thus, Poissonian probabilities below this threshold are summed up for each of these non-triggered stations.

In returning to the LDF of Eq. (2.6), the three parameters that characterize its scaling and shape are: the shower size S_{450} or S_{1000} and slopes β and γ. When these are considered with the arrival direction and the impact point, the number of parameters increases to at least eight. The Offline fit is divided into several stages in which some parameters are fixed to previous estimates. Effectively, this reduces the free parameters of the problem, leading to an improvement in convergence. For the SD-1500, β and γ are fixed. As was more recently done with the SD-750, parameterizations may also be obtained from a reconstruction method where all events are simultaneously fit in an iterating procedure in order to obtain a global fit of the LDF parameters [118, 122]; this improved method, which when applied to the SD-1500, will improve the LDF parameterization for different core distances and allow for the parameterization of azimuthal signal asymmetries. The latter improvement would remedy the bias present in the reconstructed shower core positions[12] and prevent biases from being inherited in derived values. An example LDF fit is shown in Fig. 2.5. The SD-750 and SD-1500 parameterizations of the LDF slope are depicted in Fig. 2.6.

[10] probability density function
[11] It takes ≈ 1 VEM with the ToTd and MoPS triggers.
[12] See Fig. 3.20 for the bias of the core as a function of energy and zenith angle as found with simulations.

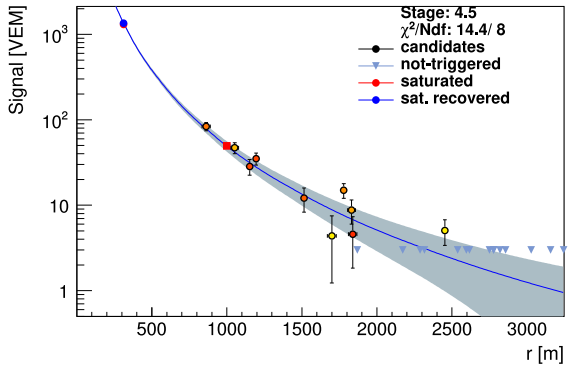

Figure 2.5: Fit of the lateral distribution function to the measured signals of the SD-1500 event in Fig. 2.1a. This event includes one saturated station with a successfully recovered signal. The recovered signal is used in the fit of the LDF in addition to the non-saturated signals and the non-triggered stations (from Offline EventBrowser).

2.4 Constant intensity cut method

As explored further in Chapter 3, the development of an EAS is mostly dependent on the traversed atmospheric overburden ΔX. An air shower with an incident zenith angle of 60° passes through roughly twice the amount of atmosphere that a shower at 0° would. It, thus, follows that the signals observed at ground level depend on the zenith angle of the incident particle. At all but the highest energies, the flux is isotropic. Thus, an empirical method —known as the *Constant Intensity Cut* (CIC)— is employed to derive a zenith-independent signal size $S_{\theta_{ref}}$. The idea is to normalize each shower size to the size of an equivalent shower at the median zenith angle.

2.4.1 Event selection criteria

In the derivation of the CIC as well as other SD-based analyses, SD events must pass certain pre- and post-reconstruction criteria. During the reconstruction process, events passing the following conditions are considered:

- Based on T2 information, stations that were inactive at the time of the event are not considered during the reconstruction.
- As mentioned in Section 2.1.4, bad PMTs are not considered for the signal estimation. In the event that all PMTs within a station were bad, this station is removed.

Post-reconstruction, SD events are selected using the following *Advanced Data Summary Tree* (ADST)[13] criteria which are implemented in Offline:

- Events must pass a 6T5 selection (defined in Section 2.1.4).
- Lightning events are rejected.
- The event rate and exposure are continuously monitored and analyzed. If the expected rate of events or communication relays for the SD are temporarily disturbed, events during this time period are added to the bad periods file and removed from analysis [123].

[13] The structured ROOT files produced in Offline after reconstruction are known as ADSTs.

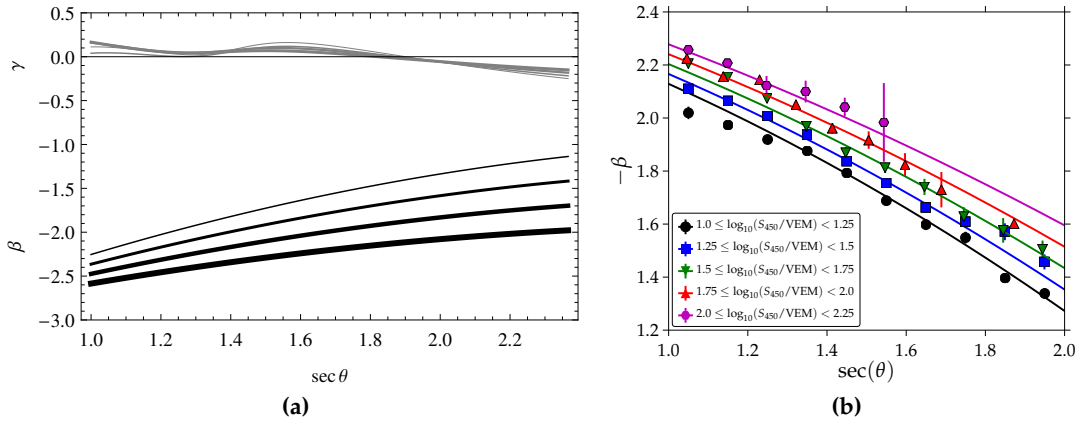

(a) **(b)**

Figure 2.6: (a) The SD-1500 parameterizations for $-\beta$ and γ as a function of $\sec\theta$. The increasing line thickness scales with the increasing shower size estimators $S_{1000} = 1, 10, 100$, and 1000 VEM [124]. (b) The SD-750 parameterization for β as a function of $\sec\theta$ [118].

In rare cases, individual stations are manually rejected due to software or hardware changes or on-going testing. Detailed information about data acquisition and quality selection are discussed in [43, 125, 126]. The configuration files that were used for the selection of SD events are listed in Table B.1. To note, these criteria are used in the analysis of this thesis for both SD and golden hybrid events.

2.4.2 Geomagnetic and weather corrections

Beyond considering the geometrical difference of atmosphere traversed with respect to zenith angle, further attenuations and distortions are caused by the geomagnetic field and ambient weather. Prior to the CIC and, later, energy calibration, these effects must be taken into account as the shower size S_{1000} is affected.

The charged secondary particles of air showers are deflected in the geomagnetic field. Consequently, a strong azimuthal modulation in S_{1000} with a rather small dependence on the zenith angle θ is introduced [77]. The modulation trends with azimuthal angle as this determines the angle between the trajectory of the particle and direction of the geomagnetic field. Overall, the maximum change in amplitude of S_{1000} is around 2 %. The correction on S_{1000} is implemented in Offline.

Atmospheric conditions affect the shower sizes through attenuation and dispersion. The longitudinal development of an air shower depends on the amount of traversed atmosphere. The effective grammage is determined by the air pressure as a function of altitude. If the pressure is consistently larger than on average, the showers will effectively be in a later stage of development (*older*) when they reach the ground. Additionally, the density of the air affects the Molière radius, which is the circle around the shower core that encloses 90 % of the energy content of the air shower, and, thus, the lateral distribution of showers. For S_{1000}, the effects are on the order of ± 0.5 %, depending mostly on the ground temperature and pressure at the time of the event or shortly before [44, 53, 127–134]. For this work, due to the weather database size, the weather corrections are implemented in an external program post-reconstruction, as is done for [135].

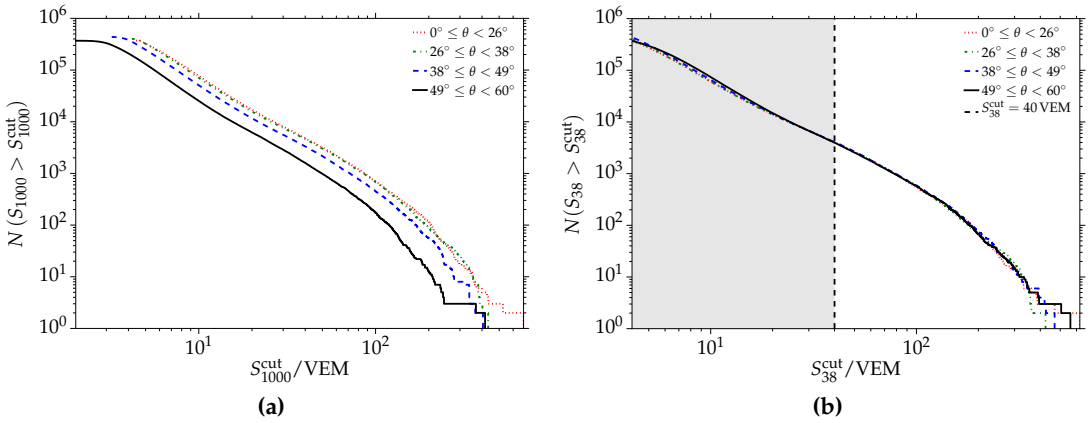

Figure 2.7: (a) Uncorrected and (b) corrected shower size distributions for different zenith angle ranges as measured with the SD-1500 [108].

2.4.3 Correction function for the signal estimator

Based upon the zenith-spectrum of the SD-1500 —which is from 0 to 60°, our reference θ_{ref} is the median angle of 38°[14] [135]:

$$f_{CIC} = 1 + (0.965 \pm 0.038)\, x + (-1.660 \pm 0.072)\, x^2 + (-1.19 \pm 0.40)\, x^3, \tag{2.9}$$

where $x := \cos^2\theta - \cos^2\theta_{ref}$. The signal estimator for SD-1500 is thus defined as:

$$S_{38} = S_{1000}/f_{CIC}. \tag{2.10}$$

The shower size distributions before and after applying the CIC correction are shown in Fig. 2.7.

2.5 Energy calibration

While the deposited signal is proportional to the energy and mass of the primary CR, the SD energy reconstruction requires calibration with an independent measurement to appropriately determine its energy-scale. A subset of Auger events —known as golden hybrid events— have been separately observed by both the SD and FD. Using these events, one may calibrate the SD energy estimates —like S_{38}— to the energy $E_{\rm FD}$. An overview of the energy calibration is provided in this section; for further information see [135].

2.5.1 Pertinent improvements to the FD reconstruction

The FD reconstruction is a complex process which requires knowledge of fluorescence yield, atmospheric conditions, the absolute calibration of the telescopes, and other parameters to best account for the differing conditions of a measured EAS. In accounting for these variables, this procedure allows us to reconstruct the longitudinal profile of the energy deposited in the atmosphere by an EAS. To then obtain the total energy, the so-called invisible energy, which is energy carried by high-energy muons and neutrinos, is added. Further details on the analysis used to obtain the Auger energy scale and estimate its systematic uncertainties are found in [136].

[14] Other detector geometries have different angular ranges. In the case of the SD-750, the reference is the median angle of 35°.

Recently, the FD reconstruction has been refined to obtain an improved determination of the primary energy and the depth of the shower maximum. The hourly measurements of the *vertical aerosol optical depth* (VAOD) have been improved to also account for the shape of the aerosol scattering phase function and multiple scattering in the atmosphere [137]. The optical efficiency —the relative FD response to various wavelengths— is now found on a per-telescope-basis (instead of a globally applied efficiency) [138]. The estimation of the invisible energy was bettered using horizontal air shower data [135]. With these changes to the reconstruction, the cumulative shift of hybrid FD energies is at most 4 % and has a slight energy dependence. Similarly, the hybrid average depth of shower maximum shifts by at most $5\,\mathrm{g\,cm^{-2}}$ with respect to energy[15].

2.5.2 Event selection criteria

In addition to the SD-based cuts presented in Section 2.4.1, golden hybrid events should also pass several FD pre- and post-reconstruction criteria to ensure the quality of data:

- Certain atmospheric conditions are critical for the proper reconstruction of the longitudinal profile. Events lacking atmospheric information are rejected.
- Events that fail to reconstruct —like when the profile reconstruction fails—are rejected.
- Above a certain threshold of light intensity, the pixels of the PMT camera saturate. This leads to an unreliable reconstruction of the shower profile. Occasionally, the pixels of the PMT camera also have bad calibration parameters. Events for which either criterion fails are discarded.
- As is done for the SD, events within known bad periods of FD operation are rejected.
- Events recorded during the process of closing the shutters of an FD telescope are rejected.
- To ensure low air contamination from aerosols, events must have a VAOD less than $0.1\,\mathrm{g\,cm^{-2}}$.
- There are many cuts related to cloud coverage as measured by the lidar systems [139]. Events are selected if they have a cloud fraction below 25 %, the X_{max} measurement is not too close to the clouds, and the clouds are not thicker than $100\,\mathrm{g\,cm^{-2}}$).
- The relative uncertainty in the reconstructed total energy is required to be below 18 %.
- To reject shower profiles that lack a distinctive Gaisser-Hillas shape, a cut is performed by comparing the χ^2 probability of a Gaisser-Hillas fit to a linear fit to the longitudinal profile. Profiles for which the Gaisser-Hillas description seems unlikely are rejected.
- A hole (or holes) in the longitudinal profile must be less than $20\,\mathrm{g\,cm^{-2}}$.
- The maximum allowed distance between the reconstructed shower core (hybrid) and the next SD station is 750 m.

[15] In this work, golden hybrid events –a subset of hybrid events which are well measured by the SD-1500– are used. The relative shifts due to the FD reconstruction updates are found in Fig. D.22

- The reconstructed $X_{\max}$ must be within the limited *field of view* (FoV)[16] of the FD with an $X_{\max}$ uncertainty less than $40\,\mathrm{g\,cm^{-2}}$. To ensure that the $X_{\max}$-distribution is not distorted by the FoV, a fiducial FoV selection is applied. In this selection, only certain geometries —for which the effective FoV of telescopes has a minimal impact on the measurement— are allowed. This is visualized in Fig. 2.8. Due to the data-driven derivation of this cut, this cut depends on the other quality cuts, and thus, it needs to be re-tuned whenever changes are made. This cut roughly removes two thirds of the remaining events. Further details are found in [33, 140].

The configuration files that were used for the selection of FD events are listed in Table B.2. A more detailed description of quality cuts and their derivation is given in [33].

2.5.3 Calibration procedure

The relationship between the FD energy E_{FD} and SD-1500 energy estimator S_{38} is well-described by the following power-law[17]:

$$E_{\mathrm{FD}} = A \left(\frac{S_{38}}{\mathrm{VEM}} \right)^{B} . \tag{2.11}$$

Implicitly, this relationship assumes that the composition of CRs is relatively constant with energy. As shown in Fig. 1.18 and Fig. 1.19, the composition varies with respect to energy, and a trend to heavier composition is seen at the highest energies. However, using information from measurements with AugerPrime (Section 1.2.6) or mass-sensitive analyses –like the one presented in this thesis, this calibration might be extended to take composition-related effects into account.

After the selection of high-quality events, a log-likelihood function is minimized to determine the optimal parameterization for Eq. (2.11). In constructing the likelihood, the following four factors are folded together [108]: the *true* distribution of golden hybrid events prior to influences of detector resolutions or efficiencies, the shower-to-shower fluctuations of the SD shower sizes, detector efficiencies, and detector resolutions. This yields a computationally expensive p.d.f., so a few reasonable assumptions are introduced to speed-up the minimization and to reduce the effort in making parameterizations (i.e. use of bootstrapping). For more details on the full p.d.f. and simplified log-likelihood function, see [108, 141–143].

The energy resolutions of the FD and SD may be estimated from their reconstruction uncertainties. The resolution of E_{FD} is only weakly dependent on energy —with an average of 7 %. In contrast, the SD-1500 resolution is around 15 %. In both cases, the dependence on zenith angle is not pronounced. Nevertheless, all of these dependencies were verified with simulations and are taken into account during the estimation of the calibration function.

After the quality selection, 2661 SD-1500 golden hybrid events remain, and the resulting energy calibration function is [135]:

$$E(S_{38}) = (0.178 \pm 0.003)\,\mathrm{EeV} \left(\frac{S_{38}}{\mathrm{VEM}} \right)^{(1.042 \pm 0.005)} \tag{2.12}$$

as shown in Fig. 2.9. The shower size estimators are also shown for the SD-750 (S_{35}) and inclined events (N_{19}).

[16] See Section 1.2.2 for further details on the field of view and description of the set-up of the telescopes of the Fluorescence Detector. A brief overview of the fiducial field of view selection is given in Section 4.2.2.1.

[17] This relationship also holds true for energy calibrations with the SD-750 array and other Auger detectors.

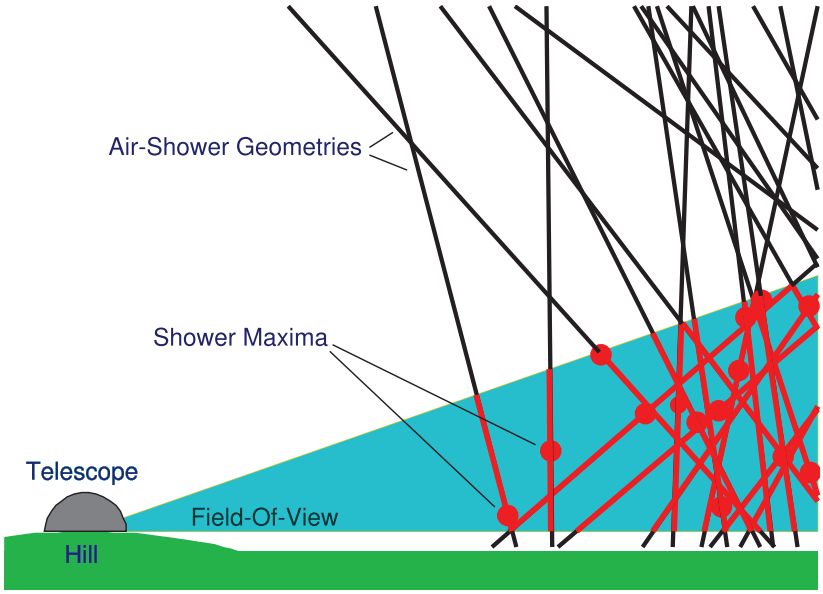

Figure 2.8: Depending on the mass of the primary particle, showers develop lower or higher in the atmosphere. Here is a sketch of different showers in the context of the FoV. When showers fall close to the telescope, the transverse area is small and many shallow/deep showers are not fully reconstructed. At large distance from the telescope, the geometrical field-of-view cone is larger; however, the emitted fluorescence light can only travel a limited distance before being absorbed. The fiducial FoV is required to remove any incurred biases due to the field-of-view [144].

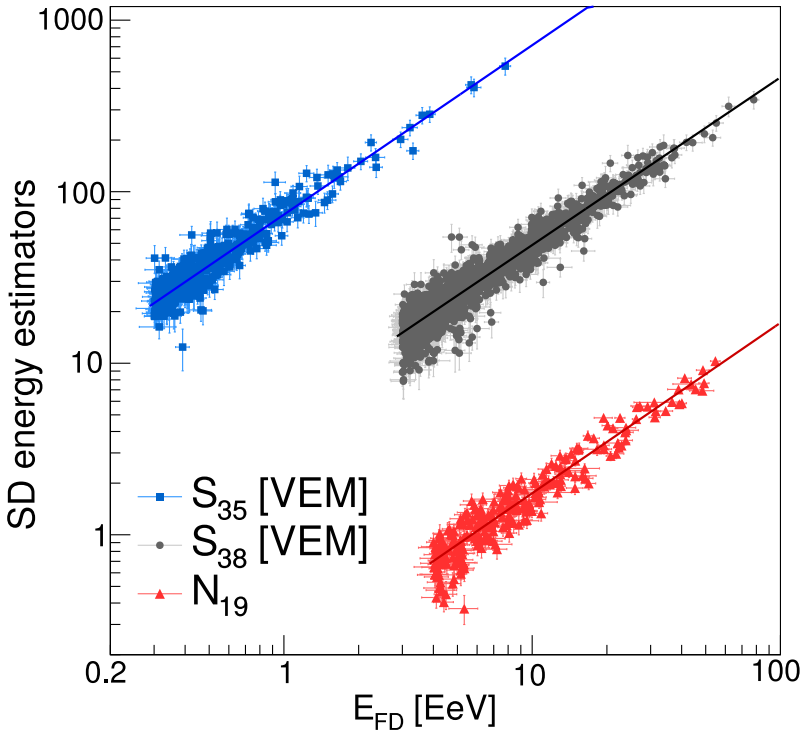

Figure 2.9: Energy calibration fits using golden hybrid SD-1500 vertical (S_{38}), SD-750 vertical (S_{35}), and SD-1500 horizontal (N_{19}) events [135].

CHAPTER 3

Air shower universality

The reconstruction procedure of the *Surface Detector* (SD) (Chapter 2) is a mostly empirical method. It is based on the average description of measured and simulated lateral distributions. Air shower universality is a phenomenological method derived from the underlying physics of an *extensive air shower* (EAS). Unlike the SD reconstruction, the universality approach encapsulates rich details of the actual physics of air showers —like the signal and timing distribution of different groups of secondary particles. This, in turn, allows a reconstruction of mass-sensitive variables —like the depth of the shower maximum $X_{\max}$ and relative muon content R_μ.

During the development of a cosmic-ray-induced air shower, the cascade of secondary particles may be described by four uniquely-defined (yet universal) components. This is possible as the distributions –e.g. normalized energy and angular distributions– of secondary particles may be described by primary-independent, comprehensive models across various energy ranges. Above an energy[1] of 10^{18} eV, the shower-to-shower fluctuations of each of these components is minimal when compared to their overall development. In Section 3.1, the methodology of universality is further discussed. Using signal (Section 3.1.3) and timing (Section 3.1.4) models, universality is able to reliably estimate the signals of the four particle components from the responses and timing of triggered detectors to reconstruct macroscopic parameters —like the energy, the depth of the shower maximum, and muonic content of an EAS. Fundamentally, shower universality may be formulated for any detector in a *ultra-high energy cosmic ray* (UHECR) experiment. In the context of Auger and for this work, we employ this method for the SD, allowing us to gain roughly ten-fold more data than the FD for mass composition and anisotropy studies. Nevertheless, universality employed with other Auger detectors —particularly the Auger upgrade described in Section 1.2.6— is of high importance as the new detection methods will help to further solidify our understanding of the development of the components and to give new physics results.

The universality reconstruction employs the signal and time models to fit the measured particle traces and provide estimates of air shower properties using the data from the *water-Cherenkov detectors* (WCDs). The universality reconstruction is implemented as a separate module in the Offline framework which is processed immediately after the SD reconstruction. Depending on the reconstruction method employed (discussed in Section 3.2.3),

[1] Initial tests of the universality models at energies as low as 10^{17} eV have been found to give consistent results [108]. Further studies and parameterizations need to be performed before relying fully on the reconstructed values at this energy.

observables —like the reconstructed primary energy— from the SD reconstruction may be used as fixed parameters in the universality reconstruction. Regardless of the chosen procedure, the overall goal in a reconstruction is to maximize the same negative log-likelihood (Section 3.2.1) to find the best, simultaneous fit of the lateral distribution and time traces of select triggered stations. In Section 3.2.3, three different reconstruction methods —known as the global, iterative, and constrained axis methods— are described and compared, The constrained axis method, developed in this work, has a reconstruction efficiency exceeding 90 % over all energies, outperforming the other two methods.

3.1 Methodology

3.1.1 Universality of the electromagnetic cascade

The use of shower universality to describe air shower development has been previously studied ([145] and references therein) for the electromagnetic component (having been thoroughly explored in [145–150]). The relative evolution stage t for the electromagnetic component of a shower is defined as [150]

$$t := \frac{X - X_{\max}}{X_0}, \tag{3.1}$$

with the radiation length of electrons in air $X_0 \approx 36.7\,\mathrm{g\,cm^{-2}}$, the slant depth X, and the shower maximum occurring at $t = 0$. A universal description of the distributions of secondary particles was best achieved as a function of t as opposed to X or composite variables involving X and $X_{\max}$. Additionally, the universal behavior of the electromagnetic shower extends to the outward momentum and lateral distributions as well as the energy and angular distributions which are shown in Fig. 3.1. The parameterization of the time distribution is also well described except at the largest values where the parameterizations do not agree with simulations.

3.1.2 Universality for hadrons

To extend the concept of universality to hadrons with $A > 1$, an additional parameter is needed to describe the muonic development —N_μ or R_μ[2] [108, 151–153]. As the universality model described throughout this chapter involves the WCDs, the shower stage is described with ΔX —the integrated atmospheric overburden between shower maximum $X_{\max}$ and the projected position of the station in the shower plane. As depicted in Fig. 3.2, ΔX differs for stations at the same radial yet differing azimuthal location.

Based upon the development of air showers in the context of Auger data and simulations, particles are divided into four components [155]:

1. Muons $\mu^\pm$ $[\mu]$
2. Electromagnetic particles[3] from high-energy π^0 decays $[e\gamma]$
3. Electromagnetic particles from muon decay or interactions $[e\gamma(\mu)]$
4. Electromagnetic particles from the decay of low-energy hadrons $[e\gamma(\mathrm{had})]$

[2] In this thesis, unless stated otherwise, R_μ refers to the relative number of muons whereas N_μ designates the total number of muons.

[3] While all of the listed particles are electromagnetic, we use this nomenclature to refer only to electrons, positrons, and photons.

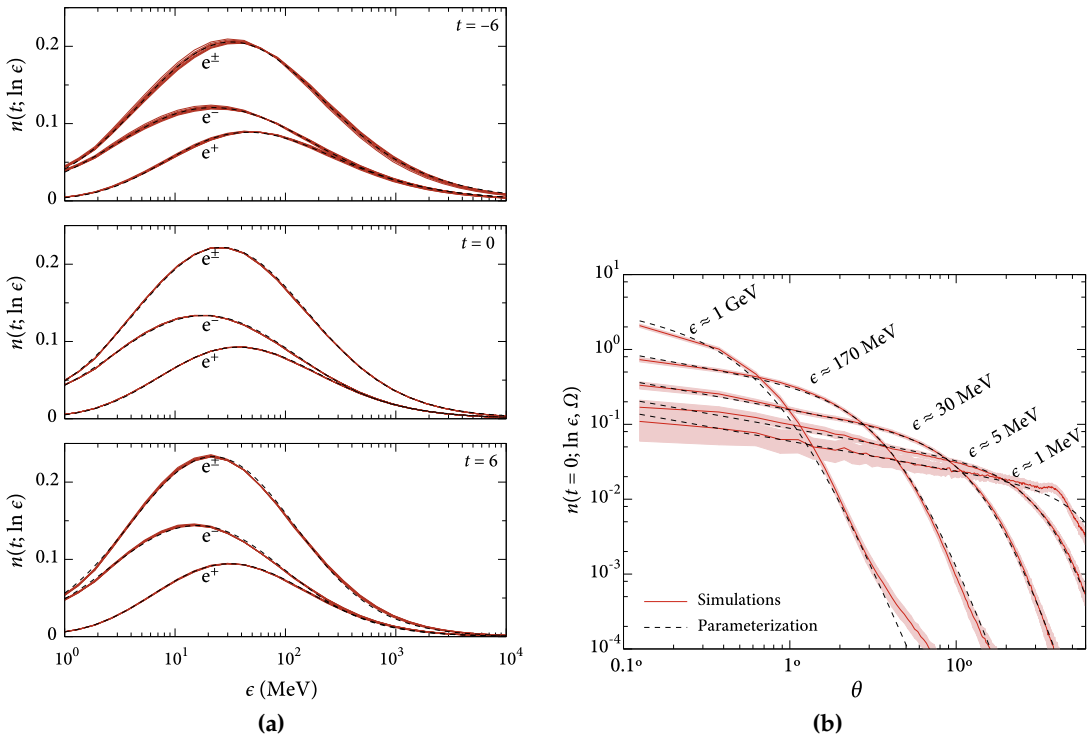

Figure 3.1: (a) The average energy distributions for the electromagnetic component for (*top*) young showers ($t < 0$), (*middle*) showers at their $X_{\max}$ ($t = 0$), and (*bottom*) older showers ($t > 0$). The background curves represent simulated distributions for proton, iron, and photon primaries, whereas the dashed lines are parameterizations from [148]. The variations observed for the young showers are mostly due to deviations in the primary energy. (b) The normalized angular distributions for 20 proton-induced showers at 10^{18} eV. The filled areas highlight the $3\,\sigma$ error margins. The dashed lines represent parameterizations depending on the secondary energy ϵ and the angle between the particle's momentum vector and the shower axis θ [150].

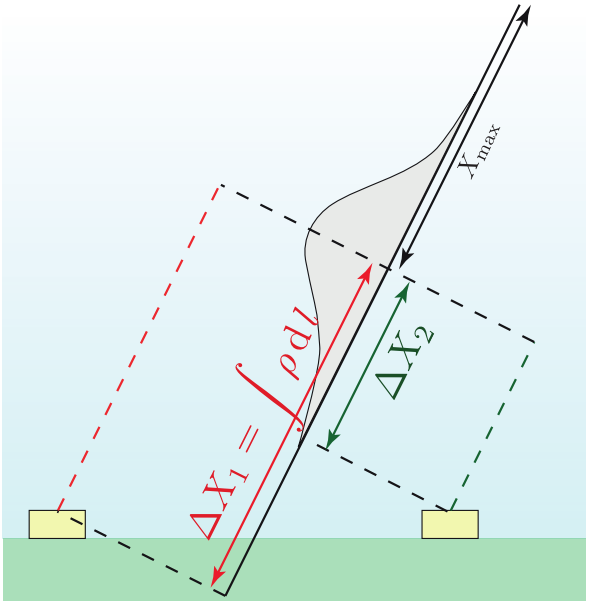

Figure 3.2: Schematic of the distance ΔX to $X_{\max}$. To illustrate the azimuthal dependence, a station is shown in the early region at a local azimuthal angle of $\psi = 0$ (*upstream*) and in the late region at $\psi = 180°$ (*downstream*). As depicted, ΔX for the late station is larger than for the early station as they are at different stages of the shower's development [154].

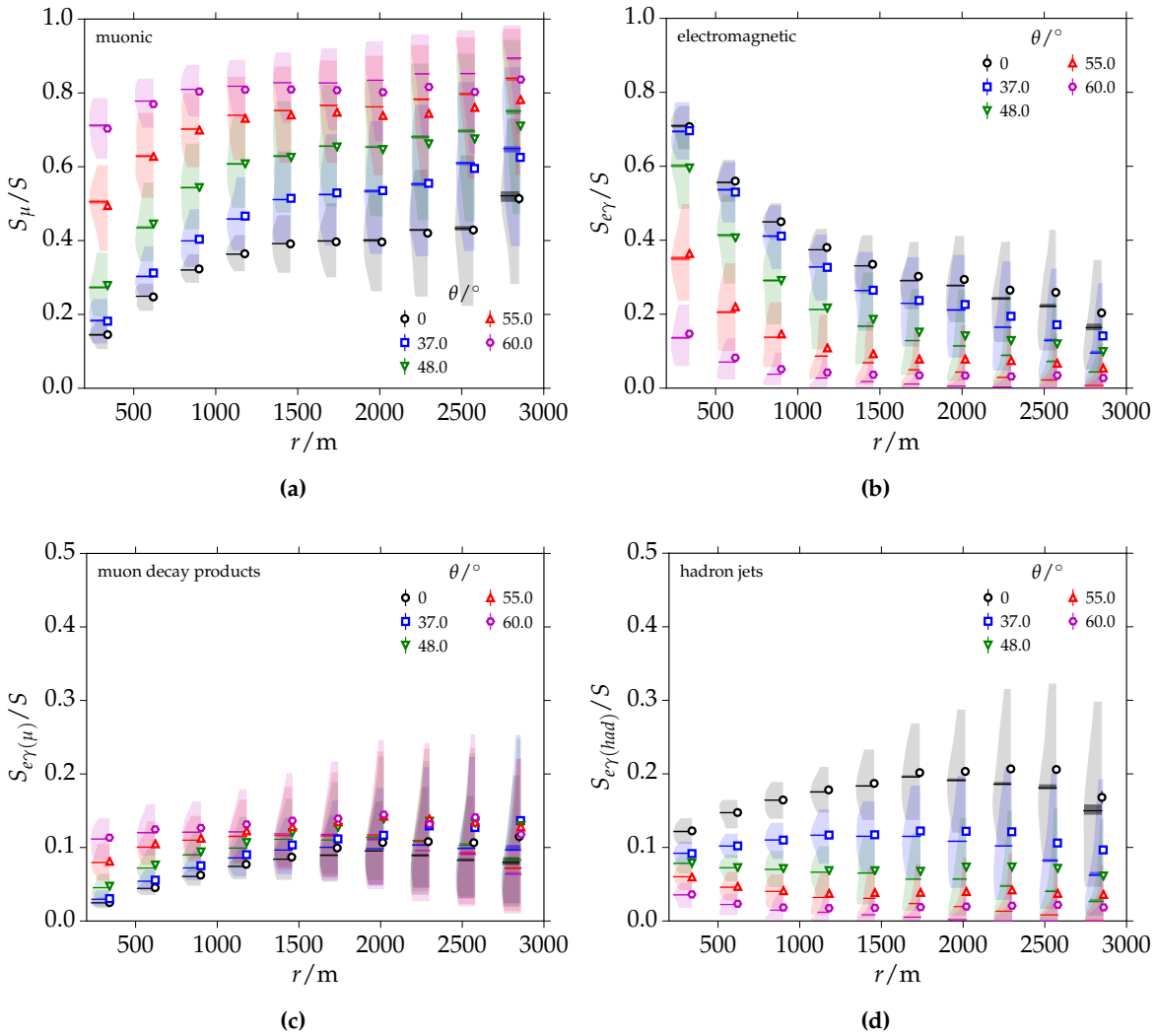

Figure 3.3: The fraction of signal from (a) μ, (b) $e\gamma$, (c) $e\gamma(\mu)$, and (d) $e\gamma(\mathrm{had})$ with respect to the total signal observed in an Auger WCD binned in zenith as a function of radial distance. As further described in Appendix A.1, the open markers in these violin plots indicate the mean values of a bin, while the median is shown with a solid line. A kernel density estimate—the violins—is used to visualize the full distribution of the ratios within each bin. The $1\,\sigma$ regimes are drawn. To better scrutinize the development of the fractions, the bottom two plots have halved ranges [108].

Each of the components is derived from and/or has distinct interactions in the shower's development. To easily refer to the components in plots, abbreviations are provided in the square brackets. To note, the second component corresponds to the standard electromagnetic cascade. In Fig. 3.3, the fraction of each signal component is shown with respect to the total signal observed in a WCD. The plots are derived from an equal mixture of simulations induced by proton, carbon, and iron primaries with energies of $10^{19.5}$ eV and 10^{20} eV.

As depicted in Fig. 3.4a, the universal lateral distribution of the electromagnetic component is a function of $x := r/r_m$. The Molière radius r_m corresponds to the radius of a cylinder centered around the shower axis that contains roughly 90 % of the shower energy deposit [157]. High-energy secondary particles are found close to the core; they are primarily created through the main electromagnetic cascade. Farther from the core, the functions deviate from universality. By turning off the charged pion decays for protons —as is done

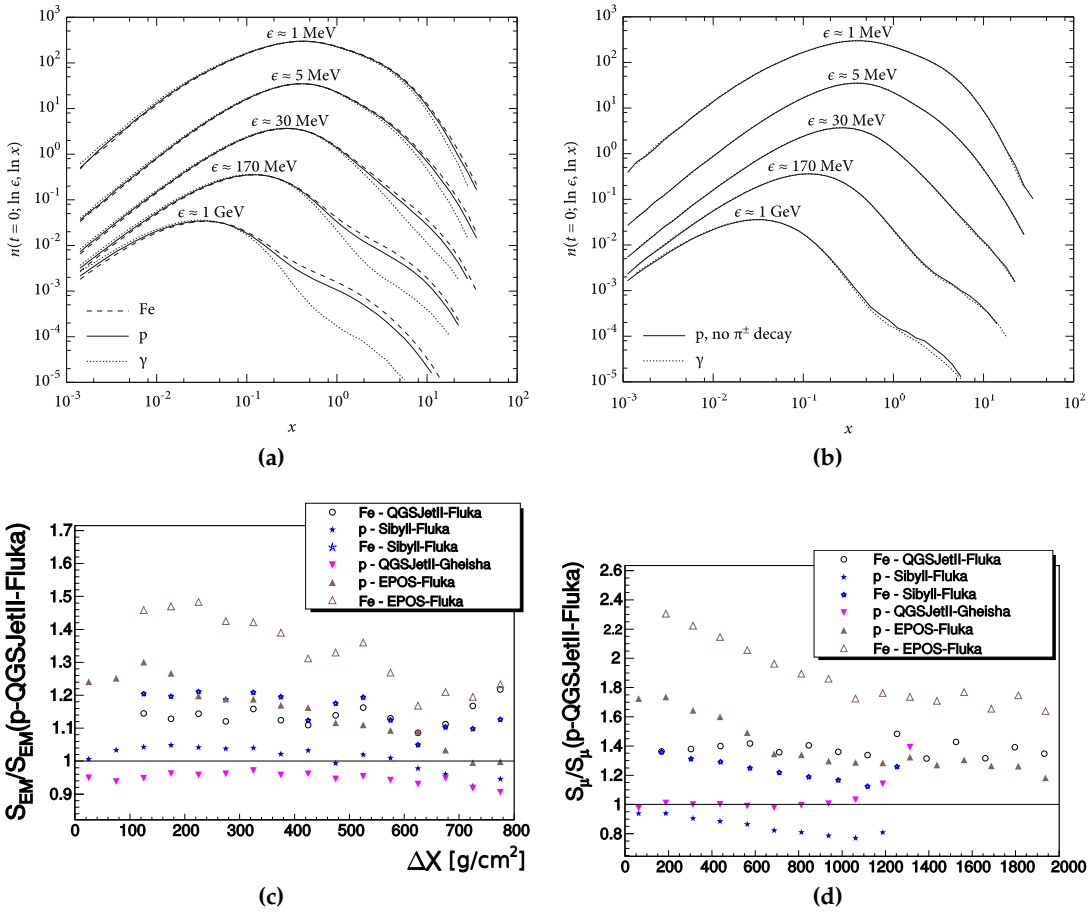

Figure 3.4: Simulated lateral distributions for (a) p, Fe, and γ primaries and (b) γ and p primaries when the $\pi^{\pm}$-decay channel is switched off [150]. In both plots, the lines above 1 GeV are shifted up by multiples of 10. (c) The electromagnetic and (d) muonic signal —relative to the average parameterized signal in QGSJET-II.03 simulations— emphasizes the absence of universality using only three particle components [156].

in Fig. 3.4b, the universal description of the lateral distribution is preserved. This vital indication highlights the importance of defining the muonic and hadronic components in air showers.

In the initial implementation of universality, only the first three components were used. As shown in Fig. 3.4c, this led to a non-universal description of the electromagnetic component. Depending on the interaction model considered, deviations up to 50 % were observed. As the muonic signals also suffered from a similar disagreement —plotted in Fig. 3.4d, the classification of a fourth particle component —relating to the overall muon content of an air shower— was necessitated.

In this fourth component, the electromagnetic component from the decay of low-energy hadrons may be identified through the projected position r_{proj} of the mother particle onto the ground — as depicted in Fig. 3.5a. The universal relationship between the signals and r_{proj} is shown in Fig. 3.5b. Nevertheless, using r_{proj} as a selection criterion requires a CORSIKA simulation[4] with enabled particle history[5]. As the particle history was not available in the simulations used for parameterization, another method was used to select particles,

[4]See the last paragraph of Section 1.1.2.2 for an overview of CORSIKA.

[5]To increase the computational time for a simulation as well as reduce the resulting file size, typically particles and their associated information are only saved near the height of observation. In order to gain

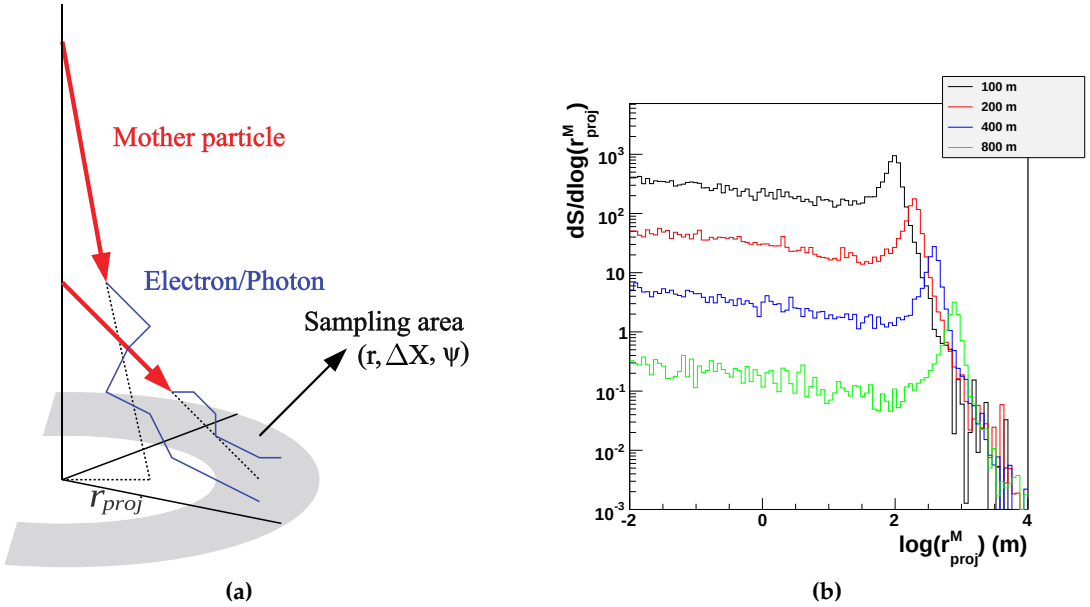

Figure 3.5: (a) Schematic of r_{proj}. (b) With increasing radial distance, the peak in the signal versus r_{proj} becomes more pronounced. This universal feature is caused by electromagnetic particles from hadrons with large transverse momenta. Particles are from a simulated proton shower at $E = 10^{19}$ eV and with a zenith angle of 45° [155].

as implemented in Offline. In Fig. 3.6, histograms of the hadronic generation[6] and the particle weight from the thinning algorithm[7] are shown. Particles with a hadronic generation count greater than 50 are electromagnetic particles from muon decays. At smaller hadronic generations, there is a peak for particle weights below 500 due to particles from the hadron jet component. Hadrons have a smaller maximum weight which their decay products inherit. As these particles are created close to the ground, they maintain their weight, which is significantly smaller than for the particles of the pure electromagnetic cascade. In Fig. 3.6b, electromagnetic particles with large r_{proj} are manually removed, leaving only the pure electromagnetic component. Thus, the fourth component may be determined with the corresponding hadronic generation and particle weight cuts[8].

3.1.3 Model of ground signals in WCDs

Using the four particle components, a model to describe the signals of the Auger WCDs was developed and later extended to AugerPrime and AMIGA [155, 158, 159]. As this work only utilizes data from the WCDs, our discussion will focus only on the WCD-based

information about the different particle components in an extensive air shower, the particle type of the previous two generations may be saved.

[6] In Corsika, the each hadronic interaction is called a generation. Universality is a possibility in EAS and not at the LHC because the number of hadronic generations is sufficiently large such that an average description can be made of the QCD soft processes.

[7] Above an energy of 10^{16} eV, the computational times for simulations because extremely long. To reduce this time, a thinning algorithm is used where only one particle is followed among a group of particles where the individual energies are below a certain fraction of the primary energy. The particle that is followed is given an appropriate value or weight. To reduce statistical fluctuations of the particle densities far from the core, there is a limitation on the weights.

[8] As aforementioned, these cuts are derived from simulations with a specific thinning level and other settings. For the correct classification of the hadron jet component, the settings of the Corsika simulations must be maintained. Otherwise, the criteria to select particle components need to be updated.

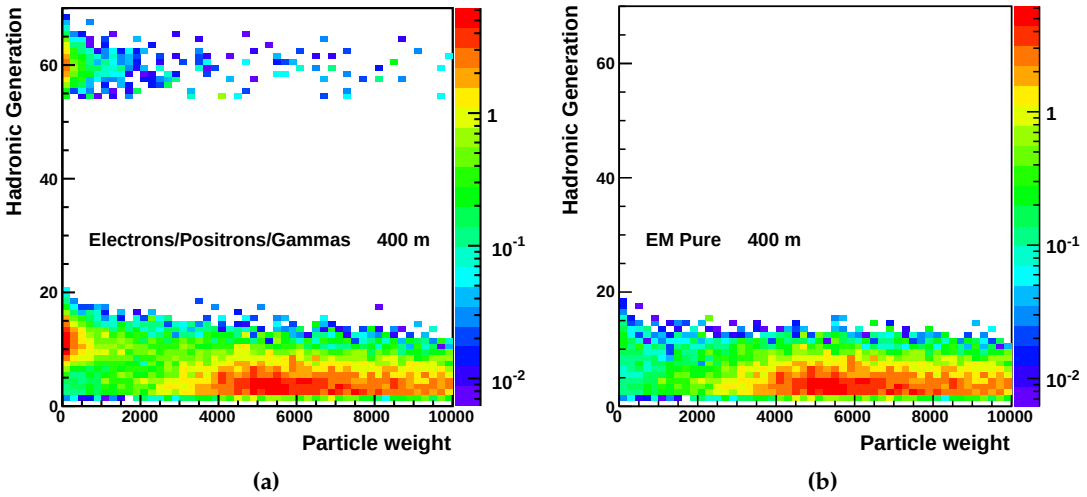

Figure 3.6: The hadronic generation versus the particle weight is shown (a) without and (b) with the manual removal of particles with large r_{proj}. The expected WCD signal for each bin is indicated by the color scale. Included are simulated particles from a sampling area within 400 m radial distance [155].

implementation. To derive the parameterizations for the signal model, a fixed library — consisting of proton and iron primaries simulated with QGSJET-II.03 and EPOS-1.99— was utilized. For each primary and interaction model combination, 10 showers were generated for each combination of zenith angle $\theta \in \{0°, 12°, 25°, 36°, 45°, 53°, 60°\}$, energy $E \in \{10^{18.6}, 10^{19}, 10^{19.5}, 10^{20}\}$ eV, and one of the 12 monthly atmospheric models. Due to the computational expenses incurred otherwise, the standard thinning level of 10^{-6} was used; thinning, thus, occurs when a particle's energy is below 10^{-6} times the primary energy. More details of the library are described in [155, 159].

For each particle component, the signal S of a WCD is derived from the signal S_0 observed in an ideal 10 m^2 spherical detector. The fundamental element of the signal model is the dependence of S_0 on the distance to the electromagnetic shower maximum ΔX, which defines the longitudinal development of air shower signals. This is described with a Gaisser-Hillas type function[9]

$$S_0(\Delta X, E) = S_{\max} \left(\frac{E}{10^{19}\,\text{eV}} \right)^{\gamma} \left(\frac{\Delta X - \Delta X_0}{\Delta X_{\max} - \Delta X_0} \right)^{\frac{\Delta X_{\max} - \Delta X_0}{\lambda(E)}} \exp\left(\frac{\Delta X_{\max} - \Delta X}{\lambda(E)} \right), \tag{3.2}$$

with $\lambda(E) = \lambda_0 + f_\lambda \lg\left(E/10^{19}\,\text{eV}\right)$. For the muonic and muon decay products components, the energy evolution parameter f_λ is 0. Results of the longitudinal parameterization $S_0(\Delta X)$ for the muonic and pure electromagnetic components are shown in Fig. 3.7. For the comparison, signals from different primary energies are included, corrected for via $\lambda(E)$, and evaluated at a radial distance of 1000 m. The parameters of the longitudinal description —$S_{\max}, \Delta X_{\max}, \gamma, \lambda_0$, and f_λ —depend on the distance to the shower core and subsequent parameterizations for these variables were found. In particular, $S_{\max}(r)$ is best described with a power-law LDF, which is independent of the mass composition and hadronic model at 10^{19} eV. When coupled together, the parameterizations of the longitudinal and the lateral distributions of the ideal signal establish the model $S_0(\Delta X, r, E)$. Thus, the signal for each particle component in a real detector is approximately given by

$$S(r, \Delta X, E, \theta, \psi) = S_0(\Delta X, r, E)\; f_{\text{trunc}}(r, \theta, \psi)\; A_{\text{eff}}(r, \Delta X, \theta, \psi). \tag{3.3}$$

[9] For further details on the derivation of S_0, see [155].

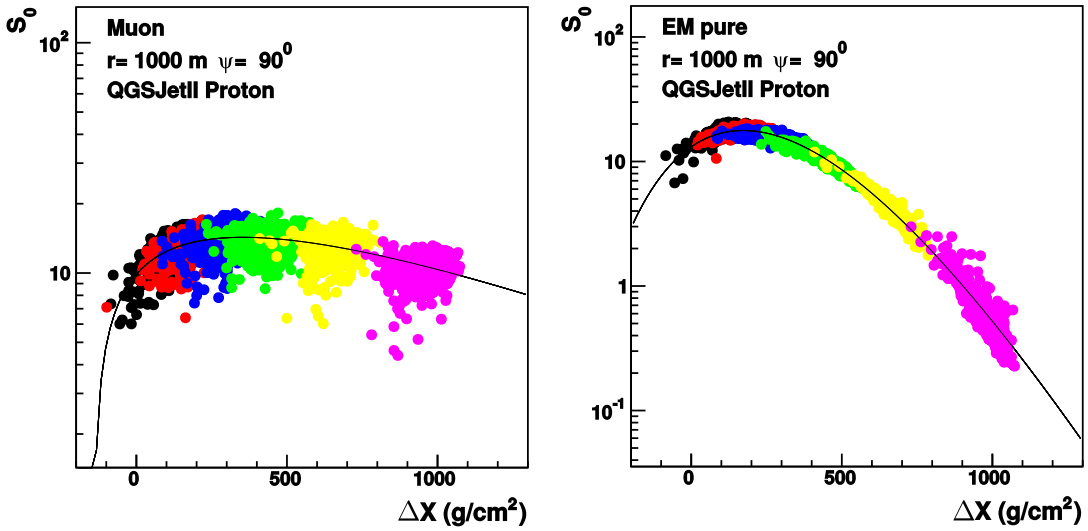

Figure 3.7: Comparison of the longitudinal dependence of S_0 in simulations (points) with parameterizations (solid line) [155] for (a) μ and (b) $e\gamma$. The simulations cover various zenith angles (black: 12°, red: 25°, blue: 36°, green: 45°, yellow: 53°, and magenta: 60°). The attenuation of the muonic component is weaker than that of the electromagnetic component. To note, the evolution of the muon decay products and hadron jet components behave like the muonic and pure electromagnetic component, respectively. For almost all regions of the parameter space, deviations in the description of S_0 are smaller than 5 % [105].

where f_{trunc} denotes truncation asymmetries due to the presence of the ground and A_{eff} arises from the geometrical asymmetries of a non-spherical detector. A_{eff} also takes into account that particles with certain transverse momenta will not reach a detector at a certain position. Using these parameterizations, the total signal is given by

$$S(r, \Delta X, E, \theta, \psi) = S_{e\gamma} + N_\mu \left(S_\mu + S_{e\gamma(\mu)} \right) + R_\mu^{\gamma(r)} S_{e\gamma(\text{had})}. \tag{3.4}$$

where the exponent $\gamma(r)$ is modeled as a function of core distance. To derive the relative muon number R_μ, the signal model is used

$$R_\mu(E) := \frac{S_{0,\mu}\left(r = 1000\,\text{m}, \Delta X = 400\,\text{g}\,\text{cm}^{-2}, E\right)}{S_{0,\mu}^{\text{ref}}\left(r = 1000\,\text{m}, \Delta X = 400\,\text{g}\,\text{cm}^{-2}, E = 10^{19}\,\text{eV}\right)}. \tag{3.5}$$

with the reference signal $S_{0,\mu}^{\text{ref}}$ from a QGSJET-II.03 proton shower at an energy of 10^{19} eV and local shower azimuth of $\psi = 90°$.

In developing the most recent timing model (discussed in Section 3.1.4), the author of [108] investigated the accuracy of the signal model using a fixed energy and zenith simulation library. The simulations consisted of proton, carbon, and iron primaries from QGSJET-II.03 and EPOS-1.99. For each primary and interaction model combination, 10 showers were generated for each combination of zenith angle $\theta \in \{0°, 37°, 48°, 36°, 55°, 60°\}$, energy $E \in \{10^{17}, 10^{17.5}, 10^{18}, 10^{18.5}10^{19}, 10^{19.5}, 10^{20}\}$ eV, and one of the 12 monthly atmospheric models. Each simulated signal S was compared to its model prediction $\widehat{S}$ from Eq. (3.4). Relative signal residuals for different primary energies are shown in Fig. 3.8. As expected, the signal model poorly predicts the signal for primaries with energies below $10^{18.5}$ eV, whereas above this threshold deviations are within ±5 %. Additionally, on average, the model overestimates small signals and underestimates large signals. For AMIGA (SD-750)

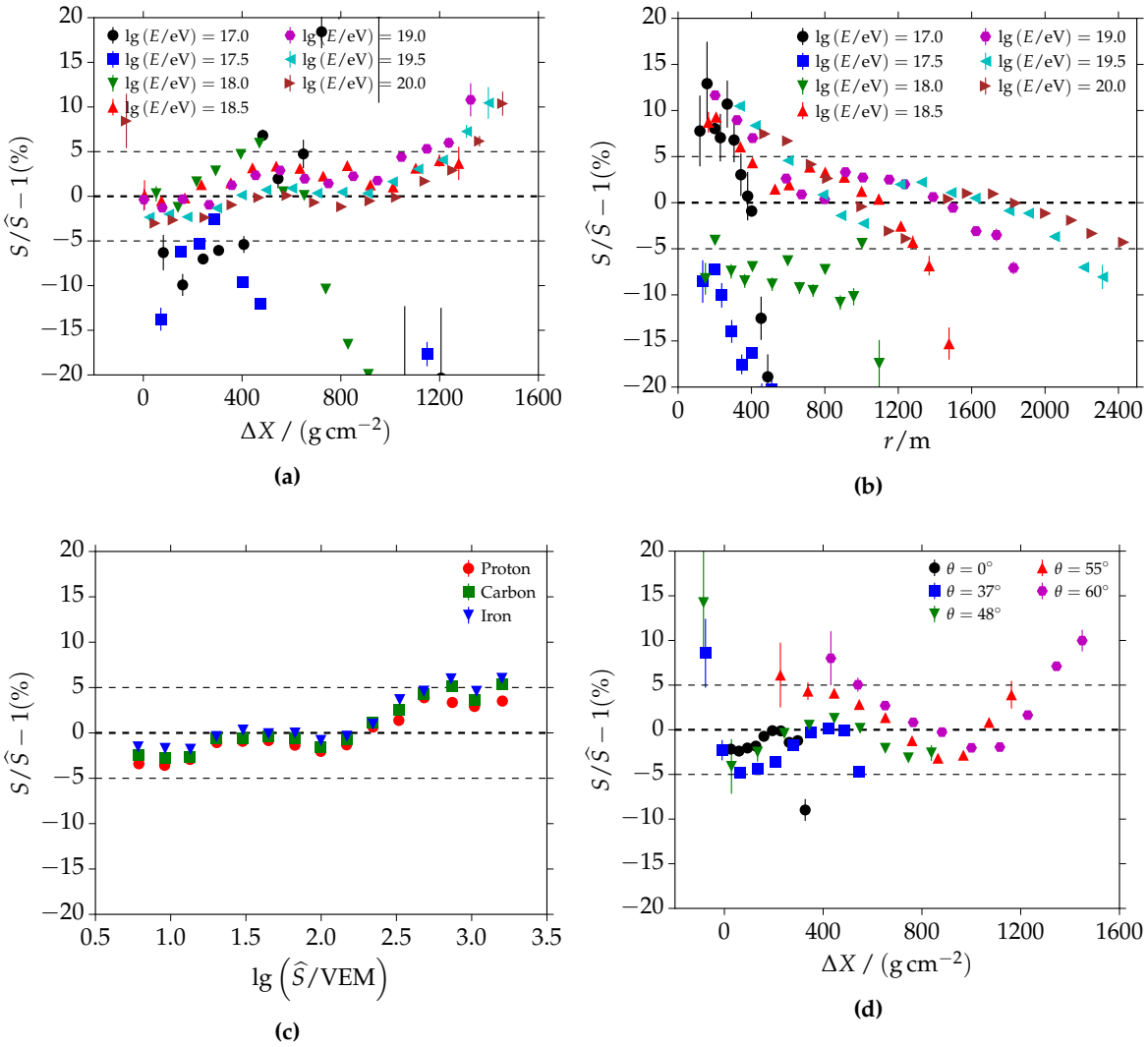

Figure 3.8: The relative difference between simulated signals and the model prediction is shown with respect to (a) ΔX and (b) r for different Monte Carlo energies; it is also shown with respect to (c) the signal for various primary particles. In (d), consideration is given to the relative signal difference with respect to ΔX and for specific zenith angles. Due to the nature of signals and the limitations of the parameterization used, certain selections were applied to ensure a valid comparison [108].

and other configurations, the signal model will need to be extended to lower energies. While a universal description of air shower signals down to energies of 10^{17} eV is possible, the shower-to-shower fluctuations at lower energies might yield fluctuations in the hadronic-generated components that are too significant for an average description to effectively be made.

Further signal residuals are depicted in Fig. 3.8. As is ideal, there are no biases with respect to primary particles and interaction models. In Fig. 3.8d, the relative signal difference is explored as a function of zenith angle. While there is no significant bias of the signal as a function of the estimated signal, there are trends with respect to ΔX that are not currently accounted for in the signal model. In future analyses, a library with more zenith angles could help improve this parameterization.

3.1.4 Time model of signals in WCDs

In addition to the signal model, universality can be extended to describe the arrival time distributions of the four particle components. While several models have been developed [105, 108, 151, 153, 155, 158, 160–163], the time model presented herein is from [108]; it is an extension to the one presented in [153, 163]. The parameterizations for this model were derived from the Monte Carlo simulations mentioned in Section 3.1.3 that were used to evaluate the signal model.

Like the signal model, the time model is using SD simulations which incorporate the hardware and calibration properties of the Auger SD[10] (Section 1.2.1). The total signal S_i of a particle component i is obtained from its instantaneous time trace via integration from the 0 % to 100 % time quantile

$$S_i = \int_{t_0}^{t_{100}} \frac{\mathrm{d}S_i}{\mathrm{d}t}(t)\,\mathrm{d}t. \tag{3.6}$$

The start time for a simulated trace is the FADC bin in which the calibrated signal exceeds 0.1 VEM. Just as is implemented for real data, the simulation start time algorithm accounts for accidental peaks and fluctuations in the traces. Nevertheless, a small portion of signal arrives earlier than the estimated start time. At this time, it is unclear whether this is due to biases from the shower resampling[11] or due to a minor bug in the Offline framework.

To note, the biases due to the resampling region's size were studied for the average arrival time of muons [164]. The study found that biases are reduced when the sampling region extends radially from a station by only 5 % —instead of the standard 10 %. The time biases are caused by the resampling coupled with the nature of the lateral distribution[12] [165]. An additional time bias results from the correction of particle arrival times with a plane shower front. As discussed in Section 2.3.1, the best description of the shower is with a curved front; the curvature, in turn, depends on the particle component [158]. For the simulations used in this work, the size of the resampling are reduced to 5 % in its radial dimension; however, the effects due to the shower front geometry are not taken into account.

For the parameterization of the time model, all times are relative to when the shower core hits the ground. As the curvature of the shower front depends on the particle component, the difference in the height between the effective time origin and shower maximum will differ for each component. In Fig. 3.9a, the height difference as a function of X_{max} is plotted for the muonic component. The linear trend with respect to X_{max} is related to the energy spectrum of muons reaching the detector. For reference, the actual start times from the curvature model are plotted in Fig. 3.9b. As most muons propagate without interaction, they will arrive before the electrons, positrons, and photons. When muons decay close to the ground, their detectable decay products ($e^{\pm}$) will arrive almost in coincidence with the first muons.

The evolution of a WCD's signal depends upon the arrival time distribution and detector response to the particles therein. Due to the various particle types and energies, an analytical expression of the detector response is rather hard to derive. To expedite numerical-based approaches which primarily use time-expensive Geant4 simulations, the

[10] Time traces of signals are simulated in 25 ns bins, which matches the frequency of station electronics. Saturation effects and baseline fluctuations are only applied to the total trace. An unsaturated version of the total trace is also stored.

[11] Because of the thinning algorithm used to expedite simulations, a resampling algorithm is used when the Corsika ground-level particles are simulated inside of a tank. The resampling essentially extrapolates the particles that were saved based upon assigned weights.

[12] Due to the radial dependence of the lateral distribution, stations close to the core are injected with too many early particles leading to a time bias.

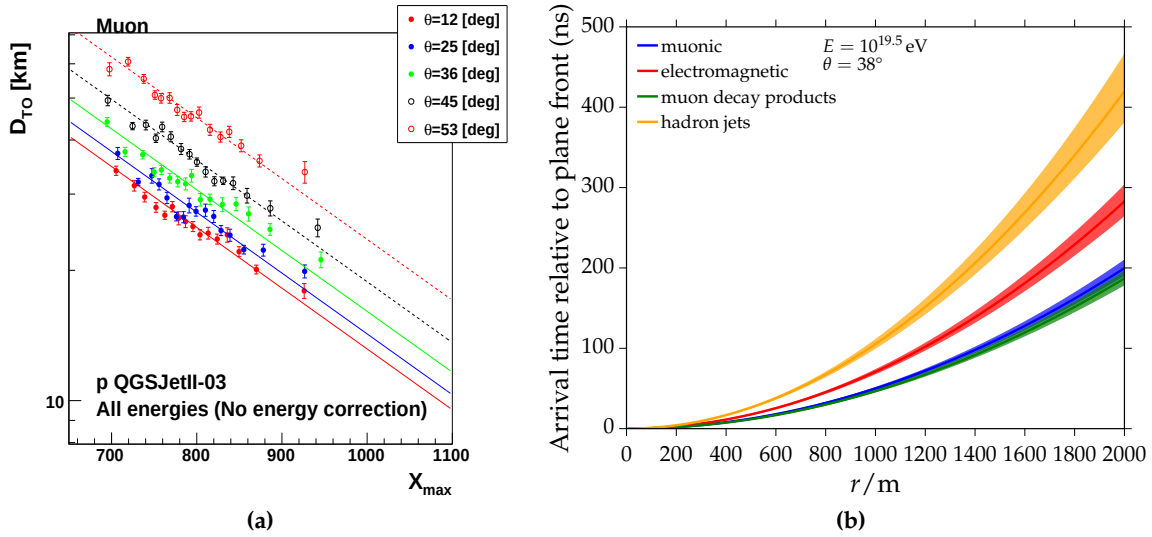

Figure 3.9: (a) Distance from the effective time origin to the shower maximum as a function of the shower maximum for proton-induced simulations with differing zenith angles [163]. (b) The start time model for the four signal components (colors) as a function of core distance for a fixed energy and zenith angle. The shaded bands around each model line represent the variation due to different azimuthal angles [108].

detector response was tabulated [166]. Thus, the parameterizations for the arrival time distributions were developed to describe the temporal signal *after* the simulation of the detector response

$$\frac{\mathrm{d}S_i}{\mathrm{d}t}(t) = \frac{\mathrm{d}S_i}{\mathrm{d}t}(t|r, \Delta X, \theta, \psi, E). \tag{3.7}$$

The parameterization of Eq. (3.7) is independently derived for each of the particle components. The best fitting distributions were achieved with a log-normal and a generalized gamma distribution[13]. The description quality of both functions is very similar; thus, a log-normal approach was chosen.

Before fitting a distribution, traces are divided into bins with respect to distance to the core r, distance to the shower maximum ΔX, primary energy E, zenith angle θ, and azimuth angle ψ. As the employed Monte Carlo shower library had fixed primary energies and zenith angles, these bins are already defined. For the binning in radial and azimuthal dimensions, a compromise between a uniform bin width and a reasonable number of entries is chosen. As the distribution of ΔX depends strongly on the particular (r, ψ, θ, E) bin, ΔX bins are chosen such that they include between 30 and 60 traces. To avoid distortions due to trigger thresholds, only traces with an expected total signal above 4 VEM—as calculated from the signal model (Section 3.1.3)—are considered. Further details of binning are discussed in [108].

Within each $(r, \psi, \theta, E, \Delta X)$ bin, a weighted average of traces is calculated to reduce statistical and thinning fluctuations. While each trace is binned in intervals of 25 ns, the traces are not in phase. To remedy this, each trace is first resampled to be in phase with a common set of time bins. Afterwards, a weighted average of all normalized traces in a time bin is calculated. The uncertainty of a signal bin is estimated from the standard deviation of the mean of all normalized signals within the bin. If there is a small number of traces, this

[13] The generalized gamma distribution has three parameters, denoted as m, s, and ℓ. For $\ell = 0$, the generalized gamma distribution reduces to a log-normal distribution with m and s —which are proportional to the mean and standard deviation.

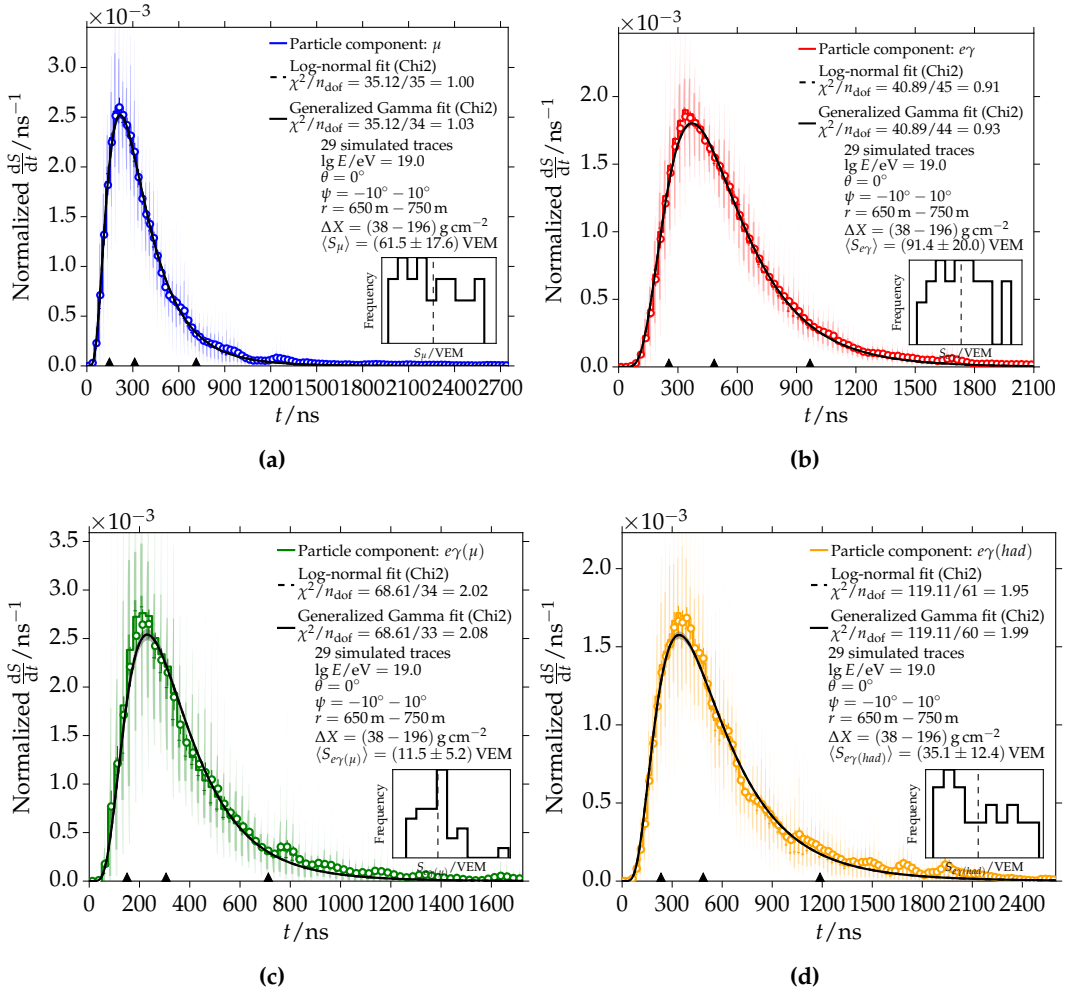

Figure 3.10: Average time distributions of ground signals in air showers initiated by proton, iron, and carbon primary particles meeting certain criteria as specified in the legends. Particle components: (a) muons, (b) pure electromagnetic, (c) electromagnetic from muon decay, and (d) electromagnetic from hadron jets. The shaded distributions show the variation of the simulated traces within the time bins. The darker regions represent the $1\,\sigma$ spread, whereas the more translucent regions extend to $\pm 3\,\sigma$. The t_{10}, t_{50}, and t_{90} time quantiles are represented by black triangles at the bottom of the plots. The small inset plots illustrate the distributions of the component signals [108].

procedure leads to an underestimated standard deviation. For these cases, a correction—on the percent level or smaller—is applied.

Next, the average traces are fit with a chi-squared fit, in which the model is integrated in each time bin to properly take into account its nonlinear shape. At large times, the time shape deviates, so only time bins below the 95 % time quantile are taken into account. Examples of fits to average simulated component traces in WCDs are depicted in Fig. 3.10. As determined via the χ^2 calculation, the generalized gamma distribution does not fit significantly better than the log-normal model.

The next step in the model building is the parameterization of the shape variables mean m and width s obtained from the log-normal fits to average traces

$$f_{\mathrm{m,s}}(\Delta X, \psi, \theta, E) = f_{\Delta X}(\Delta X) + f_{\mathrm{geo}}(\theta, \psi, \Delta X) + f_{\lg E}(\lg E, \Delta X), \tag{3.8}$$

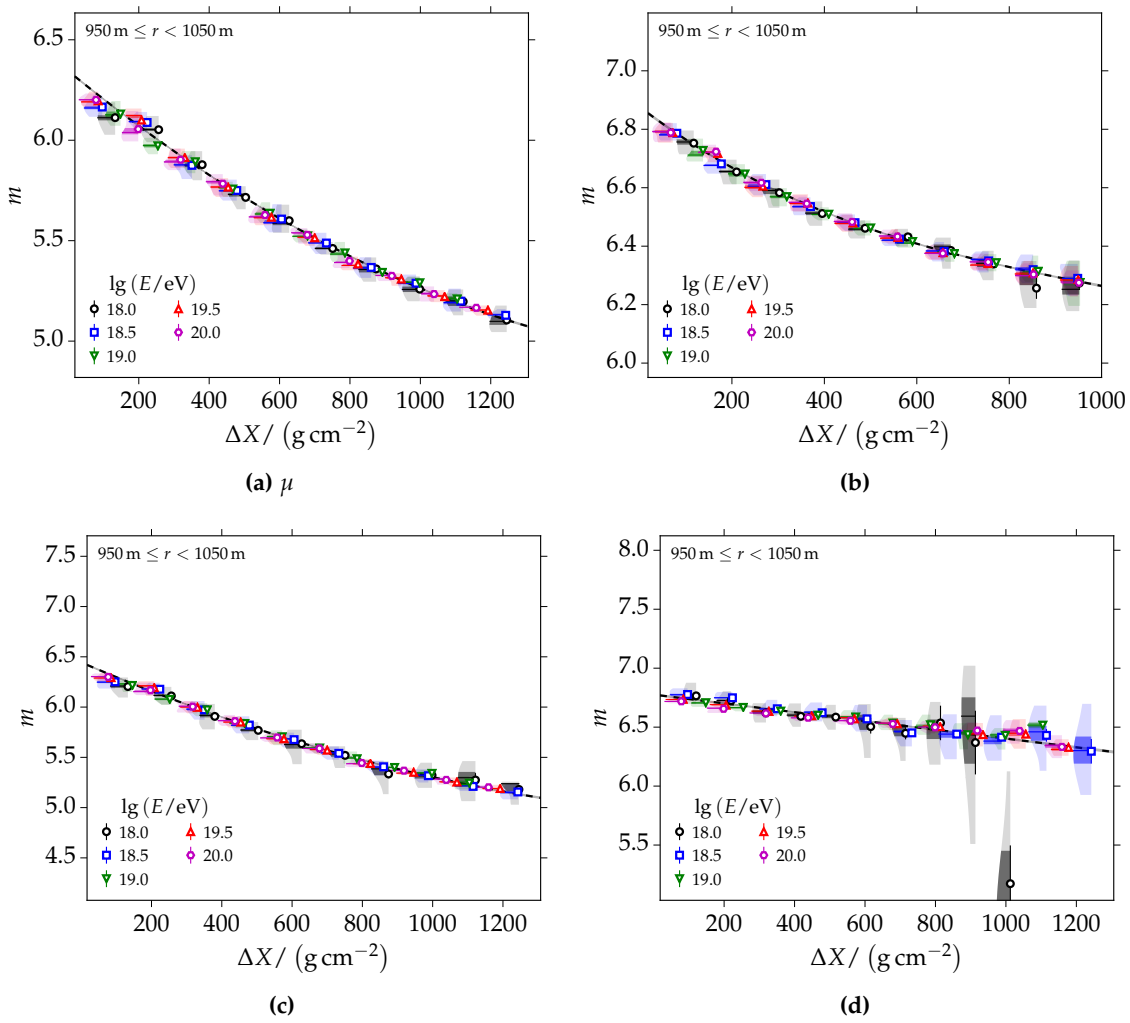

Figure 3.11: Model description of the ΔX dependence of the mean parameter m for: (a) μ, (b) $e\gamma$, (c) $e\gamma(\mu)$, and (d) $e\gamma(\text{had})$. Different primary energies are indicated with different colors and markers. Only stations in the radial distance range 950 m $\leq r <$ 1050 m are included [108].

where

$$
\begin{aligned}
f_{\Delta X}(\Delta X) &= a_{\Delta X} + \Delta X_{\text{ref}}(b_{\Delta X} + \Delta X_{\text{ref}}(c_{\Delta X} + d_{\Delta X}\,\Delta X_{\text{ref}})),\\
f_{\text{geo}}(\theta, \psi, \Delta X) &= \sin\theta(a_{\text{geo}}\,\cos\psi + b_{\text{geo}}\,\Delta X_{\text{ref}}),\\
f_E(\lg E, \Delta X) &= \lg E_{\text{ref}}(a_{\lg E} + b_{\lg E}\Delta X_{\text{ref}}),\\
\Delta X_{\text{ref}} &= \Delta X/(750\,\text{g cm}^{-2}) \quad \text{, and}\\
\lg E_{\text{ref}} &= \lg(E/\text{eV}) - 19.
\end{aligned}
$$

Depending on the particle component and parameter, the number of fit parameters is reduced by fixing higher order contributions to zero. The model holds for a specific core distance range with width Δr. To obtain a full parameterization, an iterative procedure is used. First, Eq. (3.8) is fit in each of the available core distance bins; then, analytical expressions for the fit parameters as a function of r are found. Results on the ΔX dependence of the mean parameter m for the different particle components are shown in Fig. 3.11.

After the modeling of all ΔX dependencies, each of the parameters used in Eq. (3.8) is parameterized as a function of core distance r[14]

$$f_r(r) = \sum_{i=0}^{n} a_i \left(\frac{r}{1000\,\mathrm{m}}\right)^i , \tag{3.9}$$

where n depends on the parameter and its observed change with r. Fits for all polynomial orders from 0 to 10 are attempted, and the best choice is selected with a leave-one-out cross-validation method[15] to avoid over-fitting.

Combining the parameterizations from Eq. (3.8) and Eq. (3.9) leads to a complete description of the mean and width parameters m, s of the log-normal time models. The accuracy of each parameterization is scrutinized by comparing the model prediction $\widehat{m}$ and $\widehat{s}$ to each m and s. The relative residuals $\frac{m-\widehat{m}}{\widehat{m}}$ and $\frac{s-\widehat{s}}{\widehat{s}}$ are studied as a function of all relevant quantities and physics parameters. Selected residual plots for the mean parameter of muonic time traces are shown in Fig. 3.12.

A further description of the time model, parameterizations, and the residuals for all the particle components are given in [108]. In general, the size of the relative residuals of m are below 1 % for all particle components and dependencies. The model of s is much harder to control. Deviations up to 5 % occur for the muonic and the electromagnetic components. For the remaining particle components, most of the deviations are within 5 %; however, there are two large deviations on the order of 15 %.

3.2 Reconstruction

3.2.1 Constructing the likelihood function

The reconstruction is composed of several aspects: a simultaneous fit of the time traces and start times of triggered stations as well as the lateral distribution of the total measured signals. A fit of time distributions is only attempted for stations with at least five time bins with a signal exceeding 0.7 VEM; this criterion was tuned to simulations to give a compromise between resolution and reconstruction accuracy. Thus, depending on the signal size of a given station, it may contribute to one or more of these areas.

The universality reconstruction is comprised of 9 parameters: the *core position* $\vec{x}$, *relative core time* t_c, *shower arrival direction* (θ, ϕ), *energy* E, *depth of the shower maximum* X_{max}, and *relative number of muons* R_μ. R_μ is relative to the average muonic signal created by a proton-induced air shower simulated with QGSJET-II.03 at an energy of 10^{19} eV with the zenith angle of the incoming primary particle at a local shower azimuth of 90°. Depending on the reconstruction method employed, combinations of these 9 parameters may be fixed or free during the minimization of the total log-likelihood. In Fig. 3.13, the lateral signal distributions and time distributions for each particle component resulting from the universality reconstruction of a proton-initiated event with $\lg(E/\mathrm{eV}) = 19.4$ are depicted together with details about the simulated event.

The total log-likelihood is defined as

$$\ell = \ln \mathcal{L} = \ell_{\mathrm{shape}} + \ell_{\mathrm{start}} + \ell_{\mathrm{LDF}} , \tag{3.10}$$

[14] Due to large fluctuations and remaining trigger biases, only radial distances smaller than 2250 m are considered.

[15] To avoid over-fitting with high polynomial orders used, a cross validation method is used to find the optimum order. In this general class of methods, a portion of the data (e.g. a data point) is left out when the fit is performed and later, used to compute a statistic to quantify the quality of the fit.

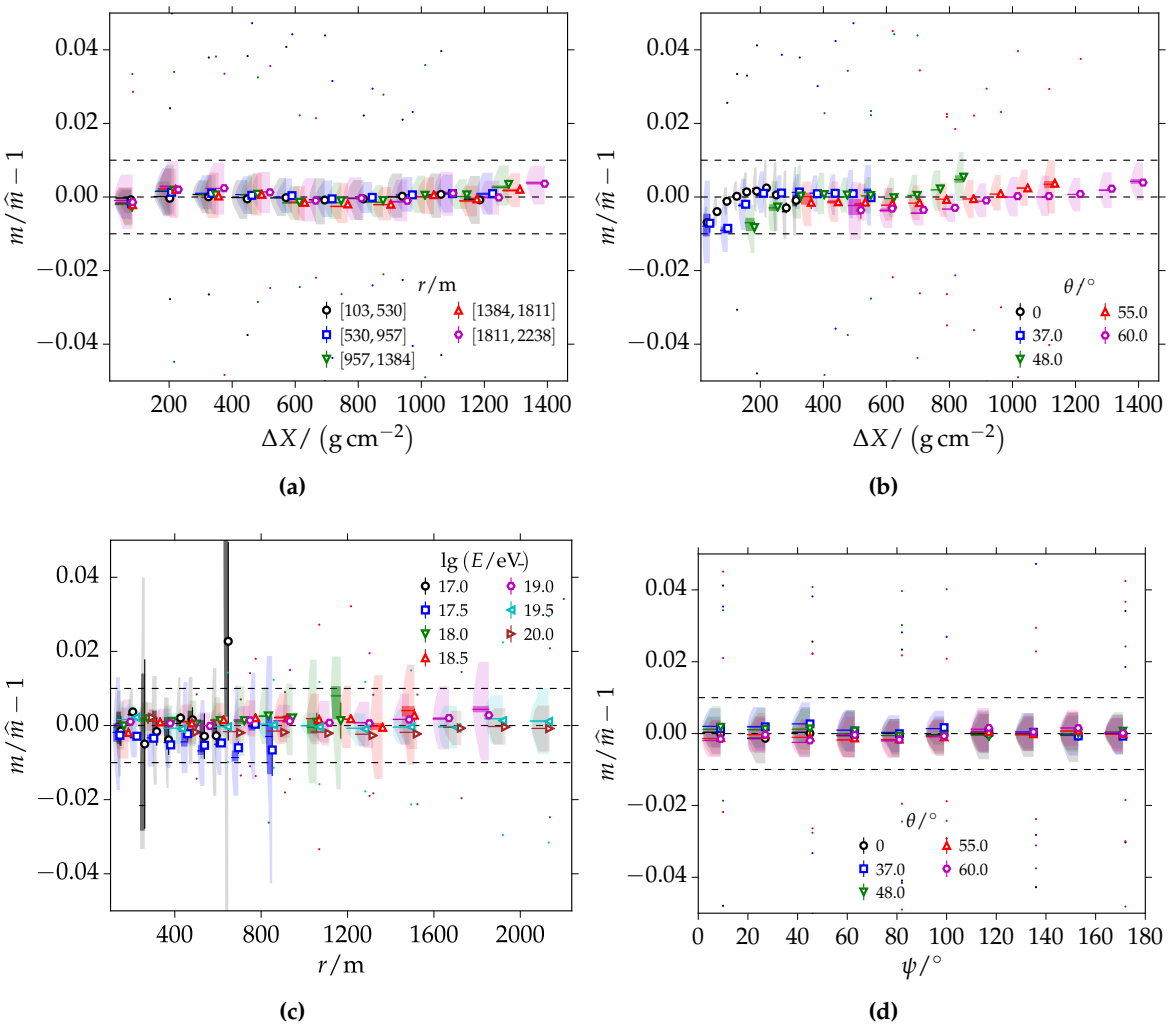

Figure 3.12: Relative residuals of the muon time model prediction for the mean parameter m. Residuals are given as a function of different quantities of interest [108].

where ℓ_{shape} relates to the fit of arrival time distributions, ℓ_{start} comes from the estimation of the start time[16], and ℓ_{LDF} is associated with the LDF fit. The individual likelihood contributions are explained in the following subsections.

3.2.1.1 Fit of arrival time distributions

As mentioned before, a fit of the time distribution —**shape fit**— is only attempted for traces with at least five signal bins above 0.7 VEM/bin. This threshold was chosen to avoid low-signal traces, particularly those which greatly fluctuate and are more sensitive to accidental muons. By considering the time and signal responses for the four particle components, each time bin may be compared to the universality prediction. The offset of the arrival times of first particles with respect to the plane front is given by the curvature model (discussed in Section 3.1.4)

$$T_c^p = T_c^p(r, X_{\max}, \lg E, \theta, \phi), \tag{3.11}$$

[16] As noted in [108], the implemented estimation of the start time often leads to poorly reconstructed values. While it is described here as a contributing factor, it is not active in the analyses shown throughout this thesis.

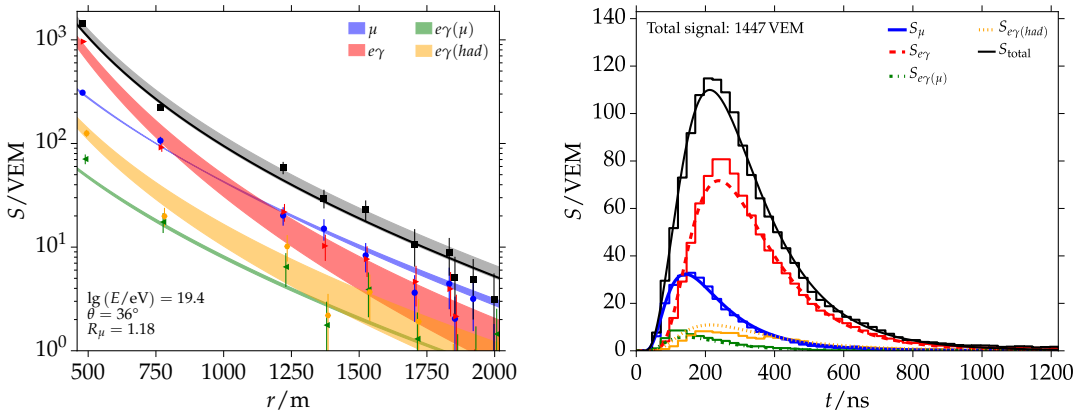

Figure 3.13: (a) Example LDFs in the universality reconstruction of a simulated event. The sum of component predictions is fit to the total signals (black). A comparison of the LDF components and their model predictions are given. (b) Results of the time fit of the hottest station. For comparison, the component traces (histograms) are plotted against the model predictions (smooth lines), which come from the fit of the total trace (black). The global reconstruction method described in Section 3.2.3 is used.

which depends on the particle component p, shower geometry, and other properties of the primary particle. The plane front time and arrival time of the first particle are extracted from the trace using a typical log-normal time distribution, as depicted in Fig. 3.14a.

To account for a non-linear shape of the time model, the model is integrated within the selected bin i and compared to the measured signal (S_i). The integrated model is found by evaluating the c.d.f.[17] of the time model at the edges of the bin, subtracting the resulting values, and dividing by the bin width. The model estimate $\hat{S}_i$ is obtained from the normalized time model f^p_{trace} and the signal model f^p_S

$$\hat{S}_i = \hat{S}(t_i) = \sum_{p=1}^{4} f^p_{\text{trace}} f^p_S \tag{3.12}$$

with a summation over the four particle components. The model dependencies of f^p_{trace} and f^p_S are: $f(r, \theta, \psi, \lg E, \Delta X, R_\mu, p, \text{month})$.

Thus, the log-likelihood is given by the summation of the logarithm of normal distributions for each time bin i

$$\ell_{\text{shape}} = \sum_{s}^{\text{stations}} \sum_{i} \ln \mathcal{N}(S_{s,i}, \mu = \hat{S}_{s,i}, \sigma = \sigma_{\text{SD}}(\hat{S}_{s,i})), \tag{3.13}$$

where μ comes from the model prediction and σ is the uncertainty according to the signal uncertainty model detailed in Eq. (2.3). The associated bin errors used in this shape fit are calculated as

$$\sigma = \sigma[\text{S}] \cdot p(f_s) \cdot \sqrt{S}, \tag{3.14}$$

where $\sigma[\text{S}]$ and $p(f_s)$ are given in Eq. (2.3) and Eq. (2.4), respectively.

[17] cumulative distribution function

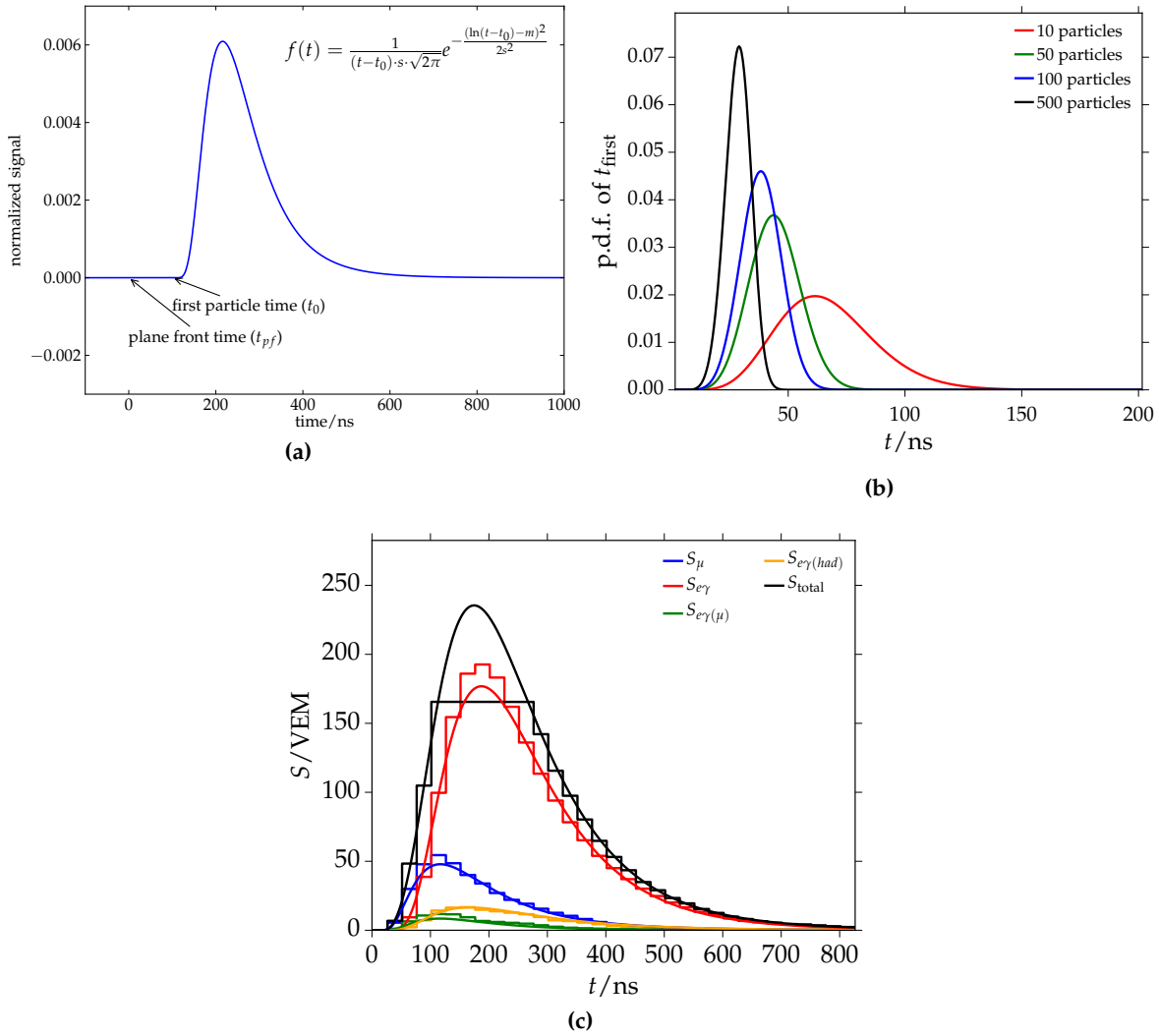

Figure 3.14: (a) The relevant times for a particle time trace — plane front time and the time of first particle arrival —are pictorially described. (b) Assuming a log-normal trace with semi-realistic parameters of $m = 5$ and $s = 0.55$ (compare to Section 3.1.4), toy distributions of arrival time of first particles are shown for various particle populations. Thus, this illustrates the different magnitudes of sampling delay. (c) A saturated, simulated event counterpart for Fig. 3.13b. As before, only the total trace in black (excluding the saturated plateau) is fit. As mentioned in Section 3.1.4, the particle component traces are saved without saturation effects (for all [108]).

For saturated events[18], only the non-saturated part of their trace contributes to the shape fit —i.e. all time bins that do not belong to the plateau. To exclude saturated bins, only bins where $S_i < 0.95 \max_j S_j$ are selected for this partial fit of the trace. An example saturated event is depicted in Fig. 3.14c.

[18] An event with at least one low-gain saturated station is called a saturated event. Saturation typically occurs in a station (stations) that is (are) closest to the core of the shower. While it is possible to recover the integrated signal of a saturated station for its possible inclusion in an LDF fit, as described in Chapter 2, the total trace itself cannot be recovered in an accurate way.

3.2.1.2 Estimation of the start time

While traces with small signals (or saturation) cannot be (fully) used in shape fits without introducing potential biases, the time structure of these traces may still be used in the estimation of the start time. Typically, the particles arriving earliest are muons. Thus, the model prediction for the start time may be obtained from the time model f_{time} for the muonic component through an *extreme value transformation*[19] to calculate the p.d.f. of the first arriving particle

$$f_{\text{first}}(t) = n_\mu \left(1 - \int_0^t \mathrm{d}t' f^\mu_{\text{time}}(t')\right)^{n_\mu - 1} f^\mu_{\text{time}}(t) \tag{3.15}$$

where time t is relative to the time given by the curvature model for muons and n_μ is estimated from the signal model of the muonic component. As only the muonic particle component is used, the above expression is only an approximation of the distribution of start times. Additionally, this p.d.f. only takes statistical sampling delays into account.

In reality, the earliest muon would be created close to the *first interaction point* X_0. As described in Section 3.1.4, the start time model is a curved shower front with an effective origin of particles along the shower axis —which in turn, depends on distance to the shower maximum, zenith angle, and particle component. Consequently, this description does not include fluctuations in X_0. Thus, the width of the distribution given by Eq. (3.15) is underestimated. An example of distributions of arrival times for different particle populations (and inherently, signal sizes) is illustrated in Fig. 3.14b. The average delay in the arrival time of the first particle increases with decreasing signal size (i.e. a smaller population of particles).

The log-likelihood for the fit of start times is summed across all participating stations

$$\ell_{\text{start}} = \sum_s^{\text{stations}} \ln f^s_{\text{first}}(t^s_{\text{start}}), \tag{3.16}$$

where t^s_{start} is the respective start time determined by an algorithm in Offline. The distribution of the expected and measured arrival time of the first particle varies from station to station. In using the extreme value transformation in Eq. (3.15), a p.d.f. of the earliest particle arrival time may be constructed. Reconstructions of simulated showers show that the use of the start time fit leads to a bias of the reconstructed X_{max} on the level of $30\,\text{g}\,\text{cm}^{-2}$ at 10^{19} eV that decreases with increasing energy[20] [108]. For this work, the start time fit is not used in the universality reconstruction in order to avoid biases in the reconstructed depth of the shower maximum X_{max}.

3.2.1.3 LDF fit

All candidate stations not used in the shape fit are included in an LDF fit that compares the total measured signal to the expectation from the signal model. The Poissonian log-likelihood has the same structure as that used for the non-saturated stations of the standard SD reconstruction

$$\ell = \ln \mathcal{L} = \sum_i^{\text{non-sat.}} \ln f_{\text{P}}(n_i, \mu_i) \tag{3.17}$$

[19] This is a special case of a general class of transformations which are used to arrive at the distributions of quantiles of time distributions.

[20] The author of [108] notes that this problem may be solved when the fluctuations in X_0 are properly accounted for in the p.d.f.

For details of the contribution to this equation, see the text surrounding Eq. (2.8). To convert signals into effective particle numbers, the signal uncertainty model —as described and used in SD reconstruction (Section 2.2.2)— is employed.

In comparing the above equation to Eq. (2.8), it is seen that the terms for the saturated and silent stations are not included. Almost all saturated stations are selected for and contribute to the shape fit; thus, such saturated stations would be counted twice if used in the LDF fit term. More detailed studies of the reconstruction accuracy of saturated stations is presented in Appendix D.2. Alternately, the addition of silent stations would only contribute significantly at the lowest energies when the number of triggered stations is less than five. As seen in Fig. 3.22a, such an addition could potentially help events with energies less than $10^{18.7}$ eV. For such an addition to be effective, the negative log-likelihood contributions would need to be normalized. As it is currently implemented, the negative log-likelihood terms are not normalized. As the energy increases and number of selected stations increases, the shape fit term —which is calculated on a bin-basis— is roughly 1-2 orders of magnitude greater than the contribution from the LDF fit.

In Appendix D.1, a deviance model is investigated where the contributions of the likelihood are scaled so that the sum is usable as a goodness-of-fit estimator. This is done using a generalized χ^2-method. When compared to the negative log-likelihood, the deviance method has similar biases and resolutions. Nevertheless, the deviance minimizing function has a decreased, zenith-dependent efficiency at the highest energies, which makes it ill-suited at this time for mass composition studies. While it is not used in this work, the deviance method —with refinement— could prove to be a powerful tool in debugging Offline reconstruction methods and providing comparisons between the fits of simulations and data. This is possible for this minimizing function (and not the negative log-likelihood) because the generalized-χ^2 lends itself to direct comparisons. Such work is outside the scope of this thesis.

3.2.2 Example reconstructions

Before enumerating the different reconstruction methods investigated in this work (Section 3.2.3), example reconstructions are shown to validate and help readers visualize the universality reconstruction. In Fig. 3.15, the reconstruction of a simulated shower from a proton primary with a true energy of $10^{19.4}$ eV is shown. The reconstruction method used for this example is one where 8 parameters are simultaneously fit while the energy is held fixed; the log-likelihood described in Section 3.2.1 is used. This reconstruction type and others are discussed in Section 3.2.3. Overall, all fit quantities are well-reconstructed and within the statistical uncertainties of the true values:

- The fit R_μ is 1.18 ± 0.11 compared to the true value of 1.23.
- The reconstructed X_{max} is $(815 \pm 30)\,\text{g}\,\text{cm}^{-2}$, which is within $14\,\text{g}\,\text{cm}^{-2}$ of the true value of $801\,\text{g}\,\text{cm}^{-2}$.
- The core position is found to be $(-2983 \pm 20, 3477 \pm 17)\,/\text{m}$. This position radially differs from the true core of $(-2986, 3489)\,/\text{m}$ by 12 m. As further discussed in Section 3.2.3.1, in comparison, the reconstructed position of the SD is biased as it fails to take into account the azimuthal asymmetry of the signal, as seen and discussed later in Fig. 3.20. For this example event, the impact point fit with the SD is $(-2991, 3419)\,/\text{m}$ and offset from the true value by 70 m.
- The reconstructed shower arrival direction (θ, ϕ) is $(36.1 \pm 0.9, -74.5 \pm 4.1)\,/^\circ$, where both elements of the coordinate are within less than 1° of the true angular coordinate of $(36.2, -73.8)\,/^\circ$.

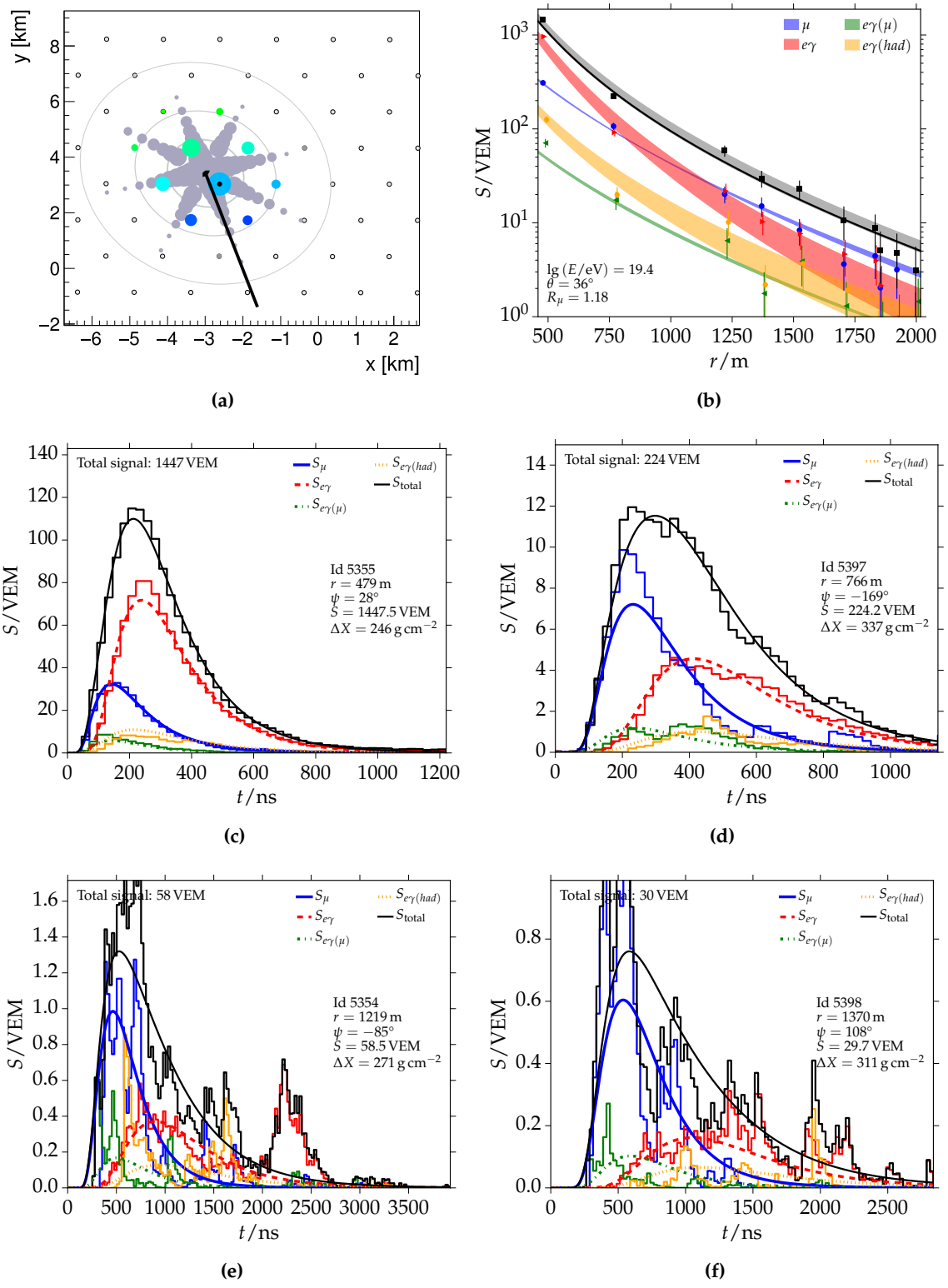

Figure 3.15: Universality reconstruction of a simulated proton-induced shower with an energy of $10^{19.4}$ eV. (a) The footprint of the shower as simulated in an ideal dense array (taken from the Offline EventBrowser). Only stations corresponding to the ideal array of the SD-1500 (in shades of blue and green) are used in the reconstruction. The arrival direction and core location are shown with the black line. (b) Only the total LDF (black) —as measured by the WCDs— is used in the LDF fit. The predicted LDFs of the four particle components are compared to the signals they each deposited in the stations. (c) - (f) Shape fits for the four hottest stations where only the total traces from the WCDs are fit. The traces of the four particle components are compared to the model predictions. (e) and (f) contain lower signal traces with increased fluctuations.

In total, ten stations were triggered, of which four contributed to the shape fit and the remaining six to the LDF fit. As the shape fit contribution is calculated bin-wise, it dominates the log-likelihood with a value of -229.92, whereas the LDF contribution is calculated on the station-level and equates to -14.27.

In the universality reconstruction, the total LDF is compared to the sum of the expected distributions of the four particle components (Fig. 3.15b), which are derived from the signal model discussed in Section 3.1.3. As only the data (black points) are fit, distributions for the individual components are shown with respect to the model predictions. The shaded regions around the model lines represent their azimuthal asymmetries. All in all, the universality models give an accurate description of the component signals. The uncertainties of the total and particle component signals are calculated using the signal uncertainty model described in Eq. (2.3). While this uncertainty is reasonable for the total signal, it is not strictly valid for the component signals as the uncertainty model is an empirical description of the fluctuations of the total signal only.

In considering real data, the underlying parameterizations and fitting procedure of the universality reconstruction are the same as that used for simulations. In Fig. 3.16, the reconstruction of a high-quality event measured with both the SD and FD is considered. The event was observed on April 16, 2010 and is identified with the Auger ID 101056563000 and SD ID 9464726[21]. The longitudinal development of an extensive air shower was independently measured with the FD telescopes located at *Los Leones* (LL) and *Los Morados* (LM). As the longitudinal profile is directly correlated with the pure electromagnetic component, the FD does not have direct access to R_μ. 15 stations of the SD-1500 triggered. The primary reconstructed energies are $E_{\mathrm{SD}} = (25.6 \pm 1.1 \pm 0.4)$ EeV, $E_{\mathrm{LL}} = (28.3 \pm 1.2 \pm 2.5)$ EeV, and $E_{\mathrm{LM}} = (27.6 \pm 0.4 \pm 1.5)$ EeV.

- The universality reconstructed depth of shower maximum is $X_{\mathrm{max}}^{\mathrm{Univ}} = (784 \pm 16)\,\mathrm{g\,cm^{-2}}$. The weighted average of the FD measurements yields $\langle X_{\mathrm{max}}^{\mathrm{FD}} \rangle = (795 \pm 9)\,\mathrm{g\,cm^{-2}}$; thus, $X_{\mathrm{max}}^{\mathrm{Univ}}$ is within $1\,\sigma$ of the FD value.
- While the FD gives reasonable values for the arrival direction, the SD gives a more accurate and precise result on average. The SD gives a zenith angle of $(48.5 \pm 0.2)^\circ$ and azimuth of $(58.0 \pm 0.2)^\circ$. Both of these are within 0.2° of the universality estimates for $\theta = (48.6 \pm 0.2)^\circ$ and $\phi = (58.2 \pm 0.2)^\circ$

The LDF and start times of the SD-1500 stations are shown in Fig. 3.17a and Fig. 3.17b. Like in simulations, the measured signals (black points) are fit to the sum of the expectations for the four signal components (black line). The predictions for the LDFs of the individual particle components are indicated with different colors, and the shaded regions around them represent their azimuthal asymmetries. Fits to the traces of the four hottest stations are shown in the remaining plots of Fig. 3.17. The hottest station has the largest weight in the reconstruction. While the lower signal traces exhibit larger fluctuations, their general trends are well described by the model predictions.

3.2.3 Reconstruction methods

It is not intuitive how to best define the reconstruction method of universality. In an ideal scenario where enough stations are present, one would hope that a simultaneous fit of all 9 parameters —*core position* $\vec{x}$, *relative core time* t_c, *shower arrival direction* (θ, ϕ), *energy* E, *depth of the shower maximum* X_{max}, and *relative number of muons* R_μ— would be possible. However, due to the significant correlations between these variables —particularly that of X_{max}, R_μ,

[21] The simulations and data used throughout this work are described in Appendix B.

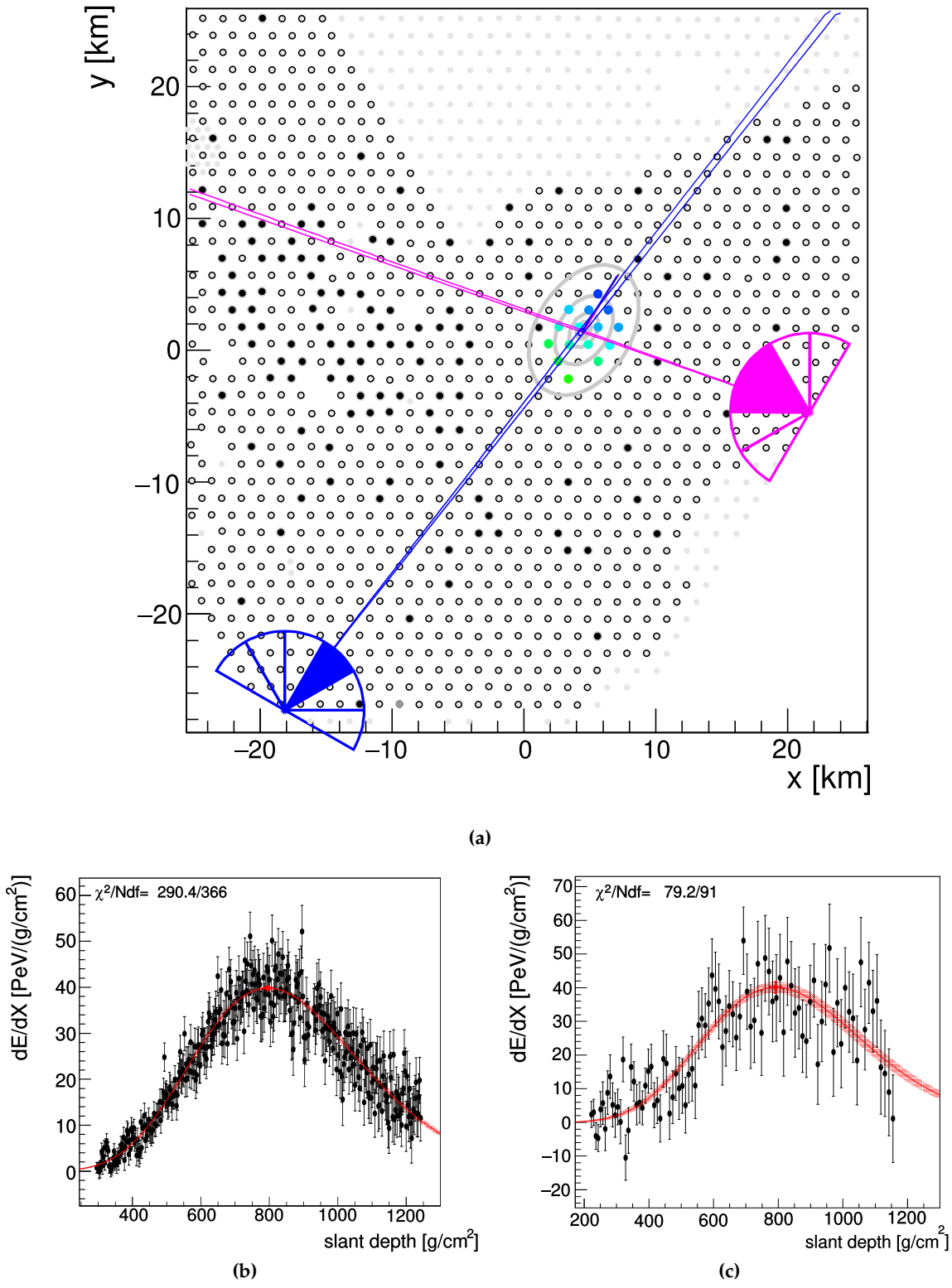

Figure 3.16: (a) The 2-D projection of the EAS on the Auger array as taken from the Offline EventBrowser for Auger ID 101056563000. The event was recorded by two FD sites and the SD-1500. The FD eyes Los Morados and Los Leones are indicated with pink and blue wedges, respectively. The number of colored wedges indicates the number of telescopes observing the longitudinal development. (b) The profile of the differential energy deposit as a function of slant depth as measured by the Los Morados FD telescope. (c) Energy deposit profile as measured with Los Leones. As seen in (a), the LL site was farther from the EAS than LM; consequently, greater reconstruction uncertainties were incurred.

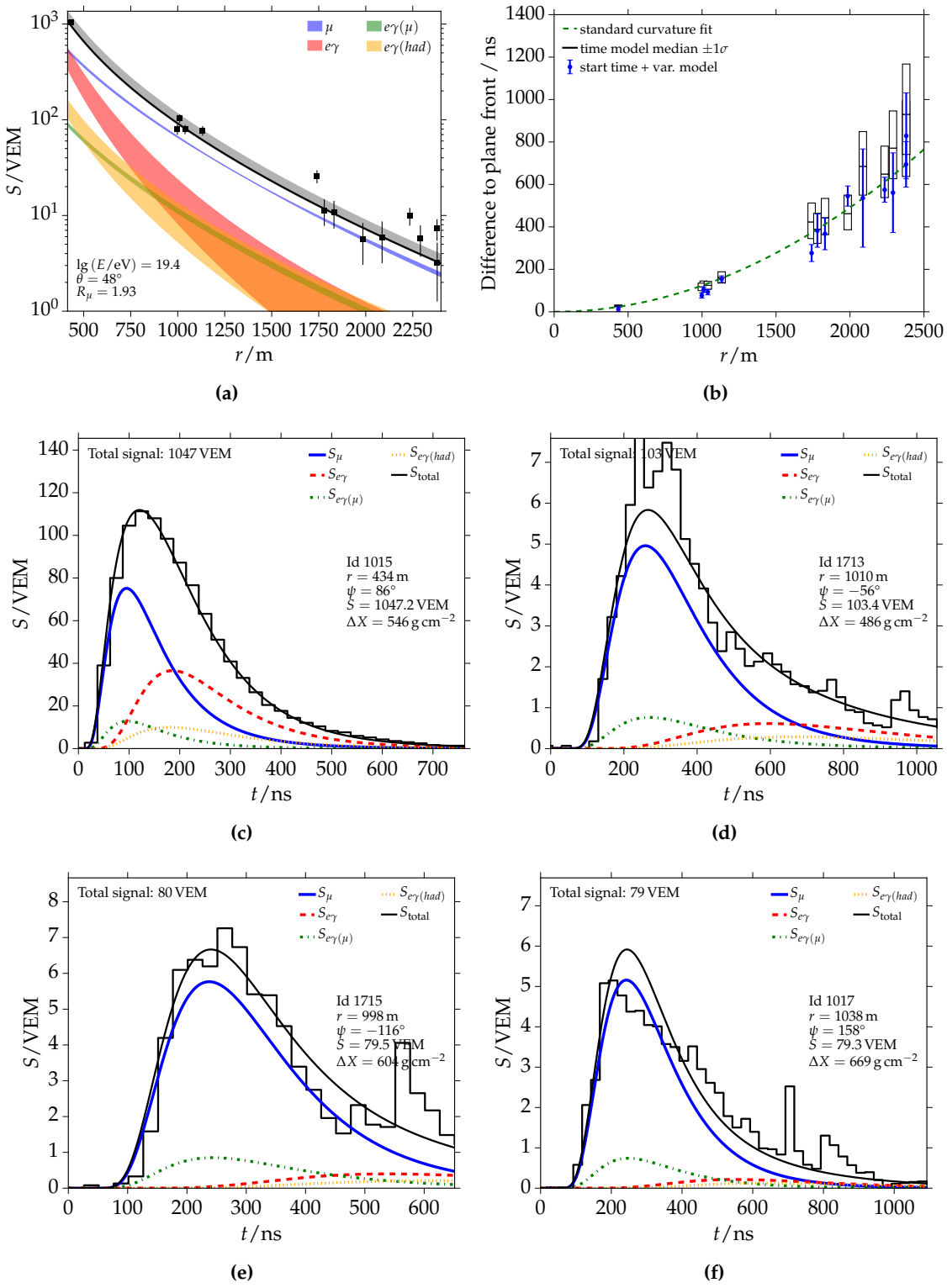

Figure 3.17: Universality reconstruction of a real event with a reconstructed primary energy of 2.56×10^{19} eV (Auger ID 101056563000, SD ID 9464726). (a) Fit of the total LDF (black). The colored LDFs show the predicted distributions for the different particle components. (b) The stations' signal start times are compared to that of a plane shower front. The expected standard curvature is shown with the dashed line, while the start time and model variance are compared to the time model median value $\pm1\,\sigma$. (c)-(f) The shape fit results of the total trace (black) for the four hottest stations. The model prediction for the four different components are plotted for comparison.

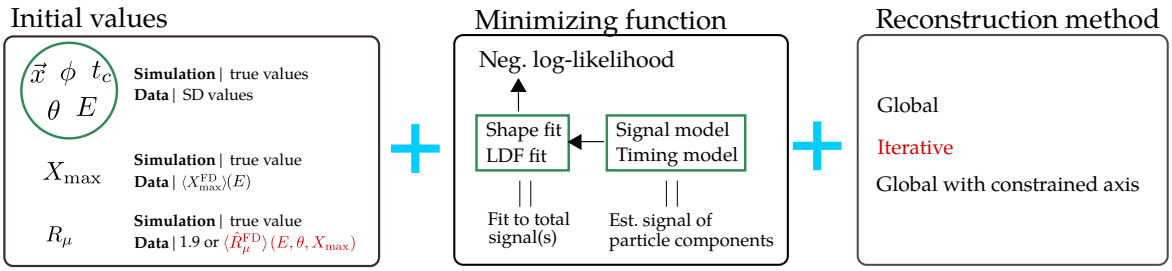

Figure 3.18: The various universality reconstructions can each be described as a combination of initial values, minimizing function, and choice of reconstruction method. Reconstruction methods listed in red (black) use $\langle \hat{R}^{\mathrm{FD}}_\mu\rangle(E, X_{\max}, \theta)$ model (the average R_μ value of 1.9). The shape and LDF fit are performed simultaneously with the negative log-likelihood. These are evaluated on the total trace measured in the triggered WCDs. The signal and time models inform this fit by providing estimates of the signal from the four particle components. The various reconstruction methods are discussed in the subsequent subsections of the text.

and E, it is necessary to add some constraints to yield reconstructed events with a high efficiency, relatively small bias (with minimum correlation with the arrival direction or other variable), and the correlations between parameters —like that of $X_{\max}$ and R_μ which contain information on the primary composition. With the implementation of AugerPrime, the degeneracy between the energy and relative muon content of the shower can be better resolved, leading to more ideal reconstructions where a simultaneous fit of the energy and mass composition parameters might be possible.

While numerous efforts to improve the reconstruction method have been made in [105], [108], and works contained therein, here I will restrict myself to describing the most promising results and, only in part, detail the methods which I have investigated. While preliminary results are presented in this subsection, the bulk of the studies involving the different reconstructions can be found in Chapter 4.

A simplified schematic of the initial values, minimizers, and fitting procedures used for the reconstruction is given in Fig. 3.18. For every reconstruction method, the initial values —before the minimization of the negative log-likelihood— are set based on the type of input. For simulations, the *nine* initial values are set to those from the CORSIKA shower. The SD reconstructed values are not used as the LDF-based SD reconstruction is sensitive to the muon deficit found in simulations. There is a 5 % to 30 % composition-dependent deficit —on average— in the reconstructed energy of the SD —as seen in Fig. 3.20a— which would yield biased reconstruction results[22].

In data, the initial values for the core position $\hat{x}$ and timing t_c, arrival directions θ and ϕ, and primary energy E come from the reconstructed SD variables[23]. The initial $X_{\max}$ value is calculated from the $\langle X_{\max}\rangle(E)$ model as parameterized from FD measurements [104]:

$$\langle X_{\max}\rangle(E) = \begin{cases} X_{\max,0} + (\lg(E/\mathrm{eV}) - \lg(E_0/\mathrm{eV}))\, D^0_{10} & E < E_0 \\ X_{\max,0} + (\lg(E/\mathrm{eV}) - \lg(E_0/\mathrm{eV}))\, D^1_{10} & E \geq E_0 \end{cases} \tag{3.18}$$

where $E_0 = (18.33 \pm 0.02)\,\mathrm{eV}$ is the energy where the elongation rate[24] changes. The other parameters and their associated statistical uncertainties are $X_{\max,0} = (750 \pm 2)\,\mathrm{g\,cm^{-2}}$, $D^0_{10} =$

[22] An energy calibration for simulations could be performed, but such a calibration would not reflect the LDF parameterization in data and would be different for each primary and interaction model.

[23] As described in Section 2.5, the shower size estimator of the SD is calibrated with the calorimetric measurement of the FD energy to provide accurately reconstructed primary energies.

[24] The elongation rate is the fit of the mean $X_{\max}$ measured by the FD as a function of energy. As seen in Fig. 1.18a, the composition below an energy of $10^{18.3}$ eV follows a linear trend towards proton, whereas the linear trend above this energy threshold is towards iron. The elongation rate is just the slope of a given line.

$(79\pm1)\,\mathrm{g/cm^2/decade}$, and $D^1_{10} = (26\pm2)\,\mathrm{g/cm^2/decade}$. The initial R_μ is set with the estimated relative muon content of FD data $\langle \hat{R_\mu}^{\mathrm{FD}} \rangle$, which is detailed in Appendix D.4.2. For single-stage reconstruction methods, the average value of 1.9 is used. For reconstructions with multiple fitting stages, the $\langle R_\mu^{\hat{\mathrm{FD}}} \rangle (E, X_{\mathrm{max}}, \theta)$ model is employed for improved accuracy.

After the initial values are set, simulations and data are run with the same shape and LDF fits with the negative log-likelihood in a minimizer. Wrapped around the minimizer is a selected reconstruction routine. Depending on the method used, 2 to 8 variables may be fit at the same time in one or more fitting stages. The methods investigated in this work are the global (Section 3.2.3.2), iterative (Section 3.2.3.3), and two modifications of the global method where the shower axis is constrained within 1° or fixed to the axis reconstructed by the SD (Section 3.2.3.4).

3.2.3.1 Reconstruction accuracy of the SD

In the context of universality, the quantities of interest from the SD reconstruction are the energy, zenith angle, azimuth, position of the core, and traces of candidate stations. As detailed in Chapter 2, Auger's surface detector samples the lateral distribution of the shower. The reconstruction of the SD uses an energy calibration —derived from high-quality, jointly-measured events with the FD— to obtain the energy of an event's primary particle from the SD's signal estimator (S_{1000}). While the signal estimator comes from the LDF log-likelihood fit, the arrival direction of the shower is drawn from a fit of the shower geometry (mostly achieved with a spherical front) which relies on each station's timing. The importance in this distinction is that the arrival direction is not derived from the LDF but in a separate fitting stage which depends solely on the time response of the candidate stations.

The energy and the core position are primarily products of the LDF fit. In SD reconstructions with Offline, the core position is biased from the true core as the LDF implemented fails to take into account the azimuthal asymmetries of an air shower. In general, the footprint of an EAS in the plane of the ground is essentially an ellipse centered about the shower axis. Projecting the observations into a plane perpendicular to the shower axis should restore the expected circular symmetry (i.e. only considering the radial distance from the core); however, this transformation is only an approximation valid at small zenith angles and core distances. As a shower becomes more inclined, this symmetry is broken as stations are viewing the shower at different stages of the developing CR shower. This is pictorially depicted in Fig. 3.2. Due to attenuation effects, the particle density —and correspondingly the observed signal— will be higher in the early region than the late one. Furthermore, this attenuation depends upon the particle component considered; the absorption of the electromagnetic component increases with zenith angle until it is completely diminished around 60°. In contrast, the muonic component is long-lived and relatively less attenuated[25]. Additionally, as the zenith angle increases so does the the traversed path length, thus, muons become more deflected by the geomagnetic field —which in turn causes a distortion of the radial geometry of the air shower as shown in Fig. 3.19.

The reconstructed energy and core of the SD in simulations is shown in Fig. 3.20 relative to the true values. The showers are rotated in azimuth such that incoming direction is to the right. On average, the SD core (blue) is biased by 23.3 m. The spread of individual values is indicated with error bars. An LDF has already been derived which would account for these azimuthal asymmetries and provide an unbiased reconstructed SD core [119];

[25] Coulomb scattering and energy losses due to ionization are sub-dominant except for $\theta > 80°$. The average decay length of a 10 GeV muon is 66 km, which far exceeds the distance from muon production to the ground for vertical showers.

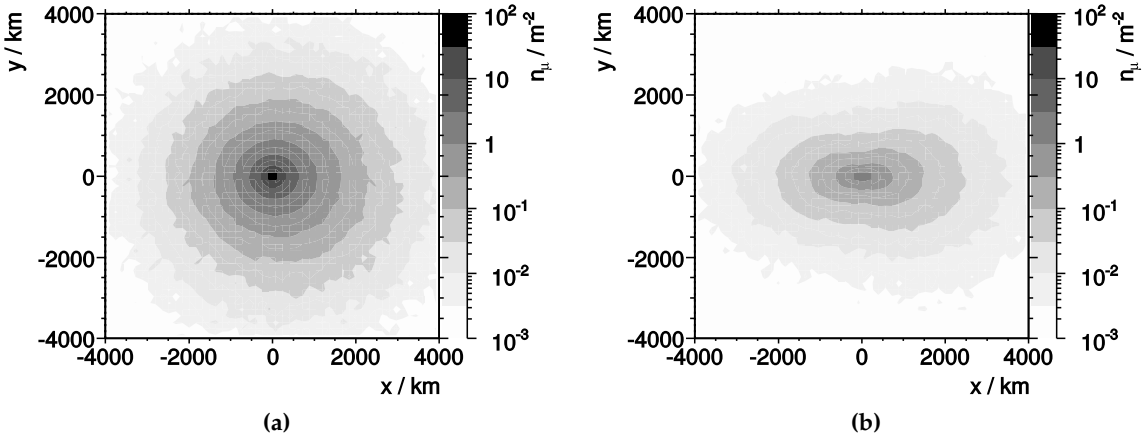

Figure 3.19: The footprints of the simulated muon density at the ground from a proton primary at $E = 10^{19}$ eV and $\phi = 0°$ for (a) 61° where the radially symmetry is slightly distorted and (b) 80° were the radial symmetry is broken by geomagnetic deflections [167].

however, it has not been implemented in Offline yet. Asymmetries in the LDF and time distributions of the particles are taken into account in the universality signal and time models. As such, the universality reconstruction (red) enables a nearly unbiased estimation of the shower core, deviating by only 1.7 m on average. The resolution of the core using the universality reconstruction greatly improves with increasing energy and is relatively constant with respect to zenith angle. In contrast, the SD core bias and resolution largely depend on zenith angle and only slightly improve with respect to increasing energy.

In data, the energy of the SD is corrected for the differing attenuation of traversed atmosphere as a function of zenith angle (Section 2.4) and calibrated with the FD (Section 2.5). During the parameterization, the jointly measured events are selected by using a cut which ensures that there is no bias with respect to mass composition. The detector resolution and shower-to-shower fluctuations jointly yield an energy resolution of 15 % on average. This resolution decreases with increasing energy. However, the calculation of the resolution is dominated by the energy scale uncertainty of the FD, which is 14 % on average [69, 135].

In contrast to the reconstructed core, the arrival directions of the SD are reconstructed with high accuracy and are relatively unbiased as they come from fitting the shower geometry with a spherical front. In Fig. 3.21, the zenith angle, azimuth, and the shower axis of SD simulations are compared to their true values from proton-induced simulations. The shower axis is a directional vector describing the geometry of an air shower; the zenith angle and azimuth are components of the axis. While general trends may be interpreted from the difference between the reconstructed and true axis, it is more intuitive to consider the angular resolution[26], which is calculated as the following

$$\sigma_{\text{ang}} = \frac{3}{2\sqrt{2}} \sqrt{\sigma^2(\theta) + \sin^2(\theta)\,\sigma^2(\phi)}\,, \tag{3.19}$$

with the resolutions of the reconstructed zenith and azimuth angles $\sigma(\theta)$ and $\sigma(\phi)$. With increasing zenith angle, the angular resolution improves from around 0.5° to 0.25°. There is a slight improvement on the order of 0.1° as the energy threshold is increased. The zenith angle, on average, is unbiased from the true value and is well-reconstructed regardless of the saturation status of an event. The angular difference does, however, have larger

[26] See Appendix A.2 for a derivation and discussion of the angular resolution equation.

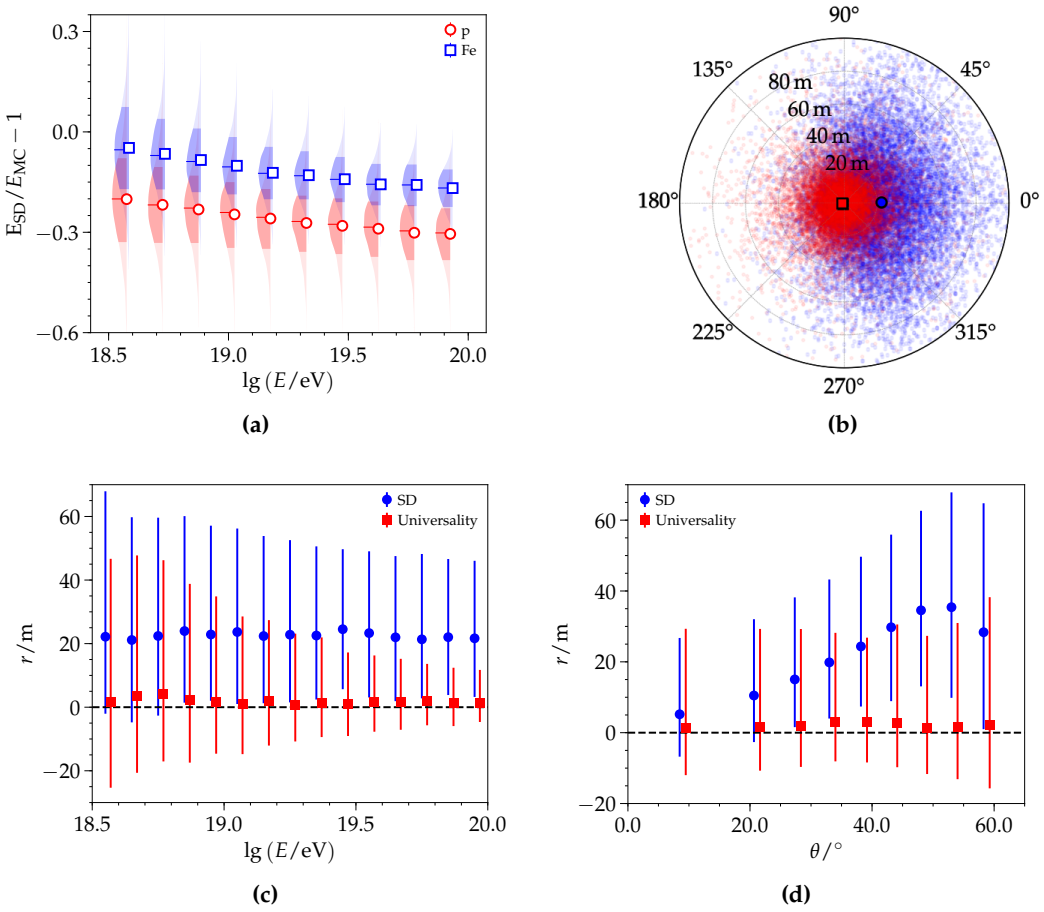

Figure 3.20: Comparisons of the reconstructed SD values to the Monte Carlo values for QGSJET-II.04 simulations from the Napoli library (Appendix B.2). (a) Relative difference between the SD and MC energy for simulated air showers induced by proton and iron primaries. The mis-reconstructed SD energy reflects the deficit of muons found in simulations and exhibits differing biases with respect to the composition of the primary particle. (b) As the LDF employed in the SD reconstruction does not include the azimuthal asymmetry of the signal, the reconstructed SD core (blue) is biased relative to the true Monte Carlo core (at origin). The universality reconstructed core (red) is unbiased. In considering the core distributions as a function of distance to the core with respect to (c) energy and (d) zenith angle, the overall bias of the SD core is 23 m on average with $1\,\sigma$ of events in a range of 60 m, which depends on zenith angle. In contrast, the spread of the universality core positions is dependent on energy (number of candidate stations) and is relatively independent of zenith angle. For the core plots, nearly 15 000 proton-induced shower simulations are used. The universality counterpart considered was reconstructed using the global method.

spreads associated with lower zenith angles[27]. Similarly, the reconstructed azimuth angle is unbiased with a large spread of 3° near a zenith angle of 0°. In considering the trends in three-dimensions, the bias of the reconstructed zenith angle can be seen as a nearly constant offset depending on θ. The spreads seen in both the azimuth and zenith angle also reflect this trend. The spreads of both variables are greatest for small zenith angles because there are less triggered stations, resulting in a less well-constraining geometry and associated timing of the shower front.

[27]The bins in the plots with respect to zenith angle are chosen in equal-width $\sin^2\theta$ bins —the underlying distribution — to ensure similar event numbers.

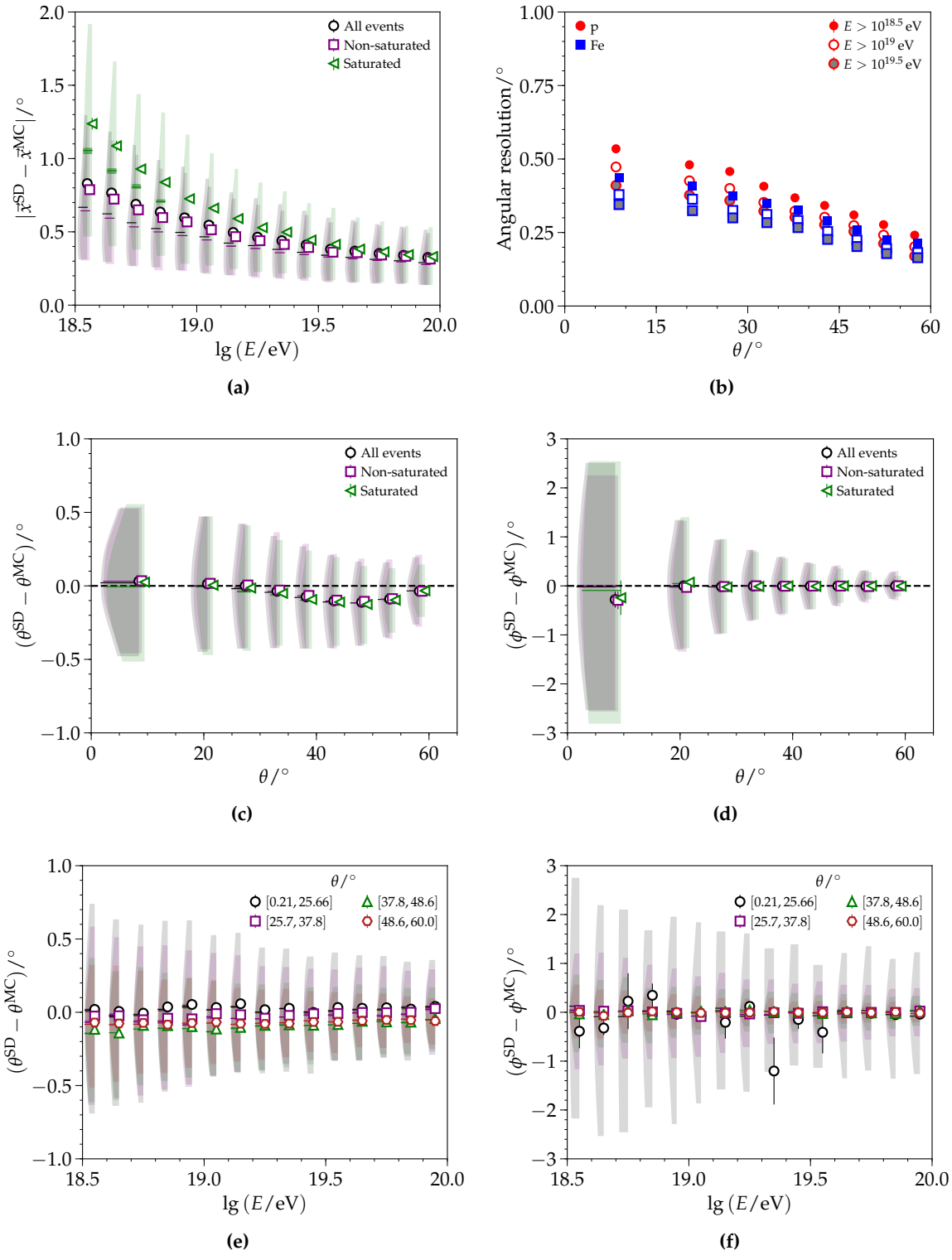

Figure 3.21: QGSJET-II.04 proton-induced simulated showers from the Napoli library. (a) The difference in the true and reconstructed SD axis with respect to energy, where the saturation status of the event is considered. The axis deviates the most at low energies and zenith angles due to the correspondingly large resolutions. (b) The angular resolution for proton- and iron-initiated simulations as a function of zenith angle and energy. The differences between the true and SD (c) [(d)] zenith angle and (d) [(f)] azimuth are shown to be relatively unbiased with respect to zenith angle [energy]. The reconstructed zenith angle maximally deviates from the true by 0.1°, on average, between 35° to 55°. This is due to the increasing azimuthal asymmetry of the separated electromagnetic and muonic components. This bias is reduced around 60° as the electromagnetic component has fully diminished; the asymmetry will increase again at more inclined zenith angles as deflections from the geomagnetic field grow in magnitude.

3.2.3.2 Global reconstruction

Developed in [105], the most conservative reconstruction method —known as the global method[28]— fixes the energy to that reconstructed by the SD and simultaneously fits the remaining *eight* variables in a single step. The highlights of the global reconstruction are that it validates the universality parameterizations in simulations and data[29] while fully incorporating the correlations of R_μ and $X_{\max}$. The universality models (discussed in Section 3.1.3 and Section 3.1.4) have complex relationships that rely on the eight physics parameters, yet, as the number of candidate stations becomes fewer at lower energies, there is not enough constraining information to yield reasonably reconstructed quantities. The relationship between the number of candidate stations triggered at a given energy is depicted in Fig. 3.22a and Fig. 3.22b.

The reconstruction efficiency for the global method is explored in Fig. 3.23. While many events are deemed successful by the minimizer at energies around $10^{18.5}$ eV, they have been found to have $X_{\max}$ and θ values that significantly differ from the true ones by 100 g cm^{-2} to 500 g cm^{-2} and 5° to 10°, respectively (**Successful with outliers**). Several efforts have been made in [108] and this work to identify whether such outlying populations (**Outliers**) exhibit a consistent underlying cause that may be remedied or not. Many of these outliers are recovered when more constraints are used in the reconstruction method employed, as later seen with the iterative fit results of Fig. 3.24. Due to the general arbitrariness of an event being and remaining designated as an outlier —as well as the lack of knowledge of the true $X_{\max}$ and θ when measuring data, outliers are defined as events with $X_{\max} \notin [500, 1050]$ g cm^{-2} and $|\theta_{\text{Univ}} - \theta_{\text{SD}}| > 5°$[30]. The reasoning behind these selection criteria is based upon the 1-D and 2-D distributions of these variables as depicted and further described in Fig. 3.22c. Similarly, the 4.6 % of events which **failed** to pass the minimization is greatly reduced as further constraints are used in the reconstruction. The **successful** events after rejecting outliers are also considered with respect to zenith angle. These efficiency plots are made by performing a selection of events (e.g. **Successful**), binning that selection with respect to energy, and dividing the binned selection with the binned total number of events. Because of the selection process involved, the results can be treated as binomially distributed variables. Thus, the uncertainties are calculated using a binomial proportion confidence interval spanning 1 σ. The error bars are not visible for simulations due to the large number of events in each energy and zenith bin[31]. To view the various populations in the efficiency plots, minor offsets in the x-axis were consistently added.

The bias and resolution of the reconstructed depth of the shower maximum and relative muon number are shown later in Fig. 3.26; they are compared to the results of the other reconstruction methods discussed in this section[32]. Below energies of 10^{19} eV, the $X_{\max}$ bias is, on average, 20 g cm^{-2} to 30 g cm^{-2} and the difference between the median and mean is on the order of 10 g cm^{-2}, indicating the presence of outliers. The $X_{\max}$ at the highest energies is negatively biased, leading to a 50 g cm^{-2} absolute difference in the means across all energy bins. The resolution of the depth of the shower maximum decreases from around 100 g cm^{-2} to 30 g cm^{-2} with respect to increasing energy. At the highest energies, the constrained axis

[28] In previous works like [108], it was called the **classic** method.

[29] Unlike the iterative method (Section 3.2.3.3), the global method does not include a calibration with real FD events. Such a calibration is only possible through the explicit use of initial values.

[30] As shown in Fig. 3.21, the SD reconstructed zenith angle is within 0.5° of the true value, so this is a rather conservative criterion. A more rigorous event selection for the purposes of mass composition and anisotropy studies is presented for each reconstruction method throughout Chapter 4.

[31] While SD data is more numerous than the proton or iron simulations, it follows an $E^{-2.5}$ energy spectrum whereas the simulations have an E^{-1} dependence, which yields a flat distribution in a lg E plot. For further information on the data and simulations used in this work, see Appendix B.

[32] A more rigorous event selection for the global method is presented in Appendix D.3.

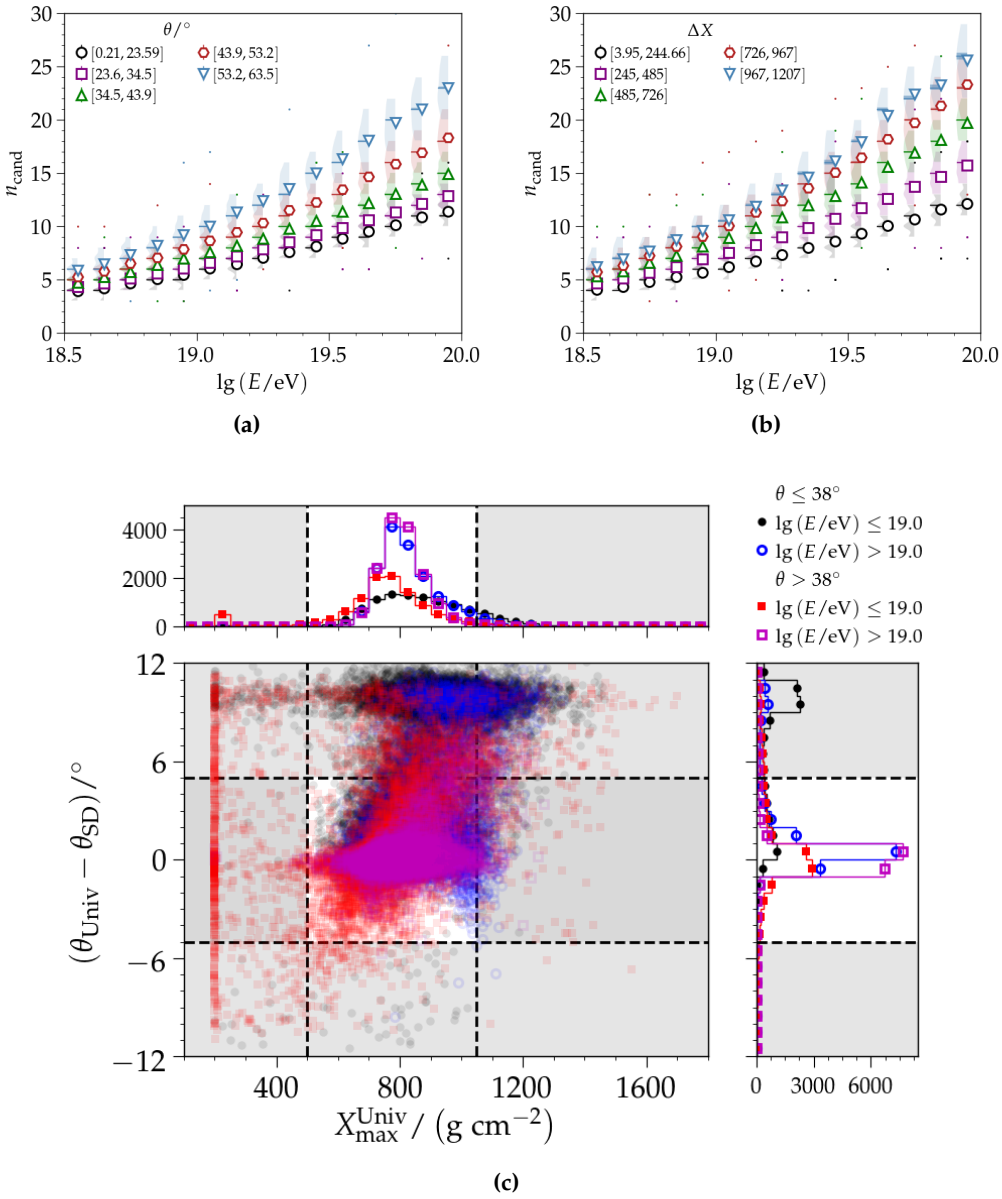

Figure 3.22: QGSJET-II.04 proton-induced shower simulations from the Napoli library reconstructed with the global method. The relationship between the primary energy and number of triggered stations is considered with regard to (a) the zenith angle and (b) the slant depth from the station to the depth of the shower maximum (Fig. 3.2). (c) Outliers of non-saturated events are identified based on the reconstructed depth of the shower maximum and the absolute difference between the universality and SD reconstructed zenith angle. Individual events are shown in transparent points that identify their zenith and energy group; the distributions along the x and y-axis are 1-D projections of the variable. The grayed out regions indicate events identified as outliers ($X_{\mathrm{max}} \notin [500, 1050]\ \mathrm{g\,cm^{-2}}$ and $|\theta_{\mathrm{Univ}} - \theta_{\mathrm{SD}}| > 5°$). The vertical, linear population around $200\,\mathrm{g\,cm^{-2}}$ and horizontally-oriented, elliptical region around $|\theta_{\mathrm{Univ}} - \theta_{\mathrm{SD}}| > 8° to 10°$ are centered about the respective lower and upper limits enforced during the reconstruction; they indicate that the reconstruction gets stuck on a false minimum and is unable to recover. Many of the outlying events of the depth of the shower maximum have energies below $10^{19.0}$ eV and a zenith angle above 38°, which correlate with a stricter timing constraint. Alternately, outlying events in the difference in the reconstructed zenith angle can be attributed to low energy events with a zenith angle below 38°, which corresponds to fewer triggered stations.

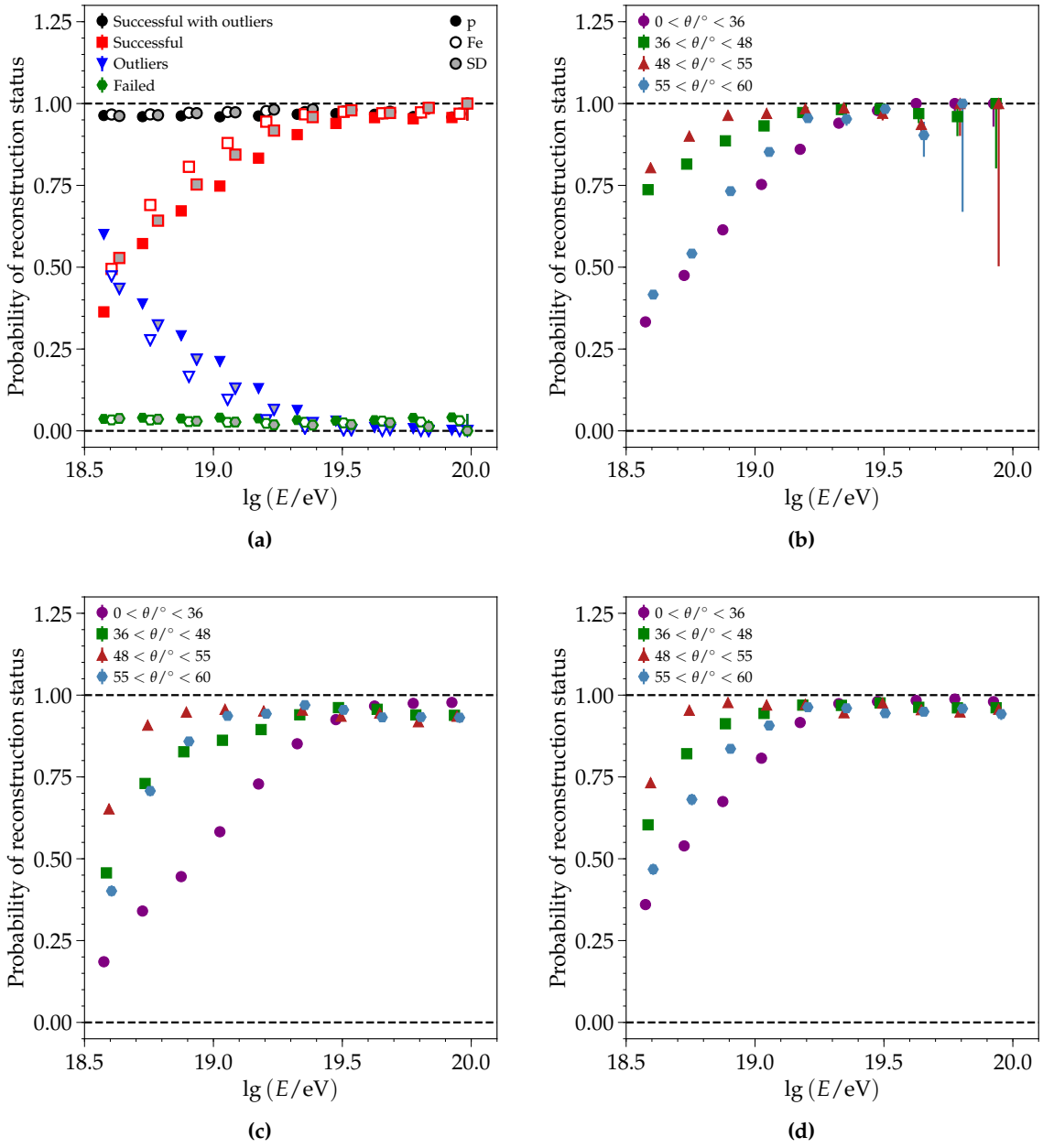

Figure 3.23: Reconstruction efficiency for non-saturated events with respect to energy for the global fit. (a) The overall efficiency for non-saturated events is shown for QGSJET-II.04 simulated showers initiated by proton and iron primaries in comparison to SD data from 2004-2016. **Successful** reconstructed events are analyzed with respect to energy and zenith angle for (b) SD data and (c) proton- and (d) iron-induced simulations. Events with lower zenith angles have less triggered stations than their higher zenith counterparts. At low energies, this leads to too few stations to constrain the reconstruction for the determination of the shower geometry. With further constraints, such events can be recovered. In contrast, events with a zenith angle above 55° are difficult to reconstruct as their timing constraints are much stricter. Iron and SD data are found to have worse efficiencies for zenith angles between 0° to 36° and 55° to 60° than proton. In data, the other zenith angle ranges have a higher reconstruction efficiencies at the lower energies than in simulations. This could result from the threshold cuts and usage of the SD energy in the data binning procedure. In other words, the simulation efficiencies at the lower energies are worsened as the Monte Carlo energy is used (due to the mis-reconstruction of the SD energy), and it is not easy to apply an equivalent threshold.

and global method have similar resolutions. In the case of the relative muon number, the average biases and resolutions for the global method agree with the constrained method above $10^{19.2}$ eV, which is where the efficiency is close to 95 % for all zenith angles.

3.2.3.3 Iterative reconstruction

Due to the zenith-dependent biases, large resolutions, and inefficiencies due to the number of candidate stations of the global method, the author of [108] investigated several reconstructions where further constraints were added. Of the methods the author investigated, the most promising one —the iterative fit— involved fixing and fitting certain variables in several stages to improve the resolution of reconstructed quantities and to produce an unbiased reconstruction even with a small number of candidate stations:

1. The core position and energy are fit while all other parameters are fixed[33]. As only the core and energy are fit, only the signal likelihood is used, where the energy is constrained to $\pm 20\,\%$ of the true (MC) or the SD energy.

2. Step 1) is repeated with updated predictions of $X_{\max}$ and R_μ using the new estimate of the primary energy E. Again, the energy is constrained to $\pm 20\,\%$ of the previous result.

3. While all other quantities are fixed, the relative core time t_c is fit together with $X_{\max}$.

4. R_μ, energy, and the core position are fixed. $X_{\max}$, t_c, and the components of the shower axis —which are separately and weakly constrained to be within an angular standard deviations of $1^\circ \approx 2\,\sigma$— are fit together.

5. R_μ is fit while all other quantities are fixed to previous fit results. Due to the explicit dependence of R_μ on the signal, only the signal likelihood is used.

6. $X_{\max}$ is fit together with the shower geometry while all other quantities are fixed to previous results. The zenith angle and azimuth are separately constrained to be within an angular standard deviation of 1.0°.

7. After fixing all the other quantities to previous fit results, the energy is re-fit, where it is constrained to $\pm 10\,\%$ of current value. Both the signal and time likelihoods are used.

8. R_μ is re-fit after fixing all other quantities to previous fit results. Only the signal likelihood is used.

For all constraints, normal distributions with the given standard deviations are added into the calculation of the negative log-likelihood[34]. Through its various fitting stages, the iterative method includes a reconstruction of the primary energy E, the depth of shower maximum $X_{\max}$ and the relative number of muons R_μ. While the energy is constrained, neither the $X_{\max}$ nor R_μ are constrained during the reconstruction procedure. As specified earlier and pictorially depicted in Fig. 3.18, the $X_{\max}$ estimate —set before steps 1 and 2 —is calculated using the elongation rate. Similarly, the R_μ initial value comes from the estimated relative muon content of FD data $\langle \hat{R}_\mu^{\mathrm{FD}} \rangle$, which is detailed in Appendix D.4.2.

[33] As the SD does not measure the $X_{\max}$ or R_μ in data, these values are parameterized using high quality events measured by both the FD and SD (golden hybrid events). An updated calibration which is based upon the original method is presented in Appendix D.4.2. In simulations, the true R_μ and $X_{\max}$ values are used.

[34] Constraints using the MINUIT-2 utility itself should not be used as they will perform not only non-linearly but also without participating directly in the likelihood calculation.

The reconstruction efficiencies of the iterative fit are shown in Fig. 3.24. With the constraints, 100 % of the events successfully pass the minimization. However, events simulated with zenith angles above 55° are poorly reconstructed around 20 % of the time. In contrast to the global method where lower zenith events fail due to too few stations and a subsequent, lack of constraints, the outlying events of the iterative method have, on average, higher zenith angles, which are difficult to reconstruct as their timing constraints are much stricter.

The bias and resolution of the reconstructed depth of the shower maximum and relative muon number for the iterative fit are shown in Fig. 3.26 to be relatively constant with respect to energy. The average bias and resolution of the depth of the shower maximum are less than $10\,\mathrm{g\,cm^{-2}}$ and $30\,\mathrm{g\,cm^{-2}}$, respectively. The R_μ-bias and resolution are less than 0.5 %; this minimal deviation from the true relative muon content indicates that the iterative fit is so tightly constrained that the R_μ is not able to vary much from its initial value. As such, only the average depth of the shower maximum should be used for mass composition studies.

3.2.3.4 Constraining the axis of the global reconstruction

While the iterative fit provides a robust estimate of the depth of the shower maximum, it fails to independently reconstruct the relative number of muons and to provide reasonable correlations of it with X_{max}. While attempts have been made to relax the iterative fit in [108] and in the development of this thesis[35], such reconstructions have ultimately not had the desired success with a high efficiency, low number of outliers, and realistic correlations and resolutions for all reconstructed variables. In an effort to hopefully obtain a reconstruction possessing such traits, I returned to the basic idea of adding further constraints to the global method.

As discussed in Section 3.2.3.1, the lateral spread of the triggered stations of the SD responding to an EAS allow for a precise measurement of the arrival direction within 0.5°. As many of the outliers seen with the global and iterative method are due to misreconstructed zenith angles and the subsequent effect of that, it seems natural to use the arrival direction as a constraint in the reconstruction. This was investigated in two ways: (1) constrain the reconstructed axis to be with 1° of the true or SD axis and (2) fix the axis to the true or SD axis[36]. A cursory investigation is presented here for completeness, and an in-depth study analyzing the global with constrained axis method is given in Chapter 4.

The reconstruction efficiency is explored for the constrained axis in Fig. 3.25. With both methods, the overall efficiencies are above 90 % and asymptotically approach 100 % for energies greater than $10^{18.7}$ eV. In considering the zenith-binned efficiencies of **Successful** events for the constrained axis, it can be seen that all but the zenith bin for 55° to 60° have a relatively energy- and zenith-independent success rate above $E = 10^{18.7}$ eV. While the **Successful** events of the fixed axis method mostly exhibit a similar trend, there is a 10 % to 15 % difference in efficiency with respect to zenith angle that is seen in proton- and iron-induced simulations for energies above $10^{19.4}$ eV. Nevertheless, both methods involving the constrainment of the axis yield fewer outlying events than the iterative or global method. Furthermore, they show that the efficiency of events with zenith angles below 55° is relatively independent of zenith angle.

[35] Beyond increasing or decreasing constraining factors, an attempt was also made to add a ninth step where all variables but the energy were fit. Regardless of the changes made, the iterative fit yielded distributions in the relative number of muons that were too narrow, and, in many cases, the efficiency, particularly at the highest energies suffered.

[36] As the fixed axis is a special case of the reconstruction using the constrained axis, the results are presented in Appendix D.6

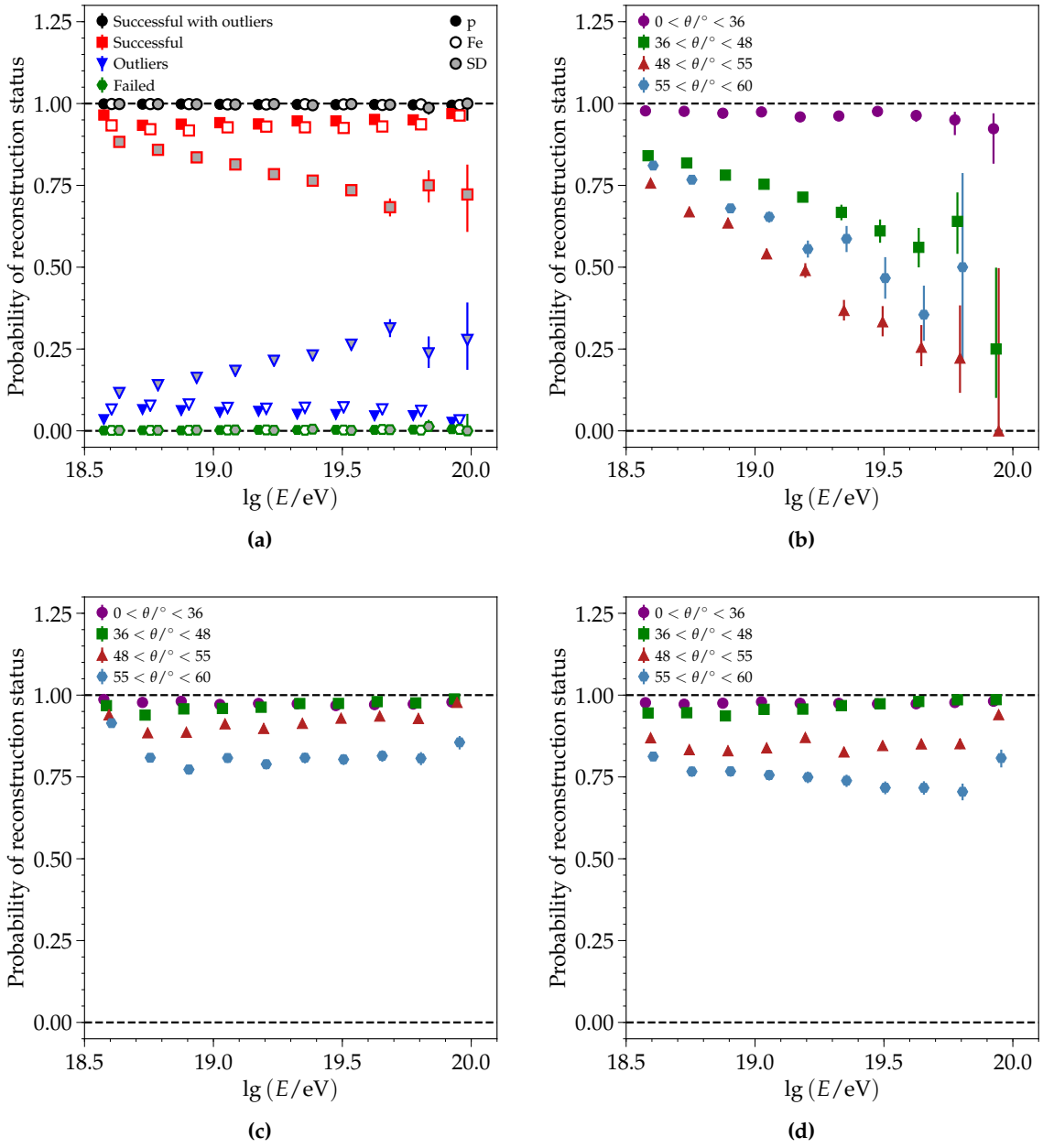

Figure 3.24: Reconstruction efficiency for non-saturated events with respect to energy for the iterative fit. (a) The overall efficiency for non-saturated events is shown for QGSJET-II.04 simulated showers induced by proton and iron primaries in comparison to SD data from 2004-2016. **Successful** reconstructed events are analyzed with respect to energy and zenith angle for (b) SD data and (c) proton- and (d) iron-initiated simulations. In simulations, the rate of **successful** events is, on average, above 90 %; the outlying events are mostly found in the zenith angle populations with $\theta > 48°$. In data, however, the **successful** reconstruction rate dramatically drops, is worse for all energies, and exhibits an inverse correlation with increasing zenith angle. It is important to remember that the iterative method uses a constraint on the zenith angle and azimuth where they must be within 1°; this renders the identification of outliers using the zenith angle constraint $|\theta_{\mathrm{Univ}} - \theta_{\mathrm{SD}}| > 5°$ not very useful. The plots are presented in this way to provide a direct comparison in this overview section; however, in Appendix D.4, the outliers of the iterative fit are better identified.

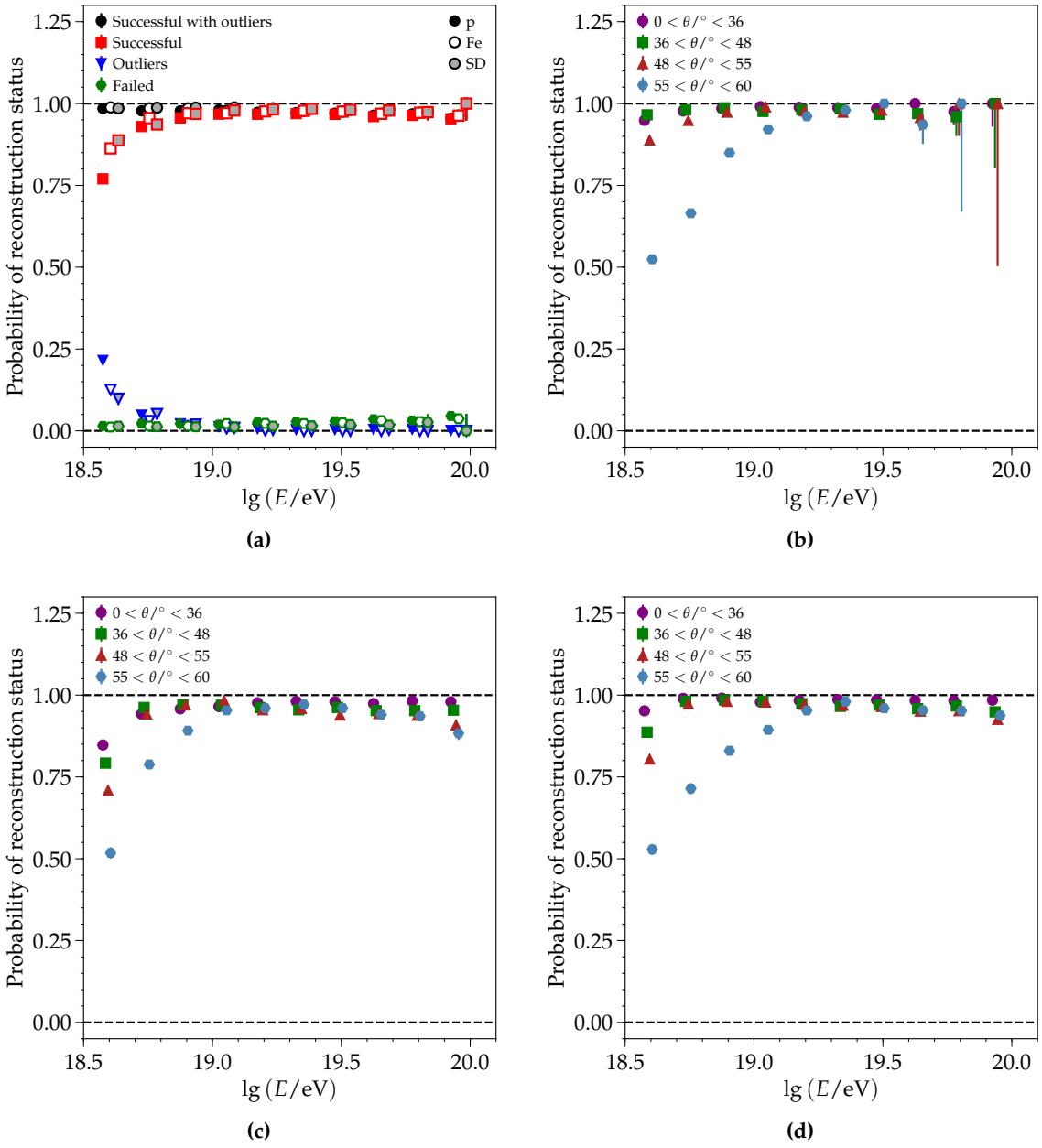

Figure 3.25: Reconstruction efficiency of the constrained axis method for non-saturated events with respect to energy. (a) The overall efficiency is shown for QGSJET-II.04 simulations from the Napoli library in comparison to SD data from 2004-2016. **Successful** reconstructed events are analyzed with respect to energy and zenith angle for (b) SD data and simulations with (c) proton and (d) iron primaries. While the efficiency is above 90 % for most zenith angle bins above an energy of $10^{18.7}$ eV, events with a zenith angle between 55° to 60° have an efficiency which rapidly worsens with respect to decreasing energy below 10^{19} eV; difficulty reconstructing such events was also seen with the iterative method. Again, the improved reconstruction efficiency of SD data relative to the simulations at the lowest energies can be attributed to the lack of an equivalent threshold applied to Monte Carlo events.

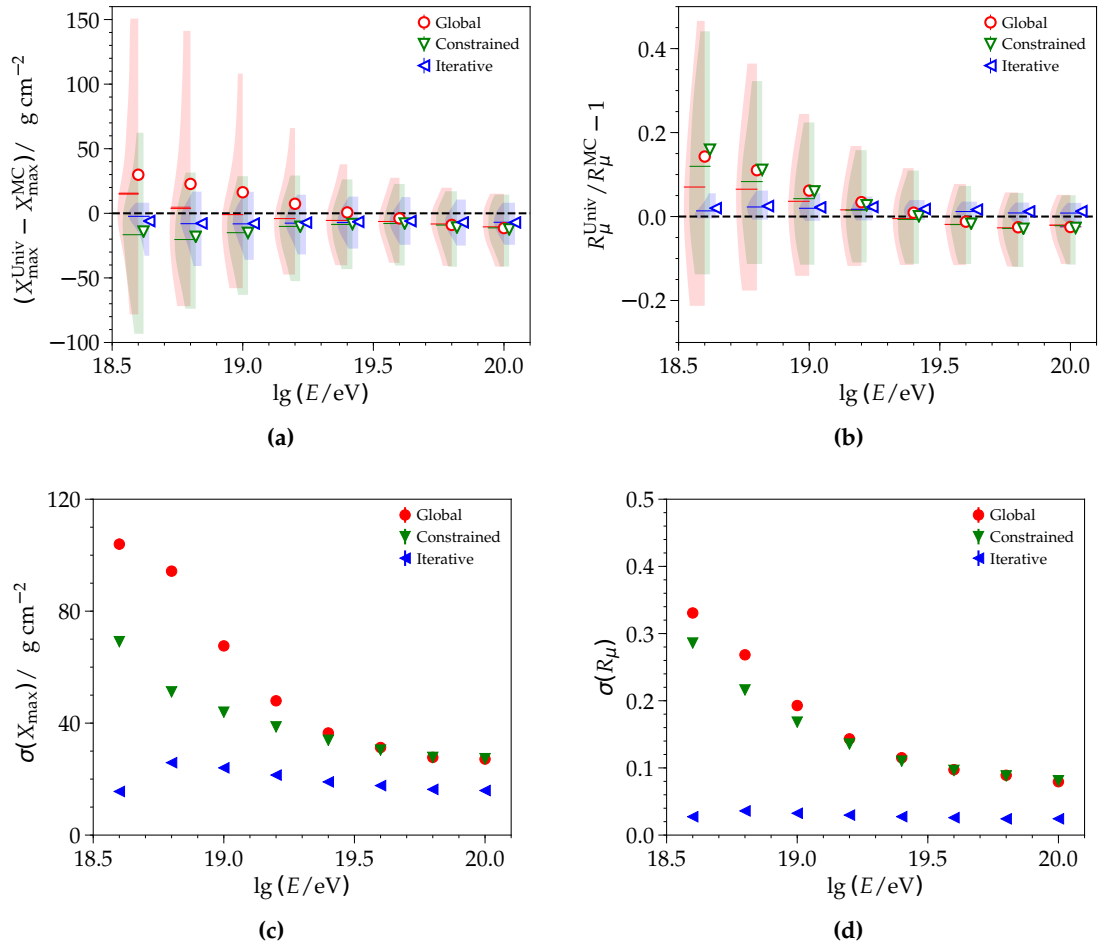

Figure 3.26: The bias of the reconstructed (a) depth of the shower maximum and (b) relative muon content for QGSJET-II.04 proton-induced simulations reconstructed with the global, constrained axis, and iterative methods. The corresponding resolutions are given in (c) and (d). Only successfully reconstructed events with $X_{\max} \in [500, 1050]$ g cm^{-2} are considered. The resolution plots are made using the *median absolute deviation* (MAD); the uncertainties are the standard deviation of the MAD as found using the bootstrap method.

The bias and resolution of the reconstructed depth of the shower maximum and relative muon number are shown for the global fit with the constrained axis in comparison to the other reconstruction methods discussed earlier in this section in Fig. 3.26. The fit with the constrained axis yields a negative bias in the reconstructed depth of the shower maximum on the order of 15 g cm^{-2}, which is 5 g cm^{-2} to 10 g cm^{-2} greater than that provided by the too-constrained iterative method. This negative bias gradually reduces as energy increases to yield a bias less than 10 g cm^{-2}. The bias and resolution of the relative muon number and the resolution of the depth of the shower maximum have decreasing deviations with respect to energy and give similar values. Above an energy of $10^{19.4}$ eV, the resolutions and biases of the fit with the constrained axis are in good agreement with the results obtained with the global method. Overall, the constrained axis method has tantalizing results that appear to include the most salient features of the global and iterative methods while having a close-to-ideal reconstruction efficiency. A more rigorous event selections for the constrained axis method is presented in Chapter 4, and the associated mass composition results are given in Chapter 5.

CHAPTER 4

Study of the constrained axis reconstruction

In Chapter 3, the basic ingredients for the air shower universality approach —namely the signal and timing model— are introduced. The most canonical reconstruction method —known as the global reconstruction— was defined, where only the energy as reconstructed by the SD is fixed while the remaining eight physics parameters are simultaneously fit. In contrast, the iterative reconstruction —developed to return an unbiased depth of the shower maximum and reduced resolution— has multiple fitting stages where pairs of variables are fixed while the remaining ones are fit. The performance of these reconstructions were studied with simulations. In particular, the downfalls of each method were discussed: large biases and resolutions result when using the global method and the iterative fit fails to describe the correlations between variables. To remedy these problems and obtain a more robust reconstruction, a new reconstruction method was developed in this work. Known as the constrained axis method, it is a modified version of the global fit where the axis is constrained within 1°. The rationale for constraining the axis to that found by the SD reconstructed axis is based upon its high accuracy and precision when compared to the true values, as detailed in Section 3.2.3.1. While the biases and resolutions for the constrained axis method seem to embody a compromise between the global and iterative reconstruction[1] (Fig. 3.26), it is important to first conduct an in-depth investigation on the effects of such a constraint on the observables and their associated correlations (Section 4.1).

Having substantiated that the constrained axis method contains all known correlations, the remaining goals of this chapter are to investigate the effects of modifications in the reconstruction, to ascertain the quality of the derived results, and to establish selection criteria for mass composition studies. First, simulations are used to perform extensive studies to determine what subset of events are systematically, poorly reconstructed (Section 4.2.1). Given those results, a fiducial selection (Section 4.2.2) as a function of zenith angle is developed, which ensures a high-quality selection of well-reconstructed events. In particular, this selection method is analyzed for several primaries and hadronic interaction models, and it is found to have consistent results between models. The resulting biases and resolutions of the variables of interest (Section 4.2.3) —the depth of the shower maximum and relative muon content— are investigated. The whole process of deriving the fiducial selection and the study of the bias and resolution are then applied to data (Section 4.3).

[1] Both methods have a resolution and bias which are smaller than the global method, yet they include a physical description of the relative muon content, making them more attractive than the iterative method.

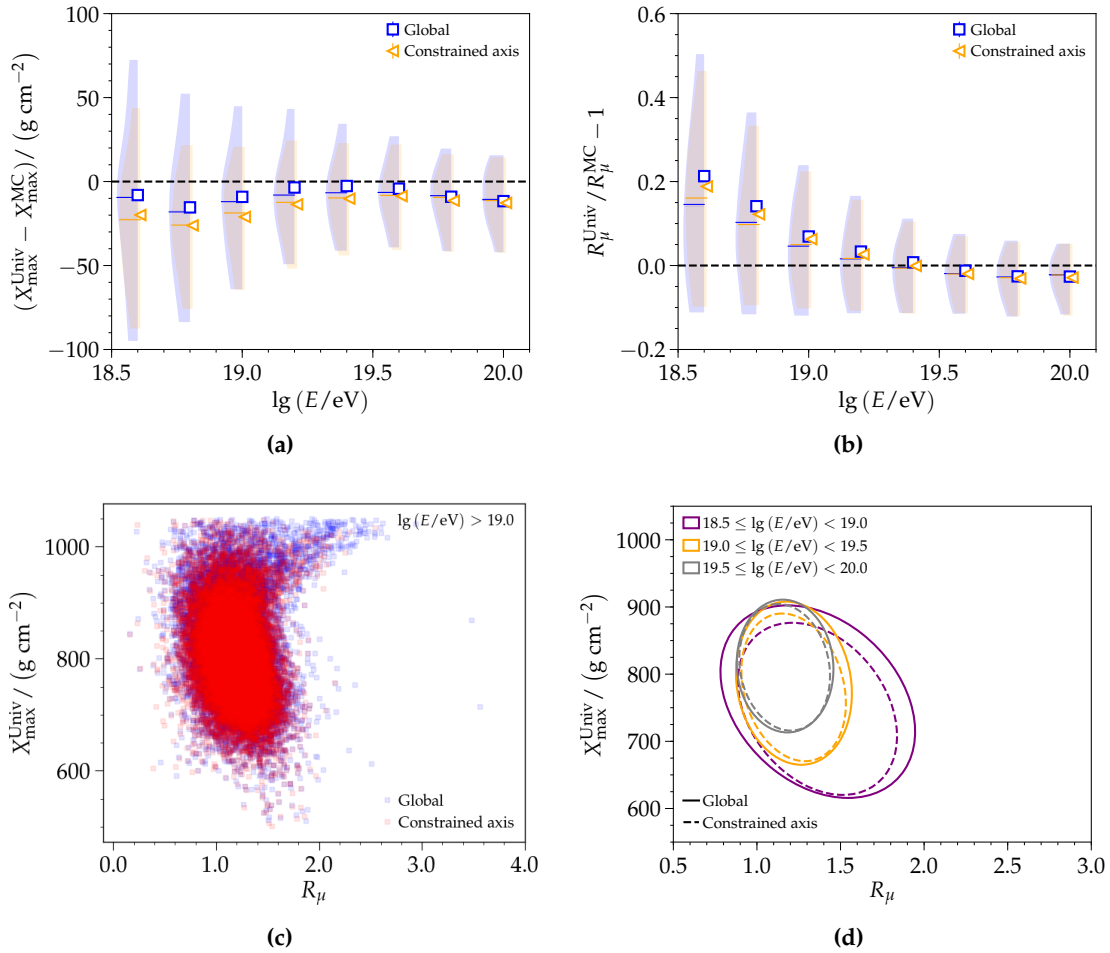

Figure 4.1: QGSJET-II.04 proton simulations of non-saturated events from the Napoli library reconstructed with the global and constrained axis methods. The bias of the (a) depth of the shower maximum and (b) relative muon content as compared with the true values. The correlation between R_μ and X_{max} is shown (c) above an energy of 10^{19} eV and (d) with $1\,\sigma$ spreads in the specified energy ranges. While the direction of the ellipse changes slightly depending on the method considered, the scatter plot indicates that the constrained axis method is better behaved and has less R_μ outliers. Thus, the change in the direction and reduction in size of the $1\,\sigma$ spreads is due to the improved resolution of the constrained axis method.

4.1 Comparison with the global method

As seen in Fig. 3.26, the bias and resolution of the depth of the shower maximum and relative muon content of the global method are similar to those found with the constrained axis method above an energy of $10^{19.3}$ eV. This agreement —as the global method is the most conservative reconstruction procedure— hints that the addition of the constraint to the reconstruction does not hinder or distort the correlations between variables —particularly that found between R_μ and X_{max}.

An event-level comparison is given in Fig. 4.1 between the constrained axis and global method. In order to perform this comparison, outliers —found in the global method— are rejected by requiring that $X_{max} \in [500, 1050]$ g cm^{-2} and $|\theta_{Univ} - \theta_{SD}| < 5°$. 40 000 events are matched between the two reconstructions and compared. On average, the constrained axis method has a constant X_{max} bias and smaller resolution with respect to energy. While it appears that the global method yields a less biased X_{max}, this is misleading as the

reconstructed depth of the shower maximum for this method is highly-dependent on zenith angle (Fig. D.16), and it is by happenstance that bias across all zenith angles is less than that found with the constrained method. In contrast, the reconstructed $X_{\max}$ is mostly independent of zenith angle for the constrained axis fit (Fig. 4.6) . The median difference between the reconstructed depth of the shower maximum for the two methods is relatively constant with respect to energy. Similarly, the difference between the reconstructed relative muon content has a median of $\pm 1\,\%$ and resolution of $\pm 4\,\%$. The correlation between the reconstructed $X_{\max}$ and R_μ is considered for different energy bins for the two reconstruction methods. The correlation of the constrained axis method is contained within that found with the global method and has a similar orientation. Overall, the reconstructed relative muon content for the constrained axis method is very similar to that found with the global method and correctly incorporates physics correlations. Thus, the constrained method may be fully used in mass composition studies[2].

4.2 Event selection in simulations

In Section 3.2.3, the event selection —for all reconstruction methods— was performed using the cuts ($X_{\max} \notin [500, 1050]\ \mathrm{g\,cm^{-2}}$ and $|\theta_{\mathrm{Univ}} - \theta_{\mathrm{SD}}| > 5^\circ$) determined for the global reconstruction method. As seen in the efficiency plots for the constrained axis method (Fig. 3.25), more than 90 % of events above an energy of $10^{18.6}$ eV are well reconstructed with minimal outliers. Below 10^{19} eV, many events with a zenith angle between 55° to 60° are poorly reconstructed. In order to perform an efficient event selection for the constrained axis, it is important to better define which events are poorly reconstructed and how they will be cut or otherwise identified.

4.2.1 Identifying outliers

Scatter plots —such as the ones shown in Fig. 4.2— are useful in visually confirming the presence of outliers. Due to the minimization used in a reconstruction, poorly reconstructed events will not exhibit the elliptical-correlations that are expected with physical data. Instead, for outlying events, a smearing effect towards the outermost limits is observed. Furthermore, when a reconstruction procedure is not well-defined or constrained enough, these outliers are seen to form bands or bunching about the limits imposed on the reconstruction, meaning that the minimizer is unable to recover from the false minimum[3]. In Fig. 4.2a, the global method has a vertical band around $200\,\mathrm{g\,cm^{-2}}$ and a horizontally-oriented, elliptical region around $|\theta_{\mathrm{Univ}} - \theta_{\mathrm{SD}}| > 8 - 10^\circ$, which corresponds to the lower and upper limits implicitly enforced during the reconstruction.

In contrast, the reconstructed zenith angles of the constrained axis method are almost entirely within 4° of the SD value[4]. Because of the constrainment of the axis, the number of events with a mis-reconstructed depth of the shower maximum is also greatly reduced. The events with $X_{\max} > 1050\,\mathrm{g\,cm^{-2}}$ follow an elliptical shape, reminiscent of the well-reconstructed data (highlighted with the white box). There are still a few events which are mis-reconstructed at significantly low values of the depth of the maximum shower ($200\,\mathrm{g\,cm^{-2}}$).

[2]For more studies of the constrained and fixed axis methods which validate the preservation of correlations and investigate the use of the SD axis in Monte Carlo reconstruction, see Appendix D.6.

[3]For a in-depth discussion on the role of the minimizer in the reconstruction and how outliers are created, see Appendix D.5.1.

[4]In comparing the outlier identification plot for the constrained axis to its counterpart for the iterative fit (Fig. D.19), it is clear from the lack of large deviations in the reconstructed zenith angle that the constraint on the axis is preferred to the separate constrainment of the zenith angle and azimuth.

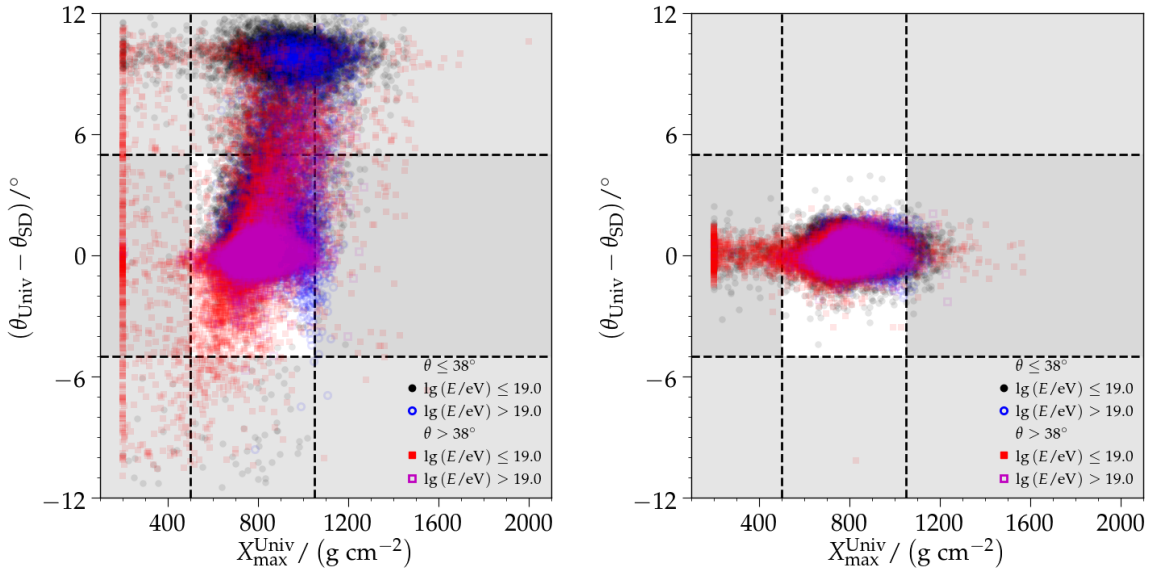

(a) **(b)**

Figure 4.2: Outliers of non-saturated events are identified based on the reconstructed depth of the shower maximum and the absolute difference between the universality and SD reconstructed zenith angle. The same 50 000 proton simulations from the Napoli library are reconstructed using the (a) global and (b) constrained axis fits. Individual events are shown in transparent points that identify their zenith and energy group; the grayed out regions indicate events previously identified as outliers ($X_{\mathrm{max}} \notin [500, 1050]$ g cm^{-2} and $|\theta_{\mathrm{Univ}} - \theta_{\mathrm{SD}}| > 5^\circ$). With only the MC energy fixed and no further constraints, the global fit has proportionally more outliers, which are primarily at energies below 10^{19} eV.

In the global method, explicit cuts on the reconstructed depth of the shower maximum were used. However, such selection criteria present the risk of accidentally rejecting well-reconstructed events which have true values that merely deviate more from the average or median than the rest of the data. As the average and range of the depth of the shower maximum with respect to energy depends on the mass of the incident primary, such cuts could lead to a bias in the measured mass composition. The violin plots of the true depth of the shower maximum is shown in Fig. 4.3a for proton, helium, oxygen, and iron EPOS-LHC simulations. Regardless of composition, the depth of the shower maximum is not below 550 g cm^{-2}, but with proton simulations, it is possible to have a depth of the shower maximum above 1050 g cm^{-2}. In order to remedy these problems and still derive cuts that can be used with real data, a data-driven fiducial selection is performed [5]. In a given energy bin, this method separately evaluates the mean X_{max} as a function of $\sin^2\theta$. When the mean X_{max} deviates by more than 20 g cm^{-2}, the cut threshold in $\sin^2\theta$ is defined for that energy. In simulations with a pure mass composition, such a method is derived and used separately for each primary mass and model.

4.2.2 Fiducial selection

The concept of the fiducial selection of events is based of the fiducial field of view implemented by the FD[6]. In FD analyses (as mentioned in Section 2.5), a fiducial field of view selection is used to ensure that the distribution of the depth of the shower maximum is

[5] This is further described in Section 4.2.2.

[6] Further details on the FD fiducial field of view are found in [33, 140].

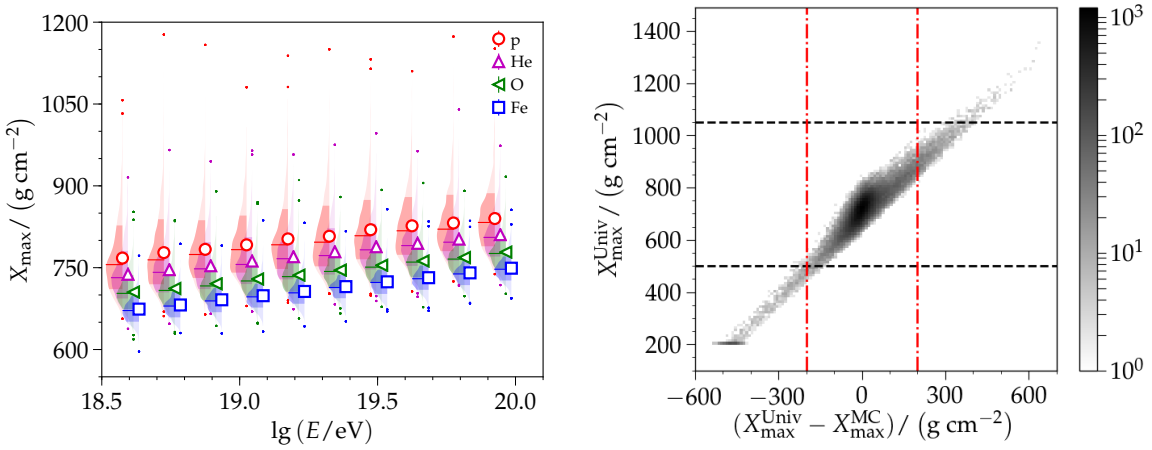

Figure 4.3: (a) True depth of the shower maximum with respect to energy for QGSJET-II.04 proton, helium, oxygen, and iron simulations of the Napoli library. (b) The difference in the reconstructed and true depth of the shower maximum is shown with respect to the reconstructed value for iron simulations. The black dashed lines represent the previously applied cuts, whereas the red lines mark where the difference first exceeds 200 g cm^{-2}. The average bias for a reconstructed X_{max} value of 1050 g cm^{-2} is around 300 g cm^{-2}, whereas the average bias at $X_{max} = 500$ g cm^{-2} is around −200 g cm^{-2}.

not distorted by the field of view of the detector. A brief introduction to the ideas behind the FD fiducial selection is given in Section 4.2.2.1 to motivate a similar selection for the universality reconstruction.

In the universality approach, data from the SD, which samples the lateral distribution, is used. As such, the SD, through the differing time responses of triggered stations, is able to effectively sample different slant depths (shower stages) and, through this, to reconstruct the depth of the shower maximum. Unlike the FD, the SD has a roughly 180° aperture for accepting CR showers. So naively, one might assume that the mass composition measured by the SD and reconstructed with universality should be unbiased. However, the signals that will be deposited in the stations are attenuated based on the amount of atmosphere traversed, which depends on zenith angle[7]. On average, low energy showers develop higher in the atmosphere (corresponding to low X_{max} and high ΔX values). Due to the X_{max} distributions in simulations, this region in ΔX is sparsely covered; thus, larger deviations in the signal and time model parameterizations are to be expected, as depicted in Fig. 4.4 (and Fig. 3.8d). This is further complicated as low energy events trigger fewer stations.

At high X_{max} values, the observed ΔX will be just above or below ground. At $\theta = 0°$, the maximum X_{max} which may be observed as above ground at Auger is roughly 860 g cm^{-2}, so the maximum X_{max} that is above ground for a given zenith angle is $\approx 860/\cos\theta$ g cm^{-2}. In returning once more to the X_{max} distributions of different primaries shown in Fig. 4.3a, it can be seen that some proton, helium, and, even at the highest energies, oxygen showers have X_{max} values exceeding 860 g cm^{-2}. During the parameterization of universality, only events with X_{max} values above ground were used. As such, large deviations (Fig. 3.8d) are expected for events with small or negative ΔX values. With an improved parameterization,

[7]For an idea of the magnitude of the attenuating effects, check out the the *Constant Intensity Cut* (CIC) (Section 2.4) used in SD reconstruction. It is used to account for the zenith-dependent attenuations of the signal estimator S_{1000}.

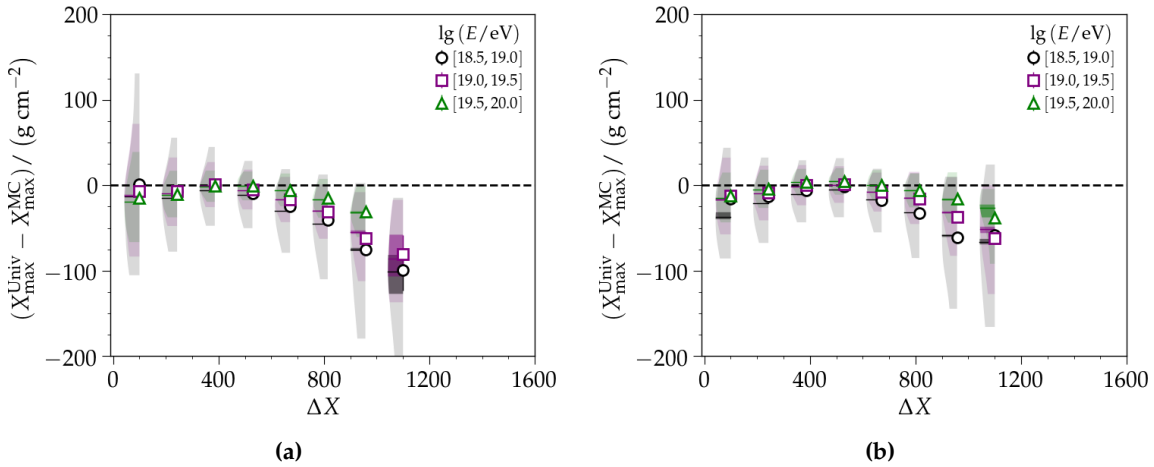

Figure 4.4: QGSJET-II.04 simulations of (a) proton- and (b) iron-induced showers from the Napoli library reconstructed using the constrained axis method. The reconstructed X_{max} bias is shown with respect to the true ΔX. Proton-induced showers are more likely than iron ones to have develop closer to the ground. Conversely, iron-induced showers are more likely to develop higher up in the atmosphere. Thus, the large bias in proton showers around 1100 g cm^{-2} is due to lower event statistics; when compared to the results in iron in the same bin, the maximum difference in the average X_{max} bias for the different energies is on the order of 25 g cm^{-2}. For this comparison, only events with $X_{max}^{Univ} < 300$ g cm^{-2} were rejected.

universality should be extended to cover this range[8]. A re-parameterization of the signal and time models is outside the scope of this work. Instead, a fiducial selection in zenith angle (Section 4.2.2.2) will be used to select events that are well-described by the currently implemented parameterizations, which corresponds to well-reconstructed events.

4.2.2.1 Interlude on the FD fiducial field of view selection

A visual depiction of the effect of the field of view with various shower geometries is given in Fig. 4.5. When one considers the X_{max} distributions of different primaries (shown in Fig. 4.3a), it becomes apparent that the field of view of the telescopes would observe more deeply penetrating showers —like proton-induced showers— on average more than shallower showers —like iron-induced showers. This is further complicated as (1) the true depth of the shower maximum is proportional to the natural logarithm of the primary energy, (2) the measured mass composition is thought to evolve with respect to energy, and (3) the observation of a shower, leading to a well-reconstructed event, depends on several quality cuts. Thus, in order to have an unbiased measurement of the mass composition, the fiducial field of view selection must be performed after all quality cuts (listed in Section 2.5) have been performed, needs to be calculated in different energy bins, and should be based upon the data set considered (whether it is a pure composition in simulations or the mixed composition of real data).

[8]Most showers initiated by nuclei will have a depth of shower maximum that is just a few meters below ground. Thus, depending on the energy and zenith angle, the shower should be developed enough such that, when it is observed by the SD, enough stations were triggered to allow for a successful reconstruction. However, with extremely deeply penetrating showers —like those of photons— the depth of the shower maximum may be so far underground that the development of the shower at ground level is not sufficient to trigger enough stations to constrain the reconstruction. Nevertheless, such deeply penetrating showers would be a small fraction of the events. Such parameterizations should be done as the universality method is being applied to AMIGA; it would be useful for cross-checks and to evaluate whether a combined universality reconstruction with the MD and SD detectors is possible to cover a larger ΔX range.

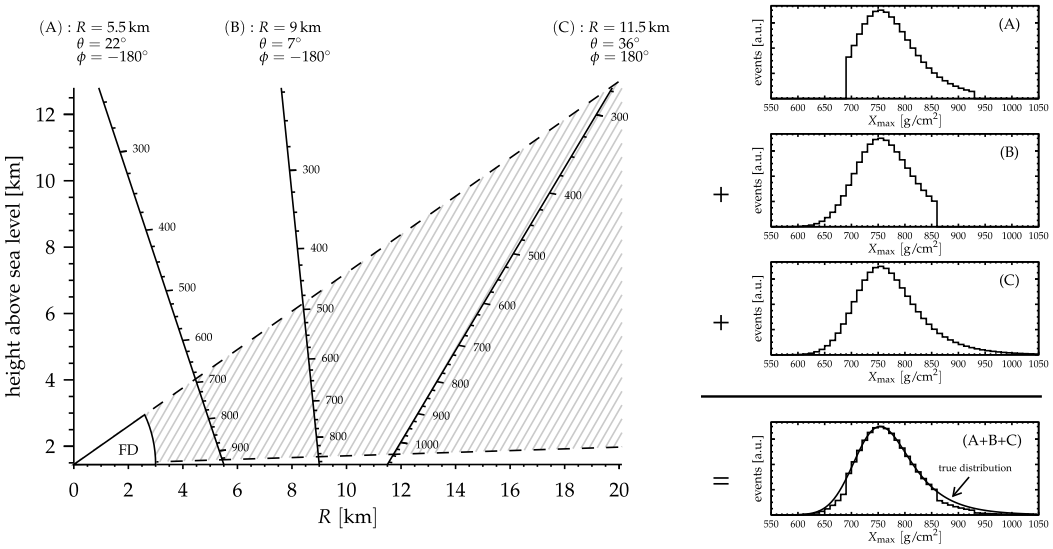

Figure 4.5: The influence of the FD field of view (hatched area inside dashed lines) on the sampling of the $X_{\max}$ distribution for three event geometries. The distance to the FD R, azimuthal angle ϕ and zenith angle θ of each example is given in the left illustration with their own slant depth axis in $\mathrm{g\,cm^{-2}}$. The corresponding example $X_{\max}$ distributions are given on the right. Cases A and B are truncated, whereas C is fully within the field of view. For this heuristic schematic, the same number of events for each geometry has been assumed [33].

In the FD, the elevation range of a telescope is from $\Omega_1 = 1.5°$ to $\Omega_2 = 30°$. Thus, the observable height h_v for vertical tracks is determined by the distance of the shower core to the telescope R and is between $R \tan \Omega_1$ and $R \tan \Omega_2$. As the distance from a detected track to the FD increases, the observable upper slant depth boundary X_{up} decreases. Similarly, the lower slant depth boundary X_{low} increases for nearby showers. A bias in the measured mass composition can be avoided by selecting only tracks with geometries fully contained in the $X_{\mathrm{low}} - X_{\mathrm{up}}$ range. As the true $X_{\max}$ distribution is unknown, the necessary cuts must be determined from the data itself. If the mean $X_{\max}$ is measured as a function of X_{up} and X_{low}, it is expected to be relatively constant if the field of view boundaries are far away from the tails of the $X_{\max}$-distribution. As the slant depth boundaries begin to cut into the distribution —like in the cases of A and B in Fig. 4.5— then the measured mean will start to deviate from its asymptotic value. A cut can then be defined where the deviation from the asymptotic value exceeds a certain threshold (e.g. $5\,\mathrm{g\,cm^{-2}}$). A Gaussian approximation of the edges of the $\langle X_{\max} \rangle$ distribution is assumed, and the mean of a truncated normal distribution is adjusted to the data. The energy dependence of these boundaries is parameterized. The fiducial field of view selection remove around two-thirds of the data which passed the previously applied quality cuts.

4.2.2.2 Fiducial selection for universality

The biases of the reconstructed observables are given in Fig. 4.6 for the constrained axis fit. The reconstructed depth of the shower maximum is biased by less than $30\,\mathrm{g\,cm^{-2}}$ for all zenith angles below 52.2° and above an energy of $10^{18.6}\,\mathrm{eV}$. At the highest energies, there is a bias — on order of $15\,\mathrm{g\,cm^{-2}}$— for proton-induced showers which increases with decreasing zenith angle. This high-energy bias arises as proton-induced showers are more likely to have values of $X_{\max}$ that will be observed close to or below ground. Iron-induced showers have a maximal development well above ground and, thus, do not exhibit such a dependence at the highest energies.

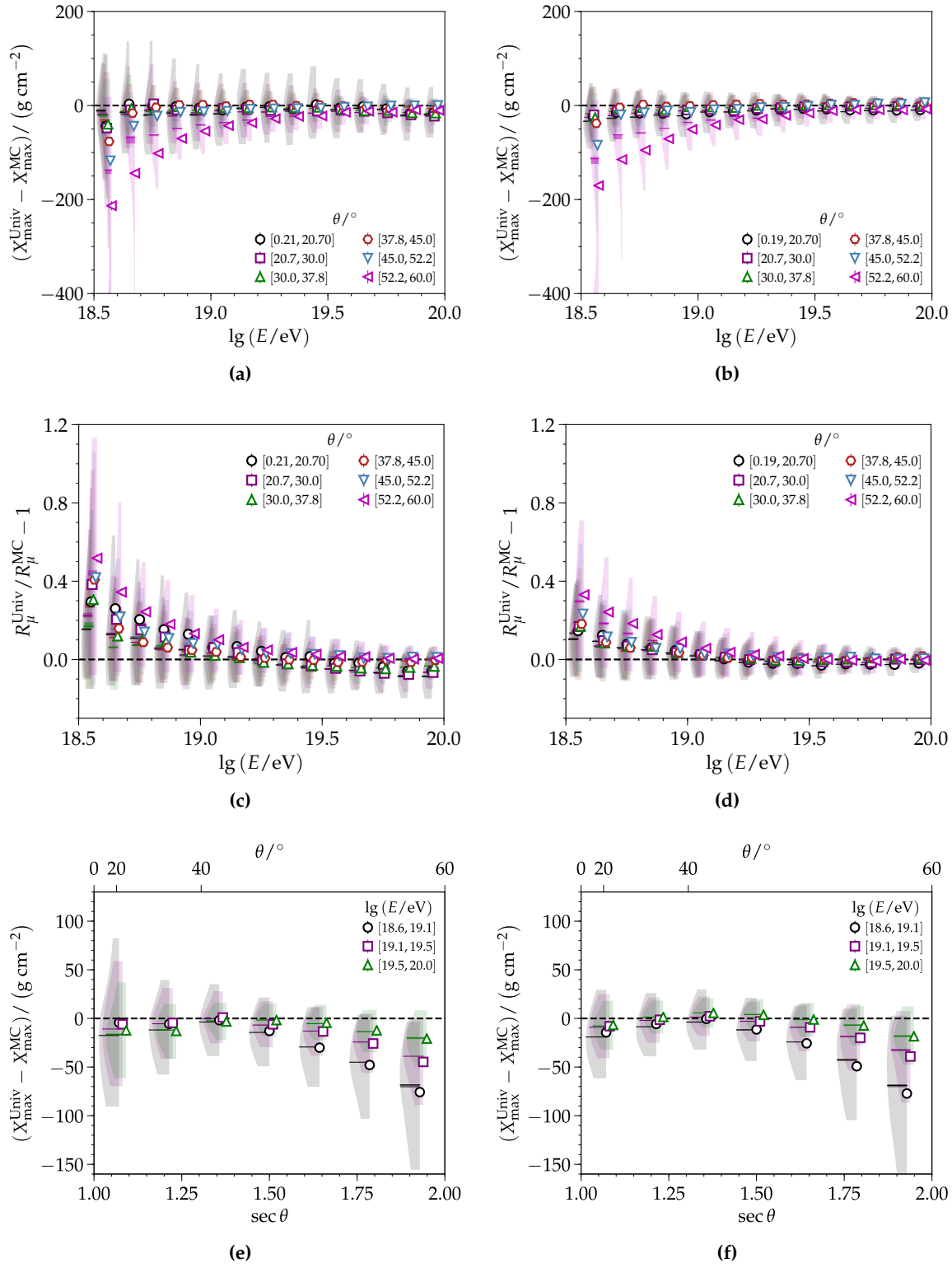

Figure 4.6: QGSJET-II.04 (*left*) proton- and (*right*) iron-induced simulations from the Napoli library reconstructed with the constrained axis method. Only non-saturated events are considered with no further cuts applied. The bias of the reconstructed (*top*) depth of the shower maximum and (*middle*) relative muon content are considered with respect to energy and zenith angle. (*Bottom*) The bias of the reconstructed depth of the shower maximum is shown with respect to the secant of the zenith angle for different energy bins. As the energy increases, enough stations are triggered to better constrain the reconstruction and yield a reconstructed X_{max} that deviates less from the true value than their lower energy counterparts

To better determine for which zenith angles the reconstruction is well-behaved, a fiducial selection that evolves with energy is performed. While the quality of the reconstruction depends on energy and slant depth ($\propto \sec\theta$) —as shown in Fig. 4.6e and Fig. 4.6f, the fiducial selection is performed in equal-width $\sin^2\theta$. This reflects the zenith angle distribution that is observed in data and ensures that the same number of events are being used. The goal of this selection is to identify and reject the subset of data which returns reconstructed values that significantly deviate from the average description.

Simulated events are binned in intervals of 0.1 in $\lg E$ from $10^{18.5}$ eV to 10^{20} eV. The width of the energy bin is sufficiently small such that the evolution of the average depth of the shower maximum with energy will be minimal. Deviations from the reconstructed $X_{\max}$ are expected at low zenith angles at the highest energies[9] and high zenith angles at low energies[10]. The expected value of the mean $X_{\max}$ is calculated with the inner tertile ($\sin^2\theta \in [0.25, 0.5]$). The upper and lower limits on the accepted zenith angle range are found when the mean $X_{\max}$ of a $\sin^2\theta$ bin[11] deviates by more than[12] 20 g cm^{-2}. To determine where this deviation first occurs, quadratic fits with[13]

$$\Delta X_{\max}(\sin^2\theta) = a + b\cdot(\sin^2\theta - \mathrm{ref}_{\sin^2\theta}) + c\cdot(\sin^2\theta - \mathrm{ref}_{\sin^2\theta})^2 \tag{4.1}$$

are separately performed for the mean values of the upper zenith angle range ($\sin^2\theta \in [0.25, 0.75]$, $\mathrm{ref}_{\sin^2\theta} = 0.5$) and lower zenith angle range ($\sin^2\theta \in [0, 0.5]$, $\mathrm{ref}_{\sin^2\theta} = 0.25$). The interpolated values from these fits are then subtracted from the expected $X_{\max}$ value. Examples of the fiducial selections for three energy bins are given in Fig. 4.7.

As shown in Fig. 4.8, the upper limit for the allowed zenith angle range gradually increases from around 48° to 60° with increasing energy. For proton, the lower limit for the allowed zenith angle range begins to depart from 0° at $10^{19.3}$ eV and reaches a maximal value around 15° to 22° at 10^{20} eV. Nuclei slightly heavier than proton do not have a lower limit as their $X_{\max}$ distributions are not as diffuse nor do they have as many events below or close to ground as proton-induced showers. The upper limit u for the zenith range is fit with a horizontal line for $\lg(E/\mathrm{eV}) > 19.5$ and with a quadratic equation for $\lg(E/\mathrm{eV}) \leq 19.5$ of the form

$$\sin^2_u\theta(\lg E) = a + b\cdot(\lg E - 18.5) + c\cdot(\lg E - 18.5)^2. \tag{4.2}$$

To ensure that the two equations meet, they are simultaneously fit, where the continuity to the horizontal line acts as a boundary condition for the quadratic fit. Similarly, for the lower limit, a horizontal line for $\lg(E/\mathrm{eV}) \geq 19.2$ and linear equation[14] for $\lg(E/\mathrm{eV}) > 19.2$ are fit. For proton- and iron-induced showers, the upper limit follows a similar trend across all interactions models. In particular, the limits for both primaries are in close agreement for QGSJET-II.04 and SIBYLL-2.3. While the relative onset and values of the lower limit for proton-induced showers varies between interaction models, a gradual increase in the lower limit is seen with respect to increasing energy, beginning at around $10^{19.3}$ eV. Parameters for the lower and upper limit defining the allowed zenith angle range in an energy bin are given in Table 4.1 for simulations generated with QGSJET-II.04.

[9] For light elements —like proton, the observed $X_{\max}$ will be close to or below ground.

[10] The observed $X_{\max}$ will be high up in the atmosphere, the observed signals will be greatly attenuated, and, likely, not enough stations will be triggered to constrain the reconstruction.

[11] The bin width in $\sin^\theta$ ($\Delta\sin^2\theta = 0.06$) is chosen to be small enough for precision but large enough for there to be more than 40 events in a bin.

[12] This value was chosen as it is the maximal deviation in the average bias of $X_{\max}$ for the various zenith angles above an energy of $10^{19.0}$ eV (Fig. 4.6). The goal with the fiducial selection is to identify zenith bins where the quality of reconstruction vastly differs from well-reconstructed quantities.

[13] For simplicity, equations are written such that the units are implied. Anytime $X_{\max}$ is in an equation the implied units are g cm^{-2}. Similarly, $\lg E$ represents $\lg(E/\mathrm{eV})$

[14] This is the same equation as given in Eq. (4.2) where $c = 0$.

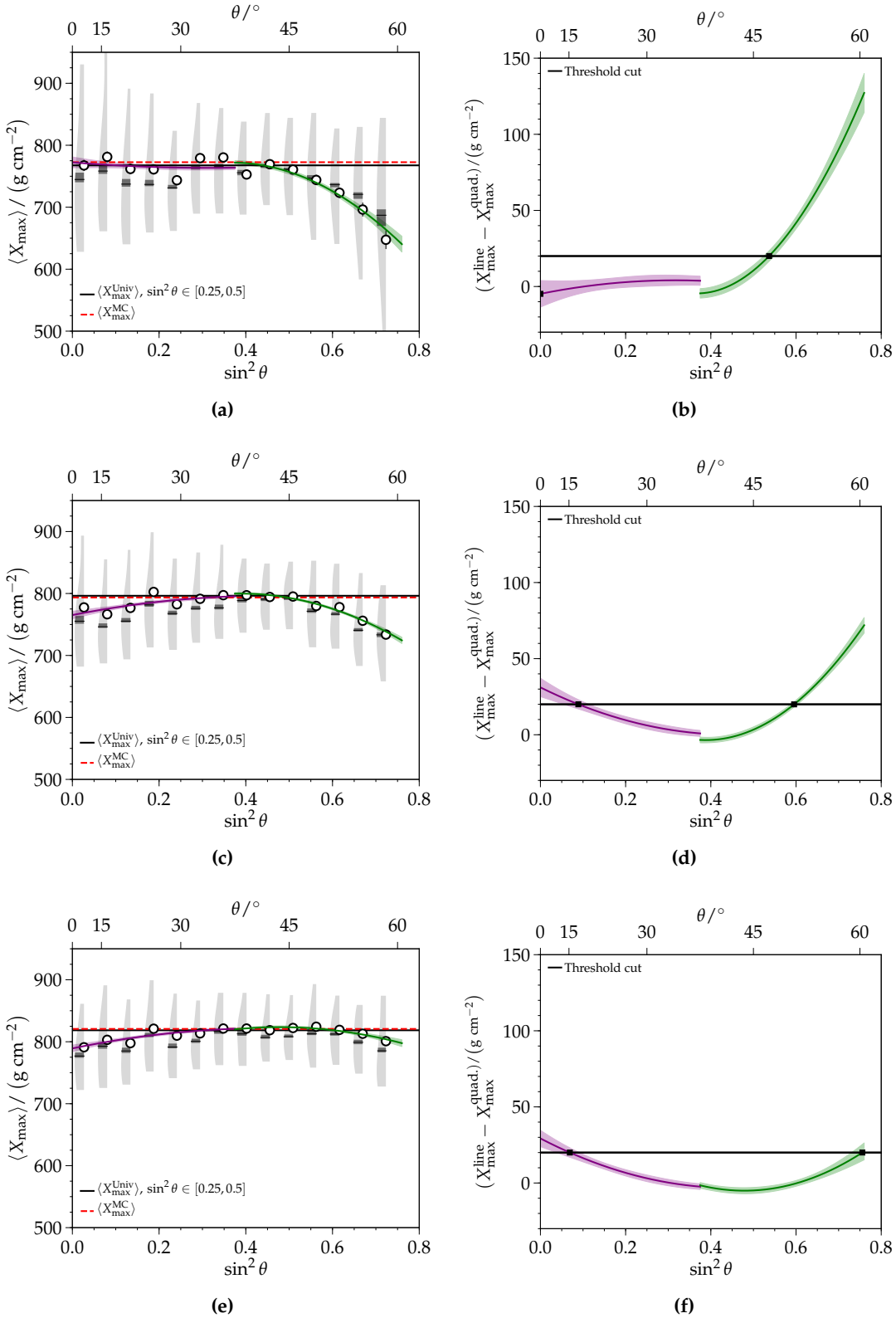

Figure 4.7: Fiducial selection using the deviation of the calculated mean in $\sin^2\theta$ for $\lg E \in$ (*top*) [18.5, 18.6], (*middle*) [19.0, 19.1], and (*bottom*) [19.5, 19.6] for QGSJET-II.04 proton-induced simulations. (*Right*) the mean values of $X_{\max}$ as a function of $\sin^2\theta$ are shown. The dashed black line is the mean of the second tertile; it is, on average, within $5\,\mathrm{g\,cm^{-2}}$ of the red line which is the mean of the Monte Carlo $X_{\max}$ values across all zenith angles. The purple and green curves are the quadratic fits to the lower and upper zenith ranges, respectively. The width of each curve is from the uncertainty of the fit. (*Left*) The difference between the mean $X_{\max}$ value and quadratic fits is compared to the threshold cut of $20\,\mathrm{g\,cm^{-2}}$. The black points are the numerically calculated values where the mean $X_{\max}$ in the lower (upper) zenith range first deviated by more than $20\,\mathrm{g\,cm^{-2}}$ from the mean value of the second tertile.

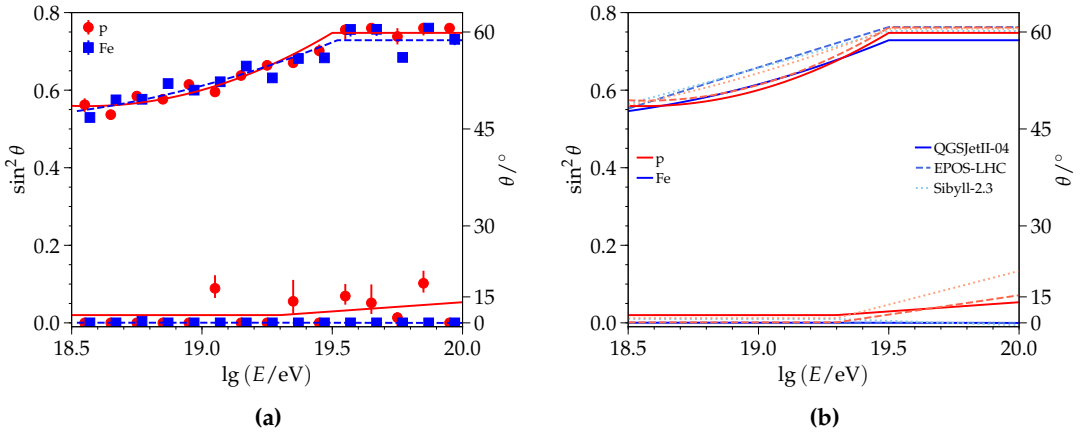

Figure 4.8: Evolution of the fiducial selection as a function of logarithmic energy for proton- and iron-induced showers generated with (a) QGSJET-II.04 and (b) QGSJET-II.04, EPOS-LHC, and SIBYLL-2.3.

4.2.3 Resulting bias and resolution

As shown in Fig. 4.9, when the derived fiducial selection criteria[15] are applied to simulations, the resulting biases of the reconstructed observables are greatly reduced. For proton- and iron-induced showers, the bias of the depth of the shower maximum is, on average, less than $25\,\mathrm{g\,cm^{-2}}$. While the zenith-dependence of the X_{max} bias remains, the bias of the relative muon content for iron-induced showers has a dependence on zenith angle on the order of 5 %. In Fig. 4.10, the parameterized bias and resolution for QGSJET-II.04 simulations are given as a function of energy for four primaries[16] across all zenith angles permitted by the fiducial selection. The biases and resolutions[17] are fit separately as functions of energy with

$$\mathrm{Bias}\,||\,\mathrm{Res.}(\lg E) = a + b\cdot(\lg E - 19) + c\cdot(\lg E - 19)^2 + d\cdot(\lg E - 19)^3. \tag{4.3}$$

The parameters for the fit of the biases and resolutions obtained with air showers simulated with QGSJET-II.04 are given in Table 4.2. Using these parameterizations, it is possible to correct for the biases that are seen in data[18].

4.3 Event selection in data

4.3.1 Fiducial selection

In Section 4.2.2.2, a fiducial selection that evolves with energy was derived for the various interaction models and primaries. While these were in close agreement, these criteria cannot be directly applied to data as the mass composition is unknown. As such, the fiducial

[15] In the energy regions where horizontal lines are fit, the upper (lower) limit is set to 60° (0°). The quadratic and linear fit for the other regions are used as specified without modification.

[16] See Fig. 4.12 for a comparison of the biases and resolutions for proton- and iron-induced showers for the different interaction models.

[17] As seen in Fig. 4.9, the ordering of the biases with respect to zenith angle for events with energies in $10^{18.5}$ eV to $10^{18.6}$ eVis greatly distorted. As such, this bin is not included in the fit of the biases and resolutions. Additionally, several functions were fit. While it is not physically motivated, the third-order polynomial provides the best empirical fit.

[18] As seen in Fig. 4.6e and Fig. 4.6f, the zenith-dependent biases of the X_{max} are also a function of energy. In Appendix D.5.2, the residual bias, after applying the bias correction as a function of energy, is parameterized as a function of energy and zenith angle.

Table 4.1: Parameters for the lower and upper limits for the universality fiducial selection of simulated air showers generated with the QGSJET-II.04 interaction model. Parameters for the other interaction models are given in Appendix C.1.

Lower limit		
Primary	a	b
proton	-0.02 ± 0.03	0.05 ± 0.04

Upper limit			
Primary	a	b	c
proton	0.56 ± 0.02	-0.02 ± 0.07	0.21 ± 0.05
helium	0.54 ± 0.02	0.11 ± 0.09	0.08 ± 0.08
oxygen	0.53 ± 0.02	0.16 ± 0.10	0.05 ± 0.08
iron	0.55 ± 0.02	0.09 ± 0.10	0.09 ± 0.08

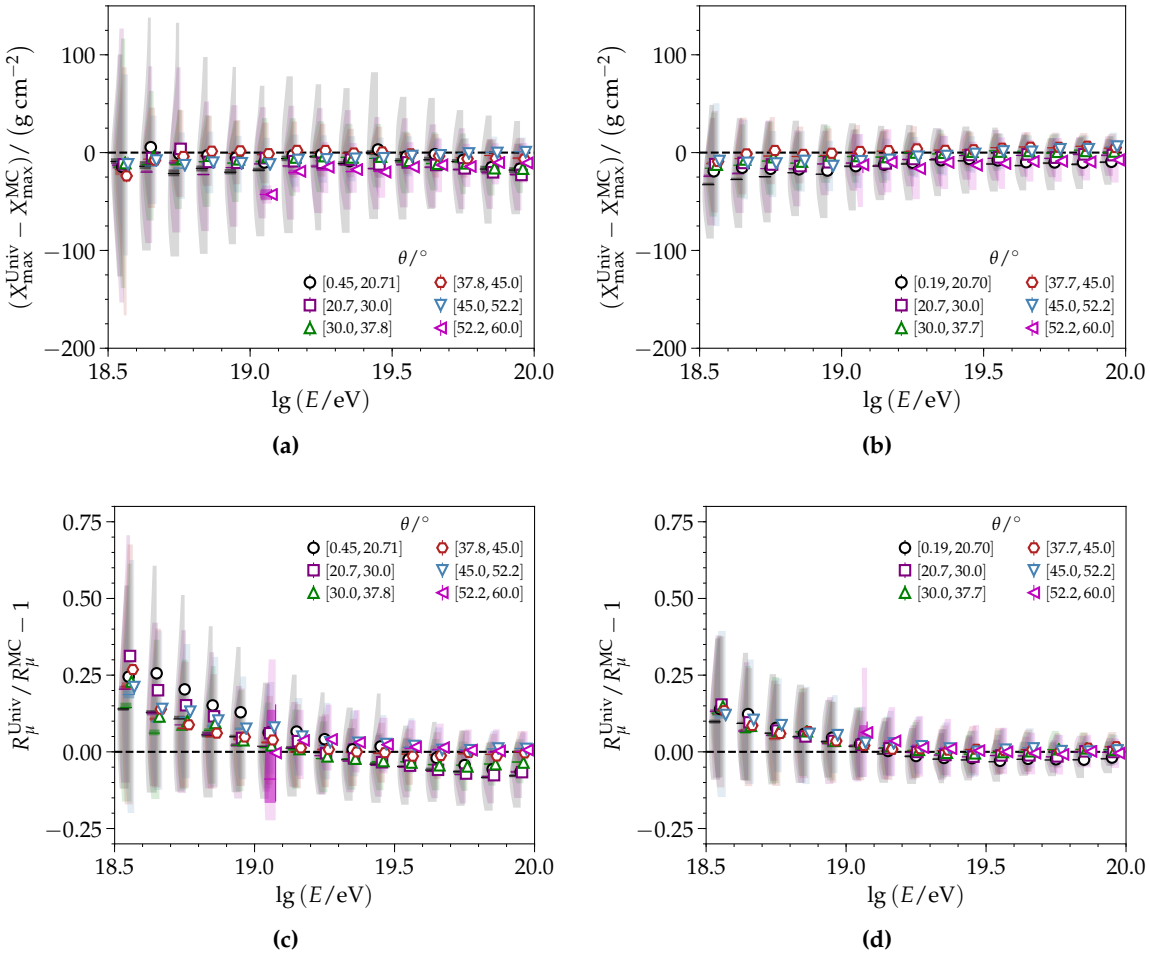

Figure 4.9: QGSJET-II.04 (*left*) proton- and (*right*) iron-induced simulations. Shown are the events after applying the fiducial selection for each primary. The bias of the reconstructed (*top*) depth of the shower maximum and (*bottom*) relative muon content are considered with respect to energy and zenith angle. To note, the large deviation of proton-induced showers at an energy of $10^{19.1}$ eV and zenith angle range of 52.2° to 60° is due to five events being grouped together. This results as the same zenith angle ranges are applied overall the whole data set.

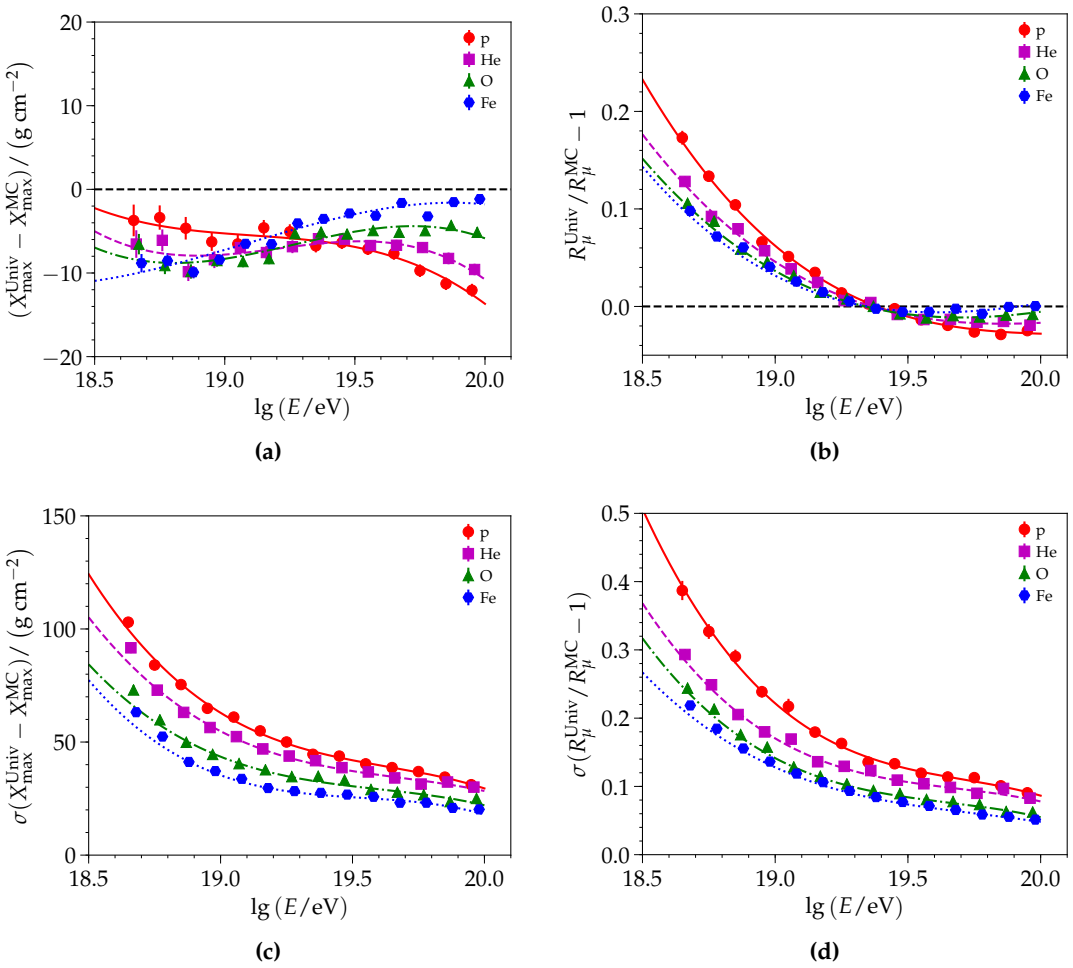

Figure 4.10: Events reconstructed from QGSJET-II.04 proton-, helium-, oxygen-, and iron-induced simulations. The (*top*) bias and (*bottom*) resolution of the reconstructed (*left*) depth of the shower maximum and (*right*) relative muon content are considered with respect to energy. The fiducial selection cuts derived for each primary are used.

selection needs to be derived separately for data. Because of the mixed mass composition that changes with respect to energy, the calculated cuts will differ from those found in simulations of a pure composition. Instead of just rejecting events which significantly deviate due to poor constrainment in a certain energy region, events will also be rejected which vastly differ from the mean depth of the shower maximum. While such a rejection is perhaps not ideal for anisotropy studies[19], it will lead, however, to an unbiased estimate of the mean $X_{\max}$ and its second moment.

The fiducial selection for data from the SD-1500 is given in Fig. 4.11. The width of each energy bin is chosen so that the bin width —$\Delta \sin^2\theta = 0.06$— is the same as was used in simulations. With an energy distribution of $\propto E^{-2.5}$, this means that data is binned in intervals of 0.1 in $\lg E$ from $10^{18.5}$ eV to $10^{19.5}$ eV and in a final bin from $10^{19.5}$ eV to 10^{20} eV. The upper limit of the fiducial selection is like the one found in simulations; however, with too few events at the highest energies, it is not possible to determine if events above an energy of $10^{19.5}$ eV may include zenith angles up to 60°. Thus, the upper u and lower l

[19]For such studies, it is recommended to at least use the upper limits found with simulations to reject events which are most likely to be poorly reconstructed. An analysis on further quality selections should also be performed.

Table 4.2: Parameters for the fits of the bias and resolution for the depth of the shower maximum and relative muon content for simulated air showers generated with the QGSJET-II.04 interaction model. Values for the other interaction models are given in Appendix C.2. The values of the χ^2/n_{dof} range from 0.7 to 2.66, with the worst fits with heavier primaries.

Bias of $(X_{\mathrm{max}}^{\mathrm{Univ}} - X_{\mathrm{max}}^{\mathrm{Univ}})$

Primary	a	b	c	d
proton	-5.3 ± 0.5	-2.4 ± 1.8	2.8 ± 6.2	-8.8 ± 5.5
helium	-7.8 ± 0.4	2.3 ± 1.5	8.8 ± 5.4	-14.0 ± 4.8
oxygen	-8.3 ± 0.3	4.8 ± 1.2	9.2 ± 4.2	-11.5 ± 3.8
iron	-7.2 ± 0.3	9.2 ± 1.1	1.1 ± 3.7	-4.9 ± 3.3

Resolution of $(X_{\mathrm{max}}^{\mathrm{Univ}} - X_{\mathrm{max}}^{\mathrm{Univ}})$

Primary	a	b	c	d
proton	62.9 ± 0.6	-71.4 ± 2.1	80.5 ± 7.4	-42.4 ± 6.5
helium	54.8 ± 0.5	-60.0 ± 2.3	65.5 ± 7.0	-31.9 ± 5.9
oxygen	43.5 ± 0.4	-46.2 ± 1.8	55.2 ± 5.8	-30.5 ± 4.9
iron	35.3 ± 0.3	-41.7 ± 1.6	64.8 ± 4.7	-40.4 ± 3.8

Bias of $(R_{\mu}^{\mathrm{Univ}}/R_{\mu}^{\mathrm{MC}} - 1)$

Primary	a	b	c	d
proton	0.062 ± 0.002	-0.229 ± 0.006	0.196 ± 0.021	-0.057 ± 0.018
helium	0.046 ± 0.001	-0.176 ± 0.005	0.152 ± 0.016	-0.038 ± 0.014
oxygen	0.036 ± 0.001	-0.152 ± 0.004	0.141 ± 0.013	-0.032 ± 0.011
iron	0.031 ± 0.001	-0.138 ± 0.004	0.150 ± 0.012	-0.040 ± 0.010

Resolution of $(R_{\mu}^{\mathrm{Univ}}/R_{\mu}^{\mathrm{MC}} - 1)$

Primary	a	b	c	d
proton	0.222 ± 0.004	-0.337 ± 0.013	0.380 ± 0.042	-0.178 ± 0.035
helium	0.170 ± 0.002	-0.230 ± 0.008	0.269 ± 0.025	-0.132 ± 0.021
oxygen	0.142 ± 0.001	-0.203 ± 0.005	0.235 ± 0.016	-0.119 ± 0.013
iron	0.128 ± 0.001	-0.174 ± 0.004	0.169 ± 0.011	-0.074 ± 0.009

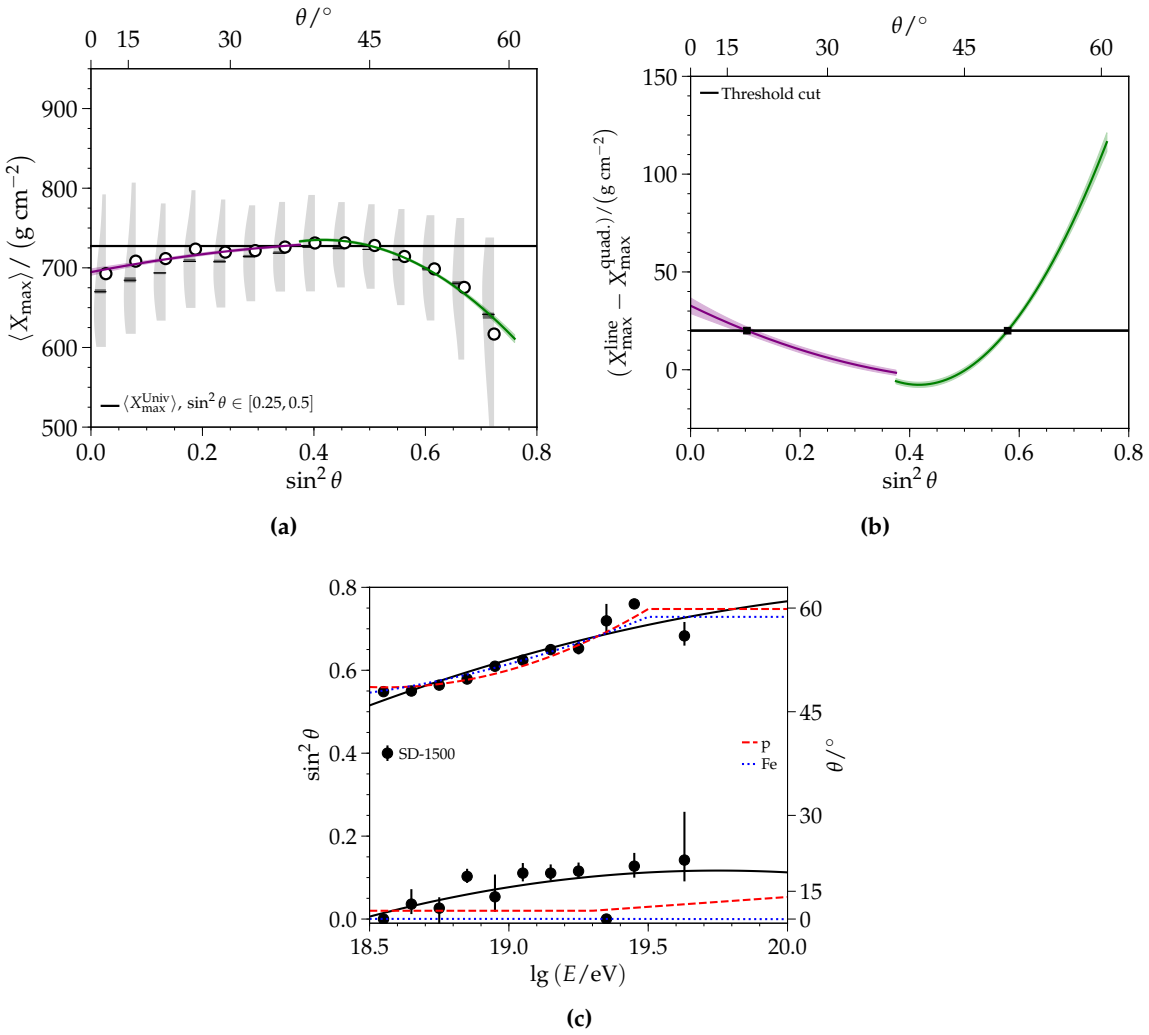

Figure 4.11: Fiducial selection using the deviation from the calculated mean in $\sin^2\theta$ for $\lg E \in [18.8, 18.9]$. (a) the mean values of $X_{\max}$ and (b) difference between the mean $X_{\max}$ value and quadratic fits is compared to the threshold cut of $20\,\mathrm{g\,cm^{-2}}$ as a function of $\sin^2\theta$. (c) Fiducial selection as a function of logarithmic energy for SD-1500 data. The fiducial selection for QGSJET-II.04 proton- and iron-induced primaries are compared.

limits of the fiducial selection are separately fit with a quadratic equation

$$\sin^2_{u,l}\theta(\lg E) = a + b\cdot(\lg E - 18.5) + c\cdot(\lg E - 18.5)^2. \tag{4.4}$$

The parameters for the corresponding functions are given in Table 4.3.

4.3.2 Data-based corrections

Having derived the fiducial selection for data, the biases and resolutions of the reconstructed variables may be calculated. Ideally, the energy correction derived from simulations could be directly applied to data to account for all biases. In reality, as seen in Fig. 4.12, the biases of the reconstructed depth of the shower maximum and relative muon content depend not only on which primary is considered but also on the employed interaction model. While such a dependence might seem alarming, these differences actually arise because the description of the relative muon content differs in each interaction model, and in all models, the relative muon content is 20 % to 60 % smaller than what is needed to

Table 4.3: Parameters for the lower and upper limit for the universality fiducial selection for the data of the SD-1500.

Limit	a	b	c
lower	0.01 ± 0.04	0.18 ± 0.16	-0.07 ± 0.13
upper	0.52 ± 0.03	0.25 ± 0.10	-0.05 ± 0.09

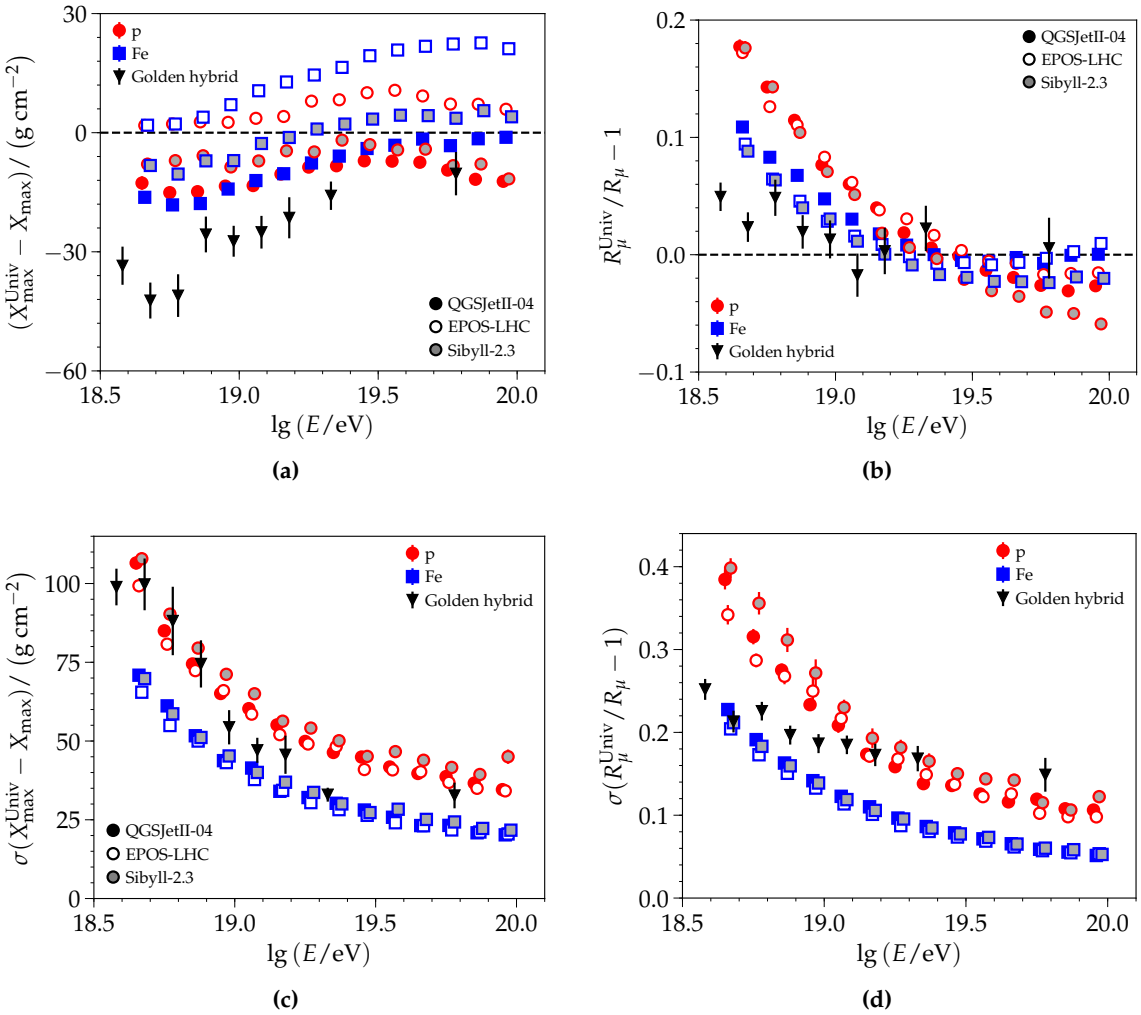

Figure 4.12: The (*top*) bias and (*bottom*) resolution of the reconstructed (*left*) depth of the shower maximum and (*right*) relative muon content are considered with respect to energy. The fiducial selection cuts derived for each primary and interaction model are used. The fiducial selection derived for SD-1500 data is applied to golden hybrid data. (Note that this is for illustrative purposes only, as the underlying zenith angle has been distorted by the fiducial field of view selection for the FD.) In simulations, the reconstructed quantities are compared to their true values. For golden hybrid events, the universality reconstructed values are compared to the $X_{\max}$ measured by the FD. In data, the R_μ is estimated from a special reconstruction where all values except the core and relative muon content are fixed to those reconstructed by the FD. A further description of this estimated relative muon content $\hat{R}_\mu^{\mathrm{FD}}$ is given in Appendix D.4.2.

describe data [57]. If a calibration procedure were performed for each data set and implemented prior to reconstruction, the present offsets in the biases would converge to a specific value, and the bias itself would be minimal[20]. Nevertheless, the general trends of the biases of proton and iron with respect to energy are similar across all interaction models. Very similar trends are seen in data, where the bias approaches $0\,\mathrm{g\,cm^{-2}}$ and 0.0 at the highest energies. The resolution for data is, on average, between the resolutions found for proton- and iron-induced showers across all interaction models.

The shape of the R_μ bias in data looks to be, on average, compatible with iron-induced showers. While the shape of the bias in X_{max} is not identical between data and simulations, the bias in data has an upward-facing curve around $10^{18.5}$ eV and a downward-facing curve around $10^{19.5}$ eV. Furthermore, the only direct source for the bias correction in data is from golden hybrid events, of which there are only 2054 non-saturated events — too few events for fitting complicated, non-linear models. As such, the bias correction with respect to energy derived for QGSJET-II.04 (Appendix C.2) is used as a first step in the correction of the bias seen in data. In order to avoid an assumption on the mass composition of data, the applied bias correction is the average found between the parameterizations for proton- and iron-induced showers. The goal by performing this correction with simulations is to obtain a bias in golden hybrids which can be fit by a more simple model (e.g. linear fit).

As seen in Fig. 4.13, the non-linear dependencies of the X_{max} bias have been mostly accounted for after applying the simulation-based bias correction. The X_{max} bias agrees, on average, for the different zenith angle ranges. A linear model is fit to the remaining bias of the reconstructed depth of the shower maximum

$$\Delta X_{\mathrm{max}} = a + b \cdot (\lg E - 18.5). \tag{4.5}$$

An exponential model of the form

$$\sigma(\Delta X_{\mathrm{max}}) = a \cdot e^{-b\cdot(\lg E - 19.0)} \tag{4.6}$$

is fit to the resolution of X_{max}.The parameters for these model are given in Table 4.4.

In golden hybrid data, the fiducial field of view applied for FD analyses distorts the underlying $\sin^2\theta$ distribution[21]. Due to this selection, as well as the small number of events, deriving and/or applying a fiducial selection for universality to golden hybrid events is not possible[22]. The bias of the depth of the shower maximum is also calculated for SD-1500 data. In order to perform this fit, the X_{max} reconstructed by universality is compared to the mean X_{max} calculated with the elongation rate[23] ($X^{\mathrm{Univ}}_{\mathrm{max}} - \hat{X}^{\mathrm{FD}}_{\mathrm{max}}$) from the FD (taken from [104]). For energies above $10^{18.32}$ eV, the elongation rate is well-described by

$$\hat{X}^{\mathrm{FD}}_{\mathrm{max}} := 750 + 26 \cdot (\lg E - 18.32), \tag{4.7}$$

with the implied units of grammage. The best fitting results of the bias for golden hybrids

[20] A calibration process is described and implemented for the iterative reconstruction in Appendix D.4.2. In order to showcase the relative quality of universality prior to data-based modifications, such a calibration was not performed for the constrained axis fit.

[21] See Fig. B.2.

[22] For exploratory purposes, the fiducial criteria for SD-1500 data is applied to golden hybrids in Appendix D.5.3. With the two fiducial selections applied, the best fitting parameters for the bias as a function of energy greatly differ from those presented in this section. This lack of agreement arises from the zenith-dependent biases of the universality-reconstructed X_{max} —as seen in Fig. 4.9— coupled with the largely attenuated zenith distribution of the golden hybrid events. While it is not investigated in this work, perhaps it is possible for the FD quality cuts to be relaxed so that the universality-derived fiducial selection may be used.

[23] The elongation rate is the fit of the mean X_{max} measured by the FD as a function of energy. As seen in Fig. 1.18a, the composition below an energy of $10^{18.3}$ eV follows a linear trend towards proton, whereas the linear trend above this energy threshold is towards iron. This comparison is done for exploratory purposes. Again, it would be better if the FD selection criteria could be relaxed to perform a comparison with a more inclusive zenith angle distribution.

Table 4.4: Parameters for the bias and resolution of the reconstructed X_{max} in data.

Bias			
Data set	χ^2/n_{dof}	a	b
golden hybrid	1.27	-51.43 ± 2.81	54.96 ± 5.12
SD-1500	2.54	-52.21 ± 0.59	48.97 ± 1.32

Resolution			
Data set	χ^2/n_{dof}	a	b
golden hybrid	1.34	53.17 ± 1.68	1.43 ± 0.10
SD-1500	3.20	69.70 ± 0.52	1.26 ± 0.02

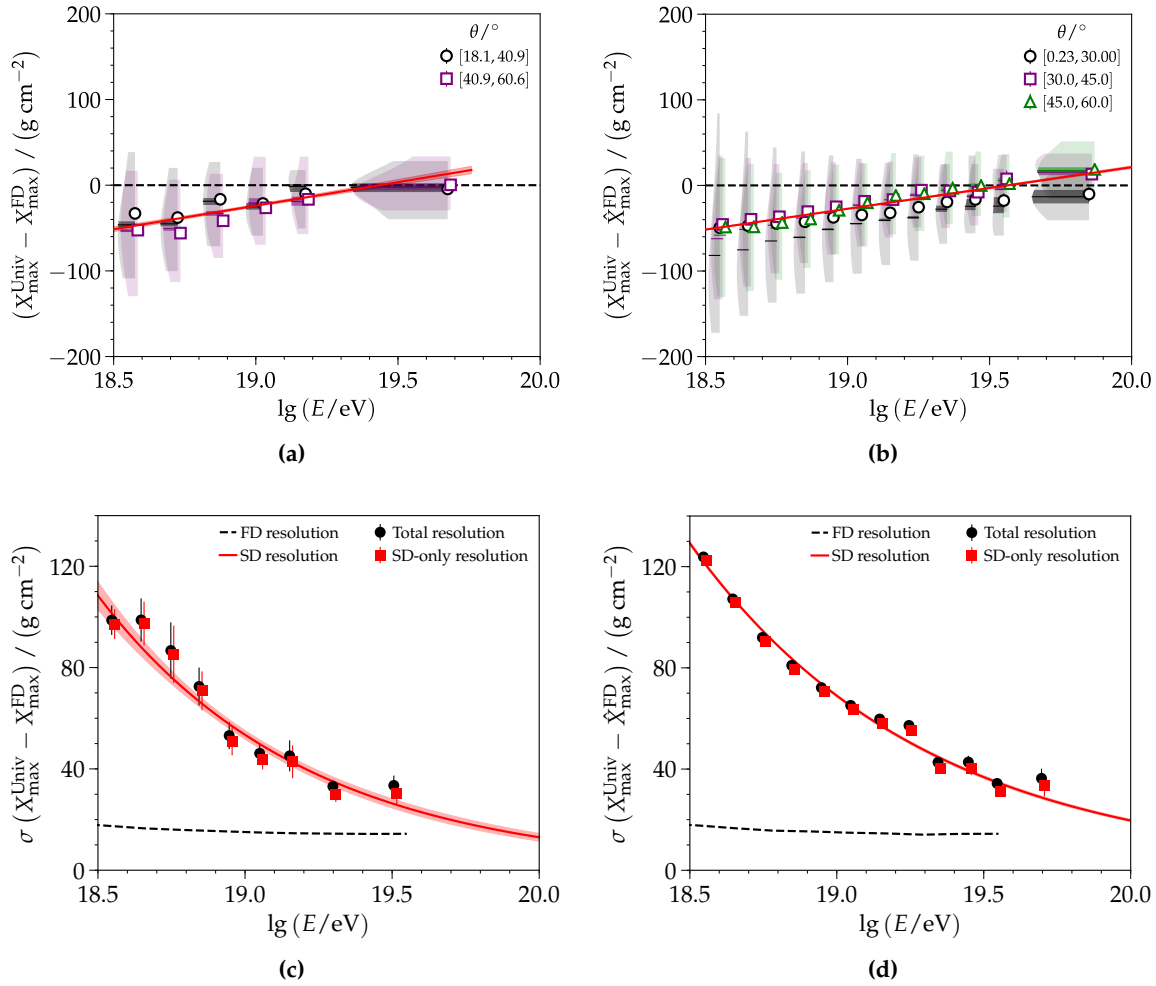

Figure 4.13: The (*top*) bias and (*bottom*) resolution of the reconstructed depth of the shower maximum is determined for (*left*) golden hybrid and (*right*) SD-1500 events. The fiducial selection for universality is only applied to SD-1500 data. The values for the FD resolution are taken from [33].

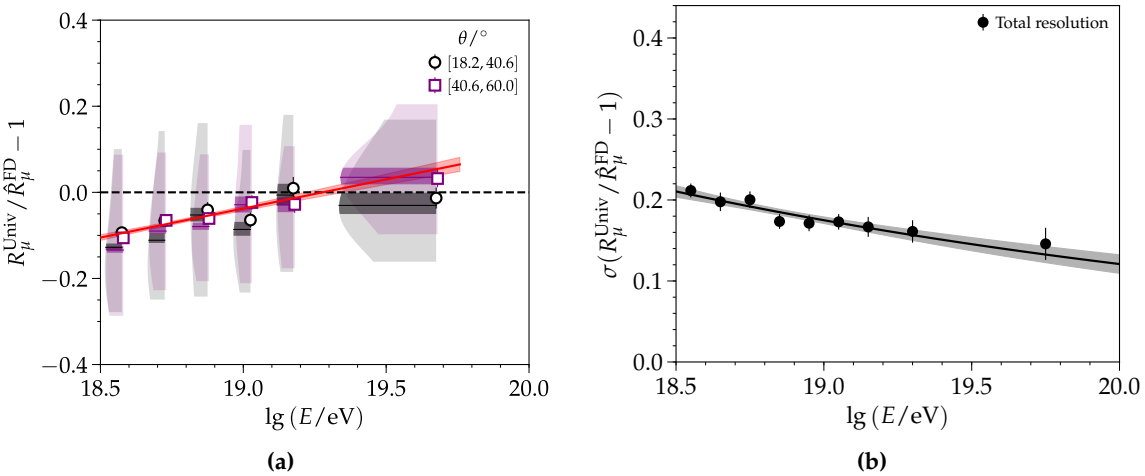

Figure 4.14: The (*left*) bias and (*right*) resolution of the reconstructed relative number of muons is determined for golden hybrid events. As in Fig. 4.13, the fiducial selection for universality is not applied.

and SD-1500 are compatible[24]. The golden hybrid parameterization is used for the bias correction of data with respect to energy.

Similarly, the bias of the relative muon content may also be parameterized. As was done before in Fig. 4.12, the reference value for the relative number of muons will be estimated from the FD using the reconstruction procedure where all values but the core and R_μ are fixed to those reconstructed by the FD[25]. As seen in Fig. 4.14, the bias of the relative muon content is relatively linear and independent of zenith angle. Its resolution as a function of energy is compatible with an exponential fit[26] (though a linear or constant fit would also yield reasonable descriptions). The parameters of the best fits are given in Table 4.5. The parameterization of the R_μ bias suffers from the same zenith selection effect as demonstrated for $X_{\rm max}$. Thus, there might be remaining correlations which are not fully taken into account.

After applying the previous bias corrections, there are still changes in the properties and the detector response of the aging SD stations which need to be accounted for. Event-by event energy differences between the SD-1500 and FD as a function of time was first observed in [168]. While the reasons for these attenuating responses are a topic of ongoing studies, there seems to be correlation with the time periods where the tanks freeze. Initial studies indicate that the reflectivity of the plastic liner holding the water degrades. Other candidates for this attenuating effect on the signal response could result from impurities in the water and/or hardware-associated effects[27].

The variable that best correlates with the aging of the tank is the average area over peak $\langle \text{AoP} \rangle$. This quantity describes the ratio of the area to the peak value in the muon

[24] The values obtained are within the statistical uncertainties of the fits.

[25] The relative number of muons scales not only as a function of energy but also of zenith angle. Ideally, we would be able to compare the $R_\mu^{\rm Univ}$ value to a measured or estimated value that is not potentially truncated by the fiducial selection of the FD. However, at the time of writing this work, there is not a data set existing in Auger where the R_μ is measured for events with zenith angles from 0° to 60° in the energy range considered. Once the universality method is extended to lower energies ($> 10^{17.5}$ eV), the R_μ results may be compared with those found with AMIGA.

[26] The bias and resolution are fit with the same functions found in Eq. (4.5) and Eq. (4.6), respectively.

[27] The effect of the aging of the tanks on energy added as a systematic of the CIC and energy calibration for the SD reconstruction (Chapter 2).

Table 4.5: Parameters for the bias and resolution of the reconstructed R_μ in golden hybrid data.

Bias			
Fit of	χ^2/n_{dof}	a	b
Bias	0.99	-0.102 ± 0.007	0.121 ± 0.016
Resolution	0.50	0.175 ± 0.007	0.371 ± 0.0155

calibration histograms that were mentioned in Section 1.2.1 and are calculated every minute. As seen in Fig. 4.15, the change in the area over peak is representative of a change in the detector response to individual particles as a function of time since a particular tank were first deployed. The average area over peak is calculated by taking the geometrical mean of the area over peak of all stations which triggered for a given event. With increased tank age, there is nearly a linear decrease in the area over peak; essentially, as time passes, signals appear to get more compressed in time, which is only weakly dependent on the zenith angle or primary energy. To quantify the change in the reconstructed quantities with time, profiles of these quantities are studied as a function of the average tank age for all golden hybrid events —where the reference value is $X_{\text{max}}^{\text{FD}}$— and SD-1500 events —where the reference is the mean X_{max}. For the bias of the R_μ, the average relative muon content is used as the reference value[28]. These profiles are fit as a function of

$$\text{Bias}(\langle \text{AoP} \rangle) = a + b \cdot (\langle \text{AoP} \rangle - 3). \tag{4.8}$$

The parameters of the best fits are given in Table 4.6. The slopes of the parameterized biases for X_{max} and R_μ found for the two data sets are compatible (within the uncertainties of their fits). The biases of the X_{max} as a function of average area over peak for the golden hybrid and SD-1500 exhibit minimal dependence on the zenith angle. In contrast, the bias of the relative muon content seen in SD-1500 has a zenith-dependent bias at low values of $\langle \text{AoP} \rangle$ on the order of 9 %, whereas the bias found with the golden hybrid events does not differ with respect to zenith angle bin.

[28] The $\hat{R}_\mu^{\text{FD}}$ comes from a reconstruction where most of the values are fixed to those reconstructed by the FD. This restricts and obfuscates the bias of the R_μ as a function of the average area over peak. Thus, as seen in Fig. 4.14 and Table D.5, $\hat{R}_\mu^{\text{FD}}$ cannot be used to determine the relationship with the average area over peak.

Table 4.6: Parameters for the bias of the reconstructed $X_{\max}$ and R_μ in data as a function of average area over peak.

Bias in $X_{\max}$			
Data set	χ^2/n_{dof}	a	b
golden hybrid	0.8	-6.7 ± 2.0	76.3 ± 11.6
SD-1500	2.0	-3.4 ± 0.4	78.0 ± 2.6

Bias in R_μ			
Data set	χ^2/n_{dof}	a	b
golden hybrid	1.3	-0.0033 ± 0.0041	-0.1130 ± 0.0256
SD-1500	1.9	-0.0045 ± 0.0008	-0.1058 ± 0.0046

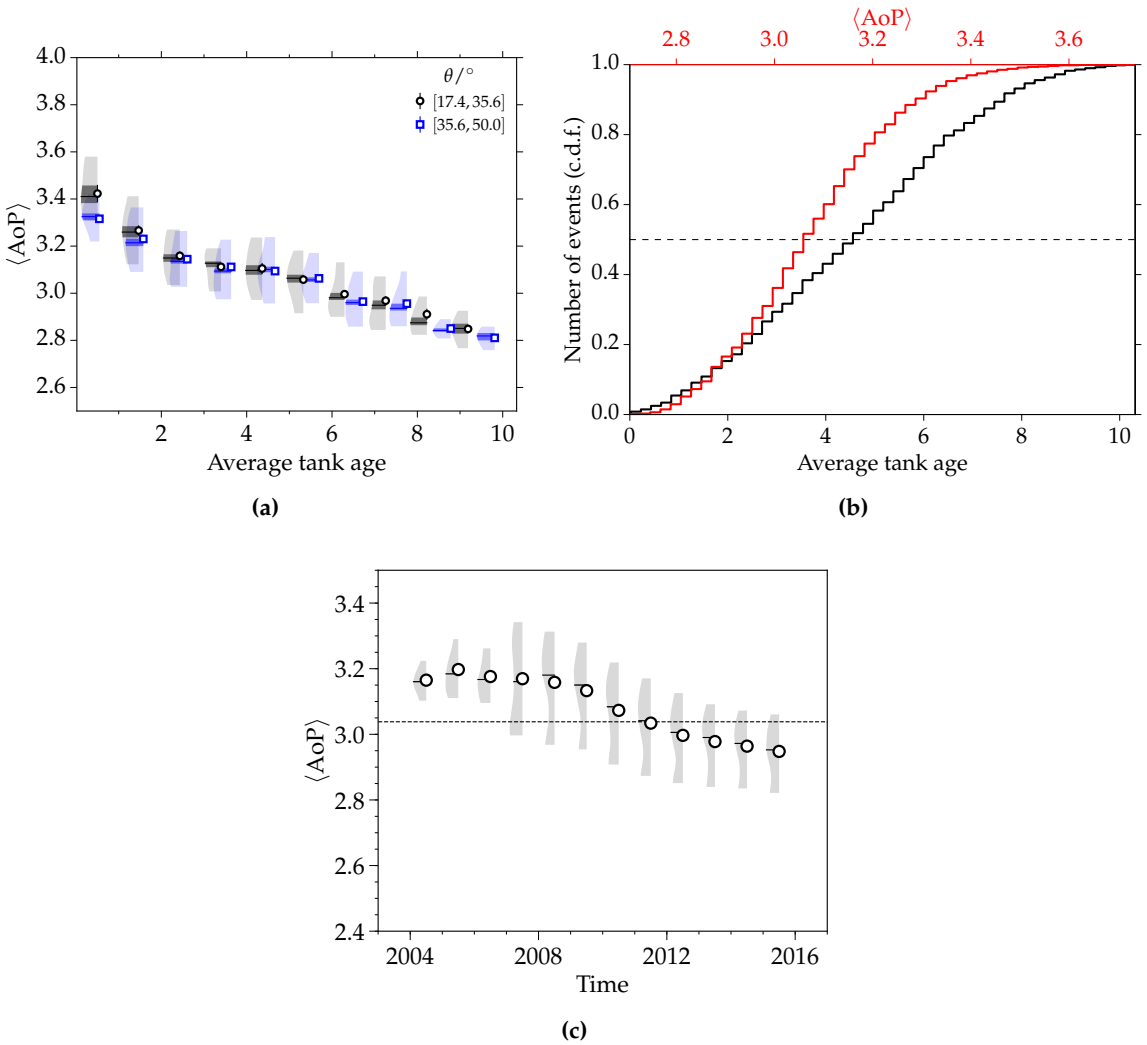

Figure 4.15: (a) The average area over peak as a function of the average tank age and zenith angle [108]. (b) The integrated histogram (c.d.f.) of the number of events as a function of average tank age and area over peak [108]. (c) While most of the construction of the SD-1500 occurred from 2004-2008, stations are occasionally replaced or added. As such, the change in the average area over peak correlates with year (this work).

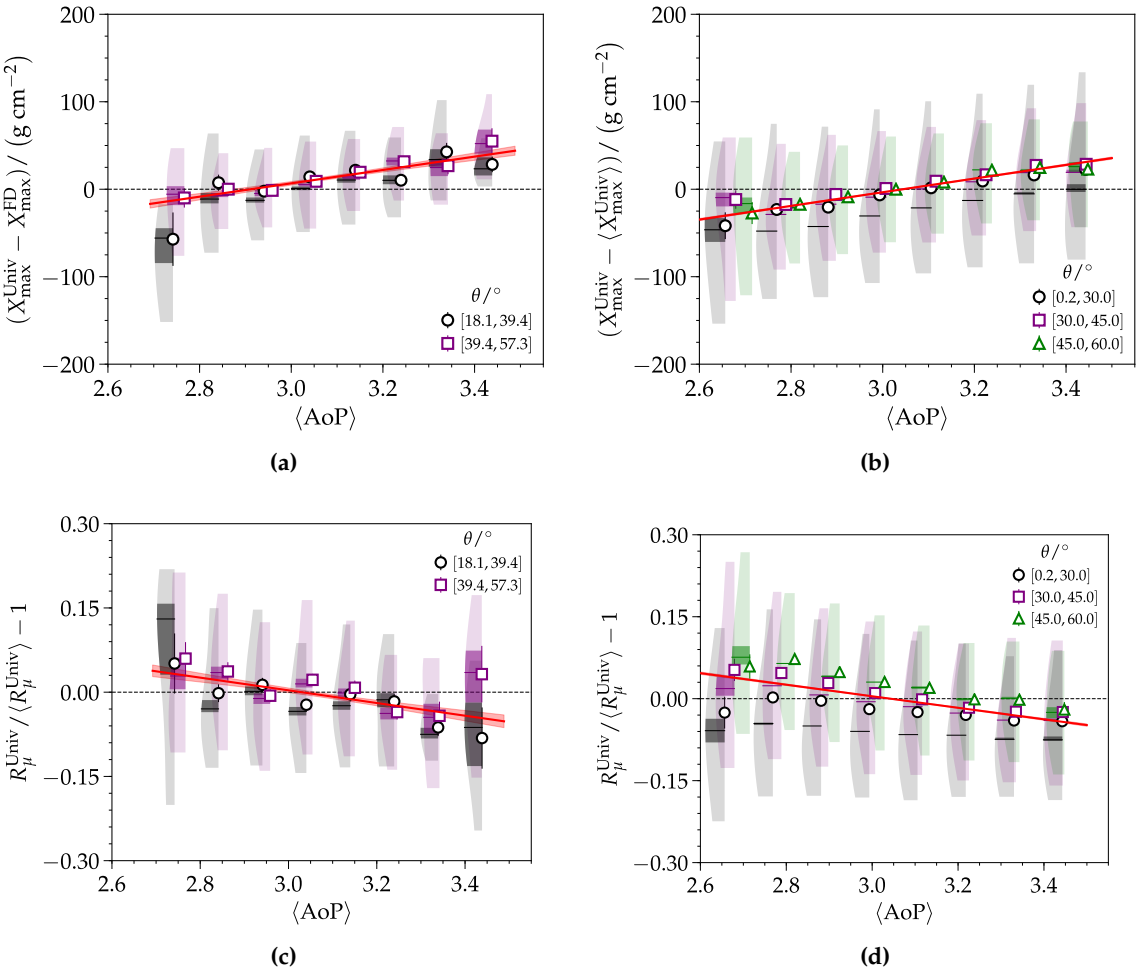

Figure 4.16: The bias of the (*top*) depth of the shower maximum (*bottom*) and relative muon content as functions of average area over peak. The biases are fit for (*left*) golden hybrid and (*right*) SD-1500 events.

CHAPTER 5

Mass composition

In the previous chapters, the reconstruction of individual events and an estimate of their mass-sensitive parameters was quantitatively described with much detail. The determination of the mass composition of ultra-high energy cosmic rays (UHECRs) is one of the foremost pursuits in astroparticle physics. The low flux of particles at the highest energies necessitates the detection of these particles through the extensive air showers that they induce in Earth's atmosphere. The mass composition is then inferred from the macroscopic properties of an *extensive air shower* (EAS) when it is observed by a large-scale detector —like Auger— and can no longer be estimated for each event. Instead, the composition is deduced statistically from an ensemble of measured air showers.

As UHECRs traverse the Universe, they interact with and are deflected by magnetic fields. The amount of deflection as well as the other ensuing interactions depend on the atomic mass A and charge Z of the nuclei and the primary energy. By identifying the nuclei that induced an extensive air shower, it may be back-tracked by applying the reverse deflections to arrive at its origin. Thus, the exact knowledge of the composition at the highest energies is needed to find cosmic accelerators, elucidate the acceleration mechanisms required for the corresponding UHECRs, and better inform galactic and extragalactic propagation models[1].

As discussed in Section 1.1.3.2, the depth of the electromagnetic shower maximum X_{max} is correlated with the primary mass A ($X_{\mathrm{max}} \propto \ln A$). The FD of Auger measures the longitudinal depth of the shower, from which the X_{max} may be directly fit [33, 99, 104, 140]. The FD measurement of the X_{max} is reliable and mostly model-independent; at the highest energies, the resolution is on the order of $15\,\mathrm{g\,cm^{-2}}$. Nevertheless, the FD has a limited duty cycle of 15 %. With the flux of data following an $E^{-2.5}$ distribution with respect to energy, the number of events are too few above an energy of $10^{19.5}$ eV to accurately determine the mass composition.

With a duty cycle of nearly 100 %, the SD-1500 data —in combination with the universality method— is used to infer information on the primary mass of measured UHECRs. As universality exploits the underlying physical phenomenon of an EAS, we have immediate access to two mass-sensitive variables derived from shower components: the X_{max} and the relative number of muons (R_μ) from the muonic development. The first two moments of the X_{max} distribution (Section 5.2.1, Section 5.2.2) are obtained from SD-1500 and are found to be in good agreement with the results of the FD. The average relative muon content as

[1] These include the magnetic fields and particle densities in interstellar space.

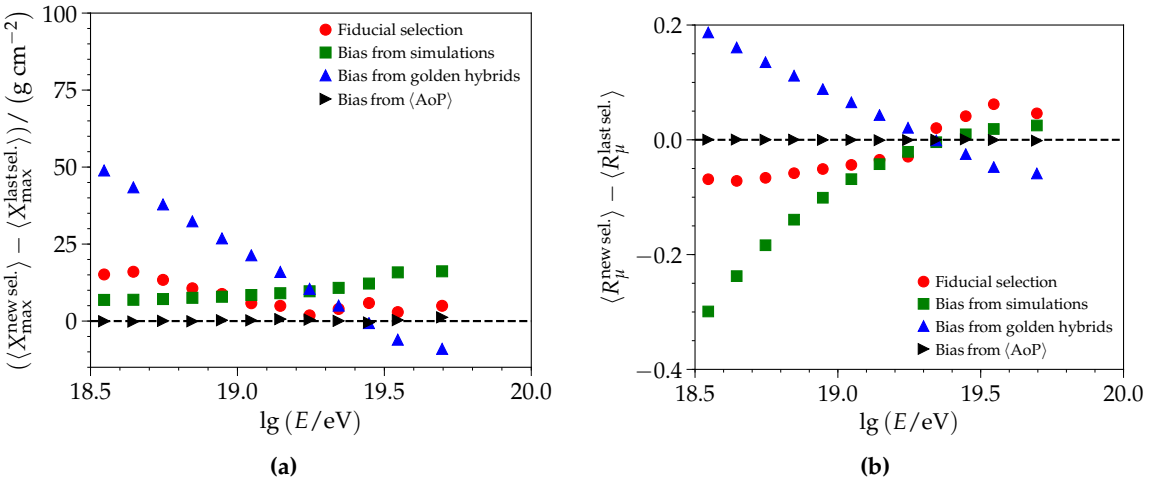

Figure 5.1: The change in the mean reconstructed (a) depth of the shower maximum and (b) relative muon content compared to the mean values obtained with the previous selection. Above an energy of $10^{19.3}$ eV, the bias correction from golden hybrids partially cancels the bias correction obtained from simulations. Similarly, the fiducial selection above this energy threshold affects the results of the mean by less than $10\,\mathrm{g\,cm^{-2}}$ and 0.1 , respectively.

a function of energy (Section 5.2.3) is also presented. To better deduce the implications of the mass composition, the average logarithmic mass $\ln A$ (Section 5.2.4) is derived using the mean X_{max} results and the superposition model. Finally, in Section 5.3, the shape of the distribution of X_{max} is fit with Monte Carlo templates for certain primaries to infer the composition. This study maximizes the information used and helps to reduce degeneracies that occur when only considering the moments.

5.1 Event selection and systematic effects

The event selection and corrections needed for mass composition studies were derived in Chapter 4. In the analyses presented hereon, SD-1500 data from 1. January 2004 to 31. December 2016 is studied. The following parameterizations have been applied to the data used throughout this chapter:

- the fiducial selection in zenith angle to reject the zenith ranges in which the average X_{max} deviates by more than $20\,\mathrm{g\,cm^{-2}}$ from its unbiased value in a given energy bin.
- the average bias of proton- and iron-induced simulations with QGSJET-II.04 as a function of energy, which is used as an initial bias correction for data due to the exhibited non-linear shape.
- the bias of data as a function of energy for SD-1500 events to correct for the differing muonic content between simulations and data.
- the bias of data as a function of average area over peak to correct for the effect of the aging SD stations on reconstructed variables.

Due to the inherent uncertainties of the first two selection methods, systematic uncertainties are assumed on the order of half of the correcting factors as a function of energy. To get an idea of how the reconstructed values change with each modification, the mean values as a function of energy are compared for each successive selection/correction in Fig. 5.1. The

Table 5.1: Average systematic uncertainty for each selection and correction applied.

	$X_{\max}$ / g cm^{-2}	R_μ
Fiducial selection	3.8	0.02
Bias from simulations	5.3	0.04
Remaining zenith bias	10.0	0.04
Total	11.9	0.06

modifications are listed in the legend in the order in which they are applied[2]. In the case of the correction due to the bias in simulations, the mean of this population is compared to the mean of the previous selection —the fiducial selection. The evolutions of the mean $X_{\max}$ and R_μ after applying these changes show that the corrections mostly affect events below 10^{19} eV. For both reconstructed variables, the average area over peak correction does not affect the average values as a function of energy; as such, it does not need to be considered in the calculation of the overall systematic uncertainties. After all the selection and corrections are applied, there is nearly a 20 g cm^{-2} and 5 % difference in the mean $X_{\max}$ and R_μ, respectively, as a function of zenith angle (as observed in simulations, Fig. 4.9). Again, half of this value[3] will be taken as a systematic uncertainty. The average systematic uncertainty for each modification is given in Table 5.1 and added in quadrature to obtain the average total systematic uncertainty. Additional systematic studies are performed for the reconstructed shower maximum and relative muon content in Fig. 5.2 and Fig. 5.3, respectively. The average reconstructed variables are considered as functions of time, day of the year, average area over peak, and azimuth[4]. There is a yearly modulation of ± 10 g cm^{-2} in the mean $X_{\max}$. This results from the average change of atmospheric parameters and the subsequent influence of these parameters on the longitudinal development of showers (and, thus, the average depth of the shower maximum). This could potentially be parameterized and corrected for in future analyses. The variation of the $X_{\max}$ with absolute time and average area over peak are within 4 g cm^{-2}. This is a residual effect due to the aging of the SD stations. Without the average area over peak correction (Section 4.3.2), the deviation of the mean $X_{\max}$ with respect to absolute time is on the order of 20 g cm^{-2}. A dependence on the azimuth angle is within 2 g cm^{-2}.

The yearly modulation of the relative muon content is on the order of 0.2, which is roughly a 10 % change. There is residual dependence of R_μ as a function of absolute year and time that is mostly corrected for and less than 0.1 on average. However, there are a few large deviations in the last few years. Perhaps if the bias as a function of average area over peak could be fit with a more relaxed FD selection then the relationship might be better described. In comparing an estimated bias correction using SD-1500 data (Fig. 4.16), there appears to be a zenith-dependence at low values of area over peak. This might be remedied by fitting the average bias of R_μ as a function of zenith angle prior to performing the parameterization for the average area of peak.

[2]For the overall effect of the modifications, see Fig. D.45.

[3]For the R_μ systematic uncertainties, the relative difference of 5 % is converted into the units of R_μ by applying the correction to all data and comparing it to the original value.

[4]Because of the fiducial selection in zenith angle that evolves with energy, a simple, direct comparison is not possible. Instead, the remaining dependencies would need to be scrutinized in bins of energy.

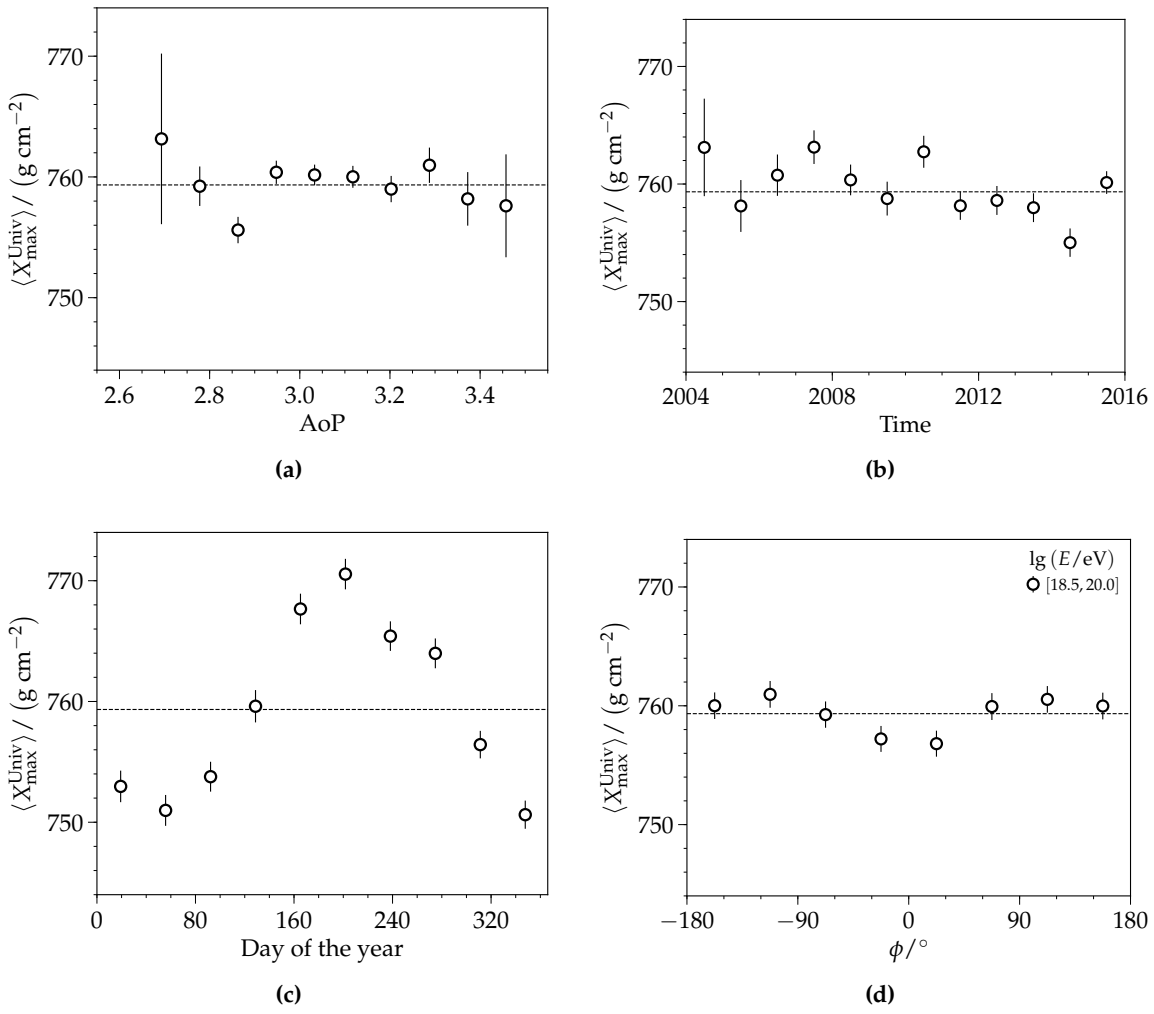

Figure 5.2: Systematic study of the change of the average reconstructed depth of shower maximum with average area of peak, time, day of the year, and azimuth.

5.2 Moment-based analysis methods

5.2.1 Average depth of the shower maximum

The first central moment of the reconstructed depth of the shower maximum is used to infer the average composition as a function of energy. Profiles of the average shower maximum reconstructed with universality are depicted in Fig. 5.4. The error bars, which are mostly smaller than the size of the markers, indicate the statistical uncertainties. Systematic uncertainties are marked with brackets. Data is compared to the average proton and iron values predicted from several contemporary hadronic interaction models: QGSJET-II.04, EPOS-LHC, SIBYLL-2.3[5]. Within the given uncertainties, the results from universality are compatible with the average measured by the Auger FD (green points). The number of events in each energy bin are given for the FD (green text) and universality (black text). Depending on the energy bin considered, the universality method has roughly four to twenty times the number of events as that in the FD.

[5]These were each tuned with data from the LHC run where the center-of-mass energy was 7 TeV.

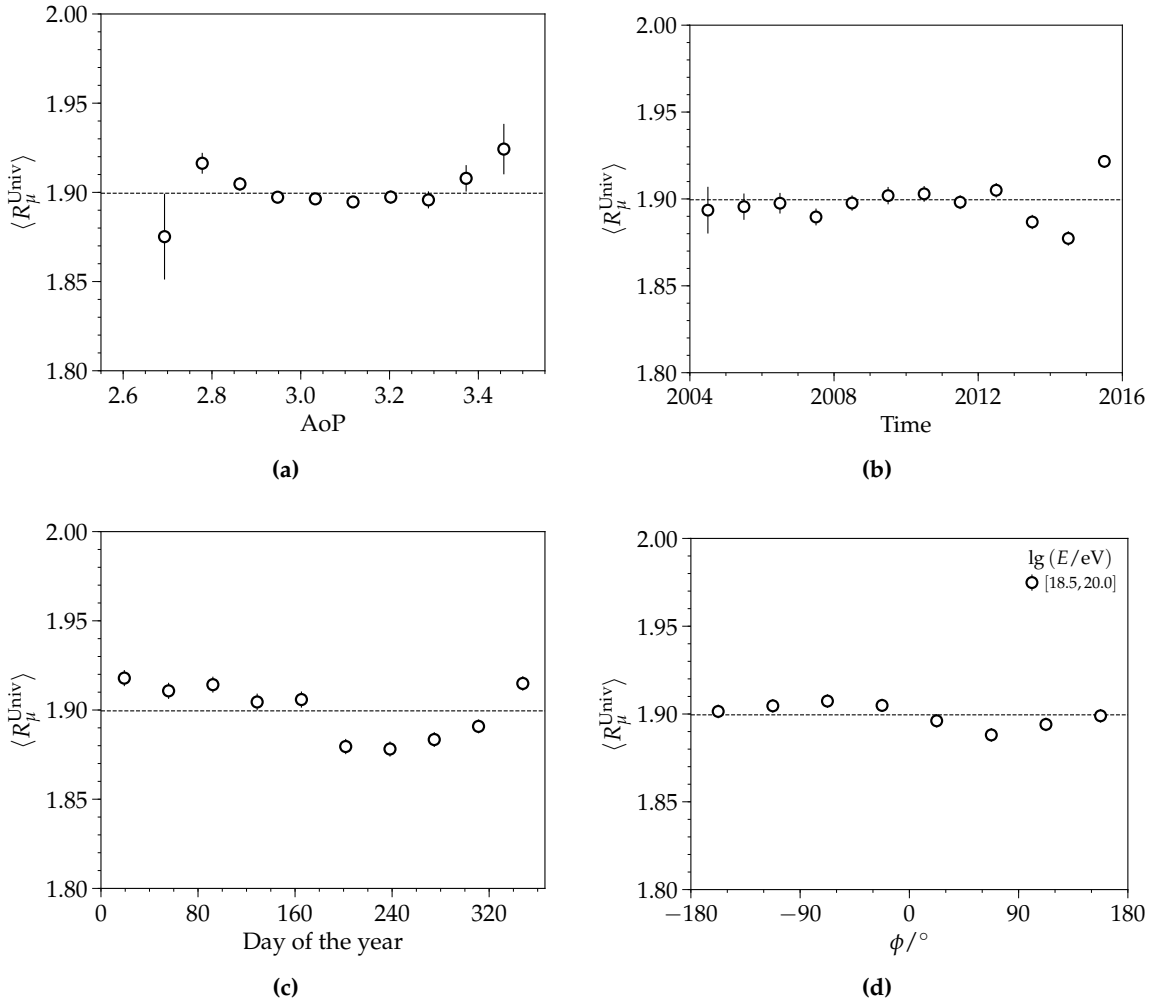

Figure 5.3: Systematic study of the change of the average reconstructed relative muon content with average area of peak, time, day of the year, and azimuth.

The changing ratio between the number of events for the FD and universality approach in a given bin is only partially due to the fiducial selection. Instead, the number reduces as the probability of a station saturating[6] exceeds 50 % at the highest energies. For most of the analyses throughout this work, only non-saturated events are considered. This is because saturated events have truncated traces which only allow for a partial fit of the shape fit term for the negative log-likelihood (Fig. 3.14c). In the reconstruction methods used in the past, events with saturated stations were poorly reconstructed, resulting in a diffuse X_{max} distribution. Preliminary results in Fig. D.11 indicate that saturated events reconstructed with the constrained axis method have a resolution that is within $10\,\mathrm{g\,cm^{-2}}$ of that obtained for non-saturated events[7] While the quality selections and corrections derived throughout this work are tuned for non-saturated events, they are applied in Fig. 5.4b for saturated events. Above an energy of $10^{19}\,\mathrm{eV}$, the profiles of saturated events are within $10\,\mathrm{g\,cm^{-2}}$,

[6]For further discussions on what causes saturation of a PMT, see Section 1.2.1 and Section 2.3.2. A detailed analysis was performed for this work where the probability of saturation was considered as a function of primary energy, zenith angle, and radius (Appendix D.2).

[7]For comparison, the global reconstruction has a difference in the resolution between saturated and non-saturated events that exceeds $30\,\mathrm{g\,cm^{-2}}$ for energies below $10^{19.3}\,\mathrm{eV}$. The minimal difference between the resolution of saturated and non-saturated events for the iterative method is $30\,\mathrm{g\,cm^{-2}}$.

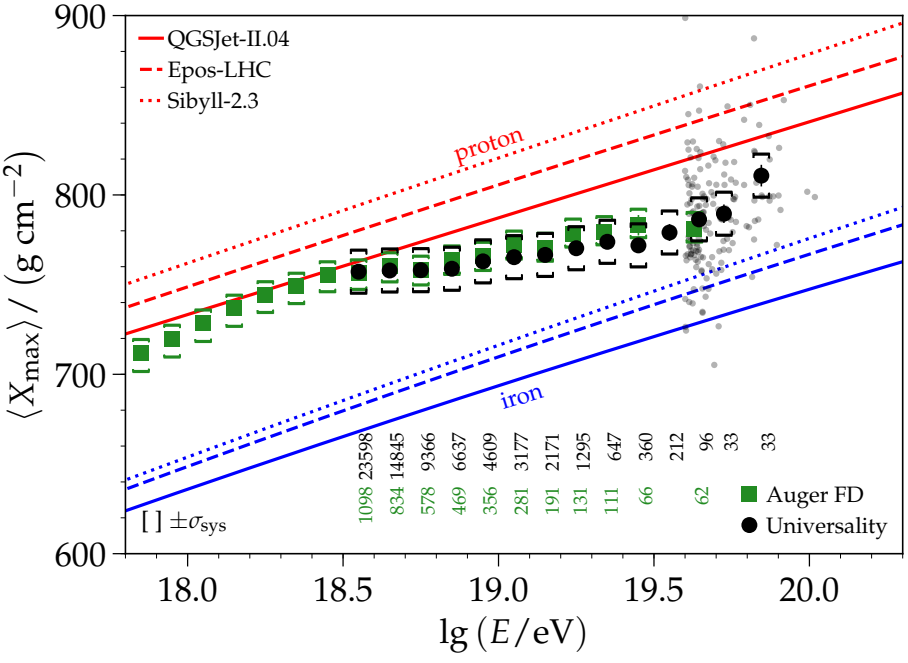

(a)

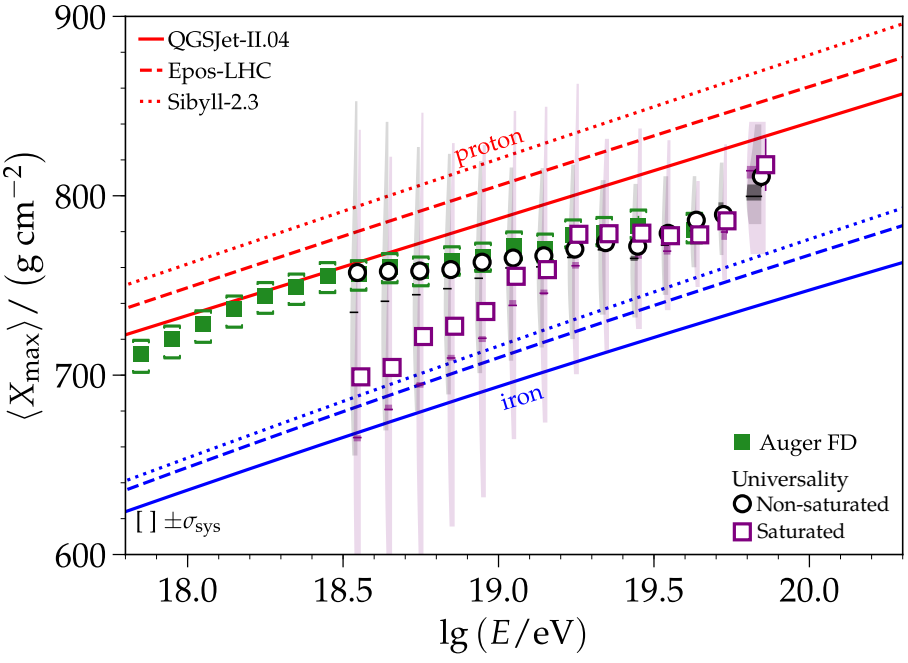

(b)

Figure 5.4: (a) Profiles of the average reconstructed depth of the shower maximum with statistical and systematic uncertainties. Individual points (gray) contributing to the three bins at the highest energies are depicted with dots. Recent results as measured by the Auger FD are shown with the green rectangles ([104]). (b) The mean X_{max} for non-saturated events (also used in (a)) are compared to violin profiles of saturated events.

and the resolution of saturated events is larger than that of the non-saturated population by less than $20\,\mathrm{g\,cm^{-2}}$ at the highest energies. Below an energy of 10^{19} eV, the means and medians of the violin profiles for saturated events greatly differ from those of the non-saturated population. Due to the complicated underlying distributions of saturated events, detailed studies would need to be performed to ensure that an event selection tailored to it was unbiased. With the addition of a small PMT and a scintillator for each station (the Auger Upgrade, Section 1.2.6), further information about the response of the particle components will help us to better understand saturation and, hopefully, successfully (and retroactively) recover these events. Additionally, a re-parameterization of the universality approach to lower energies and the proper calculation of the uncertainties used in the shape fit could help remedy the large systematic biases seen with saturated events. Based on these large differences of the bias, non-saturated events will exclusively used throughout the remainder of this work. The exclusion of saturated events does not significantly bias the mass composition. As seen in Fig. D.7 and throughout Appendix D.2, the probability of saturation is mostly independent of the primary and instead relies on the geometry of the air shower in relation to the hottest station (e.g. the core of the shower landing very close to a station causes the observed signals to saturate).

A fit to the $\langle X_{\mathrm{max}}^{\mathrm{Univ}} \rangle$ mean profile was attempted with a linear model. The resulting best fit of the data was found to be[8]

$$\langle X_{\mathrm{max}} \rangle (\lg E) = (764.7 \pm 0.4) + (21.5 \pm 1.3)(\lg E - 19), \tag{5.1}$$

which had a poor χ^2/n_{dof} of around 4.2. A better fit with a χ^2/n_{dof} = 2.5 was achieved with a fit to a broken line. Both fits are shown in Fig. 5.5. The break point in energy is fit to $\lg(E_{\mathrm{ref}}/\mathrm{eV}) = 19.21 \pm 0.06$, which is indicated with a magenta hexagon. Below E_{ref}, the elongation rate $D_{10} = \frac{\mathrm{d}\langle X_{\mathrm{max}} \rangle}{\mathrm{d}\lg E}$ is[9]

$$D_{10} = (15 \pm 2)\,\mathrm{g\,cm^{-2}}, \tag{5.2}$$

and above E_{ref}:

$$D_{10} = (45 \pm 6)\,\mathrm{g\,cm^{-2}}. \tag{5.3}$$

To better visualize the break in the plot, the model prior to the break is continued as a dashed line. To note, contemporary air shower simulations predict elongation rates for a constant composition in the range from $54\,\mathrm{g\,cm^{-2}}$ to $64\,\mathrm{g\,cm^{-2}}$. Thus, the results of this work indicate a mixed composition of UHECRs, which becomes heavier above an energy of 3×10^{18} eV. The change in the elongation rate after the break point trends to lighter elements. The distance of the last data points (above $10^{19.76}$ eV) from the linear model is on the order of $30\,\mathrm{g\,cm^{-2}}$. As shown in Fig. D.45, the overall shift in the X_{max} when applying the quality selections is greatest for the lowest energies, and at energies above $10^{19.5}$ eV, the shift is around $15\,\mathrm{g\,cm^{-2}}$. The distance of the last data point to the elongation model for the FD in units of statistical uncertainty is $3.3\,\sigma$. In also taking the systematic uncertainty into account, the significance is reduced to $1.5\,\sigma$. The distance of the last data point to the lower line from the broken fit in units of statistical uncertainty is $5.4\,\sigma$, which is lessened to $2.4\,\sigma$ when the systematic uncertainties are also considered. Based upon this, while there is an indication towards lighter elements at the highest energies, this result has not yet reached the threshold to be statistically significant with the current number of events and systematic uncertainties. A table of the results of the first two central moments of the universality X_{max} together with statistical and systematic uncertainties is included in Appendix C.3.

[8] For simplicity, equations are written such that the units are implied. Anytime X_{max} is in an equation the implied units are $\mathrm{g\,cm^{-2}}$. Similarly, $\lg E$ represents $\lg(E/\mathrm{eV})$

[9] The intercept of the line is found to be $(768 \pm 1)\,\mathrm{g\,cm^{-2}}$, as calculated at the break point.

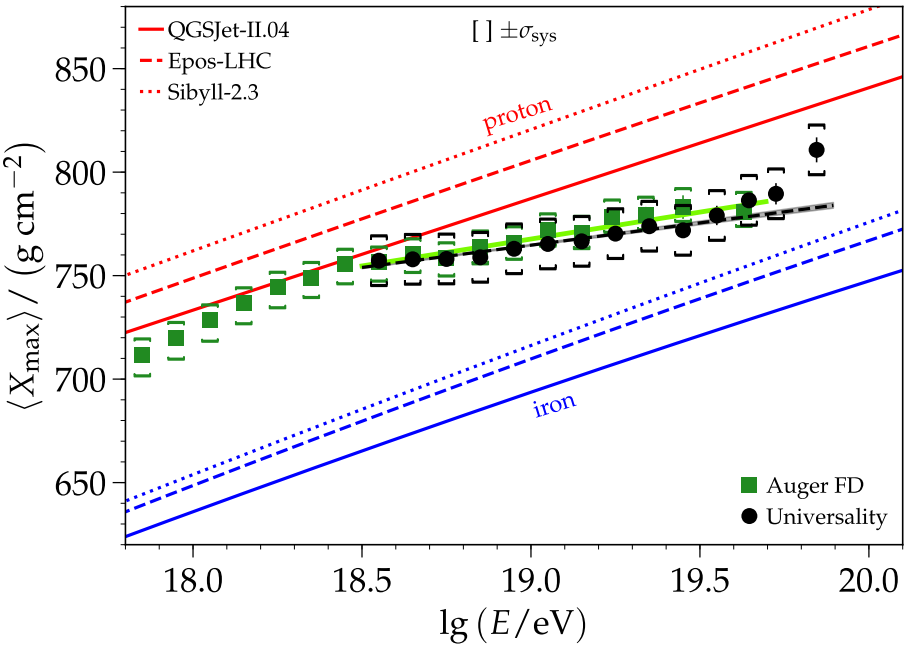

(a)

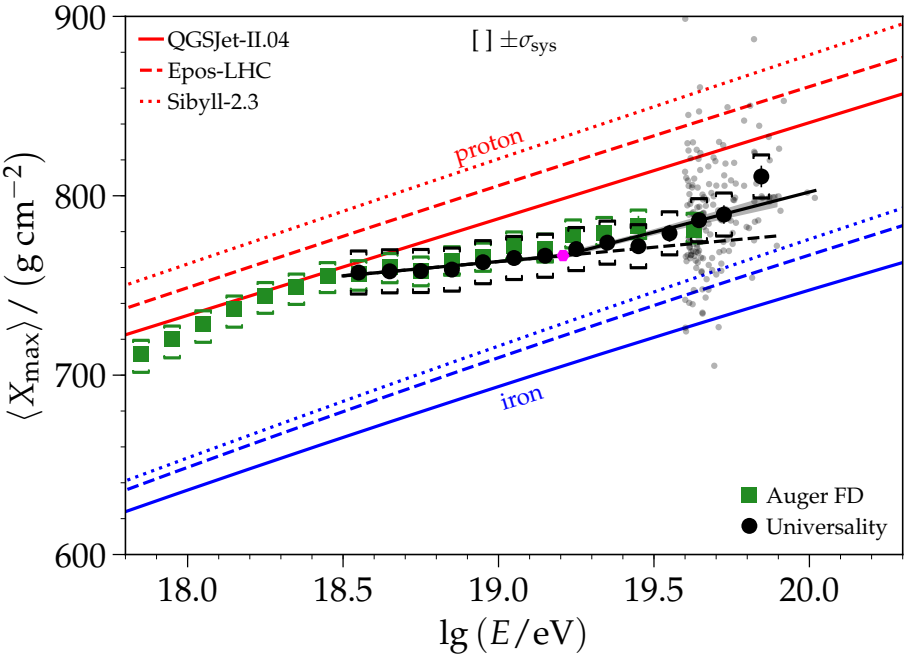

(b)

Figure 5.5: Fit of $X_{\max}$ elongation rate with (a) a line and a (b) broken line. The elongation rate of the FD as given in Eq. (4.7) is shown with the lime green line. The FD results maximally differ from the linear fit of universality data by $5\,\mathrm{g\,cm^{-2}}$ at an energy of $10^{19.5}\,\mathrm{eV}$.

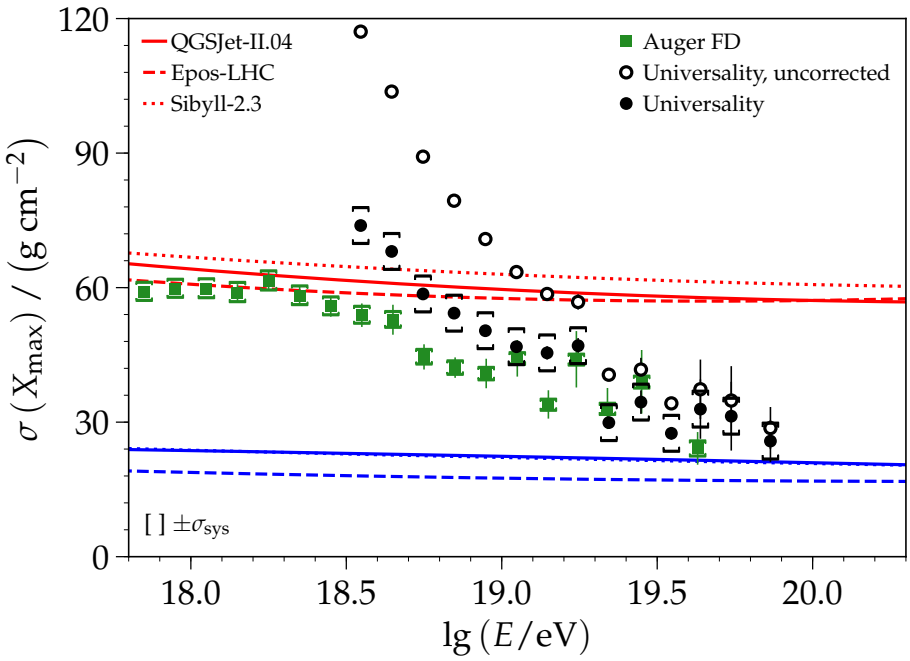

Figure 5.6: Evolution of $\sigma(X_{\max})$ as a function of energy. The uncorrected fluctuations — corresponding to the raw second moment of $X_{\max}$ are shown as a function of energy. To arrive at the physical fluctuations of $X_{\max}$, the detector resolution model —derived from golden hybrids— is subtracted from the fluctuations in quadrature. The results from the Auger FD and expectations from simulations using modern hadronic interaction models are included.

5.2.2 Fluctuations of the depth of shower maximum

The second central moment of the shower maximum distribution allows for conclusions to be drawn about the physical fluctuations of $X_{\max}$. The comparison of the results to the predictions of proton- and iron-induced air shower simulations enables conclusions to be drawn about the mass composition. The total reconstructed resolution is the quadratic sum of the physical fluctuations from the shower development and the detector resolution due to sampling fluctuations

$$\sigma^2_{\text{tot}}(E) = \sigma^2_{\text{phys}}(E) + \sigma^2_{\text{det}}(E)\,. \tag{5.4}$$

The detector resolution of universality results from the sampling fluctuations in the SD measurement of the signals. To quantify this value, golden hybrid events were used in Section 4.3.2. The resolution is extracted from the standard deviation of the difference in the reconstructed values of the depth of the shower maximum ($\sigma(X^{\text{Univ}}_{\max} - X^{\text{FD}}_{\max})$). As shown in Fig. 4.13, the much smaller FD resolution (black dashed line) is quadratically subtracted from the total resolution to yield the resolution for the SD. An exponential equation, given in Eq. (4.6), was fit[10]. Due to the low number of events at the highest energies, the model is extrapolated above an energy of $10^{19.5}$ eV. The model of the detector resolution drops from 110 g cm^{-2} at 3×10^{18} eV to less than 20 g cm^{-2} at the highest energies. As illustrated in Fig. 4.12, the shape of the total resolution is similar to that found with air shower simulations, yet its fluctuations are due to the evolving mass composition of the measured UHECRs.

The second central moment of $X_{\max}$ is corrected for using the derived detector resolution. The results before and after the correction are depicted in Fig. 5.6. For comparison, recent results from the Auger fluorescence detector are provided [104]. Above an energy of 10^{19} eV,

[10] The parameters are given in Table 4.4.

the corrected universality results agree well with the measurements of the FD. However, below this energy, the values of the second central moment are larger than those obtained by proton-induced air showers. To understand this deviation better, the resolution of SD-1500 data was estimated by comparing the reconstructed X_{max} to the elongation rate model of the FD (Fig. 4.13). In contrast to the golden hybrid-derived model, the parameterization based on the SD-1500 starts at an energy of 3×10^{18} eV with $130\,\mathrm{g\,cm^{-2}}$ to arrive at a value close to $20\,\mathrm{g\,cm^{-2}}$ at the highest energies. In scrutinizing the golden hybrid resolution further, it is seen that the values in the last two energy bins are about the same value. As such, it may be surmised that the detector resolution employed for the correction of the second central moment of X_{max} is likely underestimated below energies of 10^{19} eV. This may arise from the zenith-dependent spread of the bias (Fig. 4.9). When this is not corrected for, the resolution derived from golden hybrids will be underestimated, particularly at the lowest energies due to the different underlying distribution in zenith angle. While such a spread may easily be added to the systematic uncertainties of the average X_{max}, it is more complicated to correct for or include it for the second moment of X_{max} —a posteriori.

5.2.3 Average relative muon content

Profiles and violins of the average relative muon content reconstructed with universality are depicted in Fig. 5.8. Like the moments of the reconstructed depth of the shower maximum, the average of the relative muon content can be used to infer the average composition as a function of energy. However, as seen in the figure, the average R_μ is 1.876 ± 0.005 is, at the lowest energies, on the edge of the estimates from iron-induced showers and evolves with energy to exceed the predictions of any simulation. While these contemporary hadronic interaction models predict more muons than their predecessors, the muon excess in data is still on the order of 20 % to 60 %, depending on the considered hadronic interaction model[11]. Due to the current mismatch between the relative muon content of simulations and data, it is difficult to draw concrete conclusions on the trends with respect to the average composition. Above an energy of $10^{19.3}$ eV, the average relative muon trends towards heavier elements. This continues until around $10^{19.7}$ eV, where the trend begins to favor a lighter mass composition. A more detailed study of this evolution and that of the fluctuations of the relative muon content are not in the scope of this thesis. It is something that would be good to look into in future analyses. The average values of the relative muon content are recorded in a table in Appendix C.3.

5.2.4 Estimation of the logarithmic mass

To better infer the mass composition, the superposition model of air showers may be used to formulate linear dependencies based on the average value of a variable to derive the logarithmic mass as a function of energy. Of the mass-sensitive observables considered thus far, the average depth of the shower maximum is the easiest of the two to use in such a study, as it already lies between the predictions for proton and iron-induced showers of the different hadronic interaction models. The calculation of the logarithmic mass is based on the generalized Heitler model of air showers (Section 1.1.2). The extension of this model for the determination of the mean X_{max} for an energy E and primary mass A was given in Section 1.1.3.2 (from [39]). For the explicit derivation of the function, it is restated here as

$$\langle X_{\mathrm{max}}\rangle = X_0 + D\lg\left(\frac{E}{E_0 A}\right) + \xi\ln A + \delta\ln A\lg\left(\frac{E}{E_0}\right). \tag{5.5}$$

[11] These particular values were determined in external analyses described in Section 1.2.7.

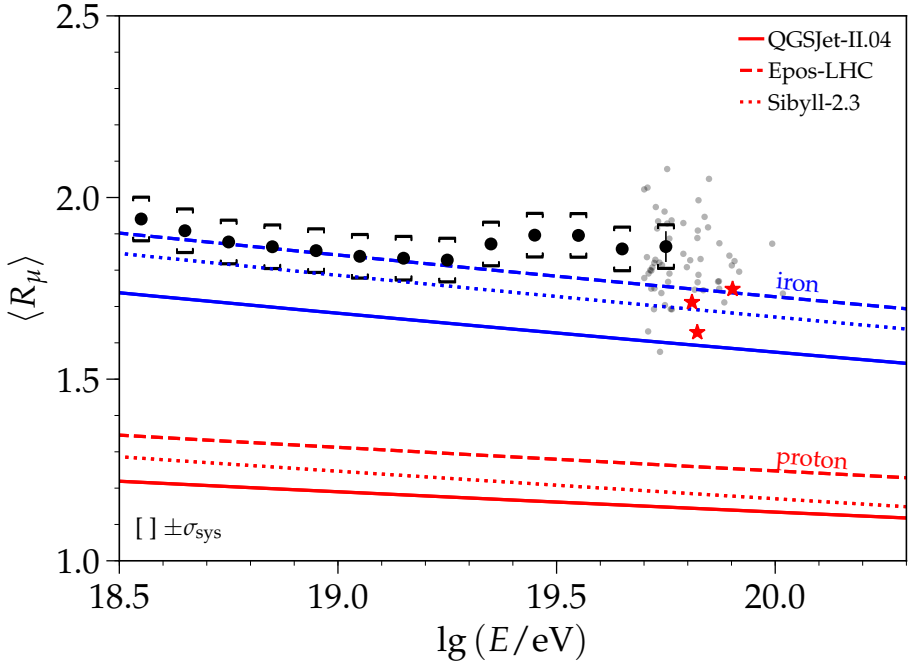

(a)

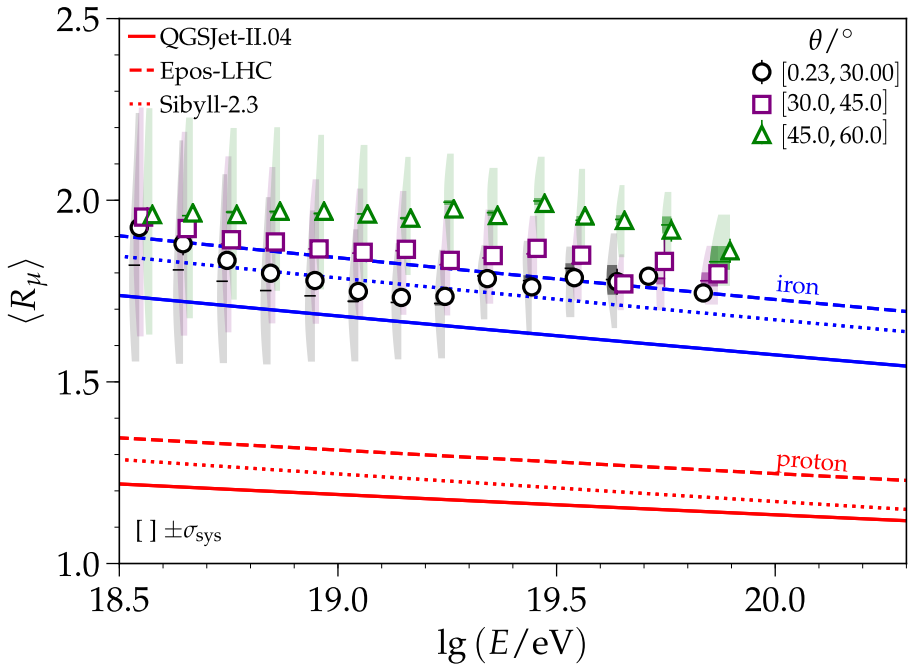

(b)

Figure 5.7: (a) Profiles of the average reconstructed relative muon content. The individual events contributing to the three highest energy bins are shown with the gray points. The red stars are three of the points from the mean depth of the shower maximum plot which have reconstructed $X_{\max}$ values exceeding the predicted value for QGSJET-II.04 proton-induced simulations and a zenith angle around 35°. (b) The violins of the average relative muon content are considered as a function of energy and zenith angle.

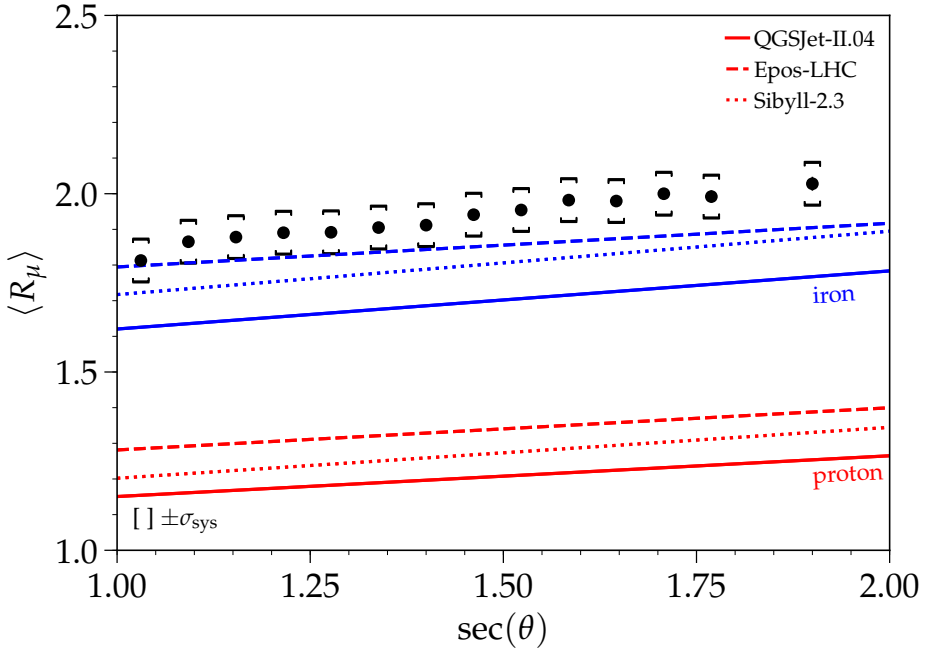

(a)

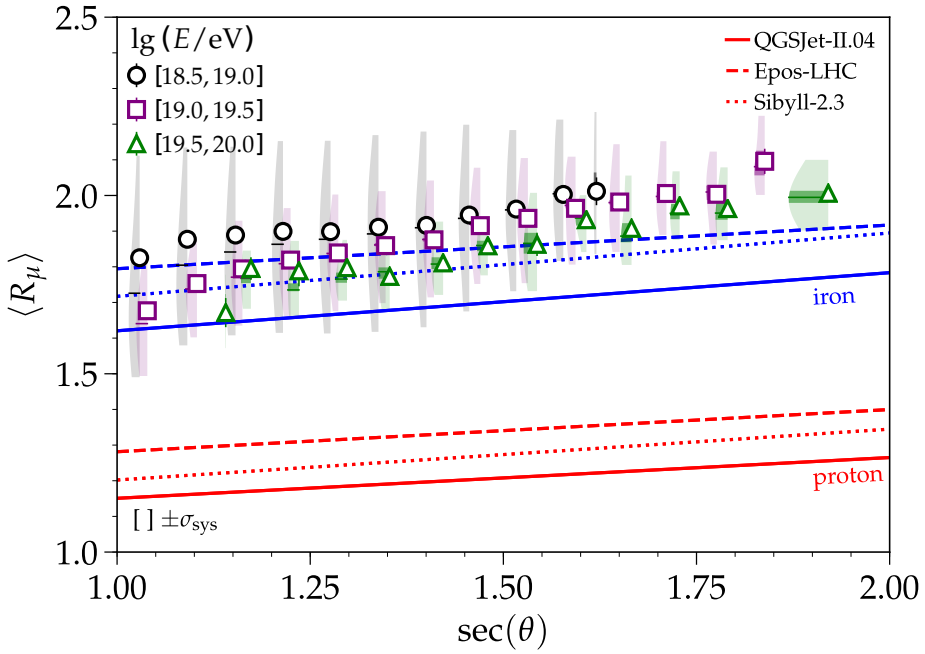

(b)

Figure 5.8: (a) The average relative muon content is shown as a function of the secant of the zenith angle; this is compared to hadronic model lines associated with an energy of 10^{19} eV. (b) By inspecting the average trend in three energy bins, the dependence of the relative muon content as a function of sec θ is shown to be mostly linear.

where X_0 is the mean depth of proton showers at an energy of E_0 and D is the elongation rate —the change of $\langle X_{\max} \rangle$ per decade in energy, and ξ and δ encapsulate deviations from the ideal superposition model. The parameters ξ and δ are calculated for each interaction model and stated in [39, 169]). In order to estimate the mean logarithmic mass from the average depth of the shower maximum, Eq. (5.5) is inverted to solve for $\ln A$. The resulting equation [39, 169] is

$$\langle \ln A \rangle = \frac{\langle X_{\max} \rangle - \langle X_{\max} \rangle_p}{f_E}, \tag{5.6}$$

with

$$f_E = \xi - \frac{D}{\ln 10} + \delta \lg \left(\frac{E}{E_0} \right). \tag{5.7}$$

$\langle X_{\max} \rangle_p$ is the average $X_{\max}$ of proton-induced air showers. The $\langle \ln A \rangle$ as a function of energy for the universality measurement are shown in Fig. 5.9 for QGSJET-II.04 and EPOS-LHC. For the calculation, the average $X_{\max}$ as presented in Section 5.2.1 is used. Recent results from the Auger FD [104] are also presented for comparison. Out of the two interaction models considered, the average composition predicted is heavier for EPOS-LHC. In the results using QGSJET-II.04, the average logarithmic mass does not go beyond the mass of nitrogen. The results from the FD and universality are in good agreement. As expected from the mean $X_{\max}$ studies, there is a change in mass composition for the universality results above an energy of $10^{19.5}$ eV with a trend towards a lighter composition.

5.3 Distribution-based analysis method

In the various mass composition studies presented thus far, the analyses rely on certain statistical moments of the data (e.g. the mean and dispersion, as pursued in Section 5.2). While providing insight into the composition, these methods intrinsically reduce the wealth of information provided to us through the full distributions of the measurements. To overcome this, one can fully employ the distributions of simulations to fit and constrain the nuclear fractions present in data. This method can be applied to both the $X_{\max}$ and R_μ distributions separately and coincidentally. In this thesis, only the 1-dimensional case of the $X_{\max}$ is considered.

Due to the changing nature of the mass composition with respect to energy, the events are binned in intervals of 0.1 in $\lg(E/\text{eV})$ from $10^{18.5}$ to $10^{19.7}$ eV and grouped into a single bin for events with energies greater than $10^{19.7}$ eV[12]. The number of events for each energy bin for both the universality approach and FD results may be found directly in Fig. 5.4a. To then utilize the $X_{\max}$ distribution for the mass composition fit, we divide the events into bins with a width of $20\,\text{g}\,\text{cm}^{-2}$.

For the comparison of simulations with data, *Monte Carlo* (MC) templates are needed, which consist of distributions that assign—given a primary energy, depth of the shower maximum, and primary composition— a probability of observing the given $X_{\max}$. Such simulation templates are found in [170, 171] for QGSJET-II.04, EPOS-LHC, SIBYLL-2.3, and other interaction models. To render the template of a given nuclear species s comparable with data, it must first be convolved with Gaussian distributions to take into account realistic detector effects

$$p(X^m_{s,j}) = \sum_k^\infty p_k(X^t_{s,k}) \cdot N(X_k, \sigma^2_k), \tag{5.8}$$

where $p(X^m_{s,j})$ is the smeared probability for $X_{\max}$ in the jth $X_{\max}$ bin, $p_k(X^t_{s,k})$ is the unsmeared MC template, X_k is the $X_{\max}$ bin center evaluated for each of the j bins and acts as

[12] For the FD results, all events above $10^{19.5}$ eV are grouped in one bin.

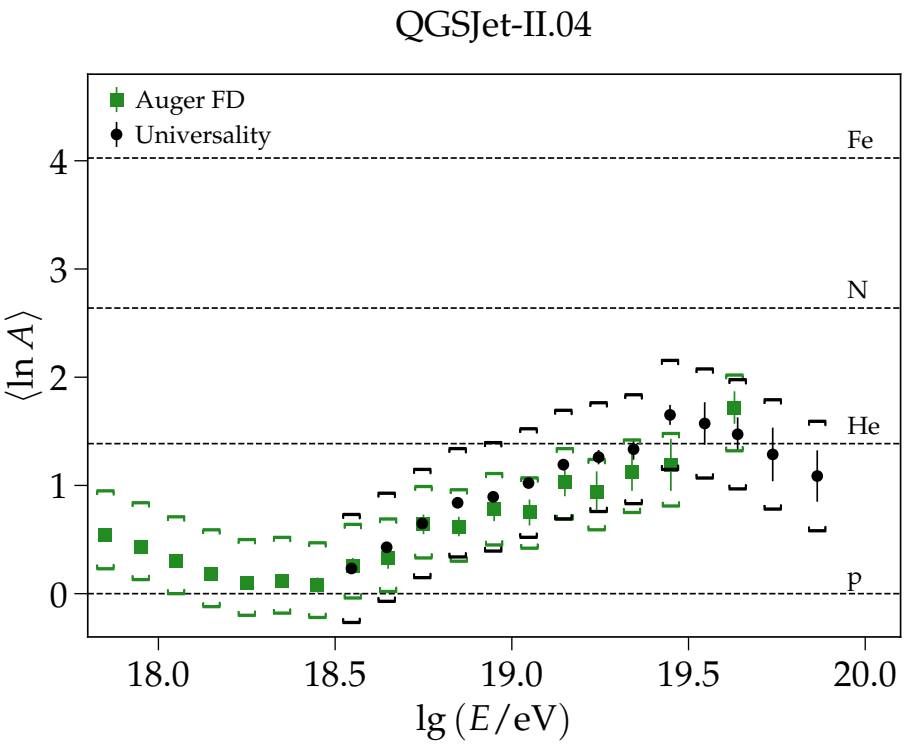

(a)

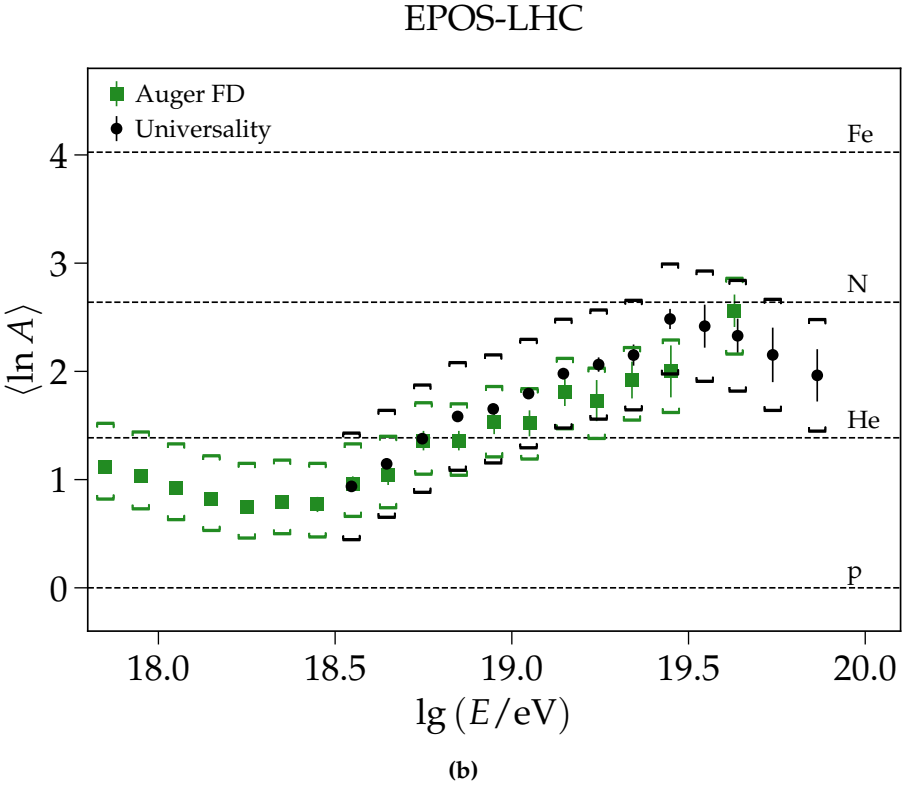

(b)

Figure 5.9: Average logarithmic mass derived from the measurement of $\langle X_{\max} \rangle$ for (a) QGSJET-II.04 and (b) EPOS-LHC.

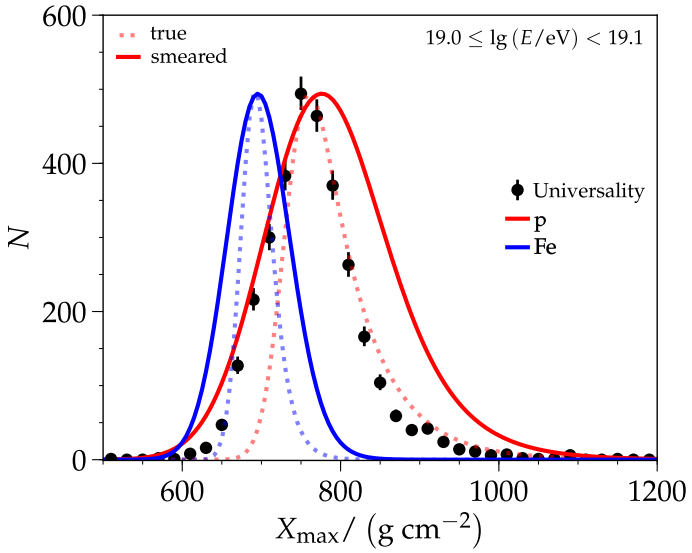

Figure 5.10: Distributions of true and smeared templates for proton- and iron-induced primaries generated with QGSJET-II.04. The detector resolution used for the Gaussian smearing is parameterized for each primary and interaction model as a function of energy. The maximum probability of the template is scaled to be the same height as the maximum number of events measured by the SD-1500 in an energy range of 10^{19} eV to $10^{19.1}$ eV.

the mean of the Gaussian distribution $N(X_k, \sigma_k^2)$, and σ_k is the resolution found from detector simulations for the specified interaction models and primaries. The effect of smearing is depicted in Fig. 5.10. To carry out the comparison with data, the smeared templates must each be weighted by their own fraction f_s for their species, and the resulting MC prediction must be normalized to the data present in a given energy bin

$$C_j = \frac{N}{N_{\mathrm{MC}}} \sum_s f_s \cdot p(X_{s,j}^m), \tag{5.9}$$

where N is the total number of measured events within the given energy bin and N_{MC} is the MC normalization term

$$N_{\mathrm{MC}} = \sum_s f_s \sum_{j=0}^{\infty} p(X_{s,j}^m). \tag{5.10}$$

Despite the number or type of nuclear species chosen, the summation of their fractions must yield 1. To preserve this in the fitting procedure, the species fractions are defined via $(s-1)$ parameters in interdependent multiplicative expressions. For instance, a three-species composition would have the following fractions defined

$$\begin{aligned} f_1 &= \alpha, \\ f_2 &= (1-\alpha)\beta, \\ f_3 &= (1-\alpha)(1-\beta), \end{aligned} \tag{5.11}$$

where $\alpha, \beta \in [0,1]$. To determine the best-fitting combination of nuclear species within a given energy bin, a binned maximum-likelihood method is used. The likelihood [99] is expressed as

$$L = \prod_j \left[\frac{e^{-C_j} C_j^{n_j}}{n_j!} \right], \tag{5.12}$$

where n_j is the number of events in the jth $X_{\max}$ bin. To remove the factorial, Eq. (5.12) is divided by the likelihood-maximizing case when $C_j = n_j$, which is permissible as it is a constant factor and its removal does not affect the maximization process. This way of writing the equation is equivalent to the deviance of a Poissonian likelihood. The resulting negative log-likelihood expression

$$\mathcal{L} = \sum_j \left(C_j - n_j + n_j \ln \frac{n_j}{C_j} \right) \tag{5.13}$$

is then minimized using NLopt [172] to obtain the best fit of the data. Examples of optimum fits are given in Fig. 5.11. To quantify the quality of the fit, mock data sets are drawn from the predicted $X_{\max}$ distribution, as described in Eq. (5.9). The fraction of mock data sets with $\mathcal{L}$ at the optimum worse than that obtained from the real data defines the p-value of the fit.

To encapsulate the correlations between the species, the statistical uncertainty for each species' fraction is determined using a generalization of the Feldman-Cousins procedure [173], known as the profile-likelihood method [174]. This method is favored to the $\Delta\mathcal{L} = \frac{1}{2}$ rule as the constraints placed upon the fit do not ensure that $\mathcal{L}$ will act as a χ^2-variable. In the profile-likelihood method, we observe the likelihood function of a single species while treating the other species as nuisance parameters and, the resulting $\mathcal{L}$ values are compared to the minimum when all species are fit. Thus, the likelihood function is defined as

$$\lambda(f_s) = 2\left(\mathcal{L}\left(\hat{f}_s, \hat{f}_n\right) - \mathcal{L}\left(f_s, \hat{f}_n\right)\right), \tag{5.14}$$

where f_s is the species' fraction of which we are seeking uncertainty values, $\hat{f}_n$ represents the remaining species' fractions which are found via a fitting procedure, and $\mathcal{L}\left(\hat{f}_s, \hat{f}_n\right)$ represents the optimum value where all species' fractions are fit. To directly observe the effect of a fixed f_s, the parameters used in the fit are reduced by one dimension, and a constant, $1 - f_s$, is multiplied by each term to preserve unity. Thus, the three species composition defined in Eq. (5.11) is redefined as

$$f_2 = c\alpha,$$

$$f_3 = c(1-\alpha),$$

where $c = 1 - f_1$ and $\alpha \in [0,1]$; the contribution of f_1 is still considered in the negative log-likelihood minimization. The resulting profile-likelihood distribution approximates a χ^2 distribution with one degree of freedom. We can thus ascertain that the upper and lower limits associated with the 68% coverage are found on either side of the fit minimum where the profile-likelihood has increased by ~ 0.989. The systematic uncertainties of the fit are estimated by shifting the Monte Carlo templates[13] by $\delta X_{\max}$ with values between $\pm\sigma$ in steps of 0.2σ. As the fit fractions are not expected to evolve monotonically, the maximum values are extracted after the scanning has been performed to set the upper and lower limits.

The overall fractional fit of the mass composition as a function of energy is given in Fig. 5.12 for the FD and universality results. Below an energy of $10^{19.4}$ eV, the optimal results found for universality are poorly fit, as determined by the p-values. For the most part, the large width of the resolution for each primary and hadronic interaction model and width of the $X_{\max}$ distribution prevent the estimated systematic uncertainties from being physically motivated. Overall, the trend in the fractional evolution for each interaction model is similar

[13] This is done to avoid systematic effects that may arise from re-binning data.

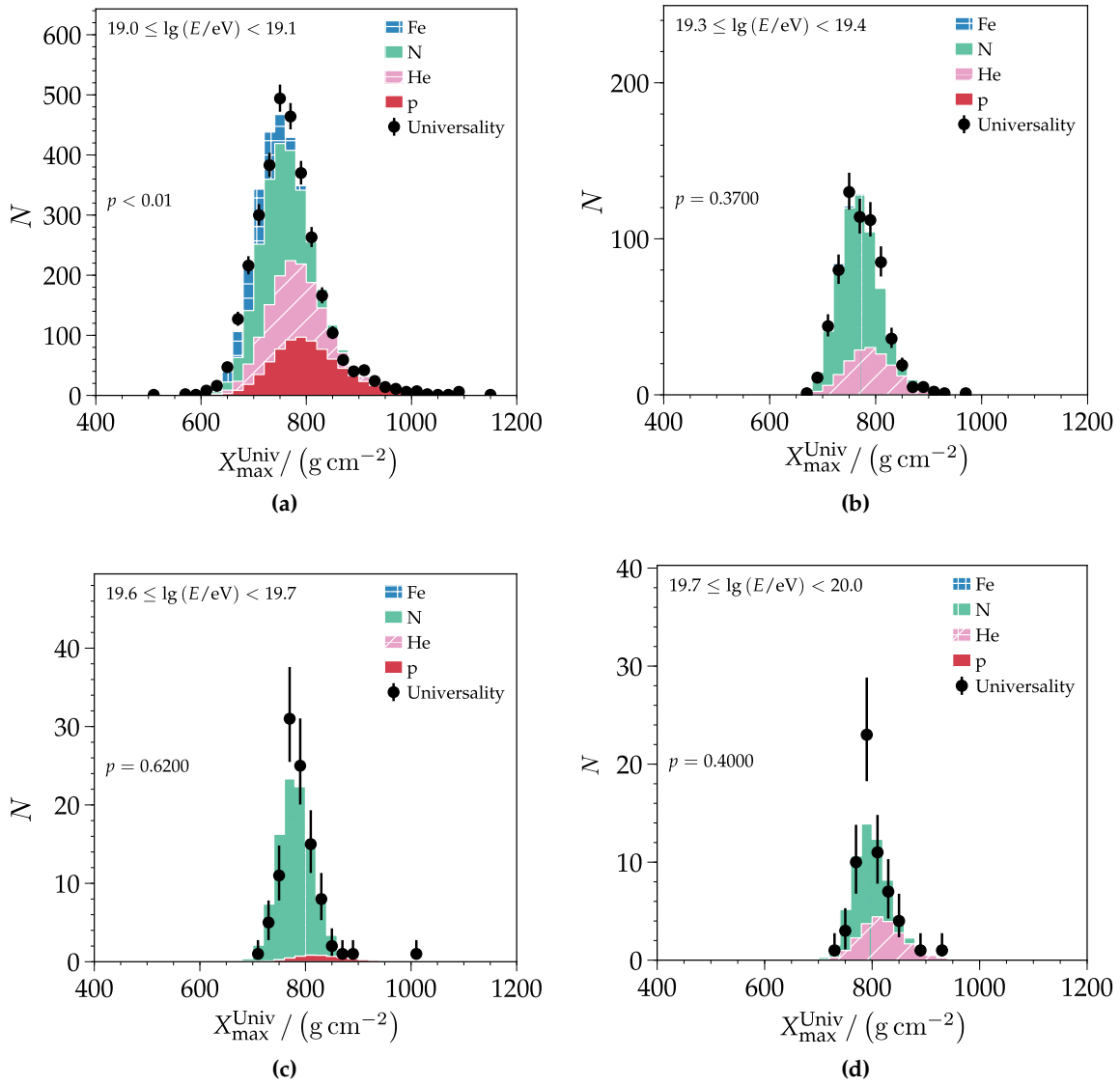

Figure 5.11: Optimal fits of the distributions of the depth of the shower maximum for $\lg(E/\mathrm{eV})$ in (a) [19, 19.1], (b) [19.3, 19.4], (c) [19.6, 19.7], and (d) [19.7, 20.1] as obtained with Monte Carlo templates from EPOS-LHC. The distribution of data being fit is shown with black points, where the uncertainties are from Poissonian statistics. The presence of a particular colored histogram indicates that the corresponding nuclear species participated in the fit. The colored histogram in the background is the stacked histograms of the combined Monte Carlo templates which best fit the data. Thus, it is the relative proportions between each histogram as you move to the foreground that represents the relative fraction found for a nuclear species. In the case of (a), there is a very small fractional component associated with iron, whereas nitrogen is relatively abundant. To directly see the fractional values of each species, see Fig. 5.12b. The significance of the fit (p-value) is given; the meaning of this is described in the text.

between the FD and universality results. In order to have better fits, it would be worthwhile for the zenith-dependence in the bias of the X_{max} distributions (as seen in Fig. 4.9) to be corrected for. While this need not be taken into account for the

average depth of the shower maximum, the spread of the X_{max} distributions is widened by these unaccounted zenith-dependencies. Additionally, as seen in the examples of optimal fits (Fig. 5.11), further quality cuts should be investigated such that X_{max} values that are nonphysical are no longer considered. With the implementation of the fiducial selection, we rid ourselves of a class of events which are poorly reconstructed. In data, however, there are events contained in classes, which are generally well-reconstructed, that may be poorly reconstructed due to hardware effects (e.g. the trace was not well measured as one or more of the PMTs were improperly functioning). Above an energy of $10^{19.4}$ eV, the universality fits become statistically significant for EPOS-LHC and SIBYLL-2.3. In general, the universality results predict a mass composition with intermediate elements, but at the highest energies, it predicts a resurgence of a lighter composition —like helium.

In order to obtain statistically meaningful fits below energies of $10^{19.4}$ eV and improve the other presented mass composition studies, further analyses of and improvements to the Reconstruction procedure need to be made. While the zenith-dependence may be removed from the biases in the X_{max}[14], these corrections do not change the correlation of the spread of X_{max} with zenith angle and energy. Among the improvements that should be considered for the reconstruction are: (1) the parameterization of the uncertainties used in the shape fit, (2) the improvement of signal and timing models to better describe showers with an X_{max} close to ground or high up in the atmosphere, (3) the extension of the universality models to lower energies so that the reconstructed relative muon content may be compared to that directly obtained by AMIGA, and (4) an investigation into terms missing from the negative log-likelihood description which could improve the reconstruction, particularly at lower energies.

[14] In Appendix D.7.2, the residual, zenith-dependencies of the bias have been corrected for. The resulting first two central moments of the X_{max} are presented.

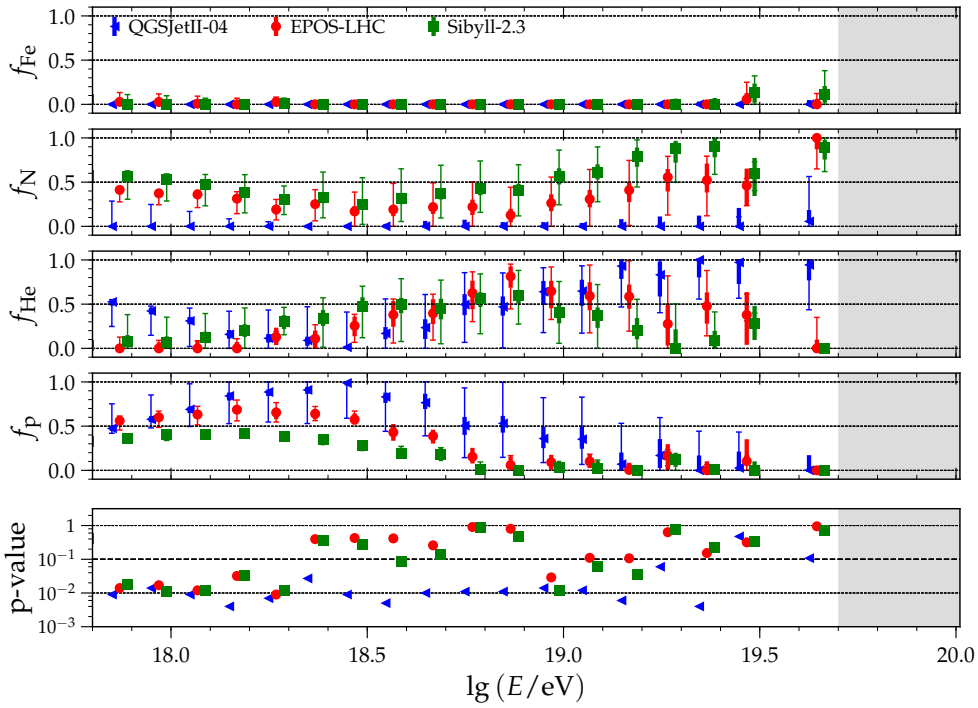

(a)

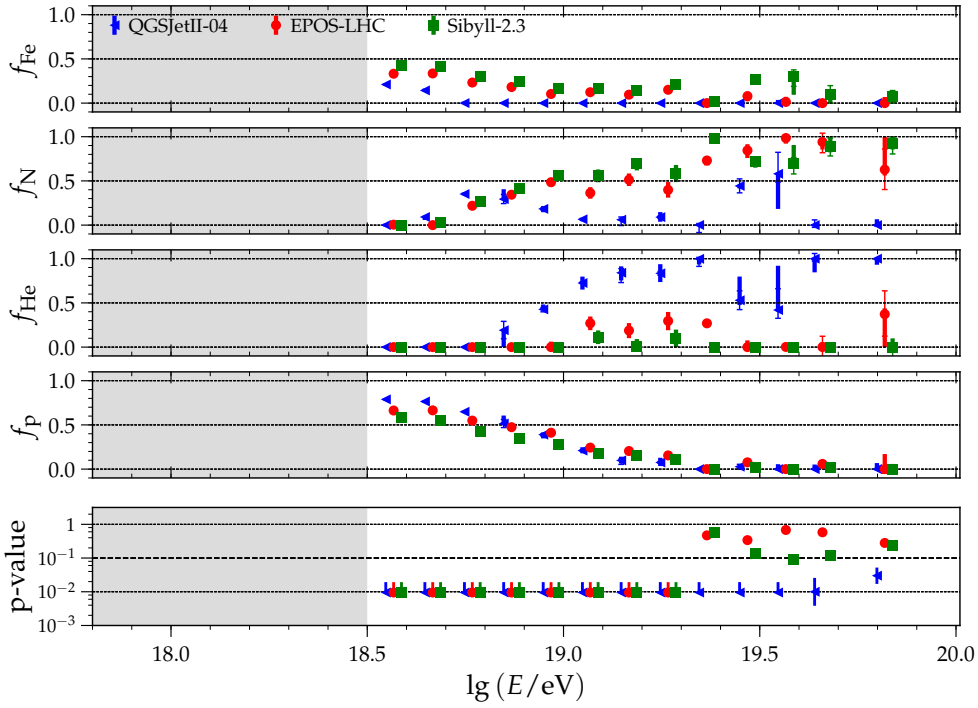

(b)

Figure 5.12: Fit of the mass composition fractions with four nuclei: proton, helium, nitrogen, and iron for (a) FD (values from [104]) and (b) universality (this work). The p-values shown correspond to the goodness of the fit. Values exceeding 10^{-1} are considered well-fit.

CHAPTER 6

Summary and conclusions

The focus of this work is to determine the mass composition derived with the air shower universality approach using data measured with the *Surface Detector* (SD) of the *Pierre Auger Observatory* (Auger). In order to perform this task, a novel reconstruction method was developed and used to derive the results presented in this work. The produced results are summarized below and were presented at several conferences and in a conference proceeding [175].

Universality reconstruction In order to reconstruct mass-sensitive parameters from data measured by the SD, the universality signal and timing models (developed in previous works) had been parameterized to describe the development of the four different particle components of an *extensive air shower* (EAS). Previously existing universality reconstruction methods are extensively studied. With the goal in mind to successfully reconstruct the majority of events, the class of events that failed to reconstruct in the previous reconstruction procedures are studied in great detail to find out the patterns for mis-reconstructed events. Of the procedures studied, the most promising one is presented in this work. Named the constrained axis fit, the shower axis is no longer a free parameter, but it is constrained within 1° to the result found with the SD reconstruction. This constrainment reduces the degrees of freedom in the negative log-likelihood while fully incorporating the correlations of the physics variables. Such a reduction in the underlying minimizing function is needed to make up for the few stations triggered by low energy events, which by themselves yield a degenerate likelihood that sometimes leads to nonphysical minima. The overall reconstruction efficiency is compared in Fig. 6.1 for a reconstruction type with no constraints and for the constrained axis fit. With an efficiency over 90 % across all energies, the constrained axis method is able to reconstruct previously mis-reconstructed events. Nevertheless, there is a reduction in efficiency at the lowest energies. In looking into the cause for this, it was determined that this occurs for events with high zenith angles, where the attenuation of the signal is significant. Interpreting this with the universality parameterizations, recommendations are made throughout this work to make the negative log-likelihood reconstruction more robust for the implementation of universality at lower energies and for its comparison to results obtained with the Muon Detector (AMIGA) and the Auger upgrade (AugerPrime). In particular, an energy-dependent adjustment of the signal uncertainty model for low signal traces is recommended.

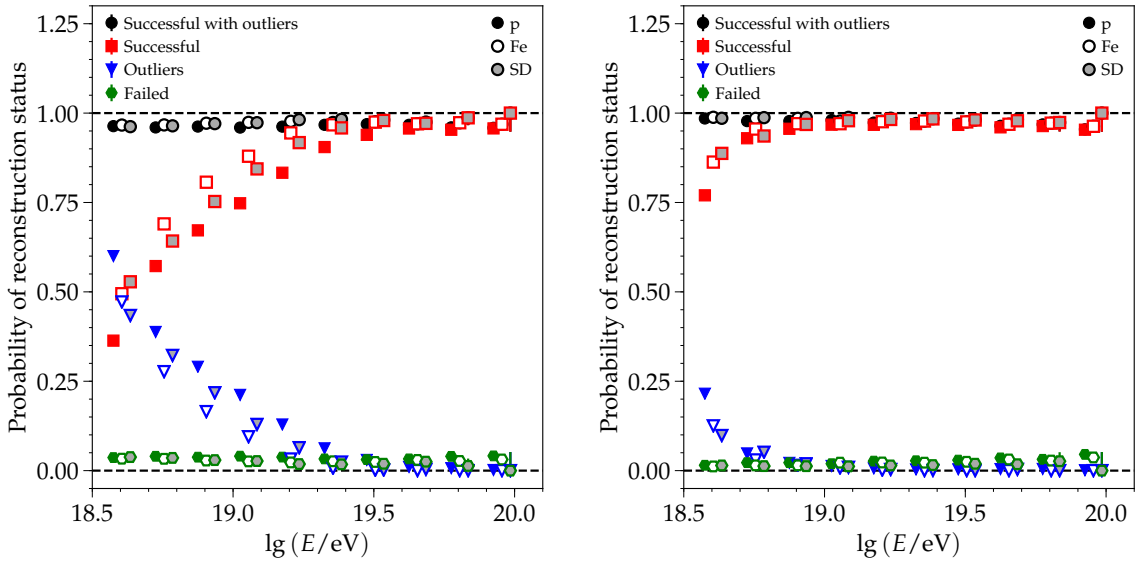

Figure 6.1: Overall reconstruction efficiency with respect to energy for the (a) non-constrained reconstruction (known as the global method) and (b) the constrained axis fit. Non-saturated events are used in this study for QGSJET-II.04 proton and iron simulations and are compared to SD data from 2004-2016. The category marked **Successful with outliers** demarks events which successfully passed the criteria of the minimization procedure employed by the reconstruction, whereas **Failed** ones did not pass. To quantify whether events that succeeded returned physical-reasonable reconstructed values, a simple selection criteria is defined as $X_{\mathrm{max}} \in [500, 1050]\ \mathrm{g\,cm^{-2}}$ and $|\theta_{\mathrm{Univ}} - \theta_{\mathrm{SD}}| < 5^{\circ}$. Events which meet these criteria are grouped into the **Successful** category, whereas those that do not are grouped in **Outlier**. Below an energy of 10^{19} eV, the reconstruction efficiency of the **Successful** events of the global method drops from around 80 % to less than 40 %. This is due to the few triggered stations at low energies which do not provide enough information to reasonably reconstruct the depth of the shower maximum and zenith angle simultaneously. By constraining the shower axis to be within 1° of what is reconstructed by the SD, the constrained axis is able to recover a significant amount of the **Outliers** of the global fit.

Quality selection of events The performance of the constrained axis method was studied with different primary particles simulated with various contemporary hadronic interaction models. Biases and resolutions were found to be reduced compared to the unconstrained method. Still, to ensure a quality event selection for mass composition analyses, a fiducial selection as a function of zenith angle and energy is derived. The goal of this newly-developed selection is to reject zenith angle ranges in a given energy bin in which the average shower maximum deviates significantly from its unbiased measured value. As shown in Fig. 6.2, this method yields consistent results among the different hadronic interaction models. As this selection is purely geometrical, it ensures an unbiased measurement of the mass composition. The resulting biases and resolutions of the depth of the shower maximum and relative muon content are fit for simulations and data (Fig. 6.3). Corrections are calculated with golden hybrid events to account for the lack of muons presently described in simulations.

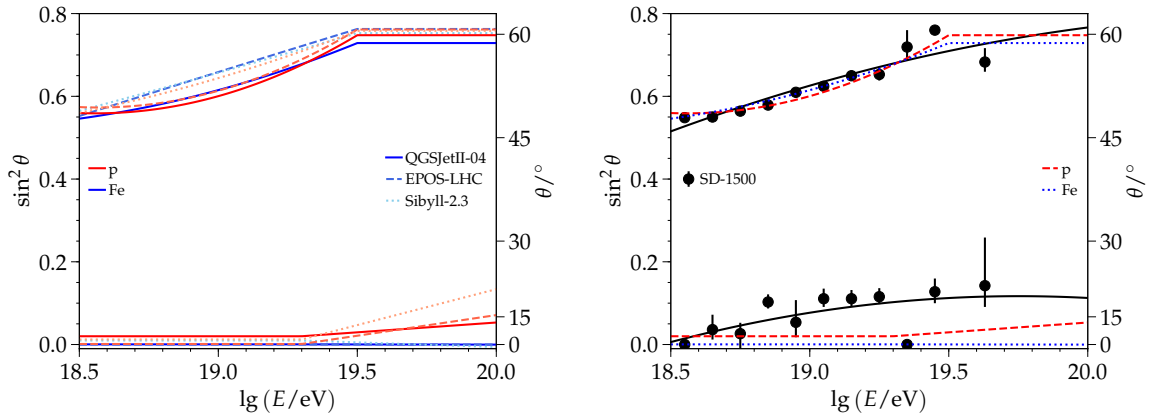

Figure 6.2: Evolution of the fiducial selection as a function of logarithmic energy. (a) The derived selection for proton- and iron-induced showers generated with QGSJET-II.04, EPOS-LHC, and SIBYLL-2.3 are in good agreement. (b) The fiducial selection for data is compared to the results found with proton- and iron-induced QGSJET-II.04 simulations. The stricter selection criteria of data for the lower bound of the zenith angle range are apparent and ensure an unbiased measurement of the mass composition.

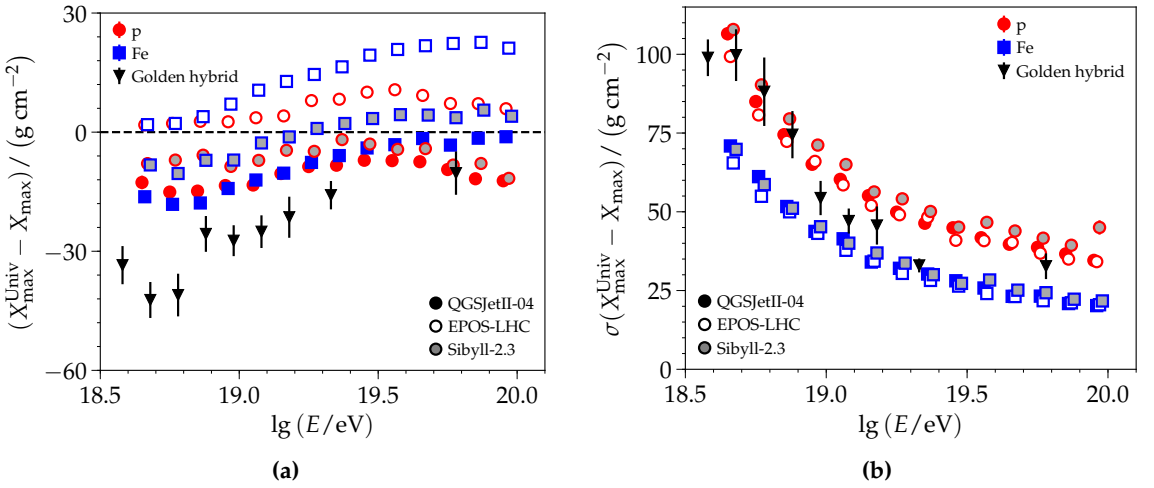

Figure 6.3: The (a) bias and (b) resolution of the depth of the shower maximum as a function of energy. The results from golden hybrid data are compared to proton- and iron-induced simulations from QGSJET-II.04, EPOS-LHC, and SIBYLL-2.3. Overall, the same non-linear trends are observed for each data set; the difference in the offset is due to the different description of each model (and of golden hybrid data) of the relative muon content. In considering the resolution of the reconstructed X_{max}, there is a general agreement between the interaction models for the proton- and iron-induced simulations. The resolution of data is mostly between the values associated with proton and iron; the fluctuations in the resolution associated with data are due to the large uncertainties and the underlying change in mass composition as a function of energy.

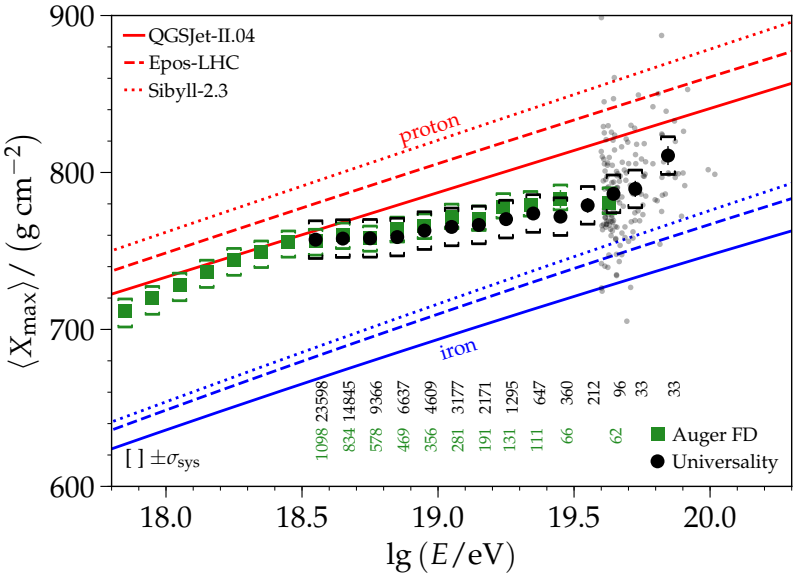

Figure 6.4: The average reconstructed depth of the shower maximum is shown as a function of energy. For comparative purposes, recent results as measured by the Auger FD are shown with the green rectangles ([104]). The event numbers for the universality method (black text) and FD (green text) are given at the bottom of the plot. The statistical uncertainties for the universality method are shown, but their values are often small enough that the marker hides them. Systematic uncertainties are shown with brackets. The individual events that contribute to the last three energy bins are depicted with translucent black dots. The average results from proton- and iron-induced simulations from contemporary hadronic interaction models —QGSJET-II.04, EPOS-LHC, and SIBYLL-2.3— are added to draw inferences on the evolving mass composition. Overall, there is good agreement between the results of this work and those found with the FD measurements. At the highest energies, the universality approach predicts a lighter composition than anticipated by the trend observed in the FD.

Mass composition The fine-tuned universality reconstruction is applied to a full set of SD data from 1. January 2004 to 31. December 2016. The average depth of the shower maximum derived in this work is compared to the result found by the Auger *Fluorescence Detector* (FD). Overall, a good agreement is seen, as shown in Fig. 6.4. Through the comparison of the average depth of the shower maximum predicted by various contemporary hadronic interaction models, it is possible to infer the trends of the mass composition as a function of energy. At the highest energies, the elongation rate of the FD trends toward a heavier composition. In contrast, the universality results which include three additional energy bins (and in general, an average of ten times the data of the FD) indicate a preference for an increasingly lighter composition. Taking into account the derived statistical and systematic uncertainties, this trend is on the order of $2.4\,\sigma$. Further studies investigating this lighter component are critical for point-source anisotropy studies. The second moment of the depth of the shower maximum is studied, and there is general agreement between the universality and Auger FD results above an energy of 10^{19} eV. Interestingly, at the highest energies, there is no trend towards a lighter composition, which creates tension between the results inferred from the first two X_{max} moments. This might point to non-trivial differences in the shower physics of data and current hadronic interaction models. The average profiles of the relative muon content validate the report of external analyses that there is a lack of muons in simulations as compared to data. While the general trend of this average is difficult to describe due to the mismatch in the relative muon content, it does, at the highest energies, return to a lighter composition. To better infer the evolution of

the mass composition as a function of energy, the logarithmic mass of X_{max} —based on the extension of the Heitler model— is studied for QGSJET-II.04 and EPOS-LHC. The derived results are again in agreement with the FD and exhibit the trend to lighter elements at the highest energies. The aforementioned mass composition studies rely on moments of the distribution of the depth of the shower maximum. The full distribution may be used in order to extract the mass composition as an evolving fraction of nuclear species with respect to energy. The same overall trends are seen for each interaction model as are found with the distribution of the depth of the shower maximum as measured by the FD. The proton-dominance at the ankle (3×10^{18} eV) evolves to a mass composition predominantly made of intermediate masses —like nitrogen.

Final remarks Several complementary studies to the main body of this work are presented in Appendix D. These include detailed studies of saturated events in data and simulations, an investigation into changing the underlying minimizing function, and event selection for the previously defined reconstruction methods.

The data analysis of the Auger Upgrade will greatly benefit from the methods developed throughout this work. In particular, the addition of signals measured with the scintillator detector will enable the disentanglement of the electromagnetic and muonic signals. Through this determination, it will be possible to improve the parameterizations of universality, which are initially derived from simulations, to better describe the physics seen in the air showers of ultra-high energy cosmic rays. Universality together with the upgraded detectors will enable an event-by-event determination of the mass composition.

List of Tables

4.1 Parameters for the universality fiducial selection of simulated showers generated with QGSJET-II.04. . . . 84
4.2 Parameters for the fits of the bias and resolution for X_{max} and R_μ for simulated showers generated with QGSJET-II.04. . . . 86
4.3 Parameters for the universality fiducial selection for SD-1500 data. . . . 88
4.4 Parameters for the bias and resolution of the reconstructed X_{max} for golden hybrid and SD-1500 data. . . . 90
4.5 Parameters for the bias and resolution of the reconstructed R_μ in golden hybrid data. . . . 92
4.6 Parameters for the bias of the reconstructed X_{max} and R_μ in data as a function of average area over peak. . . . 93

5.1 Average systematic uncertainty for each selection and correction applied to SD-1500 data. . . . 97

B.1 Cuts for the selection of SD-1500 events. . . . 128
B.2 FD quality cuts. . . . 129
B.3 Cuts for the selection of SD-1500 simulated events. . . . 133
B.4 FD quality cuts for the analysis of simulated golden hybrid events. . . . 133
B.5 FD fiducial FoV values cuts for golden hybrid simulations. . . . 135

C.1 Parameters for the universality fiducial selection of simulated showers generated with EPOS-LHC. . . . 137
C.2 Parameters for the universality fiducial selection of simulated showers generated with SIBYLL-2.3. . . . 138
C.3 Parameters for the fits of the bias and resolution for X_{max} and R_μ for simulated showers generated with EPOS-LHC. . . . 139
C.4 Parameters for the fits of the bias and resolution for X_{max} and R_μ for simulated showers generated with SIBYLL-2.3. . . . 140
C.5 Values of the first two central moments of the measured X_{max} distributions for the constrained axis reconstruction of SD-1500 data. . . . 141
C.6 Values of the first central moment of the measured R_μ distributions for the constrained axis reconstruction of SD-1500 data. . . . 141

D.1 Reconstruction results of X_{max} obtained by performing the specified modifications of the deviance function. . . . 145
D.2 Parameters for bias of the reconstructed X_{max} as a function of zenith angle and energy for the constrained fit. . . . 184
D.3 Parameters for the bias and resolution of the reconstructed X_{max} for golden hybrid data where the universality-derived fiducial selection is used. . . . 187

D.4 Parameters for the bias and resolution of the reconstructed R_μ for golden hybrid data where the universality-derived fiducial selection is used. 187
D.5 Parameters for the bias of the reconstructed R_μ for golden hybrid data as a function of average area over peak; the estimated relative muon content from the FD is used for the reference value. 188
D.6 Average systematic uncertainty for each selection and correction applied to SD-1500 data, where the residual bias of the depth of the shower maximum is corrected for. 199

Appendix A

General

A.1 Violin plots

Throughout this work, violin plots are used to aid in analyzing the relationship between variables; this plot style within Auger and specifically this work should be credited to [108]. Essentially, a violin plot is an augmented version of a profile or box plot. In addition to showing the means, medians, and standard deviation of data, it uses a thin profile to illustrate the normalized distribution of data within a given bin.

Let us consider an example to better illustrate how a violin plot is built and the benefits therein. Given a variable y which is dependent on another variable x, we average y within distinct ranges of x; when the standard deviation of these is considered and the results plotted, this would yield a typical profile plot. The construction of a profile plot allows one to reasonable assess trends and correlations between variables, assuming the data follows a perfect Gaussian. However, data follows non-Gaussian distributions more often than not and that underlying bi- or multi-modal distributions can misleading predict means where no data exists. Such a harrowing example is plotted in Fig. A.1. In Fig. A.1a, a bimodal distribution centered at 0 is created by the superimposition of two Gaussian distributions which are centered at -1 and 1. In considering the profile shown in Fig. A.1b, it is impossible to deduce the cause of the structure. However, in Fig. A.1c, the violins —constructed by a kernel density estimation of the y's contained with the bins x_i— clearly show the bimodal distribution. In this way, the violin plot is able to simplistically reveal critical information which a standard profile plot omits.

Examples of the violin plot format used in this thesis are shown in Fig. A.2; functions from the Python library SCIPY are used [176]. The distribution of y in bins of x_i are shown with the light gray shaded area. As kernel density estimates [177, 178] are used to draw the distributions, the magnitude of the distribution —violin— reflects the size of the p.d.f. at this coordinate. The length of the violin extends up to $3\,\sigma$ ($\pm 49.9\,\%$). The mean and median are shown with the point and solid black line, respectively. The error bars shown about the mean depict the standard deviation of the mean, whereas the darkest area around the median line represents the asymmetric $1\,\sigma$ uncertainties of the median. The dark part of the violin shows the $1\,\sigma$ asymmetric standard deviations ($\pm 34.1\,\%$). Due to the sample size difference, outliers are shown at the ends of the violins in Fig. A.2b, whereas no outliers are identified for Fig. A.2a. Additionally, in the latter plot, the median and mean values fluctuate more about the true mean [178].

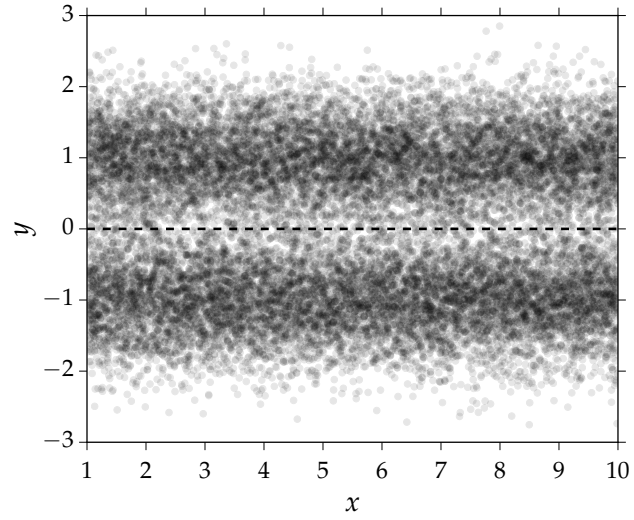

(a)

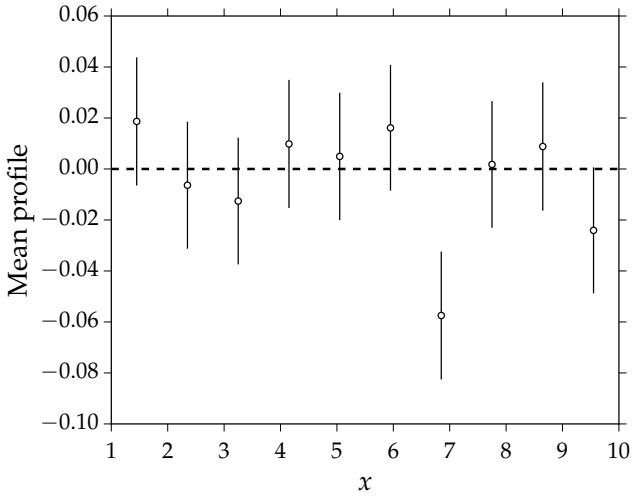

(b)

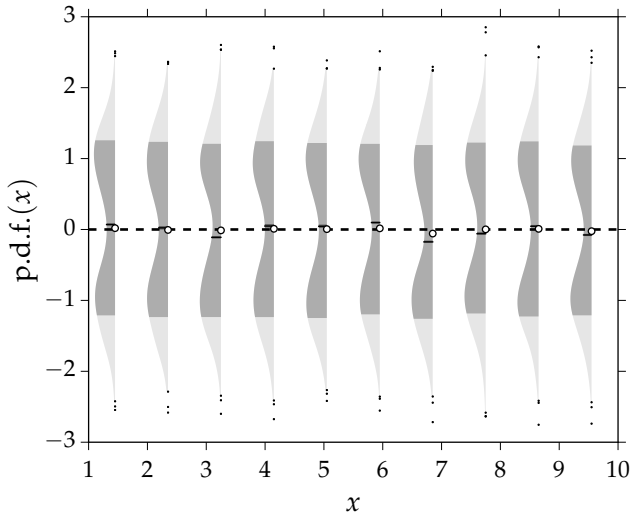

(c)

Figure A.1: A sample of 20,000 points (x, y) was drawn with x uniformly distributed between 1 and 10 and y from Gaussian distributions with a mean at either -1 or 1 and a standard deviation of 0.5. Data is shown as a (a) scatter, (b) profile, and (c) violin plot [108].

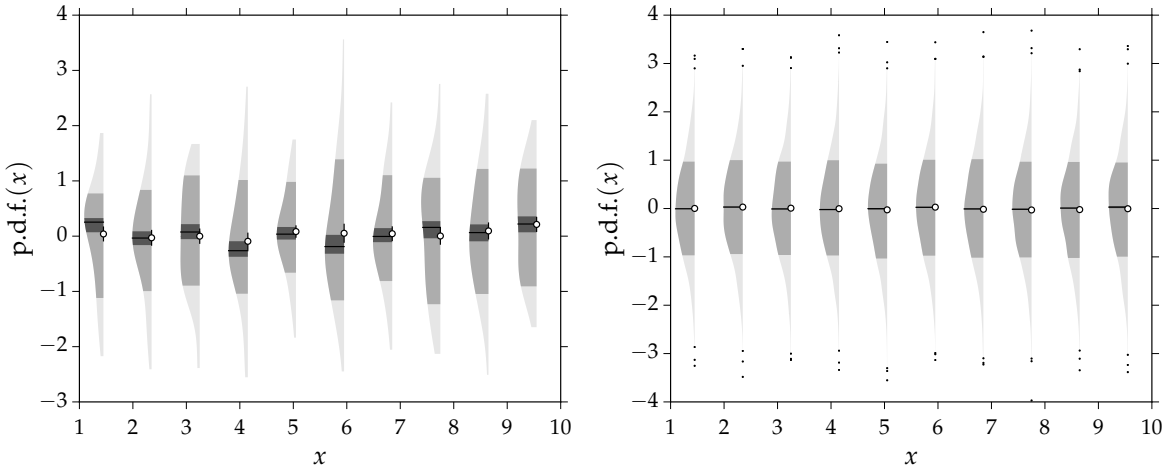

Figure A.2: An example violin plot with (a) 500 and (b) 20,000 points distributed linearly in x between 1 and 10 and normally in y with a mean of 0 and standard deviation of 1 [108].

A.2 Angular resolution

The derivation of the angular resolution is detailed in this section and follows the discussion presented in [179]. The true arrival direction is defined by a unit vector Ω_0, which is oriented by the angles θ and azimuth φ, as shown in Fig. A.3. For most events the reconstructed arrival direction Ω only slightly differs from Ω_0 by $\Delta\Omega$. For small deviations, the angle ηbetween the true and reconstructed axis can be approximated as

$$\eta \approx \sin\eta = \|\Omega_0 \times \Omega\| = \|\Omega_0 \times \Delta\Omega\| \tag{A.1}$$

The displacement vector $\Delta\Omega$ is decomposed in spherical coordinates as

$$\Delta\Omega = \Delta\theta\hat{\theta} + \sin\theta_0\Delta\varphi\hat{\varphi} \tag{A.2}$$

where $\hat{\theta}$ and $\hat{\varphi}$ are the unit vectors in the direction of Ω_0 and $\Delta\theta$ and $\Delta\varphi$ are the replacements of θ and φ around the respective components of Ω_0. In substituting this equation into Eq. (A.1), η^2 can be expressed in spherical coordinates as

$$\eta^2 = \|\Omega_0 \times \Delta\Omega\|^2 = \Delta\theta^2 + \sin^2\theta_0\Delta\varphi^2 \tag{A.3}$$

In the geometrical reconstruction used by the SD, the u and v from the planar coordinate system —direction cosines in the easting and northing directions— are used. By transforming from planar to spherical coordinates and expanding around Ω_0, η^2 can be expressed in terms of planar coordinates

$$\eta^2 = \Delta u^2 + \Delta v^2 \tag{A.4}$$

To then arrive at the angular resolution equation expressed in Eq. (3.19), some statistically-based assumptions are made. First, it is assumed that u and v follow a Gaussian distribution around u_0 and v_0 of Ω_0. Thus, the fluctuations Δu and Δv are also Gaussian and have means of zero. Next, it is assumed that Δu and Δv have the same uncertainty[1] σ. In normalizing

[1]There is some expected modulation in σ with respect to the x- and y-axis. However, the average fluctuations of Δu and Δv are approximately equal given the azimuthal symmetry of the arrival directions.

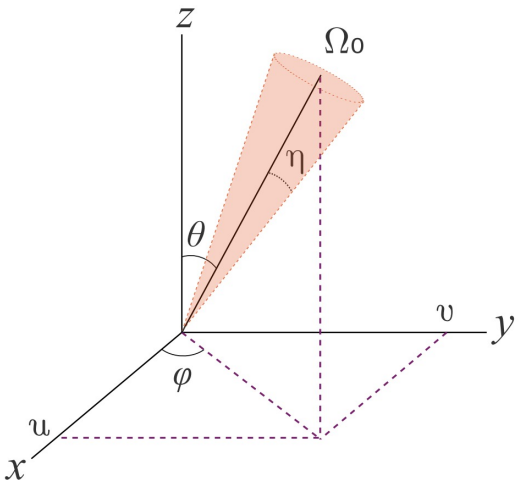

Figure A.3: The geometry of the shower axis is given for planar and spherical coordinate systems. The shaded cone represents all reconstructed axes that differ from the true axis (Ω_0) by less than an angle η [179].

Δu and Δv in Eq. (A.4) by σ, the sum of the squares of two standard normal variables (i.e. $\sigma = 1$) is given as:

$$\frac{\eta^2}{\sigma^2} = \frac{\Delta u^2}{\sigma^2} + \frac{\Delta v^2}{\sigma^2} \tag{A.5}$$

If Δu and Δv are uncorrelated, then η^2/σ^2 will follow a χ^2-distribution with two degrees of freedom

$$f(\eta^2/\sigma^2) = \frac{1}{2} e^{-\eta^2/2\sigma^2} \tag{A.6}$$

Evaluating this distribution for the 68 % spread, gives $\eta_0 \approx 1.5\sigma$. σ can then be calculated from the expected value of the terms in Eq. (A.3) or Eq. (A.4), where the means are equal to zero. Thus, the expected values of the squared terms are then equal to the variances, and it is possible to estimate σ as

$$\hat{\sigma}^2 = \frac{1}{2} \left(\mathrm{Var}[\theta] + \sin^2 \theta_0 \mathrm{Var}[\varphi] \right) \tag{A.7}$$

Thus, in combining this equation with the expression for η_0, the angular resolution η_0 ($= \sigma_{\mathrm{ang}}$) is found to be Eq. (3.19).

APPENDIX B

Data sets

This appendix provides an overview of the simulations and data used for the analyses presented in this work. For a detailed, qualitative description of how an extensive air shower is observed at the Auger Observatory and, later, reconstructed, see Chapter 2. Tables of the quality cuts used are provided; a qualitative description of the cuts employed may be found in Section 2.4.1 and Section 2.5.2. The distributions of the selected events are given to illustrate the number of events shown throughout this work.

B.1 Data

The reconstructed SD data was produced by the local KIT group —known as the Observer team[1]— for the 2017 *International Cosmic Ray Conference* (ICRC) contributions from the Auger Observatory[180]. As universality has not yet been parameterized to energies below $10^{18.5}$ eV or above zenith angles greater than 60°, only vertical events (0° to 60°) as measured by the SD-1500 were used. The quality cuts for the SD-1500 are given in Table B.1. Cuts are applied successively. An individual cut typically removes less than 5 % of the selected data; the T5Trigger criterion, however, rejects roughly 30 %. The corresponding cuts for the FD[2] (Table B.2) are more numerous as they must:

- reject laser events which are used in the nightly calibration of the FD.
- select which FD building (i.e. eyes) are used and checks if HEAT and Coihueco were both operational and can be merged to increase the field of view.
- remove periods where the communication from the FD was poor.
- ensure that the pixels of the camera were operational and well-calibrated.
- check that the weather conditions were ideal for measurements. Increased cloud coverage, low clouds, and atmospheric aerosols change and can alter the fluorescence yield.
- apply quality selection criteria for events. These ensure that the measured event was in the ideal range and meeting criteria for successful FD reconstruction. For instance, the simultaneous measurement by one or more SD stations (i.e. hybrid) allows for a better constrainment of the geometry of the shower.

[1] The author was a member of this, then, two-person team.

[2] The lines within the table denote groupings. The general purpose of these grouped cuts are provided sequentially in the list.

Table B.1: Cuts for the selection of SD-1500 events. Above an energy of $10^{18.5}$ eV, 112 932 events are selected.

Cut name	Cut value	Meaning
!lightning		reject lightning events
minRecLevel	3	successfully reconstructed LDF
maxZenithSD	60	maximum zenith angle, given in degrees
T4Trigger	2	SD was triggered by the event
T5Trigger	2	requires that the 6 stations surrounding the station with the largest signal were on-line
badPeriodsRejectionFromFile		reject events in periods where SD communication was down
minLgEnergySD	18.5	energy threshold where efficiency of the triggers reaches 100 %
timeInterval	{params : 031231 170101}	YYMMDD-specified date range

Table B.2: FD quality cuts. For the analysis of golden hybrid events, these are paired with the SD-1500 quality cuts in Table B.1.

Cut name	Cut value	Meaning
!isCLF		reject laser events from CLF
!isXLF		reject laser events from XLF
heatOrientationUp		checks uptime logs to determine whether HEAT is available to be merged with the Coihueco telescope (i.e. HeCo)
eyeCut 001111		select all four FD eyes but reject HEAT
badFDPeriodRejection		reject periods with poor communication from FD
minMeanPixelRMSMergedEyes	{params : 17 6 011111}	min. mean pixel RMS on merged eyes
minMeanPixelRMSSimpleEyes	{params : 17 011111}	min. mean pixel RMS on selected eyes
!badPixels		reject bad pixels
good10MHzCorrection		good correction of the 10MHz oscillator
hasMieDatabase		atmospheric data available for event
maxVAOD	0.1	reject vertical aerosol optical depth below [g cm^{-2}]
cloudCutXmaxPRD14	{params : 1}	cloud cut
hybridTankTrigger	2	meets SD ToT requirements
maxCoreTankDist	1500	maximum shower plane distance in m
maxZenithFD	90	max. allowed zenith angle in $^\circ$
minLgEnergyFD	1e-20	min. FD lg E
skipSaturated		deselect events with saturated pixels
minPBrass	0.9	min. probability difference between proton and iron
maxPBrassProtonIronDiff	0.05	max. probability difference between proton and iron
xMaxObsInExpectedFOV	{params : 40 20}	reconstructed X_{max} in expected FoV
maxDepthHole	20.	max.hole in depth profile in %
profileChi2Sigma	3 $-$ 1.1	max. deviation of Gaisser-Hillas χ^2 from expectation
depthTrackLength	200	min. track length in g cm^{-2}
xMaxError	40.0	max. error on X_{max} in g cm^{-2}
energyTotError	0.12	max. error on energy %
FidFOVICRC13	40 20	FoV cuts derived for the 2013 ICRC

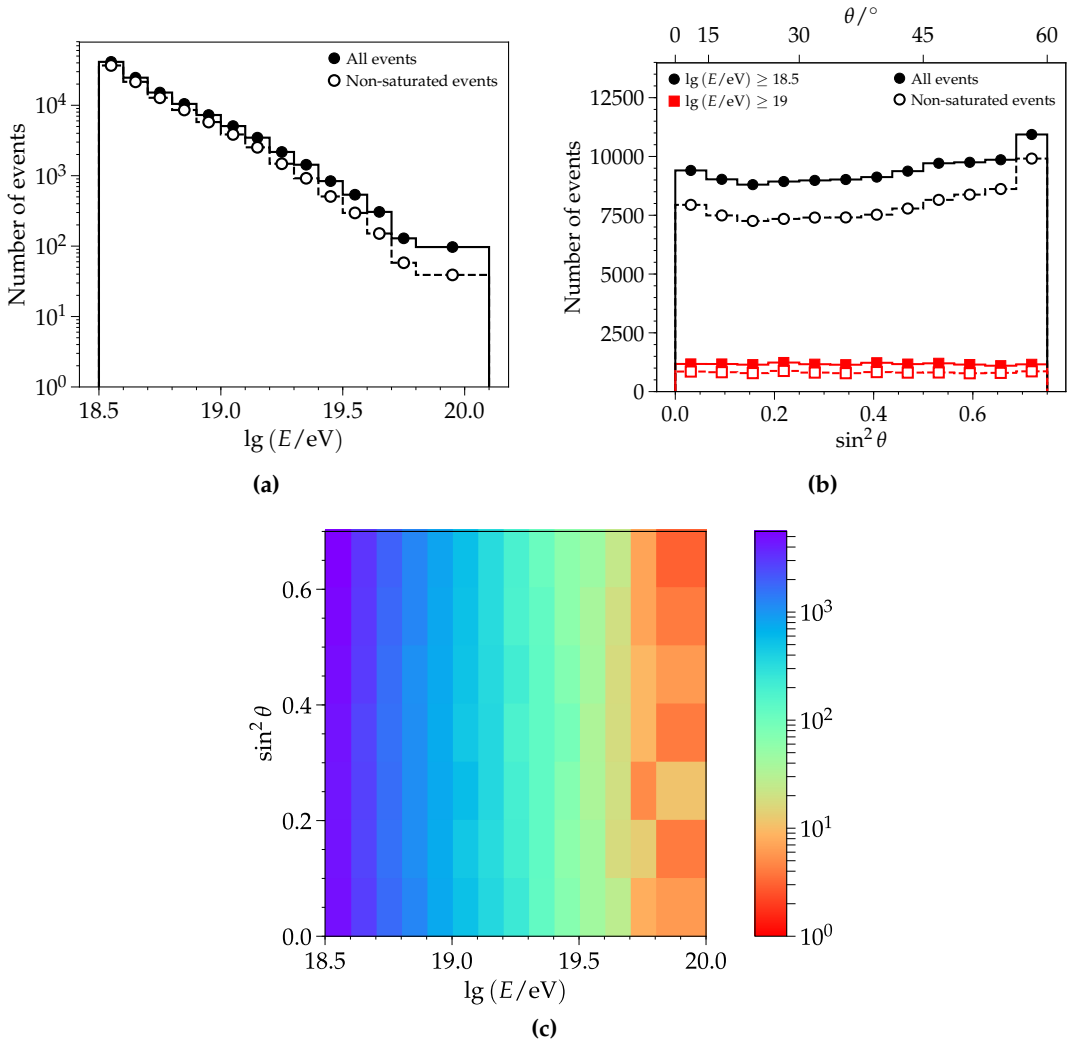

Figure B.1: Distributions of SD-1500 reconstructed events with respect to (a) energy and (b) zenith angle. All events (filled markers) and non-saturated events (empty markers) are considered. For energies below 10^{19} eV, the angular resolution is poor and there is an event migration around 60° which is unaccounted for in these plots. Above 10^{19} eV (red points), the zenith distribution is relatively flat with respect to $\sin^2\theta$. (c) The 2-D distribution for non-saturated events is shown. For all energies —except for events above $10^{19.7}$ eV, the underlying zenith distribution is preserved. At the highest energies, the bins in energy are selected such at least 30 events are present when integrated across all zenith angles.

- apply the fiducial field of view cut[3] which ensures that the distribution of the depth of the shower maximum within a given energy bin is not truncated by the physical field of view.

With the exception of the eyeCut, cloudCutXmaxPRD14, and the FidFOVICRC13 cuts, the various quality selections individually remove less than 5 % of the selected events. The eyeCut employed rejects the events recorded by HEAT. The cloudCutXmaxPRD14 cut removes around 30 % of events, whereas the FidFOVICRC13 cut selects around 23 % of the remaining events. After applying the FD quality cuts, only 2573 events —known as golden hybrid events— remain out of the 112 932 events which were selected with the quality

[3]The fiducial field of view is covered more fully in Section 4.2.2.

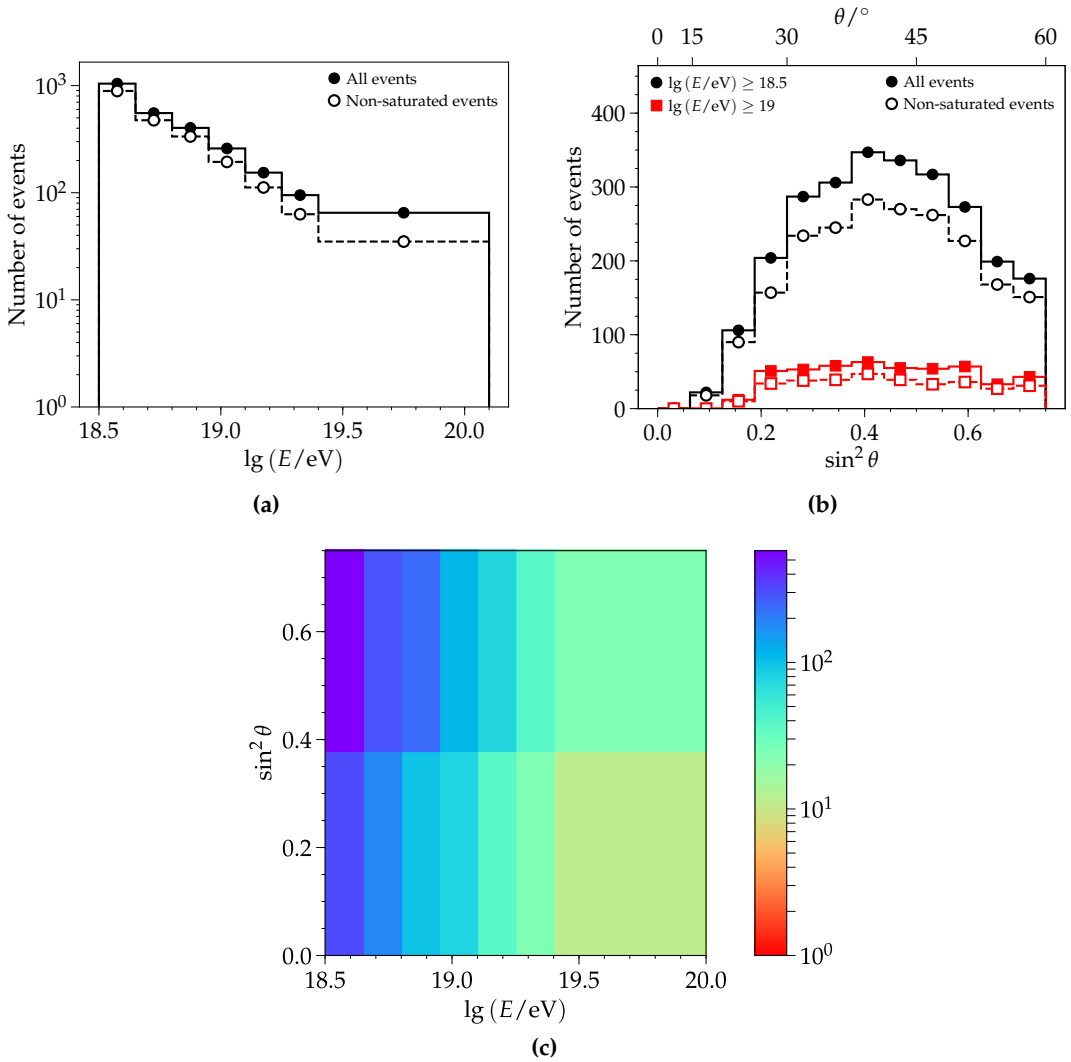

Figure B.2: Distributions of golden hybrid events with respect to (a) energy and (b) zenith angle. All events (filled markers) and non-saturated events (empty markers) are considered. The zenith distributions are truncated and distorted by the fiducial field of view which becomes stricter with increasing energy. (c) The 2-D distribution for non-saturated events is shown. Even with enlarged energy bins, there are too few events to have more than two zenith bins.

criteria for the SD. The energy and zenith angle distributions for the selected SD-1500 data are given in Fig. B.1. The data has a steeply falling energy spectrum of $E^{-2.5}$ and a flat zenith angle distribution with respect to $\sin^2\theta$. The same distributions are given for the golden hybrid events in Fig. B.2. The fiducial field of view cut unequally selects from and distorts the underlying zenith distribution. Unfortunately, there are two few golden hybrid events to perform rigorous systematic studies for the universality reconstruction. With the proposed increase of the FD duty cycle to around 21 % (Section 1.2.2), the event statistics will be improved, but unfortunately, due to the fiducial field of view, the reconstruction biases with respect to zenith angle could not be explored in-depth. Instead, it is more likely that combined analyses with the *Muon Detector* (MD) and *Scintillator Surface Detector* (SSD) will provide greater insight into the quality and dependencies of the universality reconstruction (when used for data). For this work, simulations are able to provide some insight into this area, though caution must be used due to the muon deficit.

B.1.0.1 Modifications used in universality reconstruction

In the calibration of the iterative method using golden hybrid events (Appendix D.4.2.4), a special reconstruction was performed which involved fixing the energy, depth of the shower maximum, and geometry to that found with the FD. By performing such a reconstruction, it is possible to parameterize the relative muon content and time model offset found in data as it differs from simulations. The time model offset Δm_μ has a few outliers in which the start time of the fitted trace is 50 ns to 200 ns too early, which may result from using the high-gain channel. An algorithm was developed to use the low-gain channel and to correct for the mentioned effects [181]. However, reconstruction with this algorithm led to an increase in the angular resolution [182]. Because of this unwanted by-product, this algorithm is not employed throughout this work. A small test was performed —as detailed further in Appendix D.4.2.4— which showed that a portion of Δm_μ outliers may be recovered. The modification from the general SD reconstruction is made in `SdCalibrator.xml` as specified in Listing B.1.

Listing B.1: Changes to `SdCalibrator.xml` for Δm_μ outliers in Appendix D.4.2.4

```
<!-- switch on the equal treatment of high and low gain signal when
     determining signal regions -->
<treatHGLGEqualInSignalSearch/>

<!-- check whether a found flat piece is also flat when starting from
     its end in opposite direction, reduces inclusion of the trailing
     edge of the signal -->
<applyBackwardFlatPieceCheck/>

<!-- the fluctuations on the low gain signal are smaller in terms of FADC
     bins, reduce the tolerance by one (thus, hg : 3, lg : 2) -->
<decreaseLGFlatPieceTolerance/>

<!-- in case of saturation -->
<!--alwaysCalculateSignalStartTimeFromHighGain/-->
```

B.2 Monte Carlo air shower library

The Napoli library [183] was produced by a team in Naples and created with CORSIKA Monte Carlo simulations [184–186]. An optimized thinning level of $t = 10^{-6}$ [187, 188] was used as a compromise between accuracy and time/space requirements. Within Offline, the CACHED SHOWER REGENERATOR module uses a statistical method called *shower resampling* to regain as much of the unthinned shower information as possible [165, 189, 190]. The library is continuous and:

- follows a $\sin^2\theta$ distribution (like that seen in data) and an E^{-1} energy spectrum. The zenith range is from 0° to 65°, and the energy range is from 10^{18} eV to 10^{20} eV.
- includes proton, helium, oxygen, and iron primaries for EPOS-1.99, EPOS-LHC, QGSJET-II.03, QGSJET-II.04, and SIBYLL-2.3.
- is very expansive with more than 12 000 unique CORSIKA simulations per primary per interaction model. Each simulation was tossed 6 times on to the Auger observatory to be observed with the SD-1500 and FD.

The raw CORSIKA files, hybrid simulations with the Auger SD and FD detectors (Offline files), and reconstructed data (ADSTs) have been graciously shared within the Auger

Table B.3: Cuts for the selection of SD-1500 simulated events. For the meaning of various cuts, see Table B.1. The T5Trigger in simulations is used to reject events which landed on the edge of the array and were not surrounded by a complete hexagon of stations.

Cut name	Cut value
minRecLevel	3
maxZenithSD	60
T4Trigger	2
T5Trigger	2

Table B.4: FD quality cuts. For the analysis of simulated golden hybrid events, these are paired with the SD-1500 quality cuts in Table B.3. For the meaning of various cuts, see Table B.2.

Cut name	Cut value
eyeCut 001111	
maxCoreTankDist	1500
maxZenithFD	90
minLgEnergyFD	1e-20
skipSaturated	
xMaxObsInExpectedFOV	{params : 40 20}
maxDepthHole	20.
profileChi2Sigma	2.5 −1.1
depthTrackLength	200
xMaxError	40.0
energyTotError	0.18

collaboration, and the use of it has benefited countless analyses. With more than 75 000 events per primary per interaction model (above an energy of $10^{18.5}$ eV), the ADSTs of the Napoli library have been key in the preparation of this work.

The general cuts used for simulated events are provided for the SD-1500 in Table B.3 and FD in Table B.4. The resulting distributions of SD-1500 quality events are given in Fig. B.3 for QGSJET-II.04 simulations. For the golden hybrid calibration of the iterative fit presented in Appendix D.4.2, it was necessary to derive fiducial field of view cuts[4] for the simulated FD. The code used for this analysis came from [191]. The function used to define the upper and lower boundaries of the observable slant depth ($X_{\mathrm{fid}}^{\mathrm{up}}$ and $X_{\mathrm{fid}}^{\mathrm{low}}$) is:

$$a + b \cdot (\lg(E/\mathrm{eV}) - 19) + c \cdot (\lg(E/\mathrm{eV}) - 19)^2. \tag{B.1}$$

The values for a, b, and c are given for QGSJET-II.04 and EPOS-LHC in Table B.5.

[4]The purpose of such a cut and the reason for why it is derived separately for simulated extensive air showers induced by different primaries are described in Section 4.2.2.

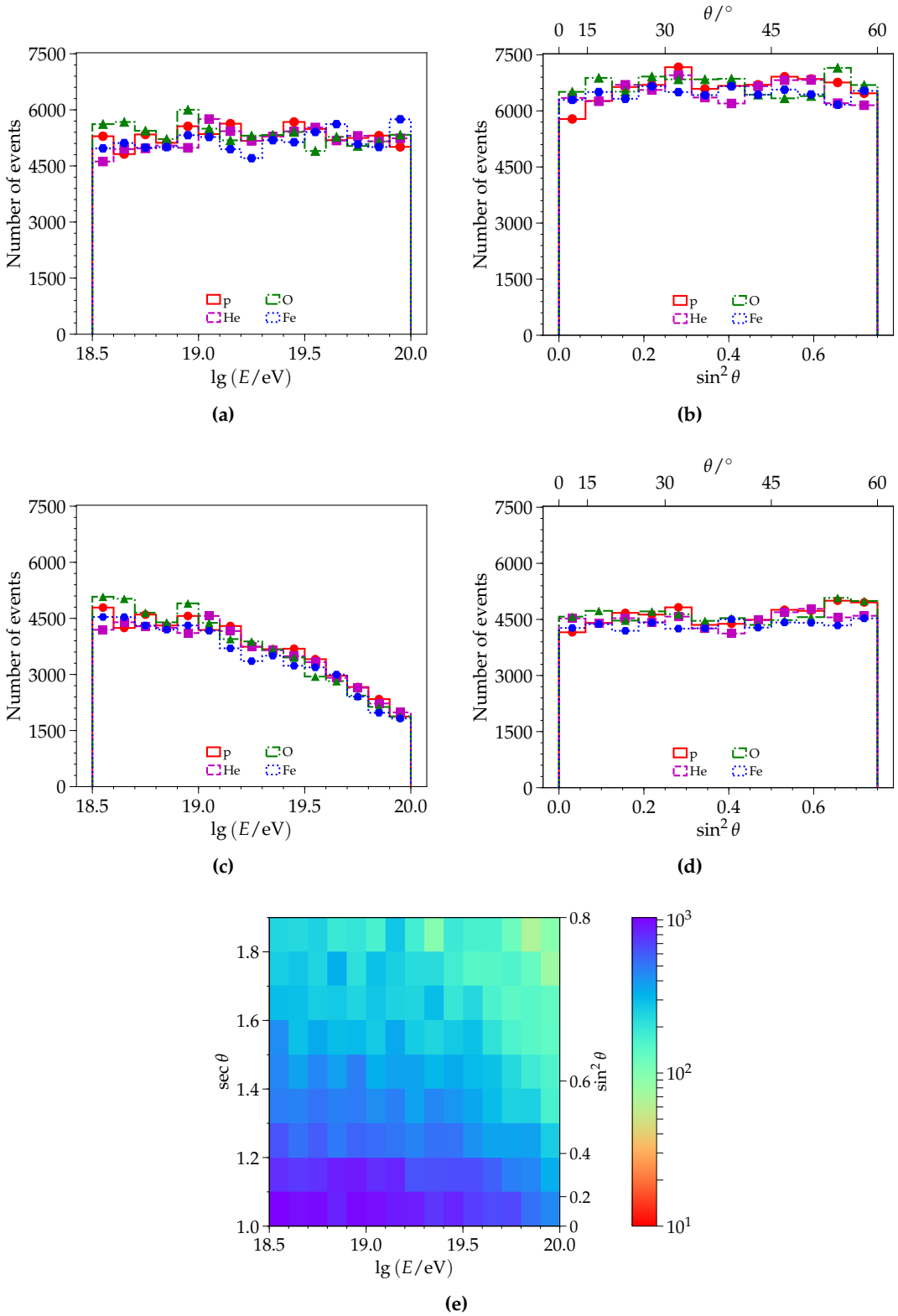

Figure B.3: Distributions of QGSJET-II.04 proton, helium, oxygen, and iron simulations from the Napoli library with respect to (a) energy and (b) zenith angle. (c) and (d) show the same distributions but for only non-saturated events. (e) A 2-D histogram with respect to energy and zenith angle is given for non-saturated proton events. The binning for this plot is given equally in $\sec\theta$ as the slant depth for a given depth of the shower maximum is $X_{\max}/\cos\theta$. In considering only the zenith angle contribution to the slant depth, it can be seen that there is already an order or magnitude difference between the number of events at low zenith angles compared to higher values. As such, this begins to illustrate the difficulties in parameterizing universality models that also well-describe large slant depths, particularly when the simulations used are less numerous than that found in the Napoli library.

Table B.5: FD fiducial FoV values cuts for golden hybrid simulations. The values given below are in the form $\{a, b, c\}$. These are paired with the cuts in Table B.3 and Table B.4.

QGSJET-II.04

Primary	$X_{\text{fid}}^{\text{up}}$	$X_{\text{fid}}^{\text{low}}$
proton	$\{934.488,\ 36.3887,\ 20.8212\}$	$\{666.065,\ 114.311,\ -25.9387\}$
helium	$\{871.638,\ 14.3515,\ -16.0098\}$	$\{649.36,\ 92.8308,\ 7.43556\}$
oxygen	$\{814.206,\ 26.8968,\ 14.1721\}$	$\{645.357,\ 80.8384,\ -15.8474\}$
iron	$\{768.464,\ 31.8157,\ -10.4293\}$	$\{633.087,\ 69.736,\ -6.17274\}$

EPOS-LHC

Primary	$X_{\text{fid}}^{\text{up}}$	$X_{\text{fid}}^{\text{low}}$
proton	$\{926.626,\ 45.4516,\ 61.4723\}$	$\{685.006,\ 109.077,\ -15.278\}$
helium	$\{875.464,\ 31.3058,\ 25.5935\}$	$\{685.408,\ 94.9017,\ -13.905\}$
oxygen	$\{818.668,\ 46.3497,\ 26.473\}$	$\{670.51,\ 89.7451,\ 8.18358\}$
iron	$\{780.284,\ 45.9568,\ 8.49168\}$	$\{661.123,\ 69.5838,\ -35.367\}$

APPENDIX C

Tables of results

This chapter includes tables of numerical results obtained in this thesis. If numbers are stated with two uncertainties, the use of the following format is implied: number $\pm$ stat.unc. $\pm$ sys.unc..

C.1 Parameterizations for the universality fiducial selections

The values of the parameterization for the fiducial selection used in universality are provided in this section. For details on the equations used and methodology employed to derive these values, see Section 4.2.2.2. The parameter values for QGSJET-II.04 and data are provided in Table 4.1 and Table 4.3, respectively.

Table C.1: Parameters for the lower and upper limit for the universality fiducial selection of simulated air showers generated with the EPOS-LHC interaction model.

Lower limit		
Primary	a	b
proton	-0.07 ± 0.04	0.10 ± 0.04

Upper limit			
Primary	a	b	c
proton	0.58 ± 0.01	-0.03 ± 0.03	0.22 ± 0.02
helium	0.55 ± 0.02	0.24 ± 0.06	-0.01 ± 0.05
oxygen	0.53 ± 0.02	0.16 ± 0.10	0.05 ± 0.08
iron	0.55 ± 0.01	0.22 ± 0.05	-0.00 ± 0.04

Table C.2: Parameters for the lower and upper limit for the universality fiducial selection of simulated air showers generated with the SIBYLL-2.3 interaction model.

Lower limit

Primary	a	b
proton	-0.13 ± 0.04	0.17 ± 0.04

Upper limit

Primary	a	b	c
proton	0.56 ± 0.02	0.14 ± 0.07	0.06 ± 0.06
helium	0.54 ± 0.01	0.28 ± 0.05	-0.05 ± 0.04
oxygen	0.55 ± 0.01	0.25 ± 0.04	-0.04 ± 0.03
iron	0.56 ± 0.01	0.18 ± 0.05	0.01 ± 0.04

C.2 Parameterizations of the biases as functions of energy

The parameters for the bias in universality-reconstructed simulations are provided in this section. For details on the equations used and methodology employed to derive these values, see Section 4.2.3. The parameters for QGSJET-II.04 are provided in Table 4.2. The biases and resolutions for proton- and iron-induced simulations from the different interaction models and golden hybrid data are compared in Fig. 4.12. Due to the few events contained in the golden hybrid data set (less than 2100), the non-linear description of the bias is first corrected for using the parameterized bias found for simulated showers of the QGSJET-II.04 interaction model. The parameterized bias of data after this correction is given in Table 4.3.

Table C.3: Parameters for the fits of the bias and resolution for the depth of the shower maxim and relative muonic content for simulated air showers generated with the EPOS-LHC interaction model.

Bias of $(X_{\mathrm{max}}^{\mathrm{Univ}} - X_{\mathrm{max}}^{\mathrm{Univ}})$

Primary	a	b	c	d
proton	9.4 ± 0.5	-1.1 ± 1.6	8.0 ± 5.8	-11.7 ± 5.3
helium	8.7 ± 0.4	4.5 ± 1.4	20.6 ± 5.1	-26.2 ± 4.7
oxygen	10.2 ± 0.3	10.1 ± 1.2	16.2 ± 4.2	-21.8 ± 3.9
iron	12.0 ± 0.3	14.5 ± 1.0	11.7 ± 3.5	-17.1 ± 3.3

Resolution of $(X_{\mathrm{max}}^{\mathrm{Univ}} - X_{\mathrm{max}}^{\mathrm{Univ}})$

Primary	a	b	c	d
proton	62.7 ± 0.5	-67.8 ± 1.8	64.3 ± 6.6	-29.1 ± 5.9
helium	53.3 ± 0.5	-59.1 ± 1.7	68.9 ± 5.9	-34.6 ± 5.2
oxygen	44.5 ± 0.4	-49.9 ± 1.6	52.3 ± 5.2	-23.2 ± 4.4
iron	36.7 ± 0.3	-38.0 ± 1.3	37.3 ± 4.0	-16.5 ± 3.5

Bias of $(R_{\mu}^{\mathrm{Univ}} / R_{\mu}^{\mathrm{MC}} - 1)$

Primary	a	b	c	d
proton	0.074 ± 0.002	-0.221 ± 0.006	0.148 ± 0.020	-0.019 ± 0.017
helium	0.048 ± 0.001	-0.176 ± 0.005	0.187 ± 0.016	-0.063 ± 0.014
oxygen	0.033 ± 0.001	-0.144 ± 0.004	0.154 ± 0.013	-0.038 ± 0.011
iron	0.022 ± 0.001	-0.128 ± 0.003	0.146 ± 0.011	-0.028 ± 0.010

Resolution of $(R_{\mu}^{\mathrm{Univ}} / R_{\mu}^{\mathrm{MC}} - 1)$

Primary	a	b	c	d
proton	0.228 ± 0.004	-0.282 ± 0.013	0.181 ± 0.044	-0.050 ± 0.037
helium	0.160 ± 0.002	-0.213 ± 0.006	0.291 ± 0.024	-0.163 ± 0.022
oxygen	0.134 ± 0.001	-0.187 ± 0.004	0.189 ± 0.015	-0.075 ± 0.013
iron	0.120 ± 0.001	-0.159 ± 0.003	0.144 ± 0.009	-0.057 ± 0.008

Table C.4: Parameters for the fits of the bias and resolution for the depth of the shower maxim and relative muonic content for simulated air showers generated with the SIBYLL-2.3 interaction model.

Bias of $(X_{\mathrm{max}}^{\mathrm{Univ}} - X_{\mathrm{max}}^{\mathrm{Univ}})$

Primary	a	b	c	d
proton	-1.0 ± 0.5	-3.3 ± 1.8	-2.7 ± 6.6	-5.1 ± 6.3
helium	-3.6 ± 0.5	$\pm 2.4 \pm 1.5$	17.2 ± 5.6	-23.6 ± 5.2
oxygen	-2.9 ± 0.4	$\pm 8.1 \pm 1.2$	14.1 ± 4.6	-23.0 ± 4.5
iron	-0.3 ± 0.3	$\pm 10.7 \pm 1.0$	-2.1 ± 3.8	-4.4 ± 3.6

Resolution of $(X_{\mathrm{max}}^{\mathrm{Univ}} - X_{\mathrm{max}}^{\mathrm{Univ}})$

Primary	a	b	c	d
proton	68.6 ± 0.6	-80.4 ± 2.0	75.6 ± 7.8	-28.3 ± 8.2
helium	59.3 ± 0.5	-57.2 ± 1.8	49.9 ± 6.4	-19.6 ± 5.8
oxygen	46.3 ± 0.4	-50.8 ± 1.6	67.7 ± 5.8	-39.6 ± 5.4
iron	38.7 ± 0.4	-41.0 ± 1.5	50.2 ± 5.0	-27.7 ± 4.3

Bias of $(R_{\mu}^{\mathrm{Univ}} / R_{\mu}^{\mathrm{MC}} - 1)$

Primary	a	b	c	d
proton	0.057 ± 0.002	-0.263 ± 0.007	0.220 ± 0.023	-0.074 ± 0.020
helium	0.035 ± 0.001	-0.195 ± 0.005	0.174 ± 0.017	-0.055 ± 0.015
oxygen	0.021 ± 0.001	-0.161 ± 0.004	0.164 ± 0.013	-0.050 ± 0.013
iron	0.016 ± 0.001	-0.135 ± 0.003	0.142 ± 0.012	-0.039 ± 0.010

Resolution of $(R_{\mu}^{\mathrm{Univ}} / R_{\mu}^{\mathrm{MC}} - 1)$

Primary	a	b	c	d
proton	0.266 ± 0.006	-0.360 ± 0.015	0.180 ± 0.050	0.011 ± 0.042
helium	0.179 ± 0.002	-0.231 ± 0.008	0.255 ± 0.027	-0.120 ± 0.025
oxygen	0.140 ± 0.001	-0.190 ± 0.004	0.208 ± 0.015	-0.102 ± 0.014
iron	0.126 ± 0.001	-0.166 ± 0.003	0.158 ± 0.010	-0.067 ± 0.009

C.3 The mass composition of UHECRs

Results on the mass composition of UHECRs derived from a shower universality analysis of SD-1500 data are discussed in detail in Chapter 5.

Table C.5: Values of the first two central moments of the measured X_{max} distributions for the constrained axis reconstruction of SD-1500 data. Only non-saturated events are included. The systematic uncertainties are fully correlated between the energy bins.

Range in $\lg(E/\mathrm{eV})$	$\langle \lg(E/\mathrm{eV}) \rangle$	N	$\langle X_{\mathrm{max}} \rangle / \left(\mathrm{g\,cm^{-2}}\right)$	$\sigma(X_{\mathrm{max}}) / \left(\mathrm{g\,cm^{-2}}\right)$
$[18.5, 18.6)$	18.546	23 598	$757.2 \pm 0.8 \pm 12.0$	$73.8 \pm 0.7 \pm 4.0$
$[18.6, 18.7)$	18.646	14 845	$757.8 \pm 0.9 \pm 12.0$	$68.1 \pm 0.9 \pm 4.0$
$[18.7, 18.8)$	18.747	9366	$758.1 \pm 0.9 \pm 12.0$	$58.6 \pm 1.0 \pm 4.0$
$[18.8, 18.9)$	18.847	6337	$758.8 \pm 1.0 \pm 12.0$	$54.3 \pm 1.1 \pm 4.0$
$[18.9, 19.0)$	18.947	4609	$763.0 \pm 1.1 \pm 12.0$	$50.4 \pm 1.2 \pm 4.0$
$[19.0, 19.1)$	19.047	3177	$765.3 \pm 1.1 \pm 12.0$	$46.8 \pm 1.2 \pm 4.0$
$[19.1, 19.2)$	19.146	2171	$766.6 \pm 1.3 \pm 12.0$	$45.4 \pm 1.4 \pm 4.0$
$[19.2, 19.3)$	19.246	1295	$770.3 \pm 1.6 \pm 12.0$	$47.1 \pm 1.8 \pm 4.0$
$[19.3, 19.4)$	19.344	647	$773.9 \pm 2.3 \pm 12.0$	$29.9 \pm 1.4 \pm 4.0$
$[19.4, 19.5)$	19.448	360	$771.9 \pm 2.2 \pm 12.0$	$34.5 \pm 2.5 \pm 4.0$
$[19.5, 19.6)$	19.546	212	$779.1 \pm 4.7 \pm 12.0$	$27.5 \pm 1.4 \pm 4.0$
$[19.6, 19.69)$	19.636	96	$786.4 \pm 3.8 \pm 12.0$	$32.9 \pm 6.5 \pm 3.0$
$[19.69, 19.76)$	19.724	33	$789.5 \pm 5.1 \pm 12.0$	$31.3 \pm 7.9 \pm 3.0$
$[19.76, \infty)$	19.845	33	$810.8 \pm 6.0 \pm 12.0$	$25.8 \pm 4.8 \pm 4.0$

Table C.6: Values of the first central moment of the measured R_μ distributions for the constrained axis reconstruction of SD-1500 data. Only non-saturated events are included. The systematic uncertainties are fully correlated between the energy bins.

Range in $\lg(E/\mathrm{eV})$	$\langle \lg(E/\mathrm{eV}) \rangle$	N	$\langle R_\mu \rangle / \left(\mathrm{g\,cm^{-2}}\right)$
$[18.5, 18.6)$	18.546	23 598	$1.941 \pm 0.003 \pm 0.06$
$[18.6, 18.7)$	18.646	14 845	$1.909 \pm 0.003 \pm 0.06$
$[18.7, 18.8)$	18.747	9366	$1.878 \pm 0.003 \pm 0.06$
$[18.8, 18.9)$	18.847	6337	$1.864 \pm 0.003 \pm 0.06$
$[18.9, 19.0)$	18.947	4609	$1.854 \pm 0.004 \pm 0.06$
$[19.0, 19.1)$	19.047	3177	$1.838 \pm 0.004 \pm 0.06$
$[19.1, 19.2)$	19.146	2171	$1.832 \pm 0.005 \pm 0.06$
$[19.2, 19.3)$	19.246	1295	$1.828 \pm 0.006 \pm 0.06$
$[19.3, 19.4)$	19.344	647	$1.872 \pm 0.007 \pm 0.06$
$[19.4, 19.5)$	19.448	360	$1.896 \pm 0.011 \pm 0.06$
$[19.5, 19.6)$	19.546	212	$1.896 \pm 0.013 \pm 0.06$
$[19.6, 19.69)$	19.636	96	$1.858 \pm 0.014 \pm 0.06$
$[19.69, 19.76)$	19.724	33	$1.865 \pm 0.042 \pm 0.06$
$[19.76, \infty)$	19.845	33	$1.817 \pm 0.019 \pm 0.06$

APPENDIX D

Analyses

The analyses contained in this appendix are supplements to those shown in the main body of the text. As such from section to section, there are no transitions, and oftentimes, there are no direct connections between the analyses. Succinct summaries are provided at the beginning of each section to provide the necessary link to the main text.

D.1 Proposed change from likelihood to deviance function

In comparing the universality reconstructed X_{max} to that of the fluorescence detector, it is possible to ascertain the quality of the reconstruction method employed. As shown in Fig. D.1a for non-saturated events, the $X_{\mathrm{max}}^{\mathrm{Univ}}$ compared to $X_{\mathrm{max}}^{\mathrm{FD}}$ has a large standard deviation of $118.5\,\mathrm{g\,cm^{-2}}$ for events with $\lg(E/\mathrm{eV}) > 18.5$. With an increased energy threshold of $\lg(E/\mathrm{eV}) > 19$, the standard deviation is roughly halved to $56\,\mathrm{g\,cm^{-2}}$. Intuitively, it makes sense that lower energy events should have a worse resolution than that of higher energy events; lower energy events have, on average, lower signals and fewer triggered stations, leading to less information to use for constraining a universality reconstruction. Nevertheless, it is possible that some of these inaccuracies associated with the reconstructed X_{max} can be attributed to the minimizing function used.

In a recent work [192], the negative log-likelihood function is replaced with a goodness-of-fit estimator using a generalized χ^2-method [193] —known as the deviance method [194]. The methodology of the deviance method is described in Appendix D.1.1. At the time of writing this work, the deviance minimizing function is not included in Offline. The comparative analysis between the two methods with is presented in this work (Appendix D.1.2) indicates that the deviance method does not perform better overall than the negative log-likelihood method and would need to be refined before being added to Offline.

D.1.1 Constructing the deviance minimizing function

The deviance method uses the ratio between the considered and saturated[1] models:

$$D = -2\ln\frac{\mathcal{L}}{\mathcal{L}_{\mathrm{sat}}} \tag{D.1}$$

[1] Here, saturated refers to a model with a parameter for each event so as to fit the data exactly. These terms are constructed from the log-normal relationships used in the negative log-likelihood.

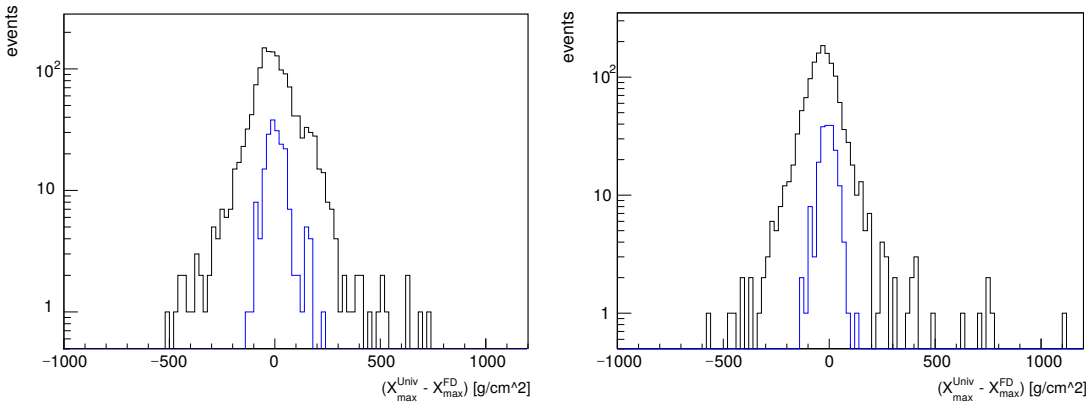

Figure D.1: Distributions of the differences between $X_{\max}$ of universality and the FD for golden hybrid events from 2004-2014. The global universality reconstruction method is used with the (a) log-likelihood and (b) deviance method. The black histogram is for all events with $\lg(E/\text{eV}) > 18.5$ and $\theta_{SD} < 60^\circ$, whereas the blue histogram has events with $\lg(E/\text{eV}) > 19$ and $\theta_{SD} < 54^\circ$ (all from [192]).

The deviance term relating to the ℓ_{LDF}, Eq. (3.17) from the log-likelihood, becomes:

$$D_{\text{LDF}} = 2 \sum_{i}^{\text{stations}} p(f_s) \cdot S_i \ln \frac{S_i}{\hat{S}_i} + p(f_s) \cdot \hat{S}_i - p(f_s) \cdot S_i, \tag{D.2}$$

where $p(f_s)$ is the Poisson factor given in Eq. (2.4), S_i is the measured signal, and $\hat{S}_i$ is the model estimate for the signal given in Eq. (3.12). Similarly, the equivalent ℓ_{shape}, likelihood term given in Eq. (3.13), for the deviance method is:

$$D_{\text{shape}} = \sum_{s}^{\text{stations}} \sum_{i} \left(\frac{S_{s,i} - \hat{S}_{s,i}}{\sigma_{\text{SD}}(\hat{S}_{s,i})} \right)^2, \tag{D.3}$$

where σ_{SD} is from the signal uncertainty model detailed in Eq. (2.3). The reconstruction using the deviance method is shown in Fig. D.1b. The standard deviation for events with $\lg(E/\text{eV}) > 18.5$ is slightly reduced to $105\,\text{g}\,\text{cm}^{-2}$, whereas the standard deviation for events with $\lg(E/\text{eV}) > 19$ is reduced to $39\,\text{g}\,\text{cm}^{-2}$.

In a follow-up study [195], the author of [192] pointed out that the bin uncertainty used for the shape fit[2] —Section 3.2.1.1— may also account for some of the mis-reconstructed $X^{\text{Univ}}_{\max}$ values. As $p(f_s)$ and $\sigma[S]$ have values close to 1, the uncertainty of the signal in each bin can be considered *quasi-Poissonian*. Based upon an analysis of the trace in comparison with these uncertainties, it was found that there may be a loss of information due to overestimation of the uncertainties, particularly in bins associated with a low signal. Using a toy model created by bootstrapping signal traces where the jumps in the trace are thought of as being bunched into clusters, it was found that the bin signal dispersion should be resized to half of its current formula[3] —given in Eq. (3.14):

$$\sigma = \frac{1}{2} \cdot \sigma[\text{S}] \cdot p(f_s) \cdot \sqrt{S}, \tag{D.4}$$

[2]Since the advent of the universality method, the bin uncertainties used for the shape fit have not been properly defined. This is critical, however, for fitting low energy events, particularly if universality were to be extended to the SD-750.

[3]As mentioned at the end of this text, a simple multiplicative factor is not sufficient to describe the changes needed for the binned uncertainties of the shape fit.

Table D.1: Reconstruction results of X_{max} obtained by performing the specified modifications (taken from [195]). Golden hybrid events from 2004-2013 were reconstructed using the ICRC2015 parameterizations [69]. The **...** indicate that the deviance method was coupled with these additions during reconstruction.

	Efficiency	Bias /(g cm^2)	RMS
negative log-likelihood	226/228 (99.1 %)	0.44 ± 3.96	59.5 ± 2.8
deviance	218/228 (95.6 %)	-13.71 ± 3.04	44.9 ± 2.2
... with bin reducing factor	215/228 (94.3 %)	-13.35 ± 3.04	44.6 ± 2.2
... with bin reducing factor & start-stop fit	208/227 (91.6 %)	-2.39 ± 2.88	41.5 ± 2.0

With this change implemented in conjunction with the deviance, the standard deviation between X_{max}^{Univ} and X_{max}^{FD} was reduced by 10 g cm^{-2} for the lower energy events[4]. Additionally, it was noted that the start and stop times for the shape fit could be made to be more rigorous[5]. To overcome this, the shape fit start time was redefined to be the start bin given by the SD reconstruction. The stop bin is then defined as the first bin above 0.5 VEM which is followed by at least two bins with signal below 0.5 VEM. This definition reduces the standard deviation of the difference between X_{max}^{Univ} and X_{max}^{FD} by 3 g cm^{-2} for all events.

D.1.2 In-depth comparative analysis to negative log-likelihood

Encouraged by these promising results, the author of [192, 195] and I worked together to create a joint Offline application from which the results of this section are derived. When the method was presented in [192] and [195], the author used golden hybrid events reconstructed with the global method and studied the resulting depth of the shower maximum distribution as a whole for events above 10^{19} eV and with a zenith angle less than 60°. In his studies, the author calculated the bias and resolution as he added each of his improvements. A sample of the plots shown from those studies are presented in Fig. D.1, and the resulting distribution parameters are summarized in Table D.1. With each new modification of the reconstruction, the resolution is seen to improve at the cost of reduced efficiency. It was hoped that the events now failing the reconstruction were ill-fitting or outliers in the negative log-likelihood, but as shown in this work, this was not the case. Furthermore, by performing studies with respect to different energy bins, it is found that the deviance method —without further modification— performs just slightly worse than the negative log-likelihood method. The deviance method is still a viable reconstruction method, but before implementing this method in Offline, further improvements and cross-checks should be performed to ensure that it is performing as well as or better than the negative log-likelihood method.

Due to its conservative nature, the global fit (Section 3.2.3.2) provides an ideal reconstruction procedure for investigating proposed changes to the function being minimized. The efficiency of golden hybrid events for the negative log-likelihood and deviance with the bin reducing factor and start-stop fit are shown in Fig. D.2. Golden hybrid events are reconstructed from 2004-2015 using the parameterizations presented in Section 2.4 and Section 2.5. The deviance method has more events successfully reconstruct from $10^{18.5}$ eV to $10^{19.0}$ eV than the negative log-likelihood. However, the efficiency of the deviance method at

[4] The higher energy events —which generally do not have low signals— were minimally reduced (less than 1 g cm^{-2}).

[5] As noted in Section 3.2.1, all bins with signal above 0.7 VEM are included, regardless of their position in the time trace.

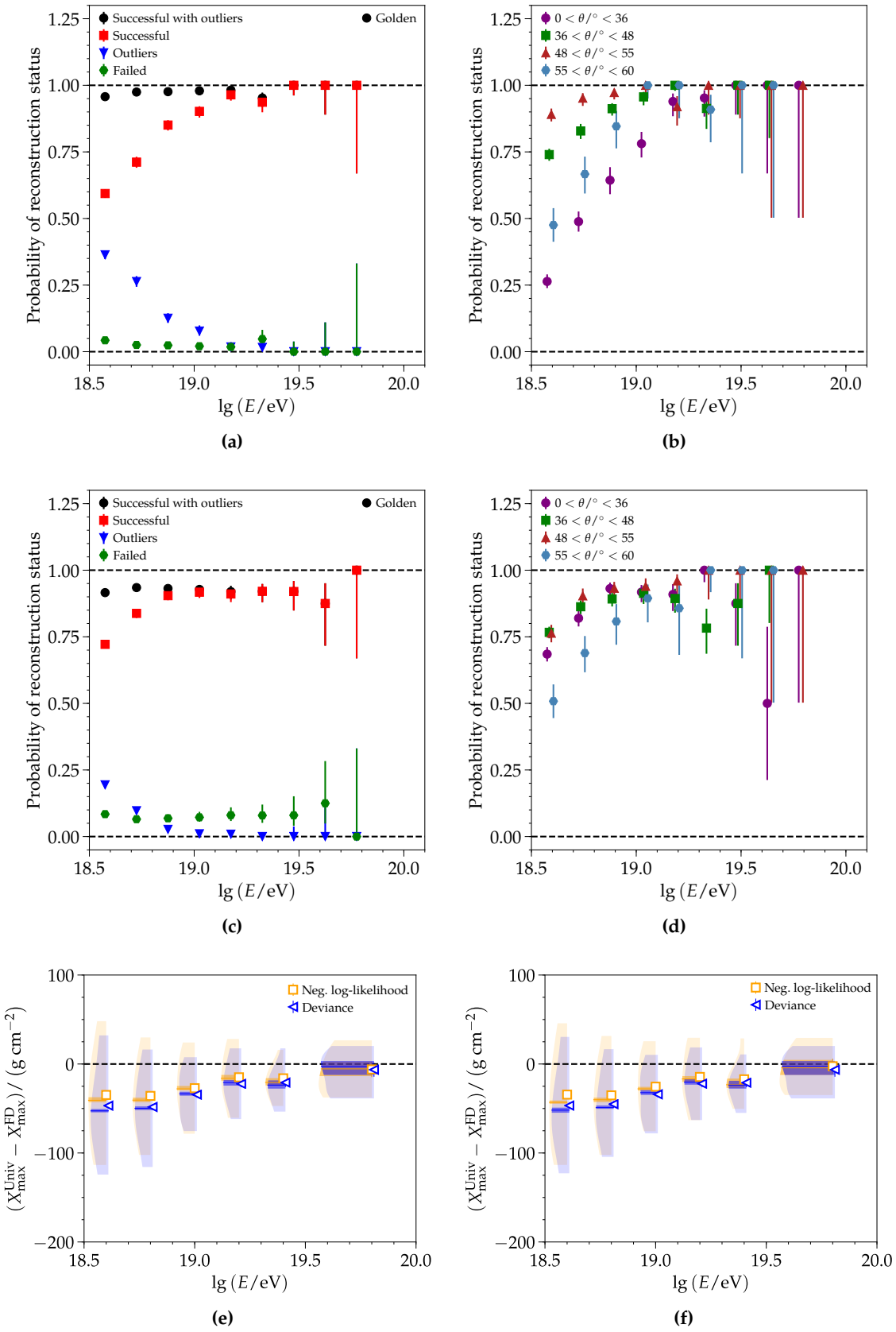

Figure D.2: The global reconstruction coupled with the (*top*) negative log-likelihood and (*middle*) deviance method. (*Bottom*) The distributions of each method are depicted with respect to energy for **successful** events where (e) all events are considered and (f) only events reconstructed with both methods are compared ($N = 1352$). To note, the **deviance** label refers to the deviance method using the bin reducing factor and start-stop fit.

the highest energies shows an increasing number of failed reconstructions. When considering the efficiency of **successful** events, it is seen that the efficiency of the deviance method at the highest energies is largely zenith-dependent. In contrast, the negative log-likelihood at the highest energies is zenith-independent and asymptotically reaches 100 %. In returning to the statistics presented in Table D.1, it can be confirmed from these plots that the reduced efficiency of the various deviance methods does not correlate with improved outlier rejection. Instead, it is rejecting higher energy events with a greater number of candidate stations (8-25) in favor of successfully reconstructing lower energy events with low station multiplicity (4-8). Due to the underlying differences in the prevalence (and arbitrariness in value) of outliers with respect to energy and zenith, it is necessary to use the same criteria to reject outliers from both the negative log-likelihood and deviance method when comparing their resulting distributions of the depth of the shower maximum. When performing the comparison, it is useful to consider cases of all successfully reconstructed events (Fig. D.2e) and only those shared between both methods (Fig. D.2f). The distributions in the non-matching instance show that both methods have a similar negative bias which decreases with energy. Furthermore, a bin-by-bin comparison of the spread indicates that at energies of $10^{18.5} - 10^{18.9}$ eV, the two are more or less the same, and at various higher energies, one method performs slightly better than the other and vice versa. In conducting a study with the events shared between both populations —where the events in the deviance are the limiting factor above 10^{19} eV, it can be seen that the deviance method, on average, has a better resolution than the negative log-likelihood by around $2\,\mathrm{g\,cm^{-2}}$ to $20\,\mathrm{g\,cm^{-2}}$.

The golden hybrid data is restricted to 2105 non-saturated events, of which 334 have energies greater than 10^{19} eV. Furthermore, due to the requirement for well-reconstructed events by the FD, the zenith angle range for vertical events is truncated to 16° to 60°. To further investigate the use of the deviance method and to resolve which aspect of the deviance method leads to the zenith-dependent efficiency seen at the highest energies and which contribute to the improved resolution, much greater event statistics are needed where it is possible to compare reconstructed observables to the true values. As such, QGSJET-II.04 proton-induced simulations from the Napoli library were used; the various deviance methods were investigated individually as depicted in Fig. D.3. In Fig. D.3a, the overall efficiency of the deviance is nearly identical to that of the negative log-likelihood global reconstruction presented in Fig. 3.23a. Furthermore, as shown in Fig. D.4, they yield nearly identical distributions above $10^{18.5}$ eV; the performance of the deviance method is only slightly worse than the performance of the negative log-likelihood approach. Above 10^{19} eV, both results are indistinguishable. This potentially indicates that the contributions of the shape and LDF fit can be rescaled to yield almost equally good results. As discussed in Chapter 3, the shape fit adds values on the bin-level, whereas the LDF fit does so on the station level. Thus, as the primary energy increases, more stations respond with, in theory, more bins meeting the shape fit criteria. At the highest energies, this means that the shape fit contributes an order of 1-2 magnitudes more than the LDF fit contribution. A detailed study of the re-scaling and influence of the fit components could further improve the universality reconstruction and allow for the option of adding silent and saturated terms to the LDF likelihood. This is not investigated further in this work.

As the pure deviance method performs almost as well as the negative log-likelihood, it is, then, the addition of the bin reducing factor and (or) start-stop fit that lead(s) to a reduced resolution. Both modifications improve the efficiency of **successful** reconstructions below $10^{19.3}$ eV. While the lower energy events exhibit relatively small dependencies with zenith angle, the events at the higher energies demonstrate zenith-ordered dependencies. In the most extreme comparison, events with a zenith angle $\theta \in [55, 60]^\circ$ are, on average, less likely to be reconstructed than those in $\theta \in [0, 36]^\circ$ by roughly 15 %. While the addition

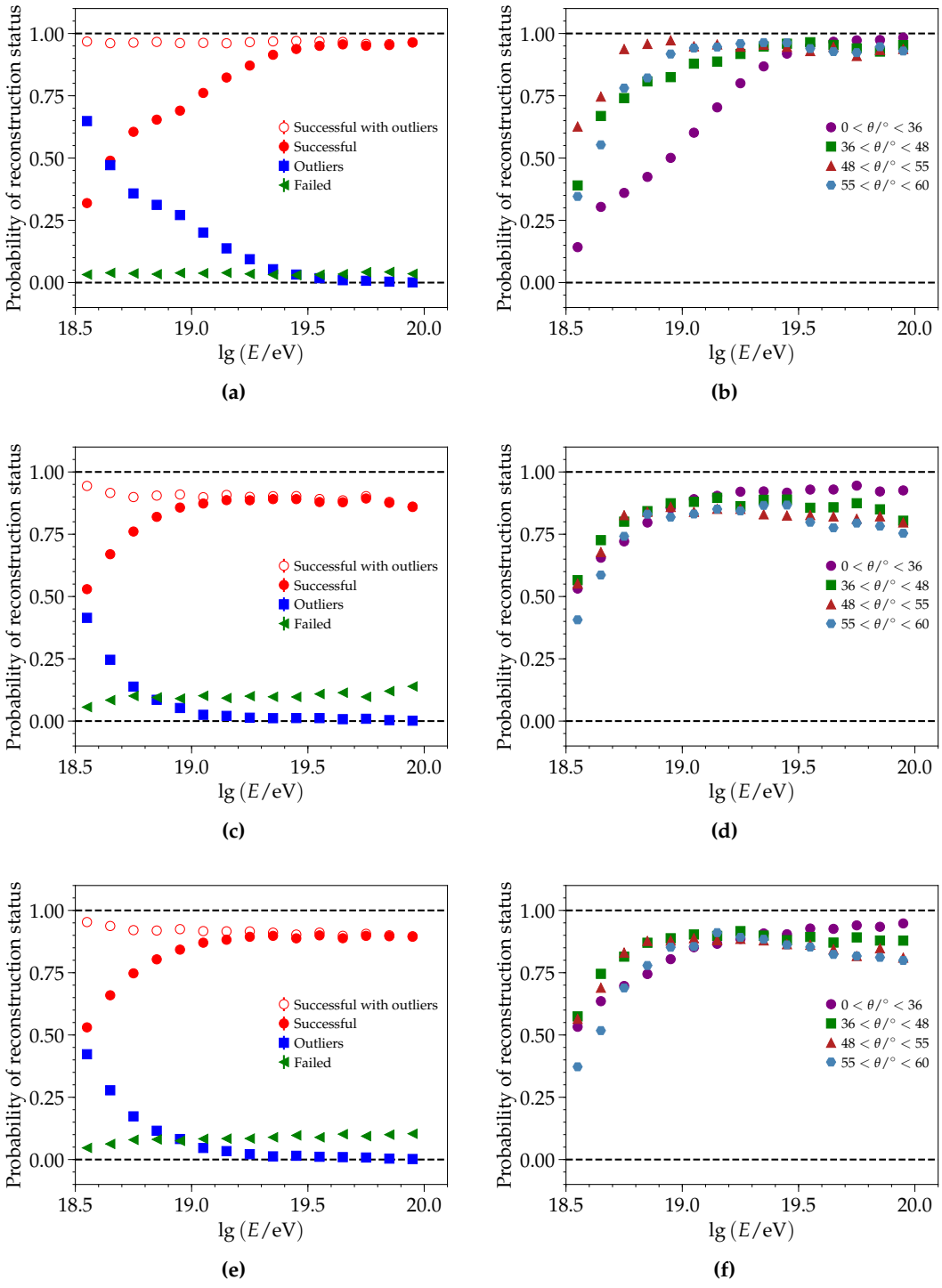

Figure D.3: QGSJET-II.04 proton-induced simulations from the Napoli library reconstructed with the global method using the (*top*) deviance, (*middle*) deviance with bin reducing factors, and (*bottom*) deviance with start-stop fit. Both of the additions to the deviance method show an improved reconstruction rate at lower energies. The method using the bin reducing factor has less of a dependence on zenith angle at low energies than the start-stop fit.

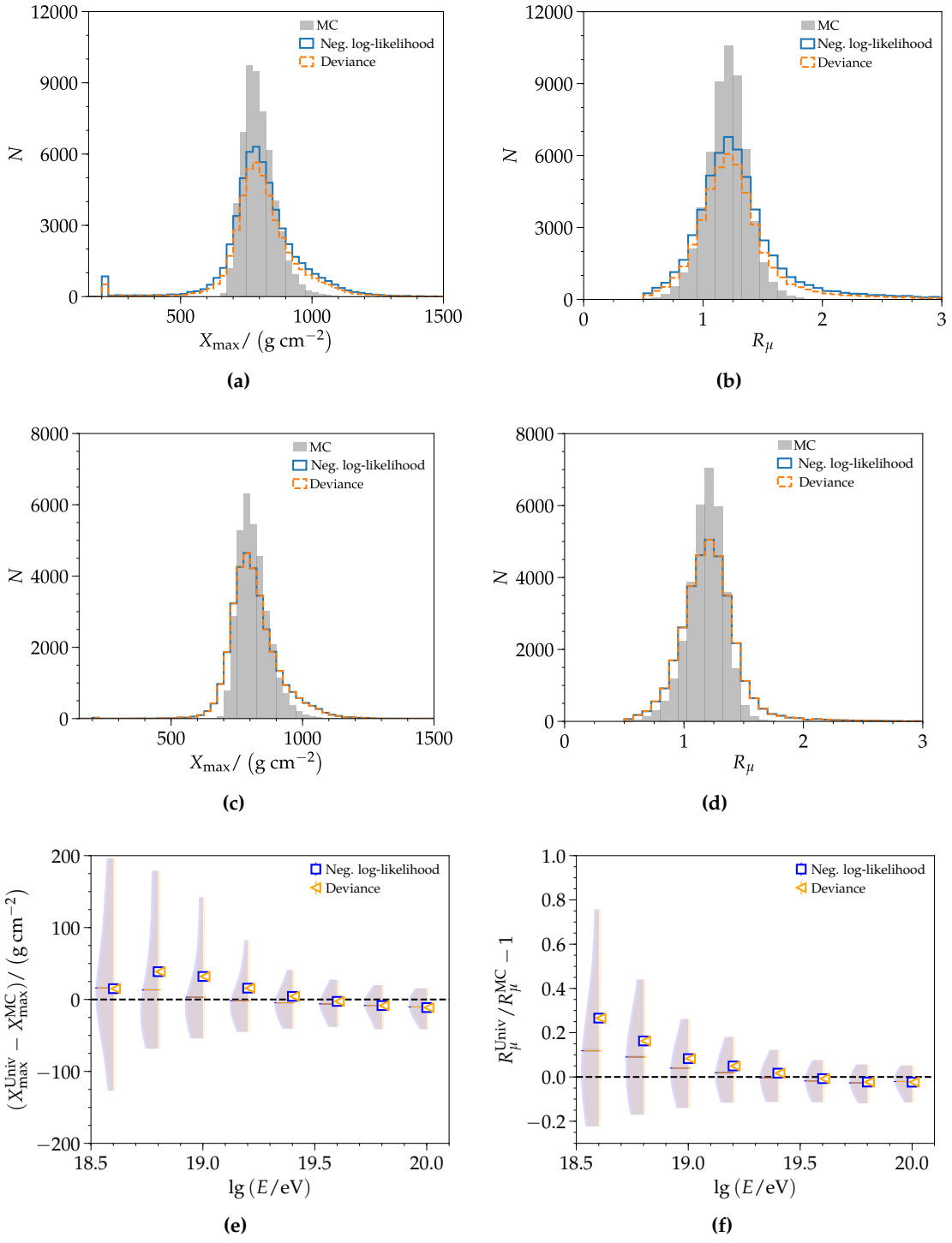

Figure D.4: QGSJET-II.04 proton-induced simulations reconstructed with the global fit using the negative log-likelihood and deviance method without further modifications. The distributions of (a), (c) depth of the shower maximum and (b), (d) relative number of muons are compared for both methods to the true value above $10^{18.5}$ eV and 10^{19} eV, respectively. In the lower energy distributions, the negative log-likelihood method is shown to contain more events than the deviance method while having a comparable resolution. (e), (f) The overall similarity of the distributions is further substantiated when considering the difference in the reconstructed value to the true value with respect to energy.

of either the bin reducing factors and start-stop fit improve the efficiency of lower energy events, their zenith-dependent failure rate at the highest energies is alarming and indicates that an improved definition to either of these methods should be investigated before they are implemented. In the case of the start-stop fit, rigorous testing should be done first to show in which cases the start and stop of the trace are poorly defined. Depending on the algorithm and intended use for the start and stop bins, coordination with the Auger SD reconstruction working group is highly recommended.

For the bin reducing factor, one might naively consider using the modifications in just the lower energy range. However, having a term in the minimizing function which is switched on or off based on an energy threshold is undesirable and would make it difficult, if not impossible, to account for (correlated) systematic effects. Furthermore, a simple multiplicative factor does not take into account the evolution of the signal with energy or other variables. Instead, the uncertainties used in the shape fit should be parameterized as a function of energy such that it can naturally be incorporated in the negative log-likelihood or deviance description. This would make sense for the shower physics as the secondary particle contributions of measured signals change with energy, composition, atmospheric conditions, and zenith angle. So an average model based on a large simulation library with various primaries and interaction models would be needed. Further development on this modification is highly recommendable as the current overestimation of the uncertainties used in the shape fit leads to an overestimation in the uncertainty of the reconstructed observables. As seen in Fig. D.5, the uncertainty calculated using the deviance and the bin reducing factor ranges from around $10\,\mathrm{g\,cm^{-2}}$ to $75\,\mathrm{g\,cm^{-2}}$ less than that found with the negative log-likelihood with respect to energy. When only the pure deviance is used, there is no discernible difference in the calculated uncertainty. This indicates that an improved calculation of the uncertainties used in the shape fit (particularly, for lower signals) could be applied to either minimizing function to yield uncertainties which better reflect the accuracies of reconstructed data.

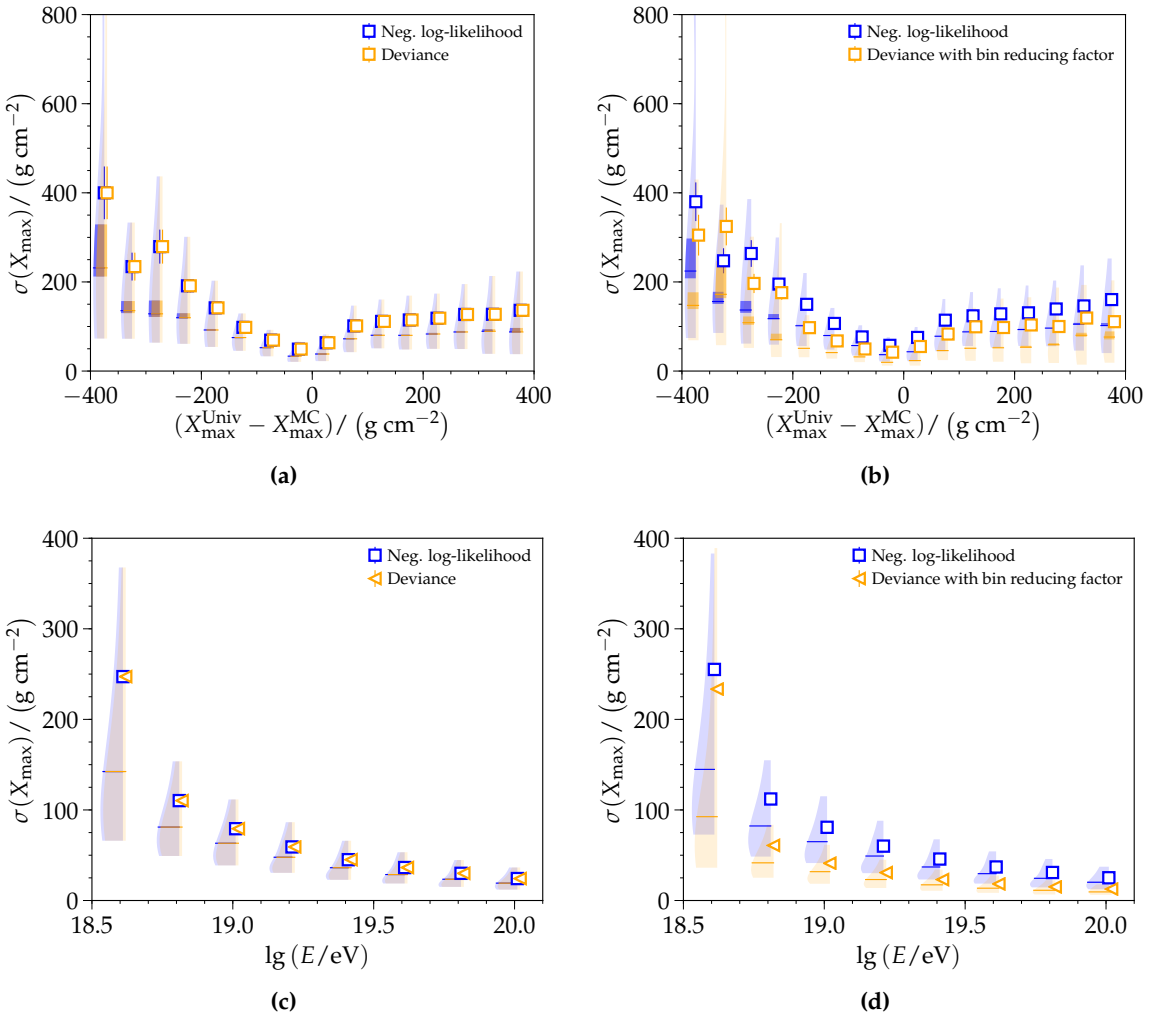

Figure D.5: Comparison of reconstructed uncertainties of QGSJET-II.04 proton-induced simulations for (*left*) the pure deviance and negative log-likelihood and (*right*) the deviance with bin reducing factor and negative log-likelihood reconstructions. More than 48 000 non-saturated events are compared without any outlier rejection. The (pure) deviance and negative log-likelihood reconstructions are indistinguishable in terms of the calculated uncertainties as a function of energy and difference in the reconstructed and true $X_{\max}$. It is, instead, the use of the bin reducing factor that leads to decreased values in the calculated uncertainty; this modification, once better defined, could be applied to either the negative log-likelihood or deviance method.

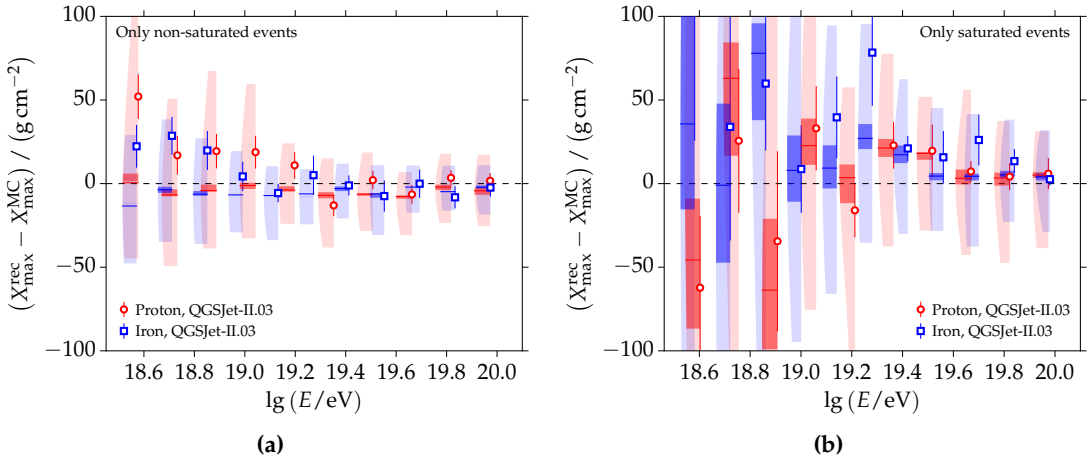

Figure D.6: Biases of the reconstructed depth of the shower maximum for (a) non-saturated and (b) saturated events. Proton- and iron-initiated simulations from QGSJET-II.03 were reconstructed using the iterative fit. Based upon the large biases seen in saturated events, it was determined that such events could only be used above $10^{19.5}$ eV; thus, all saturated events were rejected from the analysis [108].

D.2 Saturation in a WCD

In most of the analyses presented throughout this work, only non-saturated events were considered. The reason for this is based upon: (1) historical results presented in [105] and [108] (e.g. in Fig. D.6) and (2) the general view of saturation as a loss of critical information —due to a truncated trace. In the case of merely SD-based analyses, the saturation of a trace can usually be recovered and used as either a lower limit or equally-participating station in the LDF fit (as discussed further in Section 2.3.2). However, the LDF fails to account for azimuthal asymmetries and only treats the 1-dimensional lateral distribution of the shower. In the case of universality, there is a complicated yet physically-motivated description of the shower development which incorporates relationships between the core and its timing, relative muon content, depth of the shower maximum, and shower geometry. These relationships are evaluated simultaneously in the shape and LDF fit of all triggered stations. Almost all of saturated stations contribute to the shape fit term. Instead of contributing just a single-point to an LDF fit —like in the SD reconstruction, the saturated stations provide precise timing information which is evaluated over multiple bins. This is done using a partial shape fit, as shown in Fig. 3.14c and described in the surrounding text.

In light of the historical rejection of saturated events, it is essential to evaluate which shower energies and geometries are more likely to lead to one or more saturated stations. Furthermore, if saturated events need to be rejected —i.e. as they provide less precise measurements, then the probability of saturation needs to be evaluated for different primary masses to determine if mass composition biases exist in the selection of only non-saturated events. The radial distribution of saturated and non-saturated events are shown for proton-induced simulations and SD data in Fig. D.7. Due to the anticipated saturation of stations close to the shower core, the simulated CORSIKA showers of the Napoli library did not include simulation of secondary particles inside a radial distance of 100 m. Such modifications decrease the computation time and the resulting file size of CORSIKA simulations. The differences in the distribution of saturated stations between data and simulations can mainly be attributed to the differences in the overall spectral index, with more minor contributions from the difference in the composition and the underlying lateral distribution.

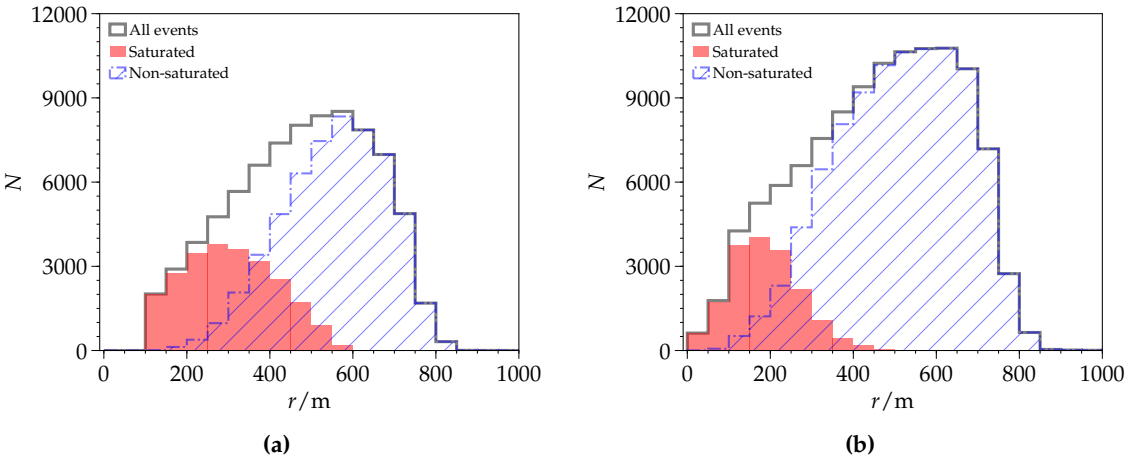

Figure D.7: (a) QGSJET-II.04 proton-induced simulations from the Napoli library and (b) SD data are used to show the distribution of saturated and non-saturated events with respect to the radial distance of the hottest station to the shower core. As simulations follow an energy distribution of E^{-1}, whereas data follows an $E^{-2.5}$ spectra, the distributions appear different. In the other plots throughout this section, energy is explicitly considered, and the distributions for data and simulations with respect to the probability of saturation are shown to be similar.

When the overall probability of saturation as a function of energy is considered, it is clear that the angular and radial dependencies for saturation are very similar in data and simulations, as depicted in Fig. D.8a. Furthermore, there are marginal differences between proton and iron simulations, which are on the order of 5 % at the highest energies. In Fig. D.8b, the probability of saturation is shown with respect to zenith angle. Due to the increased attenuating effect of the atmosphere with increasing zenith angle, saturation is more likely to occur for low zenith angles. This separation becomes negligible at the highest energies. The dominance of the radial dependence of saturation is further scrutinized in Fig. D.8c. As shown, the radius at which saturation starts to occur increases strongly with energy. The combined effect of the zenith angle and radial dependence of saturation is individually considered for simulations and data in Fig. D.9. For radial distances between 100 m to 250 m to the core, the probability of saturation is 100 % for zenith angles below 48°. As the radial range considered increases, the separation between the probability of saturation of the two zenith bins decreases.

The reconstruction efficiencies for the various reconstruction methods are given in Fig. D.10. The overall trends and the zenith-dependence (not shown for saturated) of the various reconstructions are the same as that of non-saturated events presented in Section 3.2.3. With the exception of the iterative fit, the failure rate of saturated events is greater than that of non-saturated events. In the case of the global reconstruction, the failure rate is relatively constant —around 8 % to 10 %— with respect to energy, and the rate of outliers is increased by 10 % to 25 % with the greatest increases seen at low energies. For the constrained and fixed axis reconstructions, the outlier rate of saturated events follows a less steep slope than that seen in non-saturated events. There is a slight increase —on the order of 3 %— in the number of failed events with respect to energy. Perhaps, this is due to a combination of more triggered stations yielding a stricter time constraint and proportionally less of the trace being used in the partial shape fit than at lower energies. In the iterative method, the rate of outlying events is no longer constant with respect to energy; instead, in simulations, the rate decreases from 25 % to around 7 % as energy increases.

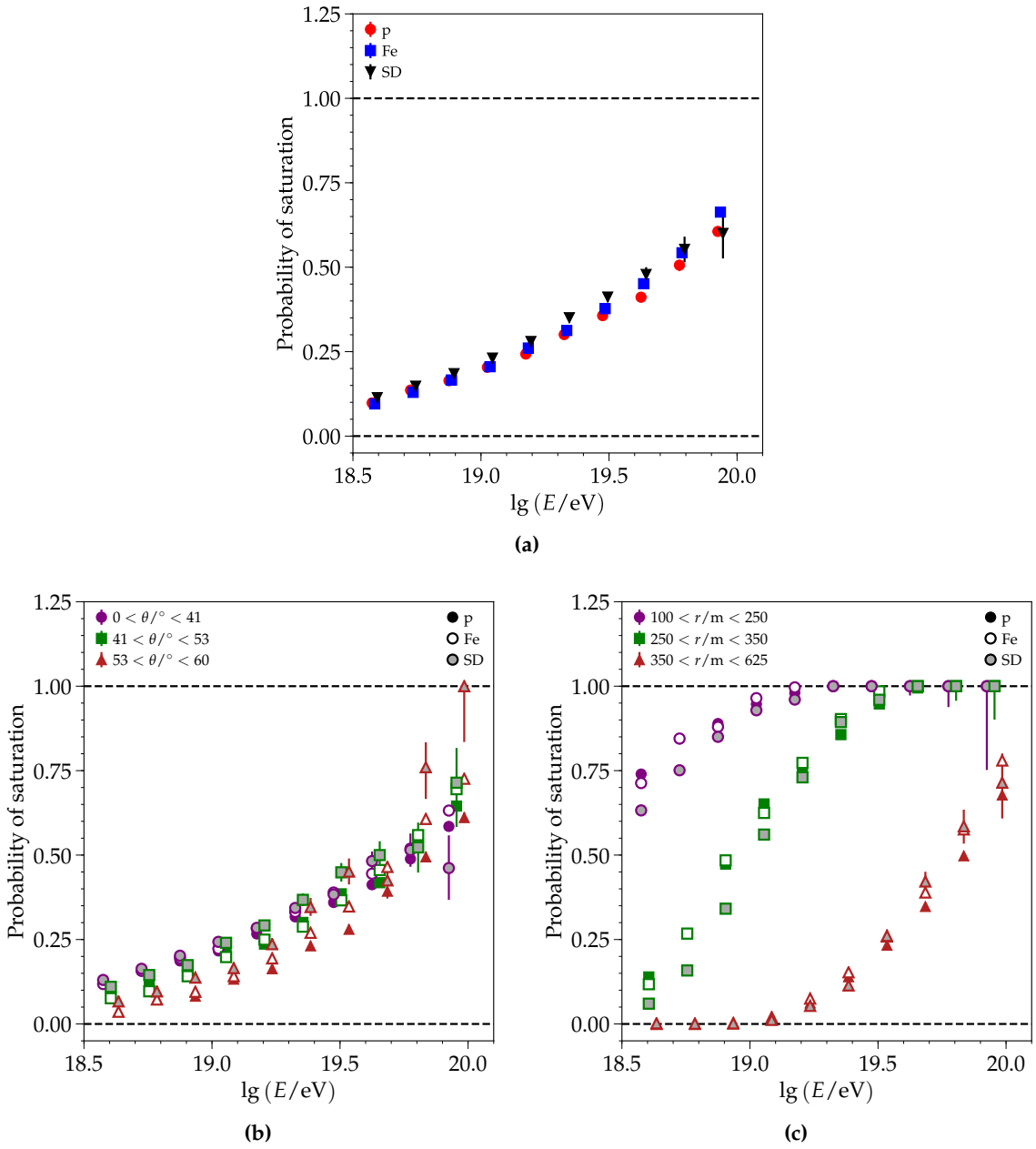

Figure D.8: Probability of saturation for air showers simulated with QGSJET-II.04 proton and iron primaries as well as for SD data. (a) Fraction of saturated events as a function of energy. The probability of saturation is considered with respect to energy for bins in (b) zenith angle and (c) radial distance from the shower core. While there are differences between simulations and data in several bins, the overall trends are similar, and the difference between the probabilities is within 5 % on average.

Encouraged by the similar efficiencies of the constrained and fixed axis method for non-saturated and saturated events, a preliminary investigation into the quality of reconstructed quantities is given in Fig. D.11; the results of other reconstruction methods are also shown. The average reconstructed biases of the axis-constraining methods are within 5 g cm^{-2} of one another, regardless of the saturation status of the events. The corresponding resolution of saturated events is, on average, 10 g cm^{-2} greater than that found for the non-saturated events. In contrast, the bias for saturated events using the global method significantly differs from the non-saturated events in the low energy range. Similarly, the difference in the

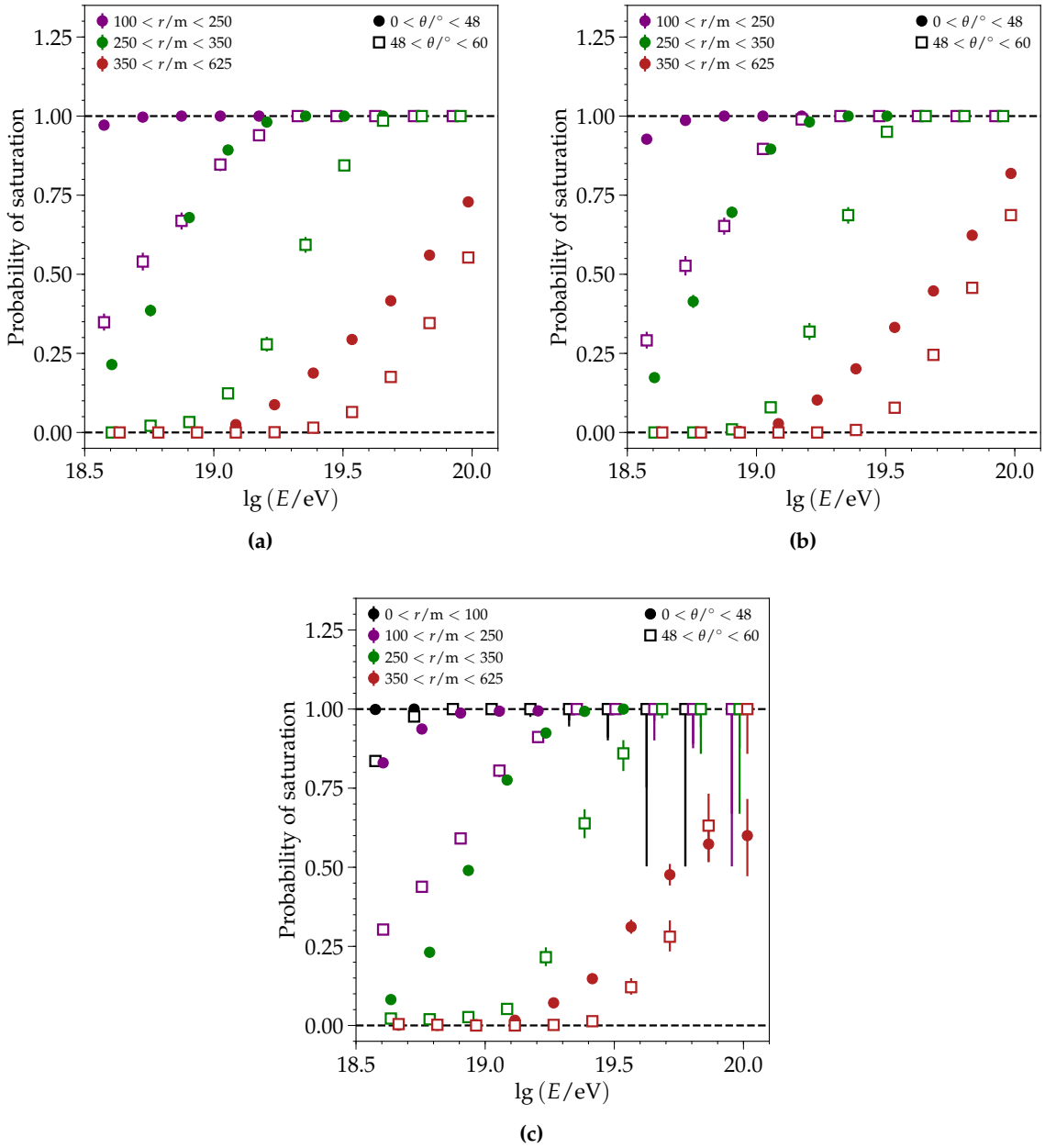

Figure D.9: The saturation efficiencies for QGSJET-II.04 (a) proton- and (b) iron-induced simulations are considered with respect to zenith angle and the minimum radial distance of a station to the shower axis —using the true values. (c) The plot of the saturation efficiency of SD data includes a radial bin from 0 m to 100 m, which is roughly 100 % for all but the lowest energy bins.

resolution of saturated and non-saturated events is, on average, proportionally greatest at low energies and decreases with increasing energy. At the highest energies, the constrained axis, fixed axis, and global methods have similar resolutions for saturated and non-saturated events. The reconstructed bias and resolution of the iterative fit vastly differ for saturated and non-saturated events (confirming what was seen in the past study presented in Fig. D.6). Based upon the results of this combined study, it seems worthwhile to consider saturated events in the constrained axis method. In Fig. 5.4b, the average X_{max} from saturated events is compared to that obtained from non-saturated events. The mean of both sets of data

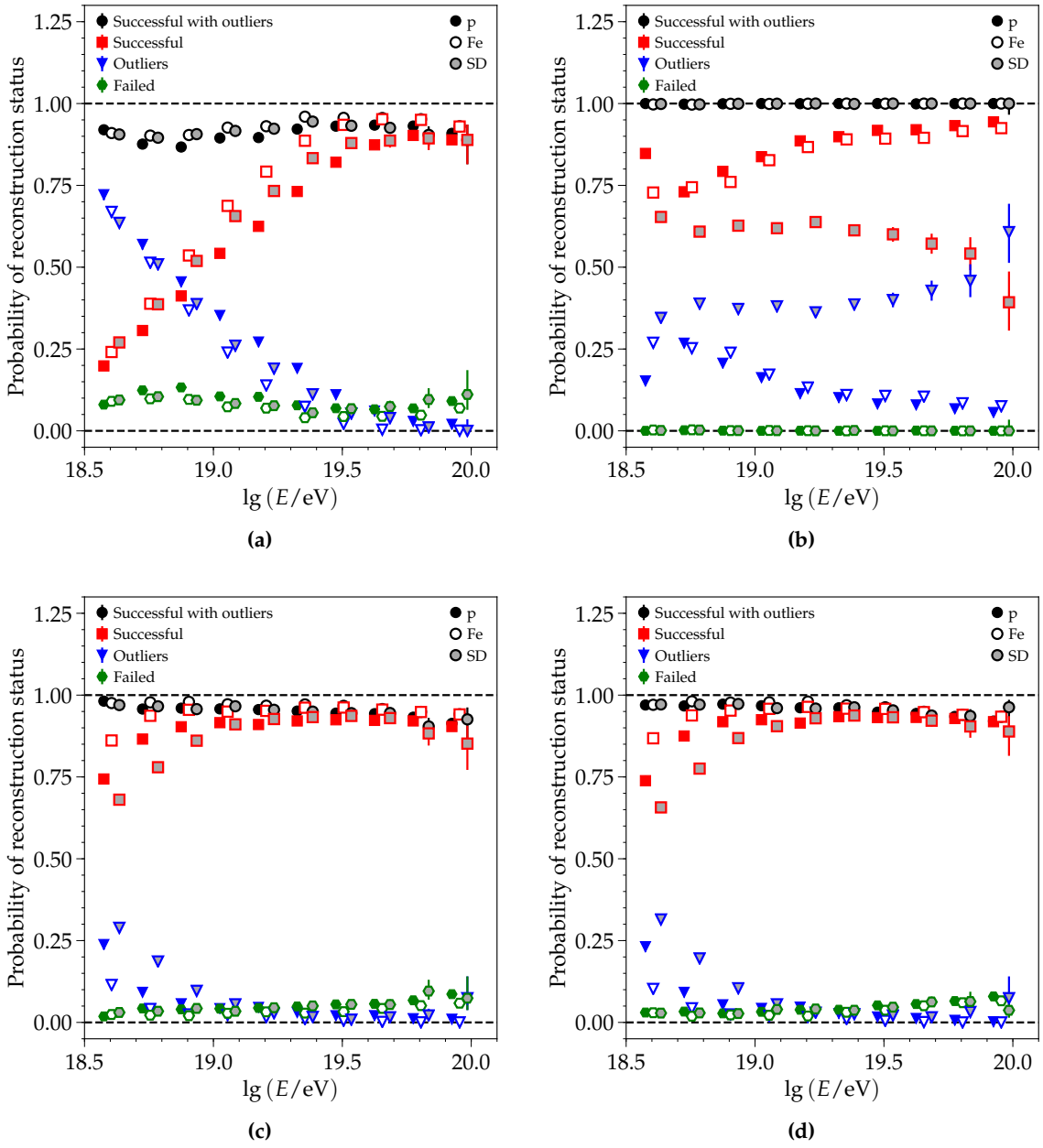

Figure D.10: The reconstruction efficiency of saturated events is shown for QGSJET-II.04 simulations and SD data which were reconstructed using the (a) global, (b) iterative, (c) constrained axis, and (d) fixed axis methods. Outliers are defined as events with $X_{\mathrm{max}} \notin [500, 1050]$ g cm^{-2} and $|\theta_{\mathrm{Univ}} - \theta_{\mathrm{SD}}| > 5°$.

agree above an energy of 10^{19} eV, but below this energy threshold, there is a significant drop in the average value for saturated events. The primary cause for this discrepancy can be attributed to the number of shape stations participating in the reconstruction. As seen in Fig. D.12, saturated events have, on average, one less station participating in the shape fit. This is due to the geometry of saturated events which requires that the shower core lands close to a station, making the next closest stations farther away from the shower core than in a non-saturated event. In considering Fig. 3.26, the reconstruction efficiency of non-saturated events first exceeds 90 % above an energy of $10^{18.7}$ eV, which corresponds to roughly 2-4 shape stations. It is not until an energy of 10^{19} eV that saturated events

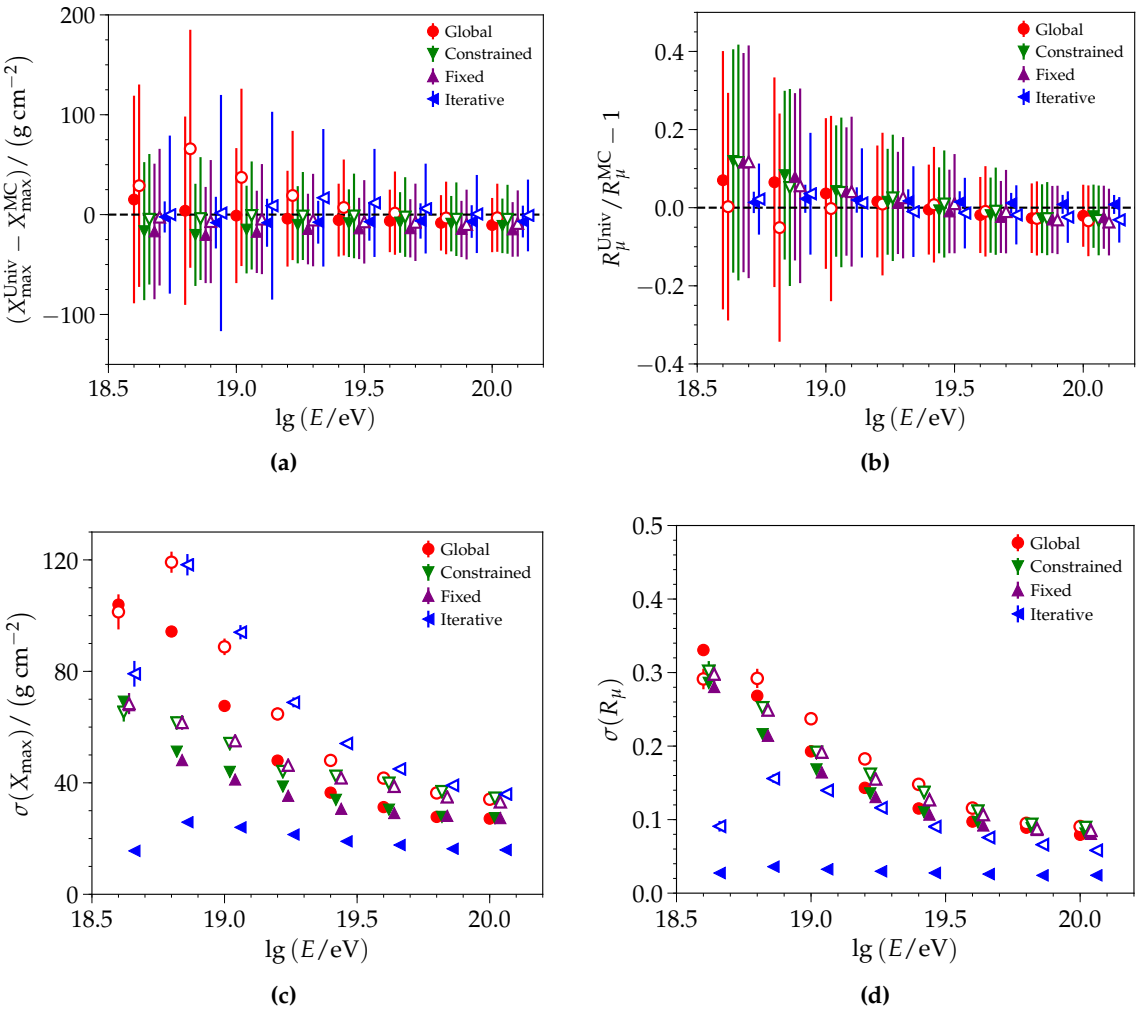

Figure D.11: The (*top*) bias and (*bottom*) resolution of the reconstructed (*left*) depth of the shower maximum and (*right*) relative muon content for QGSJET-II.04 proton-induced simulations from the Napoli library reconstructed with the global, constrained axis, fixed axis, and iterative methods. Only successfully reconstructed events with $X_{max} \in [500, 1050]\ g\,cm^{-2}$ are considered for non-saturated (full markers), and saturated (empty markers) events. In the bias plots, the median and MAD are used, and the error bars represent the $1\,\sigma$ spread. The resolution plots are made using the MAD; the errors are the standard deviation of the MAD as found by bootstrapping.

have, on average, met this requirement. Further studies are needed to assess the reliability of the partial shape fit and to determine if the small PMT of the Auger Upgrade could retroactively be used to improve the fitting procedure of these saturated events. Beyond this, quality cuts for both saturated and non-saturated events should be considered together and separately. As already shown, however, the already existing agreement above 10^{19} eV shows that saturated events are fully recovered in the reconstruction procedure and could potentially be used in mass composition and anisotropy studies.

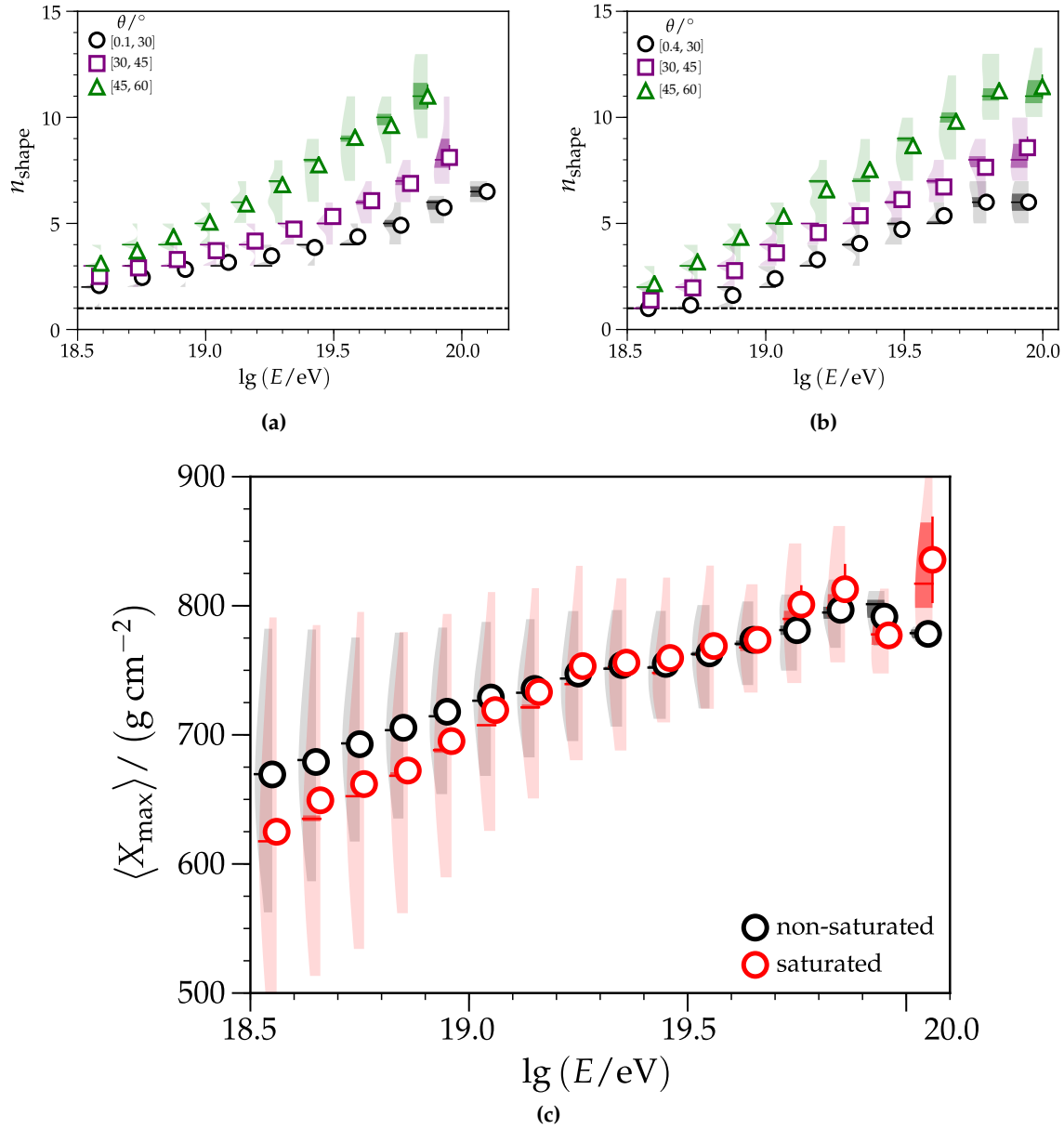

Figure D.12: Number of shape stations as a function of energy for (a) non-saturated and (b) saturated events using SD-1500 data. (c) The average depth of the shower maximum as a function of energy is shown for saturated and non-saturated events without the selection and corrections described in Chapter 4.

D.3 Event selection for the global reconstruction

A detailed description of the global reconstruction procedure is provided in Section 3.2.3.2. Unlike the other reconstruction methods, which use constraints, the global method merely relies on the parameterized universality models to simultaneously fit *eight* physics parameters while holding the energy fixed to that found through the SD reconstruction. In returning to the analyses presented thus far, it is been shown that the global fitting procedure has great difficulty in reconstructing events below 10^{19} eV, particularly those with a zenith angle between 0° to 36° (Fig. 3.23). Furthermore, the initial studies comparing the global to the constrained axis method show an agreement in the average bias and resolution of the depth of the shower maximum and relative muon number above an energy of $10^{19.4}$ eV (Fig. 3.26). Such similarity tentatively indicates that the constrained axis methods may fully incorporate the correlations[6] between the $X_{\max}$ and R_{μ}, which is the salient feature of the global method. Nevertheless, due to its low efficiencies and zenith-dependent bias, the global method is not an ideal candidate for extensive mass composition studies. However, for events with energies above 10^{19} eV, there are enough candidate stations that the zenith-dependent bias is minimal and the results of the global method begin to agree with those found with the other reconstruction types[7] (Fig. 3.26). The purpose of this section is to explicitly show the zenith-dependence of the reconstructed variables of the global method as well as perform an event selection for events above an energy of 10^{19} eV.

The bias of the reconstructed depth of the shower maximum, relative number of muons, and zenith angle are given in Fig. D.13 for QGSJET-II.04 proton and iron-induced simulations. The difference between the reconstructed and true $X_{\max}$ for the global method exhibits a zenith-dependence in its bias and resolution with respect to energy. As discussed in Section 1.1.2, the depth of the shower maximum is proportional to the primary energy and does not explicitly relate to zenith angle. However, in the universality reconstruction, the slant depth of the $X_{\max}$ to each station (depicted in Fig. 3.2) is used in the reconstruction to not only effectively encapsulate the timing of the shower front but also to successfully recover the azimuthal asymmetry of the shower. Thus, the observation of a given $X_{\max}$ by the SD becomes dependent on the zenith angle. In considering the difference between the reconstructed and true zenith angle, it can be seen that the bias is also greatest at lower energies for zenith angles between 0° to 45°. As seen in Fig. 3.22, the number of candidate stations at an energy of 10^{19} eV is, on average, five for smaller zenith angles and nine for larger zenith angles. At an energy of $10^{19.5}$ eV, the average number of candidate stations for smaller zenith angles is almost nine and for higher zenith angles nearly 16 stations trigger. Thus, the increased biases at low energies can be seen as a result of not enough triggered stations for the constrainment of the likelihood of the global procedure. Because of the high number of outliers (and, correspondingly, the large dependencies with respect to zenith angle) below an energy of 10^{19} eV, these events are removed from the analysis. Using such events would distort the underlying distributions of the observables and obscure trends where energy was not an explicit variable.

For events with energies below $10^{19.5}$ eV, the biases of the reconstructed variables still exhibit a dependence with respect to zenith angle, which improves with increasing energy. The mean bias of the depth of the shower maximum as a function of zenith angle differs, at most, by around $150\,\mathrm{g\,cm^{-2}}$. Proton-induced showers may develop deeper in the

[6] The study in Section 4.1 confirms that the constrained axis method contains all correlations found in the global reconstruction method.

[7] In such an energy range, it then becomes possible to use the global method as a benchmark by which to compare the results of other reconstruction methods. If the other reconstructions were to differ significantly from the results of the global method, it would indicate that there was something wrong in those fitting procedures.

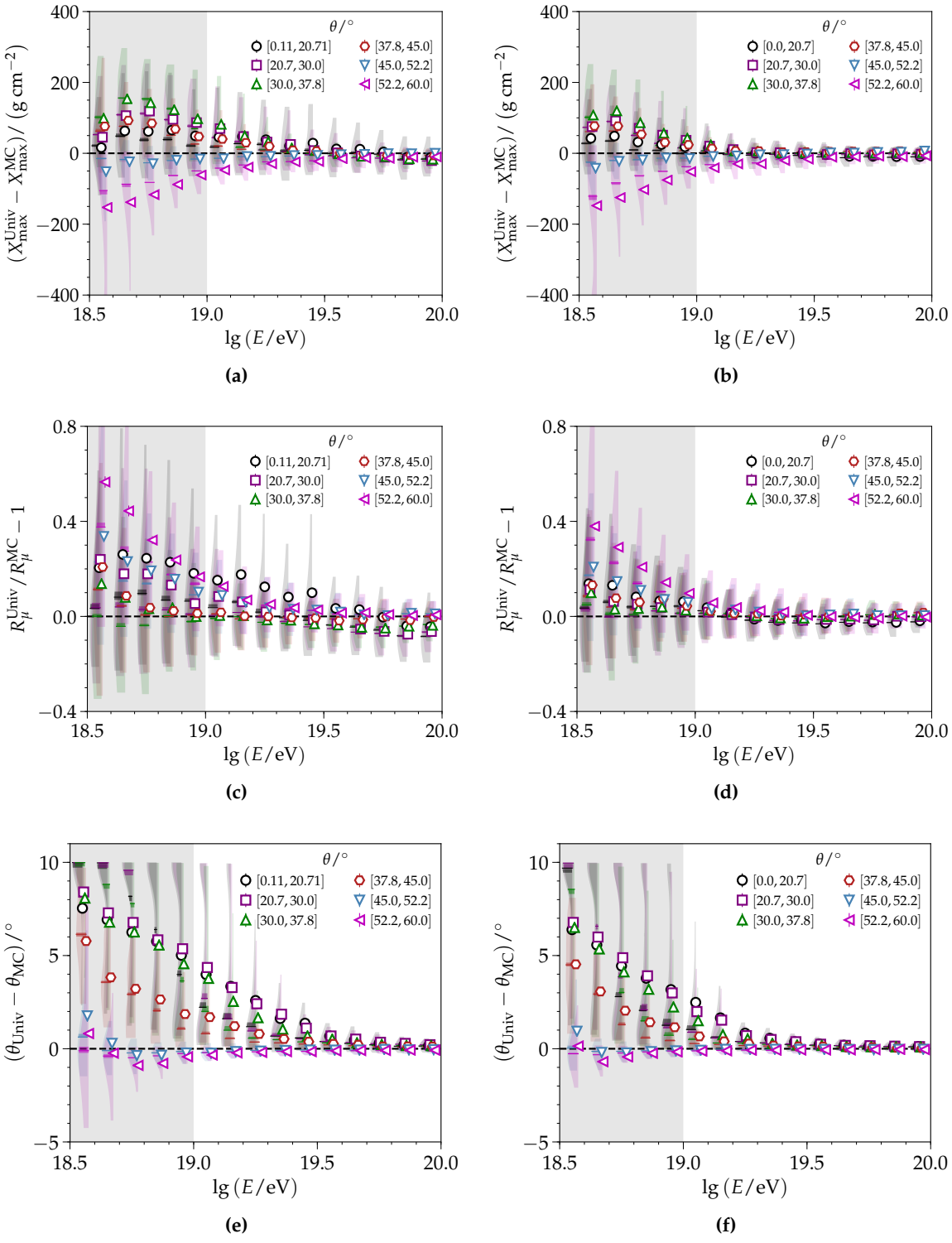

Figure D.13: QGSJET-II.04 (*left*) proton- and (*right*) iron-induced simulations from the Napoli library reconstructed with the global reconstruction method. Only non-saturated events are considered with no further cuts applied. The bias of the reconstructed (*top*) depth of the shower maximum, (*middle*) relative muon content, and (*bottom*) zenith angle are considered with respect to energy and zenith angle. The biases of the depth of the shower maximum and zenith angle are dependent on zenith angle, which is ordered by increasing slant depth. Due to the large zenith-dependent biases, the gray area (below 10^{19} eV) indicates that such events will not be considered in the quality selection; these are, however, shown merely for visual comparison with the results found with the other reconstruction methods.

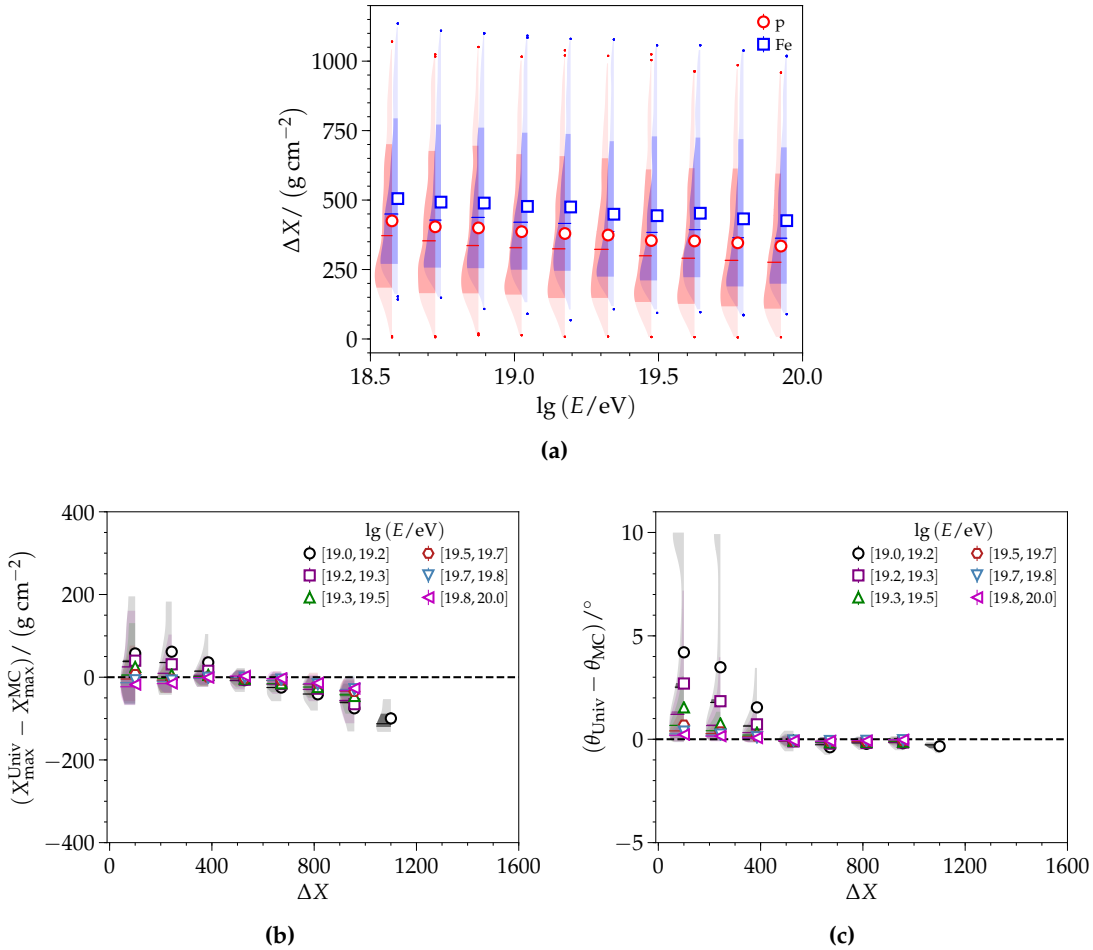

Figure D.14: (a) True slant depth with respect to energy for QGSJET-II.04 simulations of proton- and iron-induced air showers. Both non-saturated and saturated events are shown. $\Delta X = 0$ corresponds an X_{max} at ground-level. When considered as a function of slant depth and energy for non-saturated QGSJET-II.04 proton-induced simulations, the bias for the reconstructed (b) depth of the shower maximum and (c) zenith angle.

atmosphere than extensive air showers initiated by heavier nuclei. When this is taken into account with the effective slant depth for a given zenith angle, it means that proton-induced air showers are more likely to have a depth of the shower maximum closer to ground than iron-induced showers (as depicted in Fig. D.14a). The resulting biases with respect to slant depth (Fig. D.14) may thus not only a product of fewer candidate stations (Fig. 3.22) but also may be attributed to the universality parameterizations not including (enough) showers with X_{max} (close to or) below ground. As the purpose of selecting events in the global method is for mass composition studies, it is not easily possible to perform a cut in ΔX, as this —depending on the zenith angle and composition— will correspond to differing X_{max} values.

Instead, mis-reconstructed events must be identified with a common criterion. As the zenith-dependent biases are seen for all reconstructed variables, it is possible to reject events based on the quality of the reconstructed zenith angle in relation to the true value. As seen in Fig. D.15, proton and iron-induced showers have events with reconstructed zenith angles exceeding 5° of the true values around an energy of 10^{19} eV. Such large deviations in the reconstructed zenith angle to the true value correlate with the positive bias seen in the reconstructed X_{max} for events with a depth of maximum development close to ground.

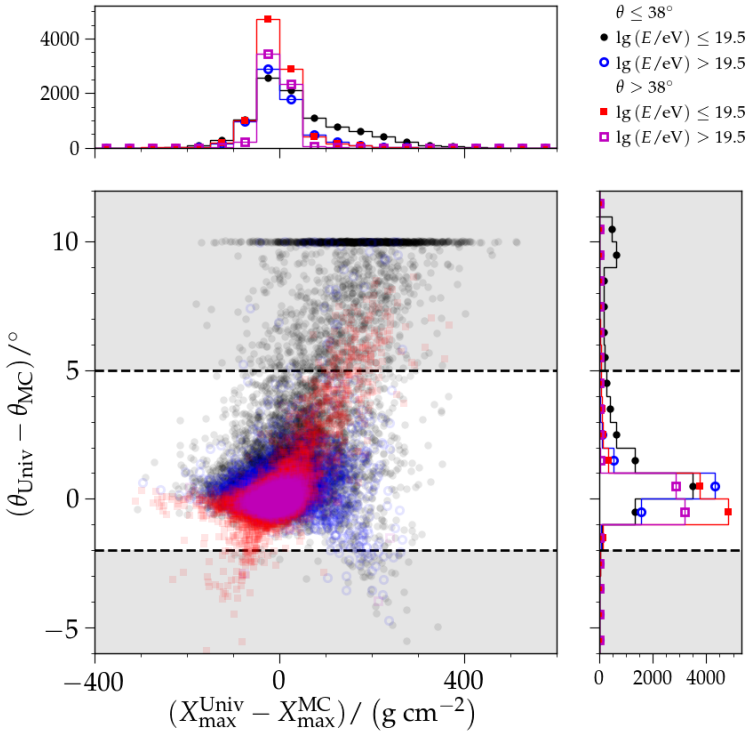

(a)

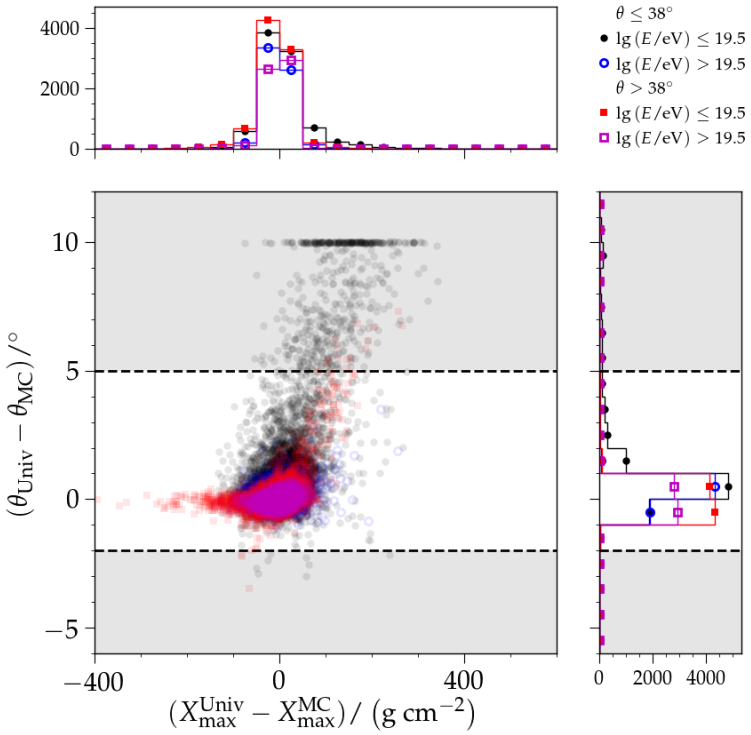

(b)

Figure D.15: The difference in the reconstructed depth of the shower maximum and zenith angle from the global fit are compared to the true values for QGSJET-II.04 simulations induced by (a) proton and (b) iron primaries. Only non-saturated events with energies above 10^{19} eV are considered. Due to its extensive range in X_{max} —from high up in the atmosphere to below ground, proton-induced showers are more likely than iron-induced showers to have mis-reconstructed values below $10^{19.5}$ eV. The gray areas indicate the rejected events, which fail to meet $-2 < (\theta_{\mathrm{Univ}} - \theta_{\mathrm{MC}})/° < 5$.

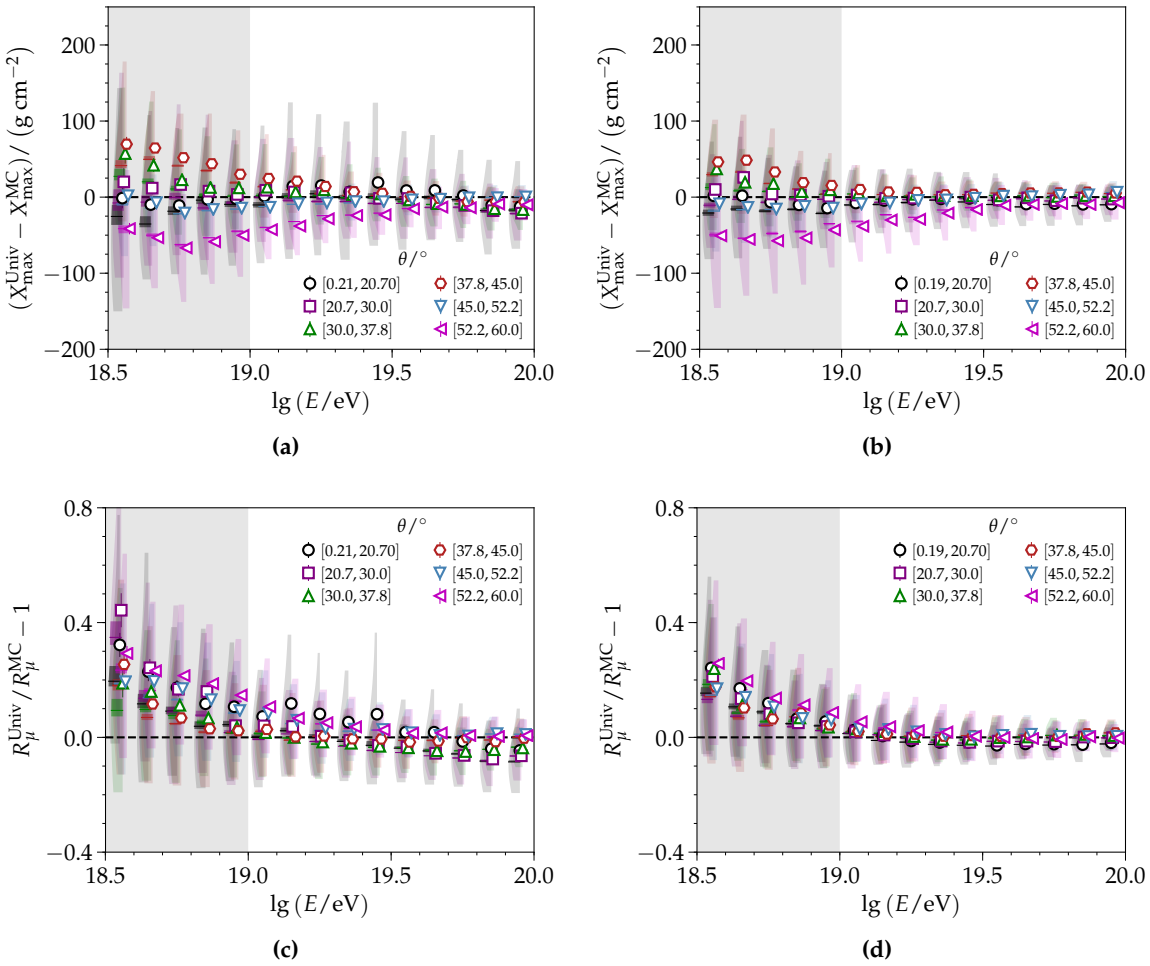

Figure D.16: QGSJET-II.04 (*left*) proton- and (*right*) iron-induced simulations reconstructed with the global reconstruction method. Only non-saturated events are considered where $-2 < (\theta_{\mathrm{Univ}} - \theta_{\mathrm{MC}})/^\circ < 5$ is met. The bias of the reconstructed (*top*) depth of the shower maximum and (*bottom*) relative muon content with respect to energy and zenith angle.

In applying a selection where $-2 < (\theta_{\mathrm{Univ}} - \theta_{\mathrm{MC}})/^\circ < 5$, the zenith-dependence of the reconstruction bias is greatly reduced, as shown in Fig. D.16.

D.4 Study of the iterative fit

A detailed description of the iterative reconstruction procedure is provided in Section 3.2.3.3. The primary purposes behind the creation of the iterative method were to remedy the zenith-dependent biases and inefficiencies at low energies (from few candidate stations) of the global method. To achieve this, this method has a multi-stage fitting procedure where certain variables are fixed or fit in combination to achieve an unbiased result. While the iterative method is able to achieve a minimal X_{max} bias with respect to energy (Fig. 3.26), it does so at the cost of neglecting correlations with the relative muon content. This in turn makes the R_μ unusable for mass composition studies and also leads to an unphysical resolution of the depth of the shower maximum. As shown in Fig. 3.24, the overall efficiency of **successful** events reconstructed by the iterative fit exceeds 90 % over all energies for simulations. In data, however, the rate of successful events rapidly decreases with increasing energy and exhibits a large dependence with respect to increasing zenith angle. Due to these problems, the iterative fit is not an ideal reconstruction method for performing extensive mass composition studies.

In this section, the quality cuts derived for the iterative method are selected with the intention that the results could be used a benchmark in the mean X_{max} plot for the constrained axis method[8]. In order for the results of the iterative fit to be used for comparison-based analyses, event selection is performed using simulations (Appendix D.4.1), and a calibration is performed using golden hybrids[9] (Appendix D.4.2).

D.4.1 In simulations

The biases of the reconstructed depth of the shower maximum, relative muon content, and zenith angle for the iterative method are compared to their true values in Fig. D.17. Events with a zenith angle in the range of 52° to 60°, which can prove harder to reconstruct due to their stricter timing constraints, are largely biased across all energies for the depth of the shower maximum, relative muon content, and zenith angle. Because the large biases are seen across all energies, only zenith angles up to 52° may be considered for the iterative fit. Additionally, the iterative reconstruction, due to its multi-stage fitting procedure, is able to reconstruct the energy; the bias of the reconstructed energy is given in Fig. D.18. The bias with respect to energy has, on average, a 7.5 % difference between the mean bias for the lowest and highest zenith angle bins.

Like in the global method, the outliers of the iterative method may be further identified with the quality of the reconstructed zenith angle in relation to the true value ($-2.5 < (\theta_{\text{Univ}} - \theta_{\text{MC}})/^\circ < 2.5$), as illustrated in Fig. D.19. In these plots, small outlier populations are seen roughly for $X_{\text{max}} < 500\,\text{g}\,\text{cm}^{-2}$ and $X_{\text{max}} < 1050\,\text{g}\,\text{cm}^{-2}$; these populations may be rejected without significantly affecting a given primary mass more than another one. After applying the quality selection criteria, the resulting biases are given in Fig. D.20. There is a zenith-dependent bias seen for the reconstructed depth of the shower maximum on the order of $20\,\text{g}\,\text{cm}^{-2}$, relative muon content on the order of 5 %, and energy on the order of

[8] As discussed in Section 4.3.2, the differing relative muon content in simulations between interaction models and data causes a difference in the offset of the observed biases. While it is possible to correct this afterwards, a calibration may be performed before reconstruction with golden hybrid events. Such a calibration is outside the scope of this work for the constrained axis fit.

[9] Due to recent changes in the FD reconstruction discussed in Section 2.5.1, the calibration for the iterative fit must be updated from what was used in [108].

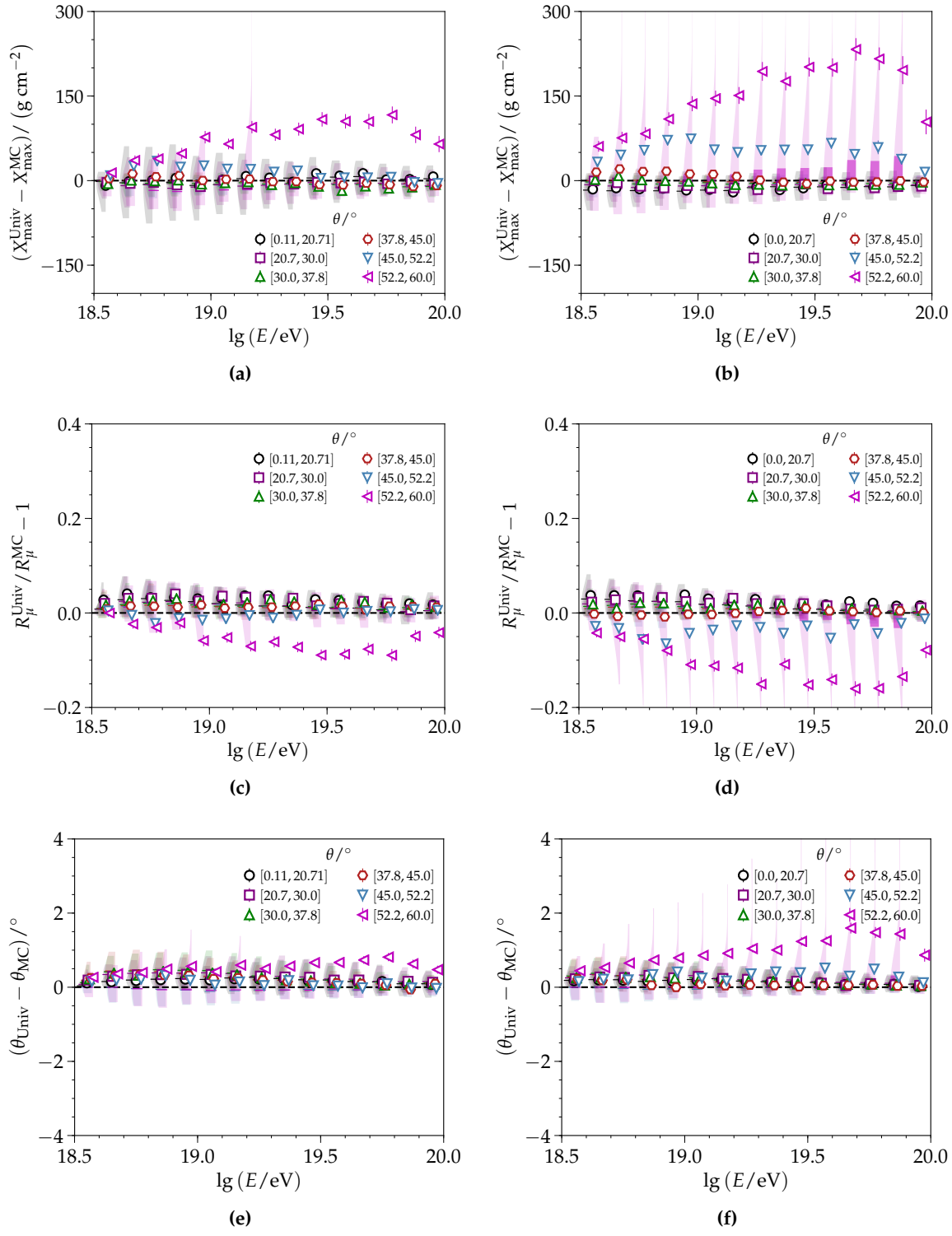

Figure D.17: QGSJET-II.04 (*left*) proton- and (*right*) iron-induced simulations from the Napoli library reconstructed with the iterative fit. Only non-saturated events are considered with no further cuts applied. The bias of the reconstructed (*top*) depth of the shower maximum, (*middle*) relative muon content, and (*bottom*) zenith angle are considered with respect to energy and zenith angle.

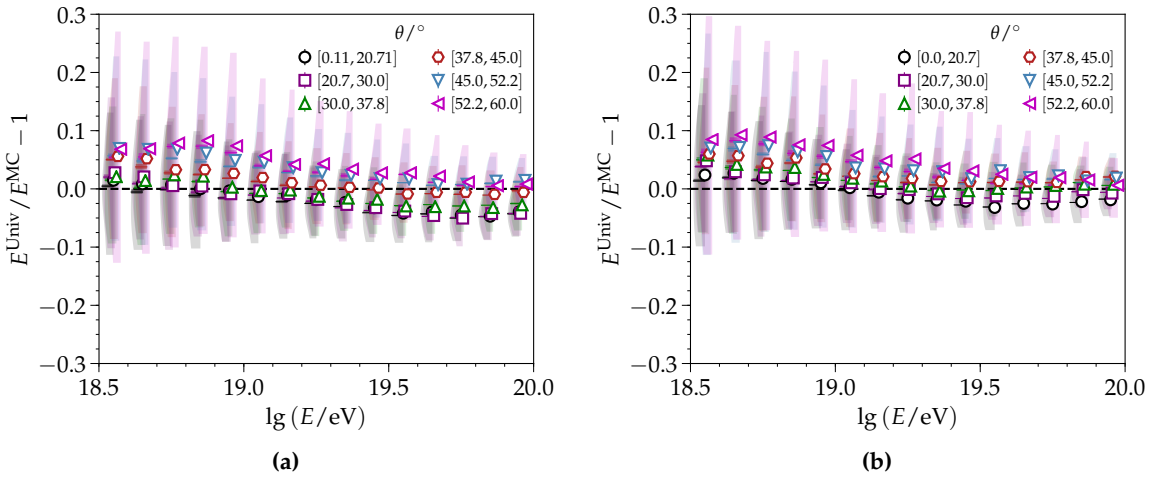

Figure D.18: QGSJET-II.04 (*left*) proton- and (*right*) iron-induced simulations reconstructed with the iterative fit. The bias of the reconstructed energy with respect to energy and zenith angle.

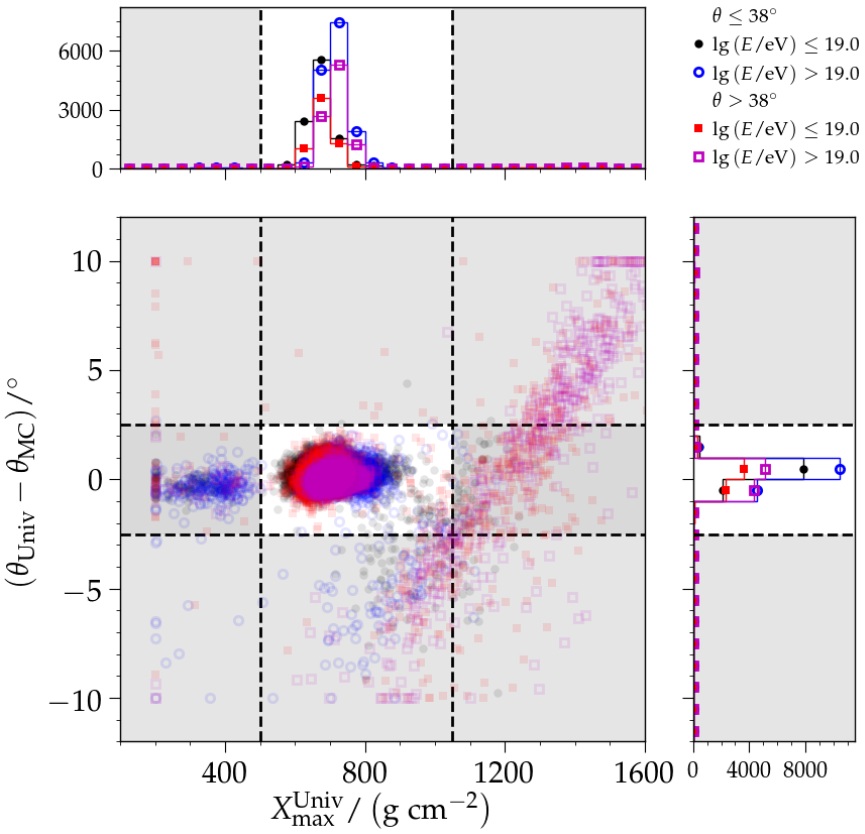

Figure D.19: The reconstructed depth of the shower maximum and difference in the reconstructed zenith angle from the iterative fit are compared to the true values for QGSJET-II.04 simulations induced by iron primaries. Only non-saturated events with zenith angles below 52° are considered.

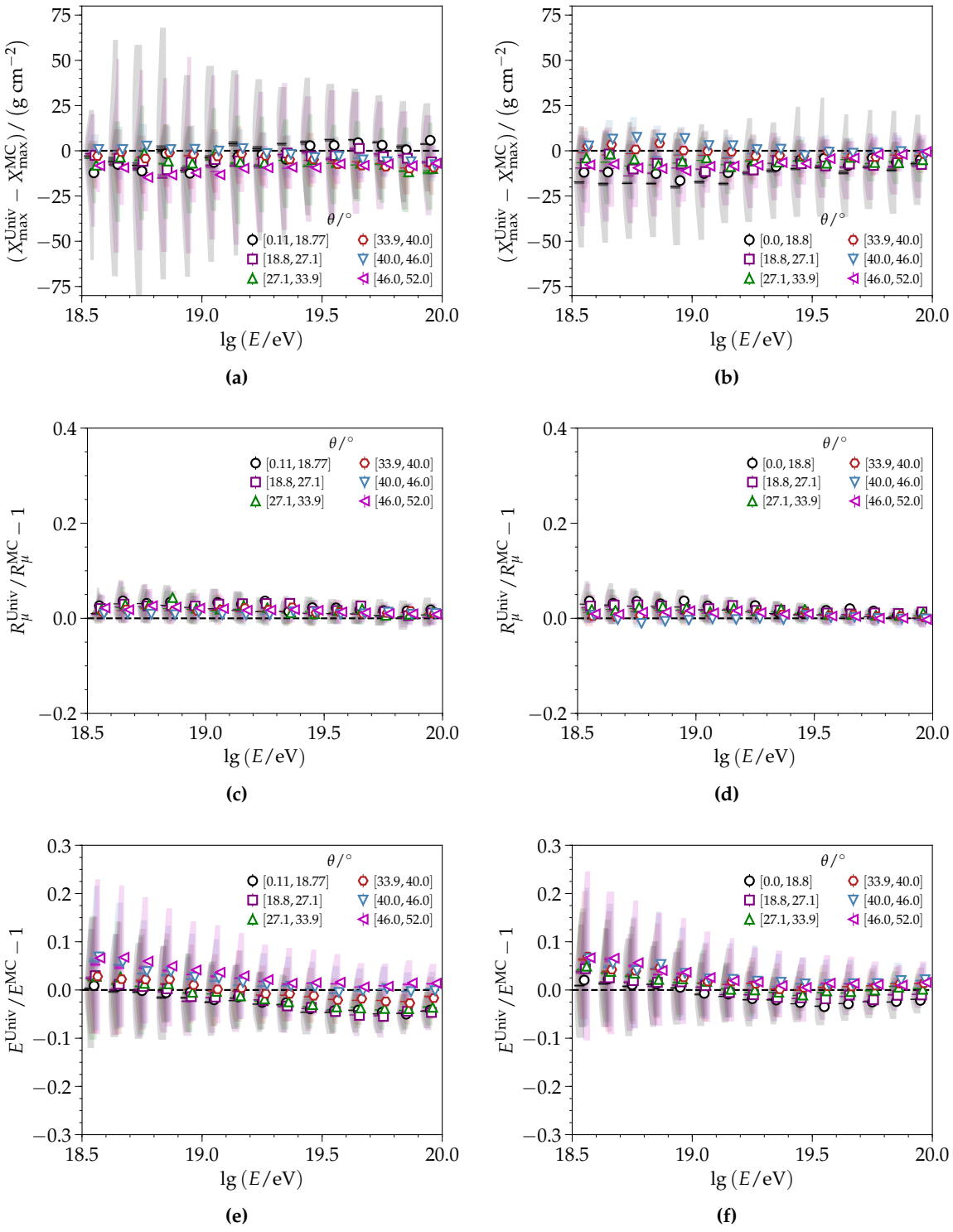

Figure D.20: QGSJET-II.04 (*left*) proton- and (*right*) iron-induced simulations reconstructed with the iterative fit. The bias of the reconstructed (*top*) depth of the shower maximum, (*middle*) relative muon content, and (*bottom*) energy are considered with respect to energy and zenith angle.

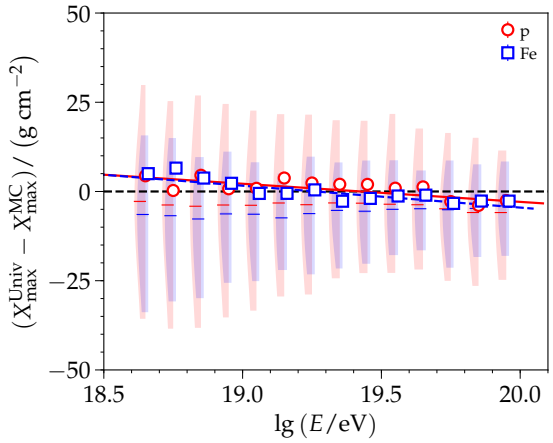

Figure D.21: Bias of the reconstructed X_{max} for QGSJET-II.04 proton- and iron-induced simulations reconstructed with the iterative fit.

9 %. The bias across all zenith angles for the reconstructed X_{max} (Fig. D.21) is parameterized with a linear function of the form[10]

$$\Delta X_{\mathrm{max}}(\lg E) = a + b \cdot (\lg E - 19) \tag{D.5}$$

where $a = (2.2 \pm 0.5)$ and $b = (-5.1 \pm 0.9)$ for proton-induced showers ($\chi^2/n_{\mathrm{dof}} = 1.8$) and $a = (1.6 \pm 0.5)$ and $b = (-6.1 \pm 0.9)$ for iron-induced showers ($\chi^2/n_{\mathrm{dof}} = 1.6$).

D.4.2 Calibration with golden hybrid data

The universality signal and timing models were developed with simulations derived from extrapolated LHC data. While these modern-day cosmic-ray simulations mostly encapsulate the development of an EAS, there is a well-known deficit in the simulated number of muons when compared to data [56, 57]. To account for this discrepancy as well as to ensure the reliability of reconstructed variables, we calibrate[11] the iterative reconstruction with golden hybrid events, which are measured with both the FD and SD-1500

To perform the calibration, all quantities are fixed to the reconstructed observables of the FD. Then, with only the signal model and LDF, the core position and R_μ are fit. Afterwards, these quantities are also fixed, while the the event timing is fit together with Δm_μ . With this reconstruction method, it is then possible to parameterize the average $R_\mu(E, \theta, X_{\mathrm{max}})$ and the time model offset of the muonic component Δm_μ.

D.4.2.1 Event selection

In [108], this calibration was performed with data from 1. January 2004 until 31. December 2014. Since then, the FD reconstruction and selection procedure was improved, as discussed in Section 2.5.1. Also, the FD calibration and aerosol databases were extended to 31. December 2015. The quality selection for SD-1500 data is the same as the selection criteria used for the SD-1500 energy calibration, as discussed in Section 2.5.2. In particular, the fiducial FoV quality selection is applied, which ensures that the primary composition is not distorted

[10] For simplicity, the equation is written such that the units are implied. Anytime X_{max} is in an equation the implied units are g cm^{-2}. Similarly, lg E represents lg(E/eV)

[11] While a calibration improves our results from SD-1500 data, it is not required for obtaining a mean X_{max} close to that found by the FD, as detailed further in [108] for the iterative fit. For the global and constrained axis reconstructions, a calibration procedure before reconstruction would help to alleviate the subsequent reconstructed biases, as depicted in Fig. 4.12.

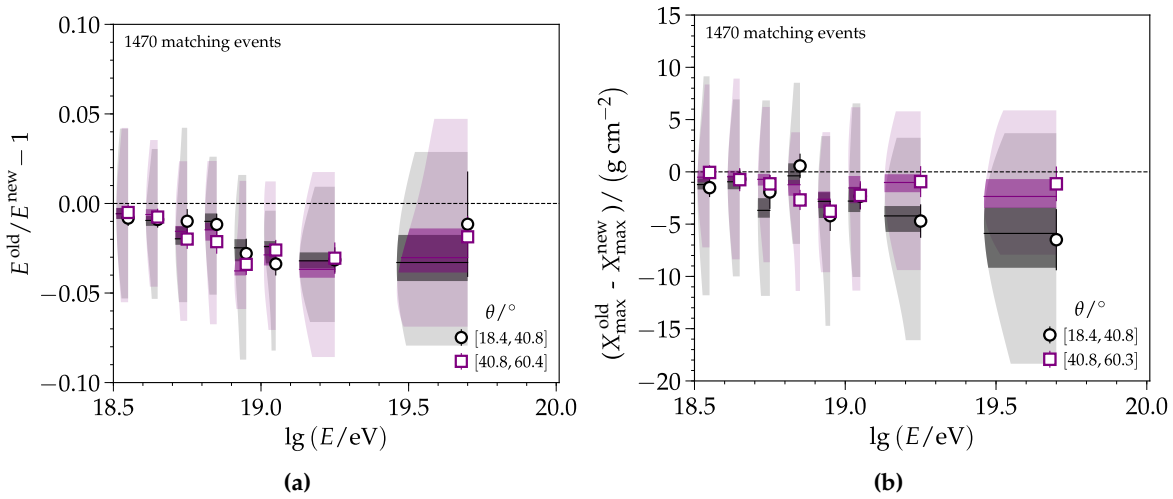

Figure D.22: Comparison of the FD reconstructed results of golden hybrid data taken from [33] (**old**) and reconstructed based on [104] (**new**) are compared on the event-level; 1470 matching events were considered. (a) The relative difference in energy and (b) difference in the reconstructed X_{max} is shown with respect to lg E and with equal-width z-binning in sec θ .

by the measurement with the limited FoV of the FD telescopes. A comparison of the past and current FD reconstruction results are shown in Fig. D.22. Overall, the FD reconstructed energy and X_{max} increased by 5 % and 8 g cm^{-2}, respectively, at the highest energies.

After performing the calibration-based reconstruction, the resulting R_μ and Δm_μ values (dubbed **new**) are compared to the those found in [108] (**old**), as shown in Fig. D.23. Using the new FD reconstructed values as parameters, the **new** R_μ decreases at most by 6 % at the highest energies and by 1 % to 2 % at the lowest zenith angles.

D.4.2.2 Selection of simulations

Throughout this section, QGSJET-II.04 and, occasionally, EPOS-LHC simulations from the Napoli library (Appendix B.2) are shown to act as references for the interpretation of the mass composition of data. While several of the cuts from Section 2.5.2 still apply, there are some hardware and atmospheric condition criteria which are not pertinent. Furthermore, as the fiducial *field of view* (FoV) cut is dependent upon previous cuts, it is necessary to define it separately for each primary and interaction model. The general fit for the upper and lower FoV was $a \cdot (\lg(E/\text{eV}) - 19)^2 + b \cdot (\lg(E/\text{eV}) - 19) + c$. For the applied selection criteria used prior to and the values used in defining the fiducial FoV, see Appendix B.2. For a brief overview and pictorial representation of the fiducial FoV, see Page 76.

D.4.2.3 R_μ calibration

Prior to fitting the relationship of R_μ, its distribution (Fig. D.23) is scrutinized for potential outliers and inclusion of saturated events. As highlighted in Fig. D.24a, the events with saturated stations are diffuse and cover most of the range; as such, only non-saturated events are used in the parameterization. In both golden hybrid data and simulations, no clear outlier population is visible.

The dependence of the average R_μ as a function of energy and for different ranges in zenith angle is shown in Fig. D.27. The following model is fit to describe the data:

$$\langle R_\mu \rangle(\theta) = (2.18 \pm 0.03) + (0.46 \pm 0.05)\,(\sec\theta - 2). \tag{D.6}$$

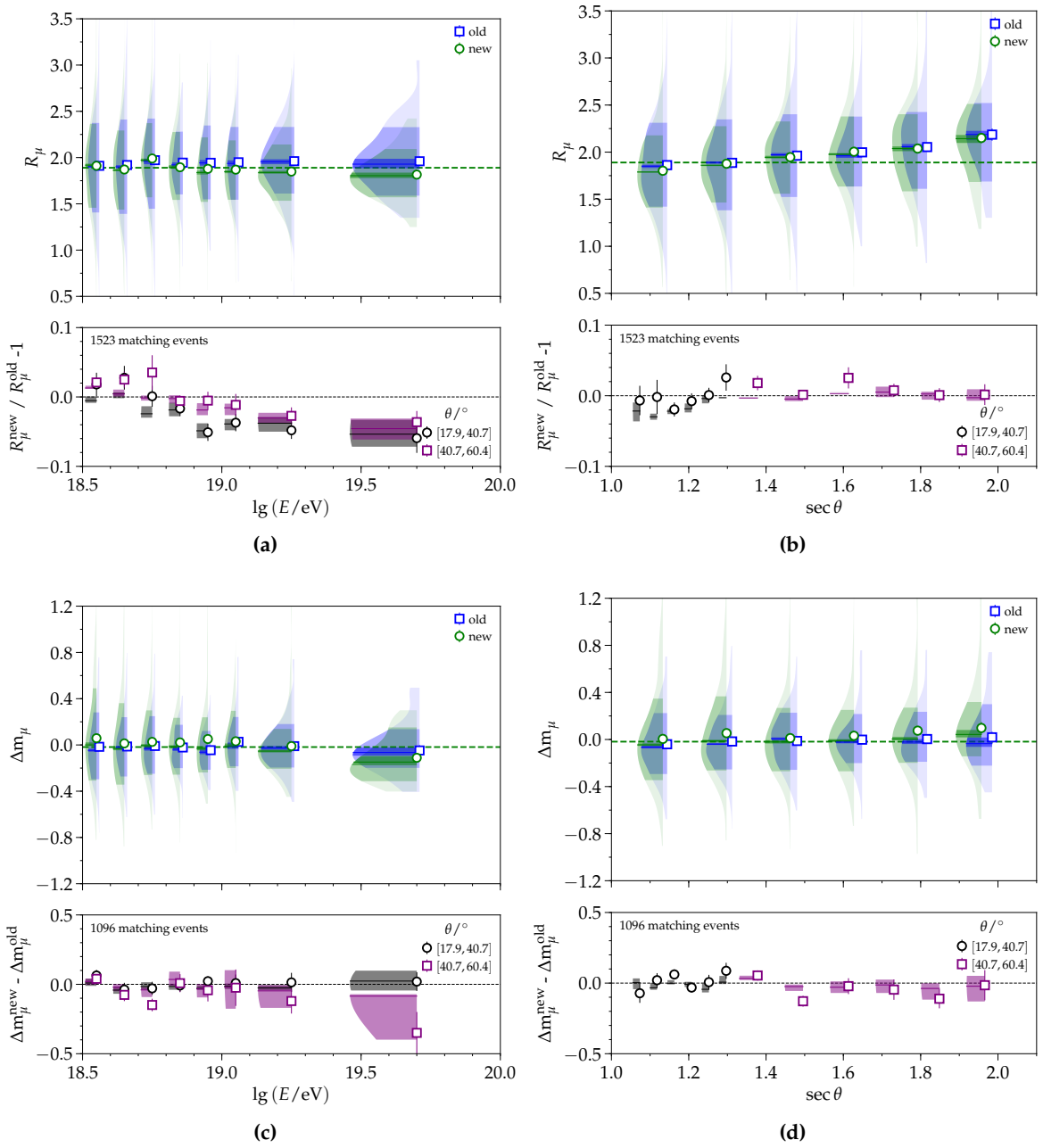

Figure D.23: Comparison of R_μ averages and percent differences with respect to (a) energy and (b) $\sec\theta$. The **new** R_μ has a smaller spread than its predecessor. The averages and differences of the new and old Δm_μ are compared with respect to (c) energy and (d) $\sec\theta$. The **new** Δm_μ was restricted to a range from −3 to 3, whereas the range of **old** was restricted to −1 to 1. This difference in limits explains some of the difference in the spread.

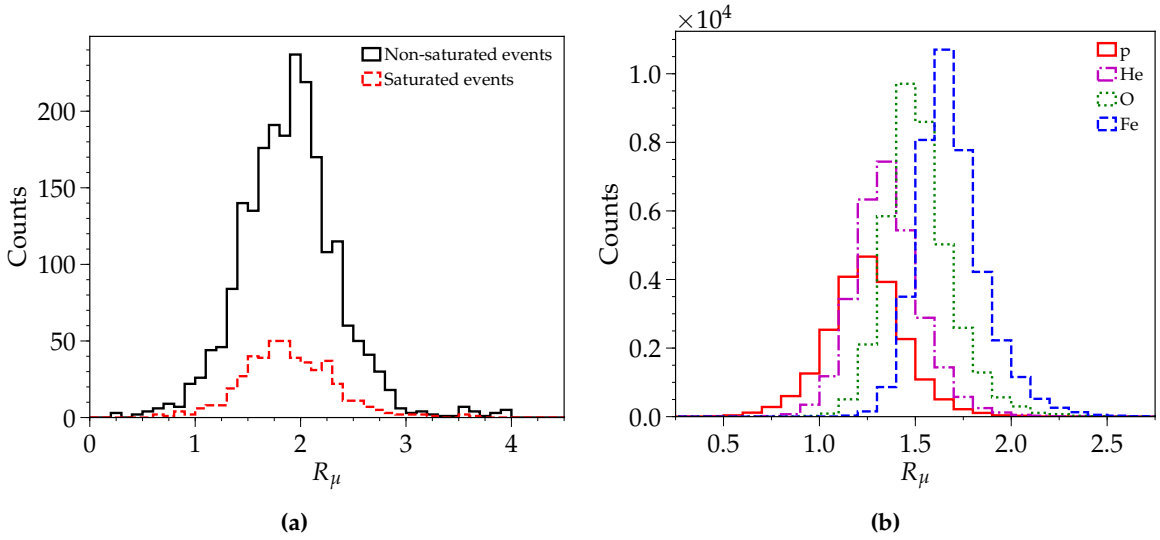

Figure D.24: R_μ distributions for (a) golden hybrid data and (b) non-saturated events in QGSJET-II.04 proton, helium, oxygen, and iron simulations.

Both the R_μ and Δm_μ models are obtained with unbinned chi-squared fits to data. The correlation of the relative muon content R_μ with $X_{\max}$ is quantified with an analysis of the normalized quantity $R_\mu / \langle R_\mu \rangle(\theta)$ as a function of $X_{\max}$. A correlation is expected due to both parameters' mass sensitivity; proton showers penetrate deeper and have a smaller R_μ compared to iron showers. The correlation is shown in Fig. D.25a for different ranges in energy and described with the following function:

$$\langle R_\mu \rangle(E, \theta, X_{\max}) = \langle R_\mu \rangle(E, \theta) \cdot \frac{1 + \frac{0.5}{\pi} \arctan\left(\frac{a \lg(E/\mathrm{eV}) - X_{\max}}{40\,\mathrm{g\,cm^{-2}}}\right)}{1 + \frac{0.5}{\pi} \arctan\left(\frac{a \lg(E/\mathrm{eV}) - \langle X_{\max} \rangle}{40\,\mathrm{g\,cm^{-2}}}\right)}, \tag{D.7}$$

where $a = (42.0 \pm 0.4)\,\mathrm{g\,cm^{-2}}$ and $\langle X_{\max} \rangle = (764 \pm 3)\,\mathrm{g\,cm^{-2}}$.

To better interpret this correlation, ensembles of events are drawn from simulations as shown in Fig. D.26. Events are binned in intervals of 0.1 in $\lg(E/\mathrm{eV})$ from $10^{18.5}$ to $10^{19.3}$ eV and grouped into a single bin for events with energy greater than $10^{19.3}$ eV. In each $\lg(E/\mathrm{eV})$ bin j of width 0.1, 500 events are divided among the primary species s based on their assigned fractions f_s. The number of events per s in a given j bin ($N_{s,j} = 500 \cdot f_{s,j}$) are randomly drawn from the simulations meeting the aforementioned quality cuts and within j. After the ensemble is created, it is fit with $\langle R_\mu \rangle(\theta, E) = a + b \cdot (\lg E - 19) + c \cdot (\sec\theta - 2)$. The resulting plot comes from the normalization of R_μ with respect to $\langle R_\mu \rangle(\theta, E)$. With a pure proton composition as in Fig. D.26a, the resulting functional shape is relatively linear. With an equal mixture of proton and iron primaries as in Fig. D.26b, the shape looks more similar to the arctangent observed in data; however, as the composition does not change with respect to energy, the distributions within each energy group look relatively similar. In Fig. D.26c, the composition is drawn based on the fractional mass composition of proton-iron for the FD [99][12]. While the composition is changing, again we see that the distributions in each energy bin are relatively similar. As seen in Fig. D.26e and Fig. D.26f, the width of the $X_{\max}$ distributions for the different primaries stay relatively constant with respect to energy while its median and mean slightly increase. The $X_{\max}$ distribution of proton covers most of the $X_{\max}$ range. Thus, with just a mixture of proton and iron (where

[12]For a quick reference, the fractional mass composition is shown in Fig. 1.19

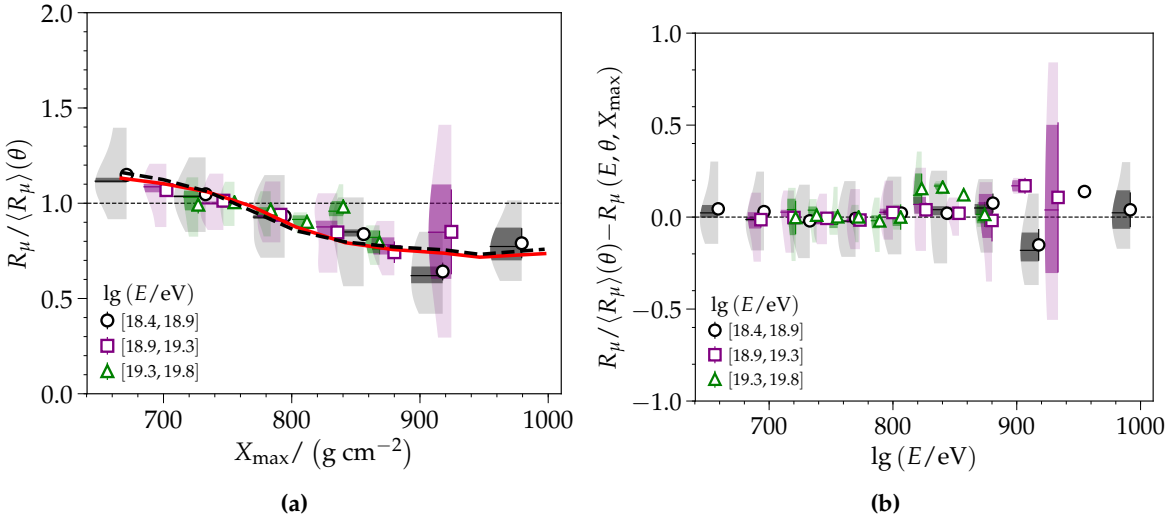

Figure D.25: Correlation between the normalized relative muon content and the average depth of shower maximum for (a) golden hybrid data. The red line is the model for this data set, whereas the dashed black line is from [108]. Despite differing normalization functions, they are in quite good agreement. (b) The residual of the current fit to data.

proton is more favored in a fit than iron), our result would be expected to cover almost the full X_{max} range. When a composition including intermediate elements is considered (Fig. D.26d), the resulting highest energy bin has an X_{max} range of around 700 g cm^{-2} to 860 g cm^{-2}, which is similar to what we see in golden hybrid data and corresponds to a composition dominated by intermediate masses —like nitrogen.

D.4.2.4 Δm_μ calibration

After performing the fit of R_μ that exclusively uses the signal model, the time model offset Δm_μ is fit using the event timing[13]. Due to the strict time-dependence of this variable, it is expected that there will be outliers when the start time of a signal is incorrectly defined for one or more stations. Such issues may be caused by jumps in the signal trace from accidental muons, an ill-defined GPS position of an SD station, or bad PMTs that have not been accounted for. Since the last universality-based thesis [108], several improvements were made in Offline: the cuts and identification of bad PMTs were greatly improved, and the time-dependent GPS positions of several SD stations were updated. In Fig. D.28, the current reconstruction of Δm_μ is shown; outliers are present in both simulations and data at the extrema of the allowed range. In Fig. D.29, the current reconstruction (**new**) is compared to the reconstructed Δm_μ from [108] (**old**). Allowed values of Δm_μ in the past reconstruction were defined as $|\Delta m_\mu| < 0.8$. In the new reconstruction, advanced studies using simulations helped to determine an improved range for the time model offset: $-1 \leq \Delta m_\mu < 2$. As anticipated from the aforementioned improvements to Offline and the change in allowed Δm_μ values, the relative proportion of outliers to well-reconstructed Δm_μ has reduced–from 17.3 % to 11.9 %. Of the outliers, 56.1 % are shared between the data sets. While roughly half of the outliers are not shared,the largest outlier population is from events with $\lg(E/\text{eV}) \leq 19$ and a low number of candidate stations ($n_{cand} \leq 9$). With such low energies, these events only have 1 to 3 stations used in the shape fit which makes their results particularly susceptible to changes in the hardware and jumps in any signal trace.

[13] A description of Δm_μ is provided in Section 3.1.4.

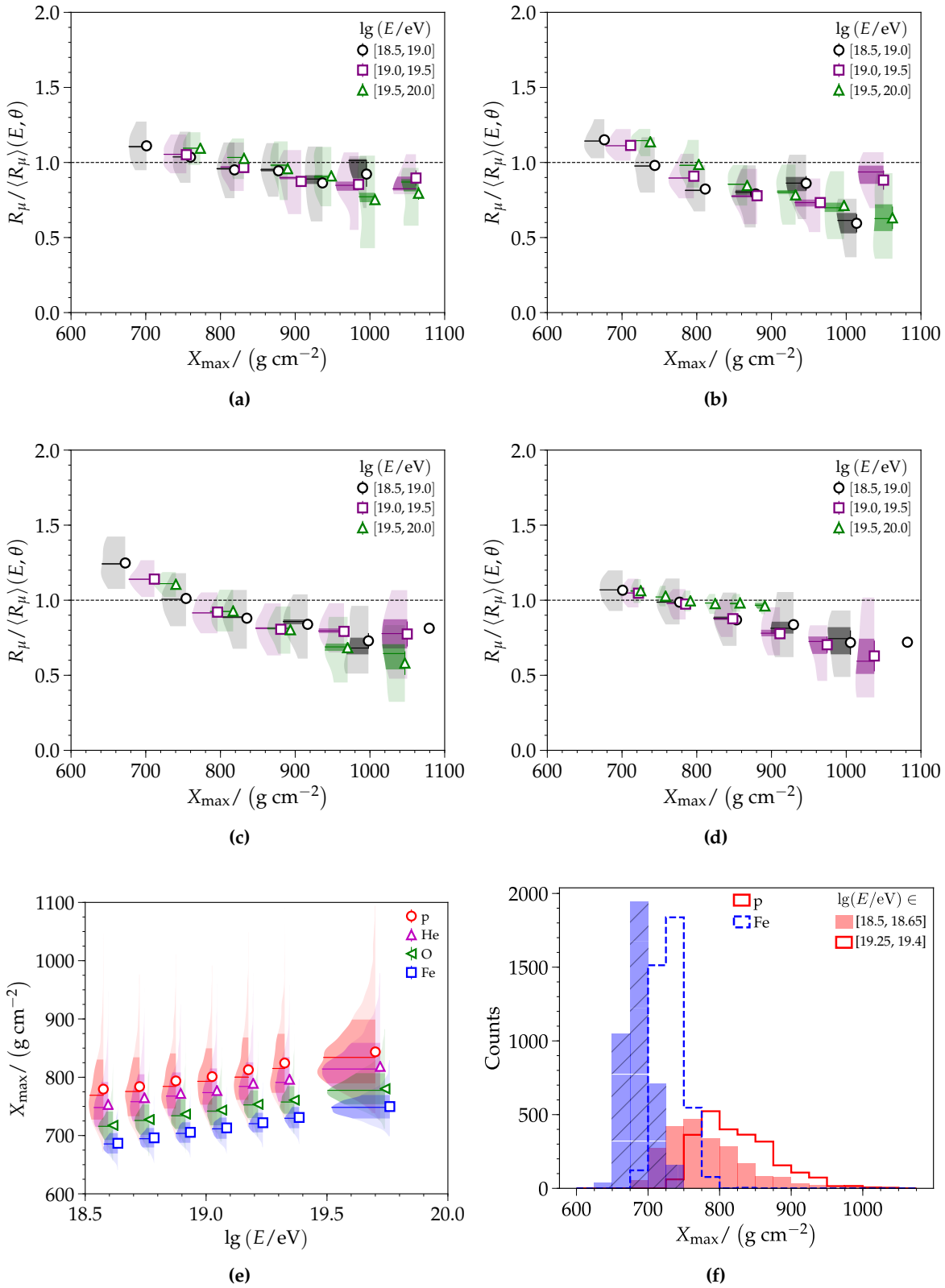

Figure D.26: Correlation between the normalized relative muon content and the average depth of shower maximum for an EPOS-LHC (a) pure proton and (b) equal mixture of proton and iron. Also considered are ensembles of events drawn based on the results of the fractional mass composition of the FD [99] with the following combination of primaries: (c) proton and iron and (d) proton, helium, nitrogen (oxygen), and iron mixture [99]. (e) Violin plots of EPOS-LHC simulations induced by various primaries. (f) The true $X_{\max}$ distributions of proton- and iron-induced showers are considered for two energy bins.

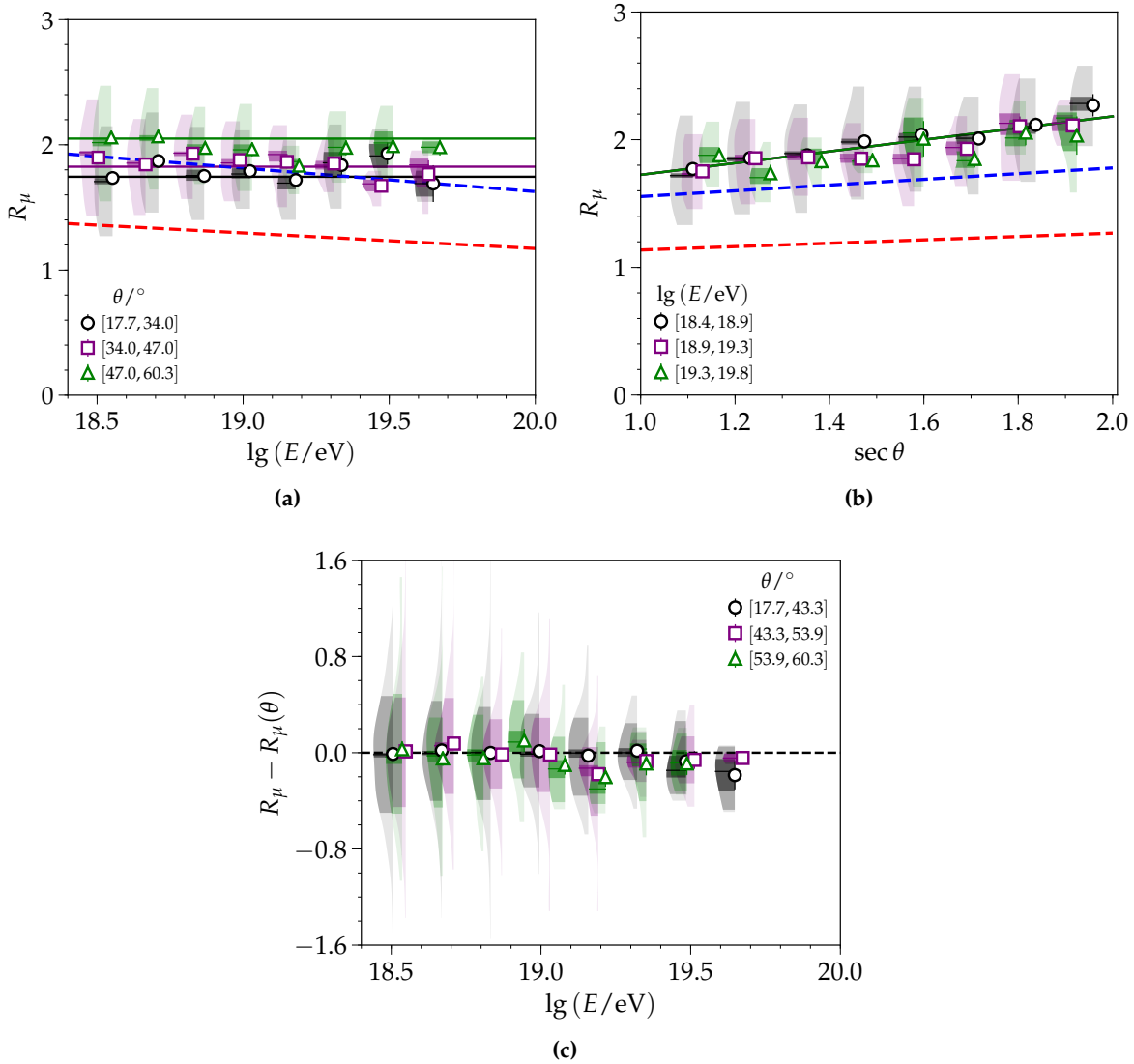

Figure D.27: (a), (b) Parameterization of the average R_μ of golden hybrid data as a function of energy and zenith angle. While the average R_μ of golden hybrid data does not change with respect to energy, this is not an indication of an insensitivity to mass composition. When considered with the average R_μ of QGSJET-II.04 proton (red) and iron (blue) lines and accounting for the muon excess in data, one can see that the composition moves from light to heavy with respect to energy. (c) The residuals of the fit. Overall, the various populations are well-described. In a second step, the time model offset is estimated as described in the text and depicted in Fig. D.30.

In an event-level check of the Δm_μ outliers, it was often found that the start time of the fit signal trace is 50 ns to 200 ns too early. In an investigation of the literature associated with another SD reconstruction method [182], I found that the calculated start and stop times may be affected by an overestimation of the baseline. Additionally, in such high-signal traces, the saturation of the high-gain channel leads to the use of the low-gain channel in

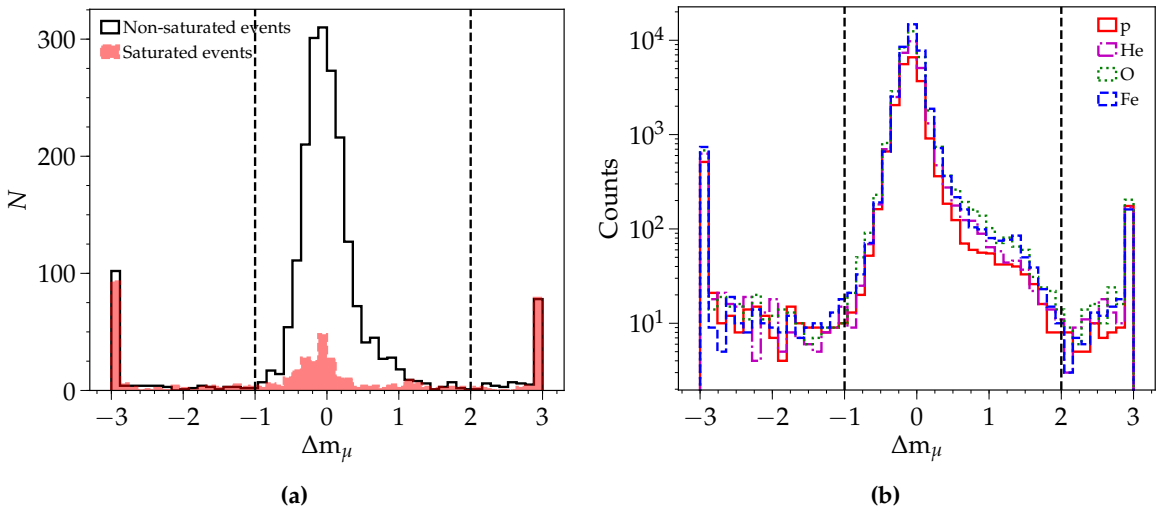

Figure D.28: Histogram of Δm_μ for (a) golden hybrid data and (b) non-saturated QGSJET-II.04 proton, helium, oxygen, and iron simulations. Like the reconstructed R_μ, events with saturation have a large spread in Δm_μ As simulations are not plagued by the changing status of hardware, the relative proportion of outliers to well-measured events is smaller than that found in data.

the reconstruction. However, the start and stop times are still defined by the high-gain channel. An algorithm was developed to use the low-gain channel and to correct for the mentioned effects. In [182], the author found that this algorithm mostly corrected the outlying events, but in using the correction for all data, it led to an increased width of the angular resolution —making it an unfavorable solution to implement fully in this thesis. To get an idea of the possible effect should this algorithm be better defined, I re-reconstructed only the outliers with specified modifications (Appendix B.1.0.1); 19.6 % of the outliers were recovered and yielded Δm_μ values in the allowed range.

The time model offset Δm_μ is described with a similar relation as R_μ but a different set of parameters and with respect to energy:

$$\begin{aligned}\langle \Delta m_\mu \rangle (E, \theta) = &(0.02 \pm 0.03) + (-0.12 \pm 0.04)\,(\lg(E/\mathrm{eV}) - 19) \\ &+ (0.05 \pm 0.04)\,(\sec\theta - 2).\end{aligned} \tag{D.8}$$

The offset is depicted as a function of energy and for different ranges in zenith angle in Fig. D.30. There are small dependencies on both energy and zenith angle. The offset is slightly positive below 10^{19} eV and negative above that energy.

D.4.2.5 Validation of calibrations

The constrained axis reconstruction (Chapter 4) illustrates that universality does not require a golden hybrid calibration to have well-reconstructed results[14]. To further solidify this statement, the previously mentioned calibration method was repeated with events where $\lg(E/\mathrm{eV}) < 10^{19}$. The low-energy parameterizations of Eq. (D.6) and Eq. (D.8) are

$$\langle R_\mu \rangle (\theta) = (2.21 \pm 0.03) + (0.49 \pm 0.05)\,(\sec\theta - 2), \tag{D.9}$$

$$\begin{aligned}\langle \Delta m_\mu \rangle (E, \theta) = &(0.01 \pm 0.04) + (-0.11 \pm 0.07)\,(\lg(E/\mathrm{eV}) - 19) \\ &+ (0.03 \pm 0.04)\,(\sec\theta - 2).\end{aligned} \tag{D.10}$$

[14] It merely requires a correction in the reconstructed bias to account for the difference in the relative muon content between hadronic interaction models and data.

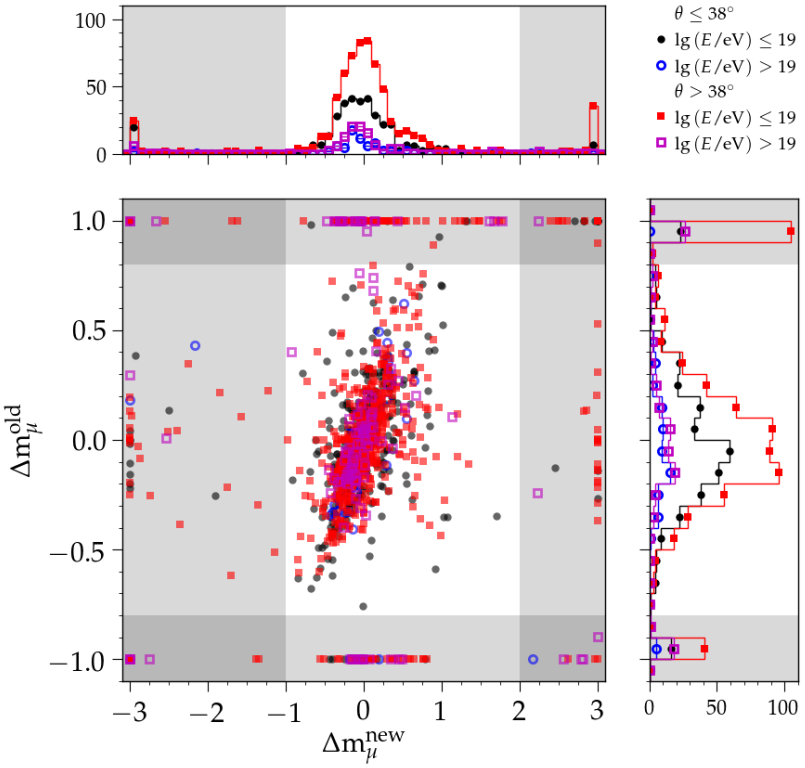

(a)

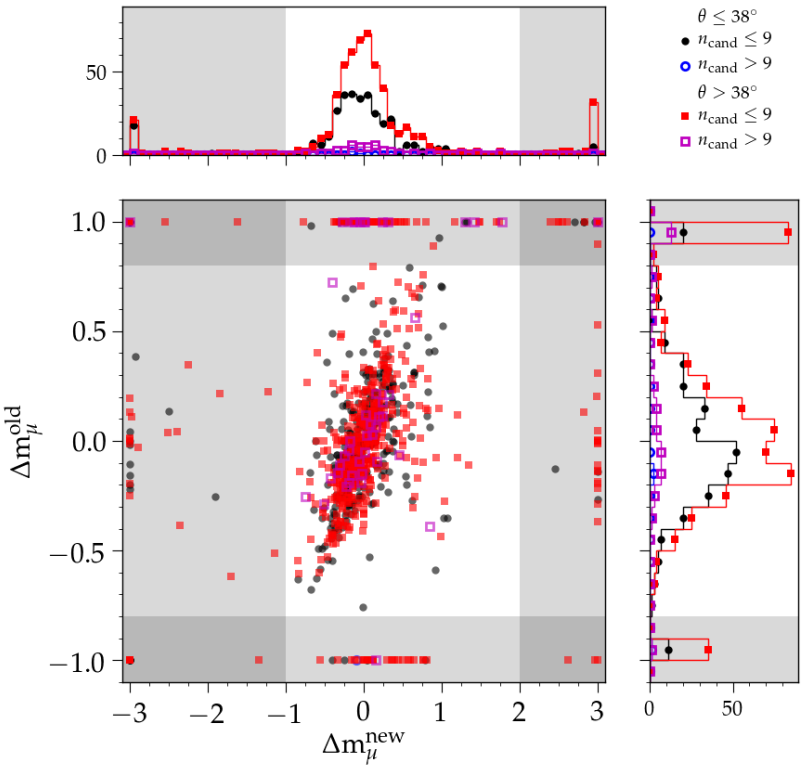

(b)

Figure D.29: Comparison of the Δm_μ values for 1239 non-saturated events for the **new** and **old** reconstruction. The comparison of the reconstructed Δm_μ is performed (a) with respect to zenith angle and energy and (b), for events with $\lg(E/\mathrm{eV}) \leq 19$, for the number of candidate stations and zenith angle. The gray areas enclose the outliers of each respective data set.

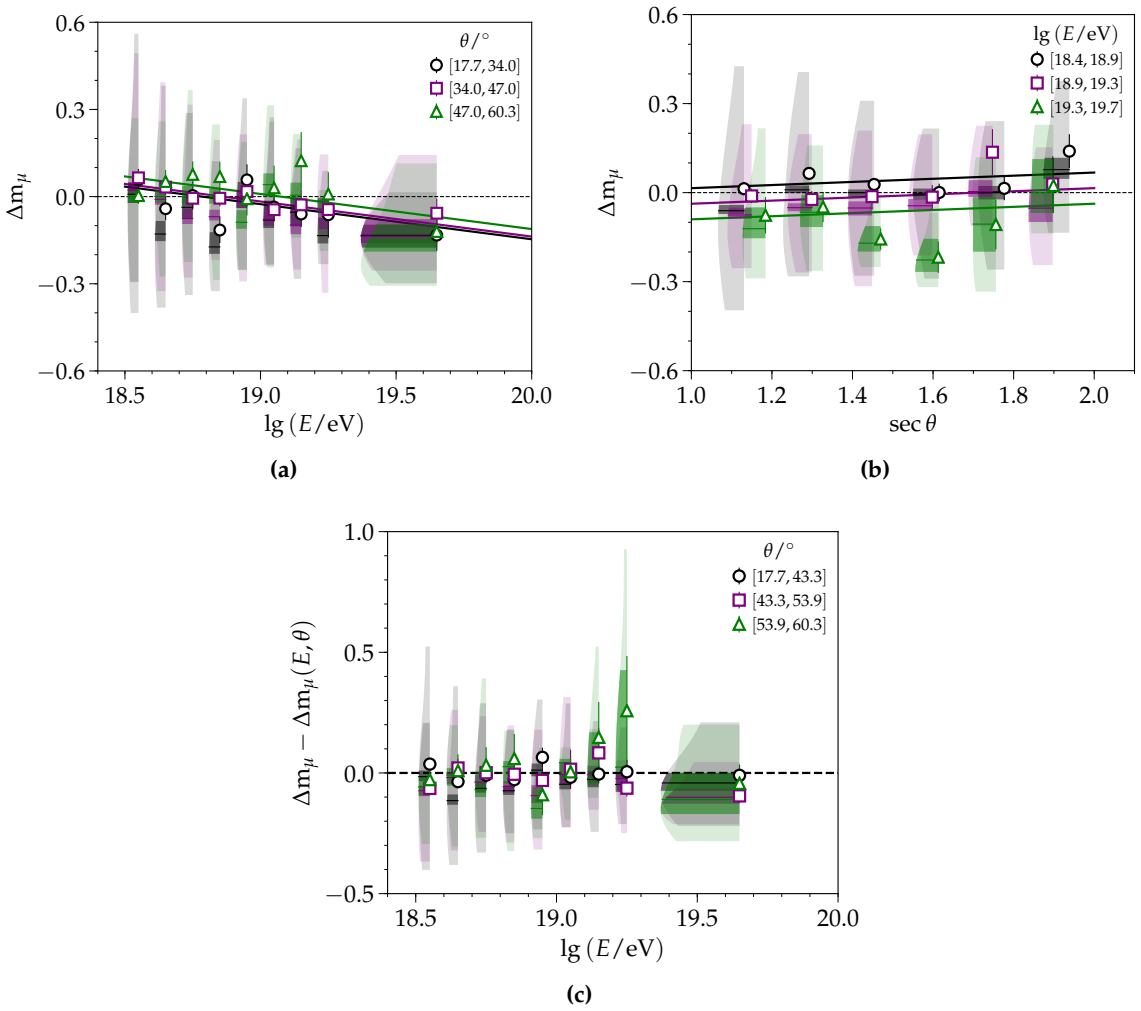

Figure D.30: Parameterization of the average time model offset for golden hybrid data as a function of (a) energy and (b) zenith angle. (c) The residuals of the fit are shown with data.

For Eq. (D.7), the functional form remains the same while a and $\langle X_{\mathrm{max}} \rangle$ are found to be $(41.8 \pm 0.4)\,\mathrm{g\,cm^{-2}}$ and $(761 \pm 3)\,\mathrm{g\,cm^{-2}}$, respectively. All of the values are within the uncertainties found from the calibration performed with the full energy range. The low-energy and all-energy calibrations are used to reconstruct golden hybrid events with the iterative method. The differences in the reconstructed observables between the two calibrations are given in Fig. D.31. On average, the difference in the reconstructed depth of the shower maximum is within $15\,\mathrm{g\,cm^{-2}}$; there is a slight trend of a decrease in the bias at the highest energies. The relative difference in the reconstructed R_μ increases, on average, nearly linearly from 5 % to 15 %. Due to the correlation between the two observables, the respective trends in the differences are in the opposite direction.

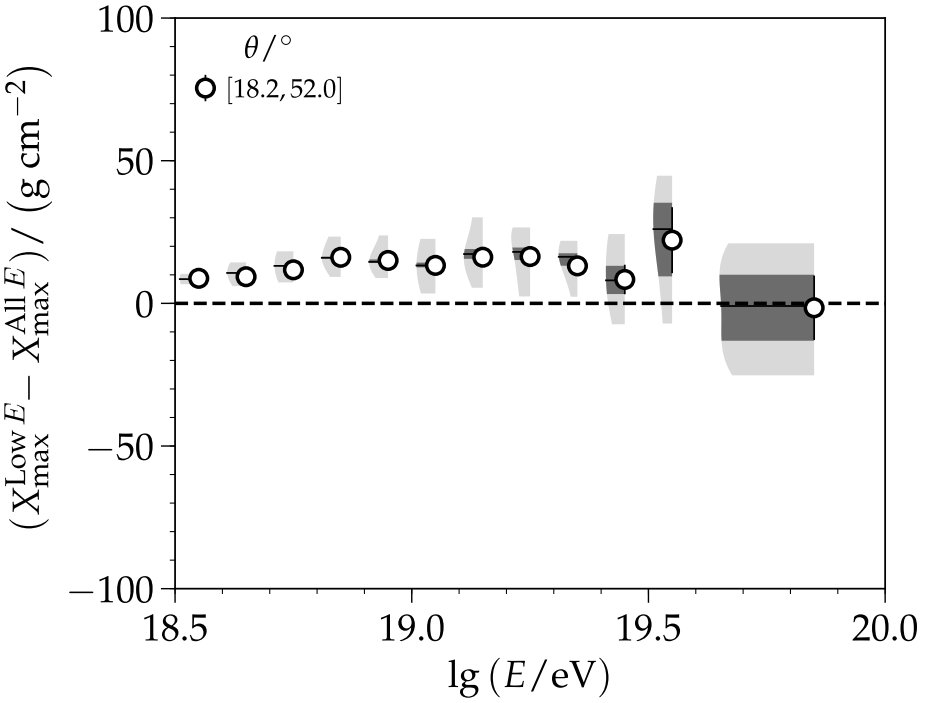

(a)

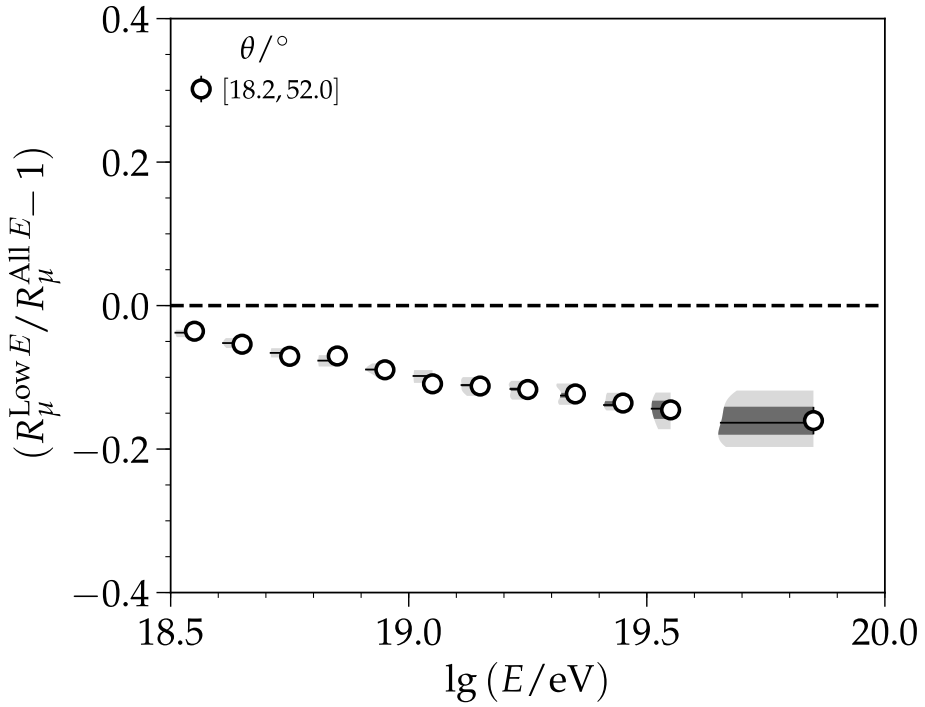

(b)

Figure D.31: Difference in the two reconstructed (a) depth of the shower maximums and (b) relative muon contents. More than 1600 non-saturated golden hybrid events are compared.

D.5 Addenda to the study of the constrained axis reconstruction

The subsections contained in this section are supplements to the section in Chapter 4 of which has a similar or matching title.

D.5.1 Event selection

In Section 4.2, the event selection for the constrained axis is studied and defined. Due to the many analyses performed, it is not a simple task to include the information needed to understand why a certain selection is made nor why there are difficulties reconstructing a certain subset of events. In this subsection, an overview of the role of the minimizer and minimizing function is provided. Having substantiated that poorly reconstructed events are passing the quality checks of the minimizer employed, a preliminary investigation into the correlation of the reconstructed uncertainty and the bias is considered. Despite a strong correlation, the reconstructed uncertainties cannot easily be matched with outlying events for all cases. Furthermore, due to the overestimation of the uncertainties used in the shape fit, the values of the reconstructed uncertainties are also overestimated. Thus, the reconstructed uncertainties may only be used heuristically until the aforementioned issue is resolved and cannot be used to remove most of the outlying events.

Before evaluating the reconstruction efficiencies, biases, and resolutions in simulations, it is important to rigorously separate well-reconstructed events from ones that are merely poorly fit and a set of events which systematically fails to reconstruct (due to some underlying, shared criteria). In an ideal scenario, the negative log-likelihood or other underlying minimizing function should —in combination with MINUIT-2 (or any other minimizer) and a reconstruction procedure— successfully reconstruct all viable SD events. In a slightly less ideal scenario, if a minimization were difficult due to a lack of constraints (e.g. less than five triggered stations in an event), then one would hope that the quality checks of MINUIT-2 would indicate that the minimum found was false or somehow poorly defined. Simply put, however, MINUIT-2 and other numerically-based minimization computer programs are only as *smart* as needed to be used for the minimization of any general function. Thus, the quality criteria used to determine if a fit was successful or not includes whether or not the minimum is:

- found within the number of allowed calls. To avoid infinite loops, the number of allowed calls is automatically specified. Typically, as long as the underlying likelihood is well-defined for the events to be fit —as in universality, the number of calls does not exceed more than 10 % of the maximum.

- associated with the successful calculation of the covariance matrix. This is the inverse of the matrix of second derivatives of the function being minimized and takes into account all parameter correlations (but does not include non-linear dependencies between parameters).

- given with an estimated vertical distance to the minimum (EDM) that is less than the specified tolerance (default = 0.1). Given the successful and statistical meaning of the covariance matrix, it is assumed that the point where the function has its lowest value (FMIN) determines the best-fitting parameter values. The region over which the function has similar small values is defined as FMIN+UP and corresponds to a confidence interval. Based upon the function type used (e.g. negative log-likelihood), UP (0.5) is assigned a value that corresponds to the $1\,\sigma$ confidence interval. The current minimum is found somewhere along this probability curve and is compared to the minimum by calculating the EDM.

If any of these criteria are not met, the minimizer will indicate that convergence on a minimum value was not possible. Despite these fail-safes, MINUIT-2 can be tricked into approving a false minimum. A simple way to improve the rejection of false minima is to re-calculate the error matrix of the minimum using an alternate method. In the case of Offline, the minimization is done with MIGRAD, and the error matrix is re-evaluated using the Hesse matrix. To further improve the rejection, a user can better define the function to be minimized. In order to do this, detailed analyses must be performed to investigate which event, parameters, or stages of the reconstruction procedure begin the descent towards a false minimum. When a strong correlation is found, it is indicative that the reconstruction procedure and/or the likelihood contribution relating to those variables should be better defined. If all else fails, the results of the error matrix itself could be used to discriminate poorly-reconstructed events from well-reconstructed ones. With the negative log-likelihood, the errors calculated are not fully correct because already the uncertainties of individual signal bins in the time distributions are not estimated correctly. This was discussed in Appendix D.1, but as shown in Appendix D.1.2, the current proposed changes are not physically comprehensive for higher-energy events.

On the other hand, MINUIT-2 can also falsely reject a minimum. In the case of universality —for both the negative log-likelihood and deviance method, the function near the minimum is slightly non-parabolic in the x- and y-coordinates of the core. In this case, MINUIT-2 overestimates the EDM and determines that the minimization did not converge. When the found core position is fixed and the minimization re-evaluated with all other variables set free, convergence is achieved with the change in the fit variables being very small relative to their initial values. Such false rejections and successful re-evaluations happen for the negative log-likelihood for around 3 % of events, whereas with the deviance method it occurs around 30 % of the time.

As shown in the efficiency plots for the global (Fig. 3.22), iterative (Fig. 3.24), and constrained or fixed axis methods (Fig. 3.25 and Fig. D.39), the reconstruction procedures and their associated constraints —whether naturally occurring (e.g. number of triggered stations) or enforced (e.g. constraining the axis by 1°)— can lead to more or less misreconstructed events. Nevertheless, as shown in the efficiencies of the various deviance reconstructions in Fig. D.3, poorly defined additions to the function to be minimized can lead to an increased false-rejection rate for events that are otherwise well-reconstructed.

Several studies in the preparation of this work and in [108] have been performed to determine what leads to outlying events. No common patterns were found that describe a majority of the observed outliers in the global and iterative fits. However, with the constrained axis method (discussed further in Chapter 4), it was found that the separate constrainment of the zenith angle and azimuth —as done in the iterative method— could be improved by deriving and constraining both quantities from their geometrical determination in the shower axis. Before, when the zenith angle and azimuth were separately constrained, the minimizer could be misled and change the zenith angle without updating the azimuth as the likelihood did not explicitly enforce the geometrical relationship. Now, as they are considered jointly, the remaining outliers are found at low energies where the number of triggered stations is reduced to $4-7$ and is greatest for high zenith angles ($\theta > 55°$) where the fit of the station times can be most difficult.

Overall, the goal of event selection is that after applying each cut, ideally, there would be no explicit dependence on primary mass and, whenever possible, a cut should preserve the underlying distributions of the zenith angle, energy, and other observables. If it were not easily possible to ensure an unbiased result with respect to mass composition, then it would become necessary to use data-driven methods to correct for biases when considering the average trends or distributions of mass-sensitive variables with respect to energy (e.g.

the depth of the shower maximum). The fiducial selection originally implemented for the FD, briefly mentioned in Section 2.5.2 and described in Section 4.2.2, is intended for this purpose.

Nevertheless, fiducial selections[15] do not address events which are poorly reconstructed but within the accepted range (e.g. in zenith angle or depth of the shower maximum). Due to the difference in the range of true X_{max} values with respect to the mass of the primary, heavier elements —like iron— are more likely than the lighter elements —like proton— to have reconstructed X_{max} values which seem reasonable (i.e. $X_{\text{max}} \in [500, 1050]$ g cm^{-2}) but may vastly differ from their true values, as depicted in Fig. 4.3b. To identify and reject such events, a selection may be derived using the uncertainty in the reconstructed depth of the shower maximum.

As mentioned earlier, the uncertainty of reconstructed values is calculated using the inverse of the matrix of second derivatives of the function being minimized. So the reconstructed uncertainties should reflect when a minimum was hard to find. As shown in Fig. D.32, there is a strong correlation between large uncertainties and large differences in the reconstructed and true values. However, the $1\,\sigma$ spread in the extrema of the range ($|\Delta X_{\text{max}}| > 200$) extends down to 75 g cm^{-2}, which is at the upper range for the $1\,\sigma$ spread of events that are less biased. Thus, it is not possible to derive a selection of well-reconstructed events that is mostly dependent upon the reconstructed uncertainties.

The uncertainty calculation for the shape fit is overestimated (Section 3.2.1.1), particularly for small signals; as such, when correctly calculated, the uncertainties in the reconstructed values will be reduced and better describe data. In Appendix D.1, the author defined a constant multiplicative factor to use on the calculated uncertainties in the shape fit. However, this simple factor, as shown in Appendix D.1.2, is not sufficient to describe the uncertainties in the signal, which relies not only on the energy but also the depth of the shower maximum, atmosphere, and geometry. While it is not investigated in this work, a more rigorous implementation of this change using the negative log-likelihood, pure deviance, or other minimizing function would lead to an improved error calculation. This, in turn, would allow for the improved rejection of events based on the associated uncertainties of the observables. Regardless, it is important to keep in mind that outlying events are mostly ameliorated by the constrainment of the axis.

D.5.2 Event selection in simulations

In Section 4.2.3, the bias of the depth of the shower maximum is parameterized as a function of energy. Nevertheless, as seen in Fig. 4.6e and Fig. 4.6f, the bias before being corrected in a complicated function where the bias is greatest at low energies and the extrema in the zenith angle range. In this addendum to that subsection, the residual bias (after applying the energy-based correction) is parameterized. While it is possible to use the functional form (given below) to correct the bias before the fiducial selection and energy-based correction, the best description is given when they are applied beforehand.

After performing the fiducial selection and bias correction in simulations as a function of energy, the remaining zenith-dependent bias of the reconstructed depth of the shower

[15] This includes both the FD fiducial field of view and the fiducial selection in zenith angle used by universality (Section 4.2.2.2).

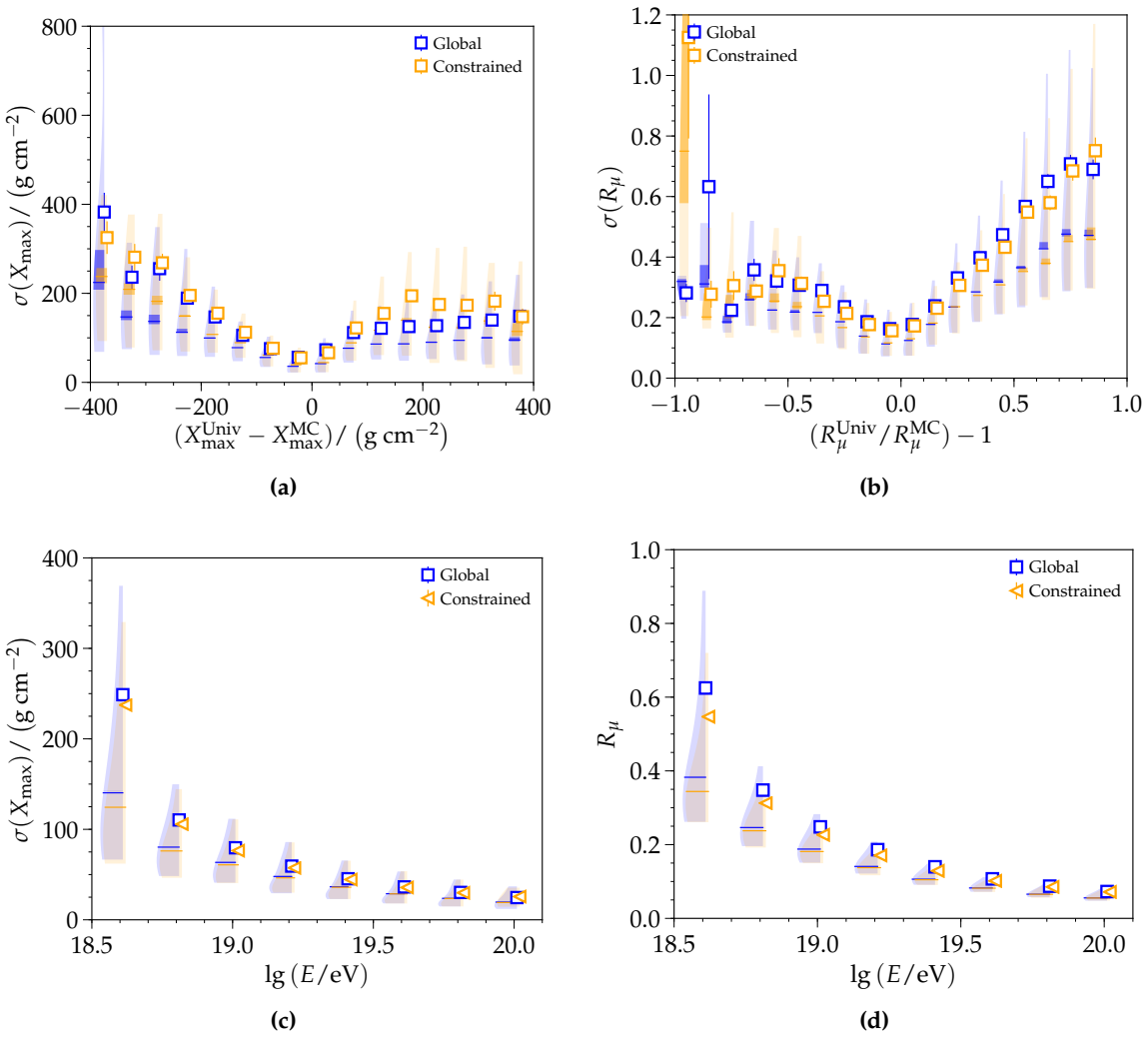

Figure D.32: Reconstructed uncertainties of QGSJET-II.04 proton-induced simulations as reconstructed using the global and constrained methods. The uncertainties of the depth of the shower maximum/relative muon content are considered as a function of (a)/(b) difference/relative difference of the reconstructed to true value and (c)/(d) with respect to energy. Only non-saturated events found in both data sets (more than 48 000 events) are considered; no outlier rejection is used. The constrained axis method has, on average, slightly smaller uncertainties at low energies than the global fit. Above an energy of 10^{19} eV, the constrained and global reconstructions are, on average, indistinguishable in their quality of reconstructions. Due to the significantly fewer outliers in the constrained method, only a few events are considered in the extrema of mis-reconstructed quantities.

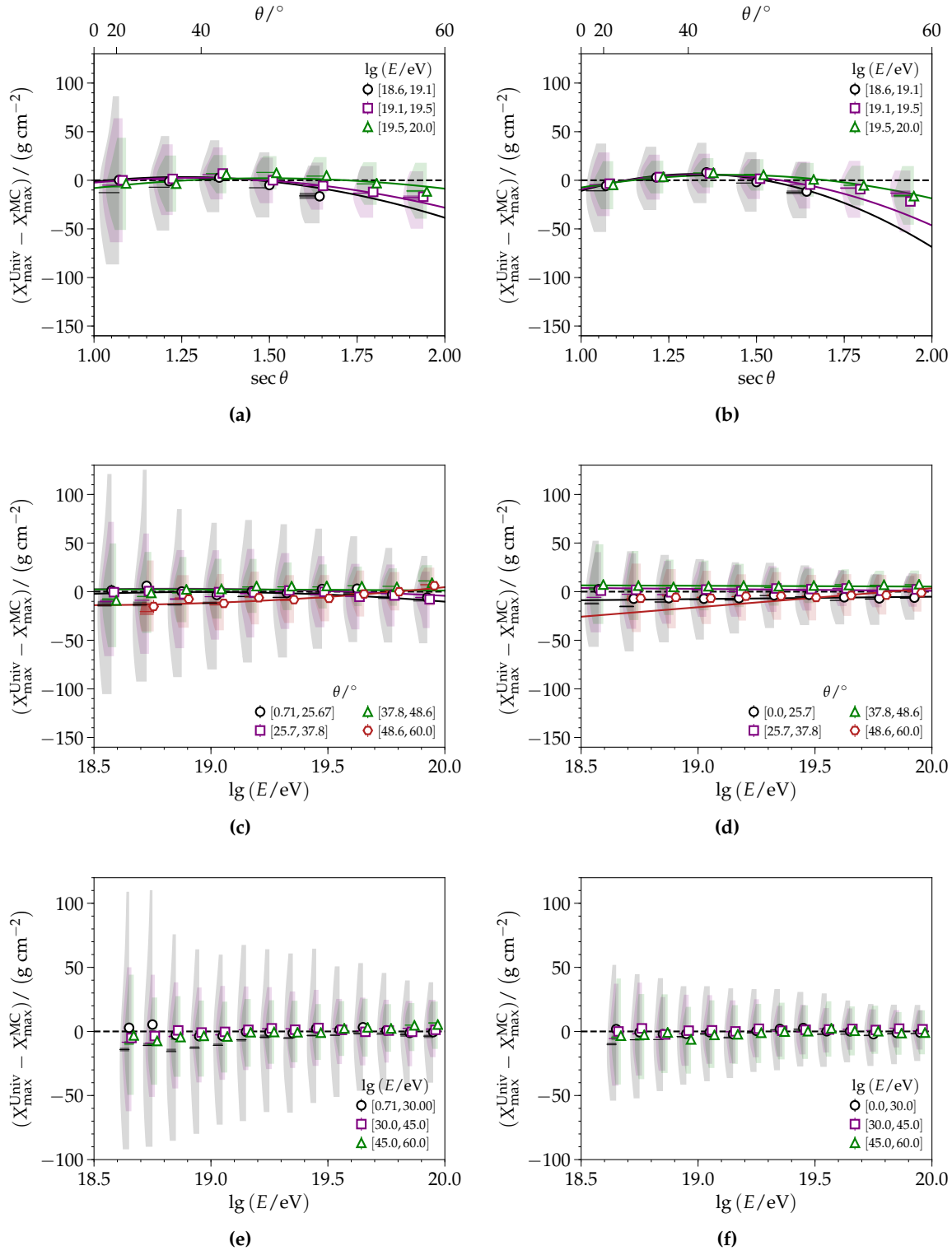

Figure D.33: Evaluation of the parameterized $X_{\max}$ bias as a function of the zenith angle and energy, as evaulated for (*left*) proton- and (*right*) iron-induced showers generated by QGSJET-II.04. The best fit is shown as function of (*top*) $\sec\theta$ with constant values used for $\lg E$ and (*middle*) $\lg E$ with constant values used for $\sec\theta$. (*Bottom*) The residual bias after applying the parameterization is given.

Table D.2: Parameters for bias of the reconstructed $X_{\max}$ as a function of zenith angle and energy. Term d is not fit for the parameterization of iron-initiated showers; it can be used, but this term is mostly needed for proton-induced showers due to the mis-reconstruction of $X_{\max}$ near ground at the highest energies.

Primary	a	b	c	d	e	f
proton	1.7 ± 0.4	-6.6 ± 1.7	40.5 ± 5.8	24.5 ± 9.5	-52.9 ± 5.8	37.0 ± 17.5
iron	5.5 ± 0.3	6.0 ± 1.0	31.3 ± 3.2	—	-103.5 ± 3.4	102.2 ± 9.9

maximum (Fig. 4.6) may be parameterized as a function of the secant of the zenith angle and energy

$$\Delta X_{\max} = a + B(\lg E) \cdot (\sec\theta - 1.4) + C(\lg E) \cdot (\sec\theta - 1.4)^2, \tag{D.11}$$

$$B(\lg E) = b + c \cdot (\lg E - 19.5) + d \cdot (\lg E - 19.5)^2, \tag{D.12}$$

$$C(\lg E) = (e + f \cdot (\lg E - 19.5)). \tag{D.13}$$

The best fits of the equation are obtained with unbinned chi-squared fits to proton- and iron-induced simulations of QGSJET-II.04. To visually check the fit, lines are shown for constant values in $\lg E$ and $\sec\theta$ in Fig. D.33, where the mean value of a given bin is used as the constant. The parameters are given in Table D.2.

While the application of this correction greatly reduces the zenith-dependence of the mean $X_{\max}$, it does not address the correlations or increased resolution seen in the largely deviating bins. In order for this to truly be remedied, the uncertainties in the shape fit need to be correctly calculated; the overall signal and time models used by universality need to be parameterized for $\Delta X < 0\,\mathrm{g\,cm^{-2}}$ and $\Delta X > 1000\,\mathrm{g\,cm^{-2}}$ (which are currently poorly described); and several analyses need to be performed to determine if additional terms need to be added to the negative log-likelihood to improve the quality of reconstruction, particularly at lower energies.

D.5.3 Event selection in data

This subsection is an addendum to the discussion found in Section 4.3; for further details, please refer to that section.

D.5.3.1 Fiducial selection

The fiducial selection discussed in Section 4.2.2 seeks to reject the nonphysical, mis-reconstructed depths of the shower maximum, which are primarily observed at low energies. In Fig. D.34, the depth of the shower maximum and energy for each non-saturated event is shown for SD-1500 data. In Fig. D.34, all events are shown; the observations are compared to the average hadronic interaction models for proton- and iron-induced air showers. After the fiducial selection is applied as in Fig. D.35, most of the outlying events have been rejected from the analysis. Further improvements to the reconstruction as well as correction methods (discussed in the next section) could allow for more robust fiducial selection criteria than have been used.

D.5.3.2 Data-based corrections

While it is discouraged due to the already greatly distorted zenith angle distribution, the fiducial selection derived for the SD-1500 is applied to golden hybrids. The resulting bias and resolution are shown in Fig. D.36, and the best fitting parameters are given in Table D.3

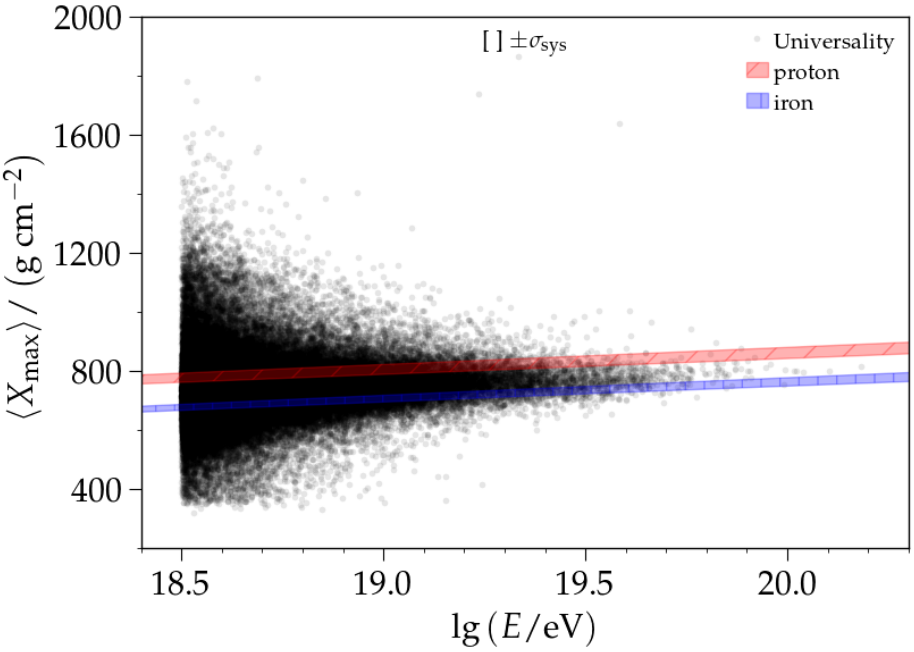

(a)

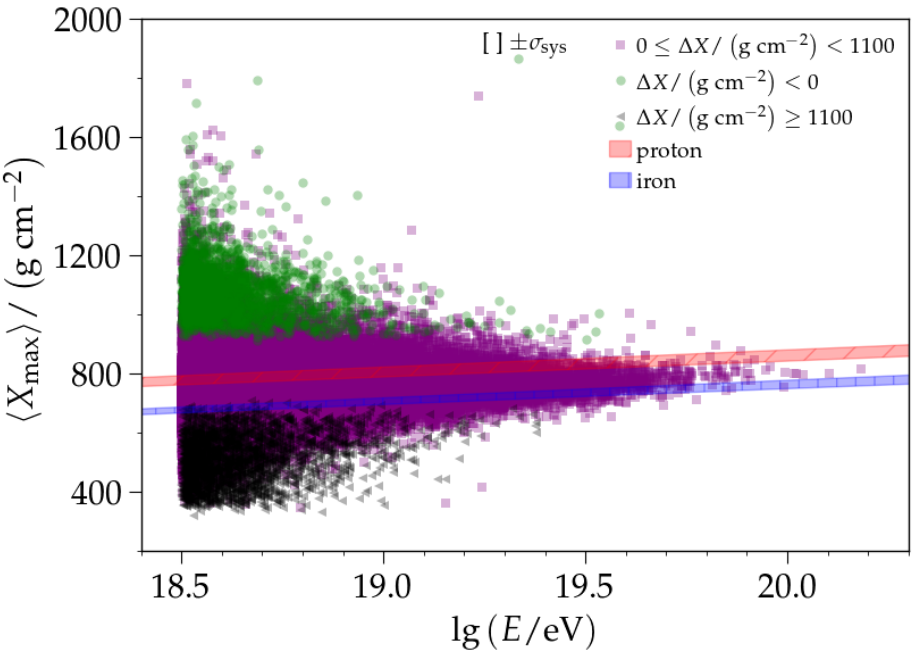

(b)

Figure D.34: The depth of the shower maximum is shown with respect to its energy for all non-saturated events. (a) The alpha-level of each point is set to a fractional value so that darker, more compact regions indicate $X_{\max}$ values more often observed. While there are a few higher energy events with values below $500\,\mathrm{g\,cm^{-2}}$ and above $1000\,\mathrm{g\,cm^{-2}}$, these outlying events are primarily seen at the energy threshold ($10^{18.5}$ eV). (b) To further put into context the state of the outlying events, they are categorized based on their slant depth. Values less than $0\,\mathrm{g\,cm^{-2}}$ are below ground, whereas those exceeding $1100\,\mathrm{g\,cm^{-2}}$ are high up in the atmosphere. In both of these cases, the observed slant depth is rather unlikely for a nucleon-induced air shower.

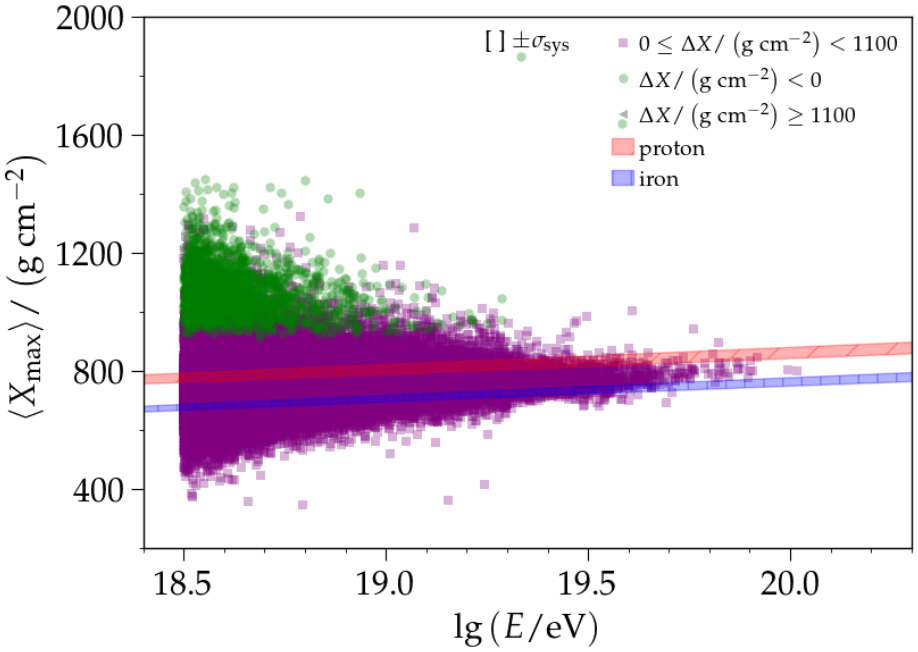

Figure D.35: The depth of the shower maximum and energy for non-saturated events selected with the fiducial criteria. A significant portion of nonphysical values have been removed; the remaining population in green requires further scrutiny to ensure a fully efficient selection. To note, in this energy range, the FD predicts a composition close to pure proton, so we do expect some deeply penetrating air showers.

and Table D.4. The bias as a function of average area over peak is shown in Fig. 4.16. While the estimated relative muon content from the FD may be used to quantify the bias as a function of energy in golden hybrid events, the reconstruction procedure used for this is too constrained and cannot fully take into account the correlations with the average area over peak. The resulting bias is given in Fig. D.37 and the associated parameters in Table D.5.

In Appendix D.5.2, the residual bias as a function of zenith angle and energy was parameterized and corrected for[16]. The corresponding data-based corrections are shown in Fig. D.38. The bias of the depth of the shower maximum for golden hybrid data is parameterized with

$$\Delta X_{\mathrm{max}} = (-46.7 \pm 2.8) + (42 \pm 5) \cdot (\lg E - 18.5). \tag{D.14}$$

This parameterization is similar to that found in Table 4.4; though, the separation in the zenith bins has been reduced to what is observed in Fig. 4.13. As only the average residual bias was corrected for with respect to zenith angle and energy, the spread has not changed. Thus, the parameterization of the detector resolution is the same as Table 4.4. The dependence of the depth of the shower maximum is fit with the average area of peak, which gives the same values as found in Table 4.6.

[16]For more details on how these parameterizations are performed, see Section 4.3.2

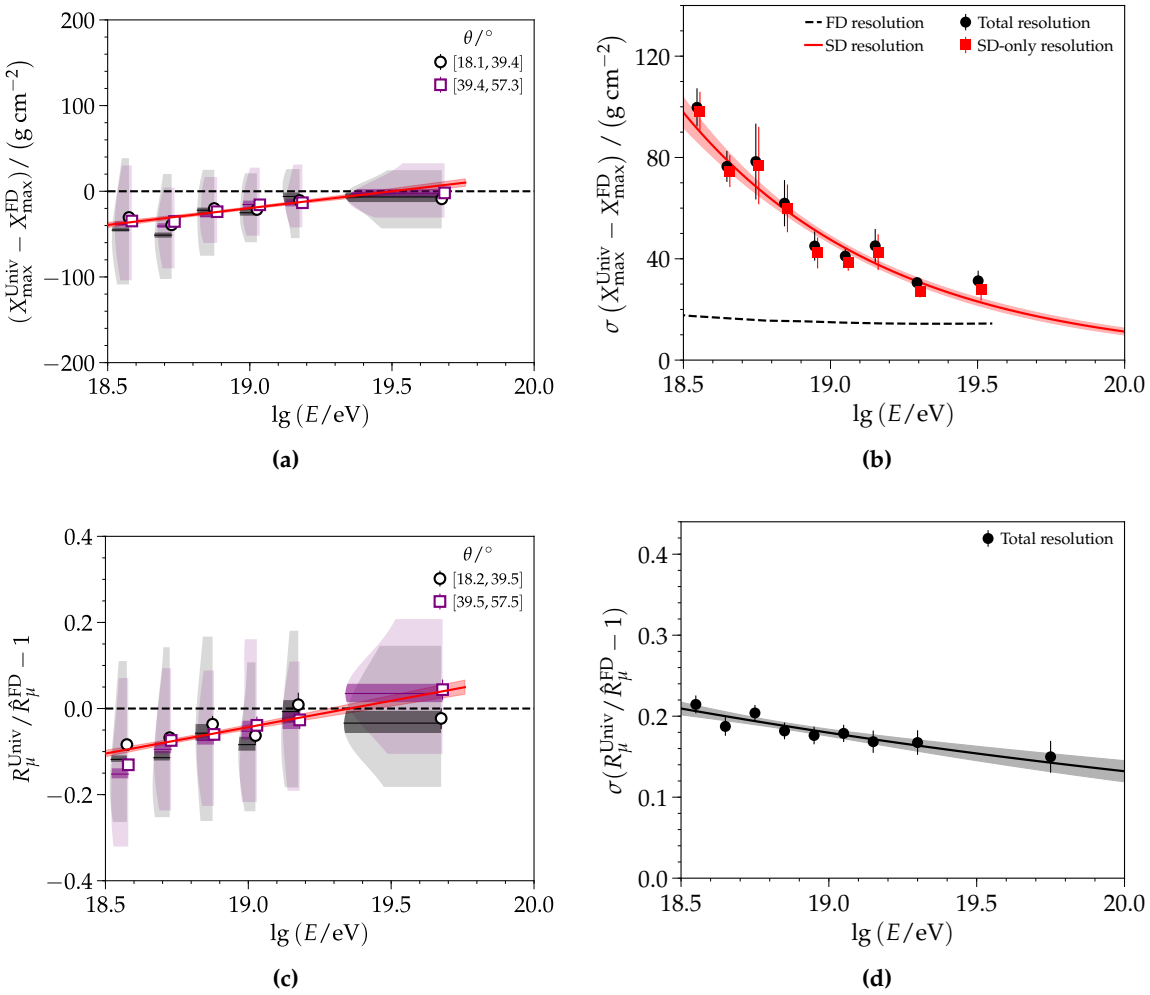

Figure D.36: The (*left*) bias and (*right*) resolution of the (*top*) reconstructed depth of the shower maximum and (*bottom*) relative muon content for golden hybrid events. The fiducial selection for universality is applied. The values for the FD resolution are taken from [33].

Table D.3: Parameters for the bias and resolution of the reconstructed X_{max} for golden hybrid data where the universality-derived fiducial selection is used.

Data set	a	b
bias	-39.3 ± 2.9	39.3 ± 5.3
resolution	47.6 ± 1.5	1.4 ± 0.1

Table D.4: Parameters for the bias and resolution of the reconstructed R_{μ} for golden hybrid data where the universality-derived fiducial selection is used.

Data set	a	b
bias	-0.104 ± 0.008	0.122 ± 0.018
resolution	0.180 ± 0.008	0.308 ± 0.017

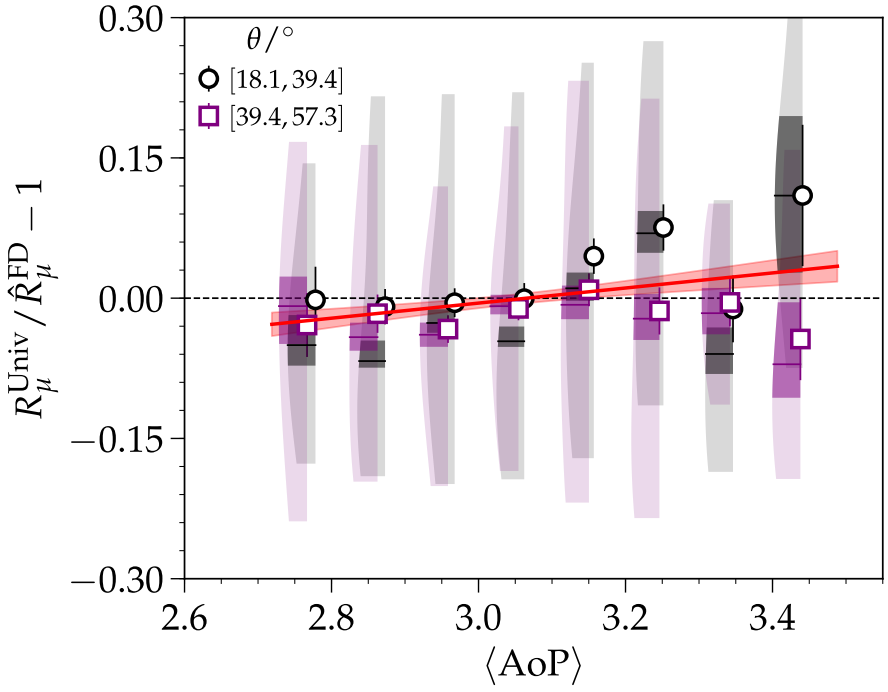

Figure D.37: The bias of the relative muon content as functions of average area over peak for golden hybrid events. The estimated relative muon content for the FD fails to take into account the correlation observed with the average area over peak seen in Fig. 4.16.

Table D.5: Parameters for bias of the reconstructed R_μ for golden hybrid data as a function of average area over peak. For these parameters, the reconstructed relative muon content is compared to the estimated relative muon content from the FD. These values greatly differ from those found in Table 4.6.

a	b
-0.005 ± 0.005	0.081 ± 0.035

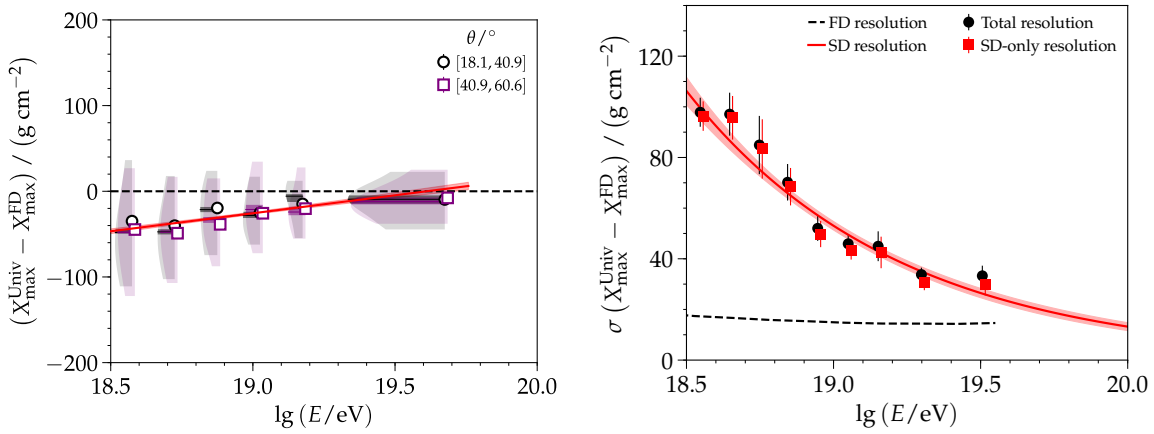

(a) (b)

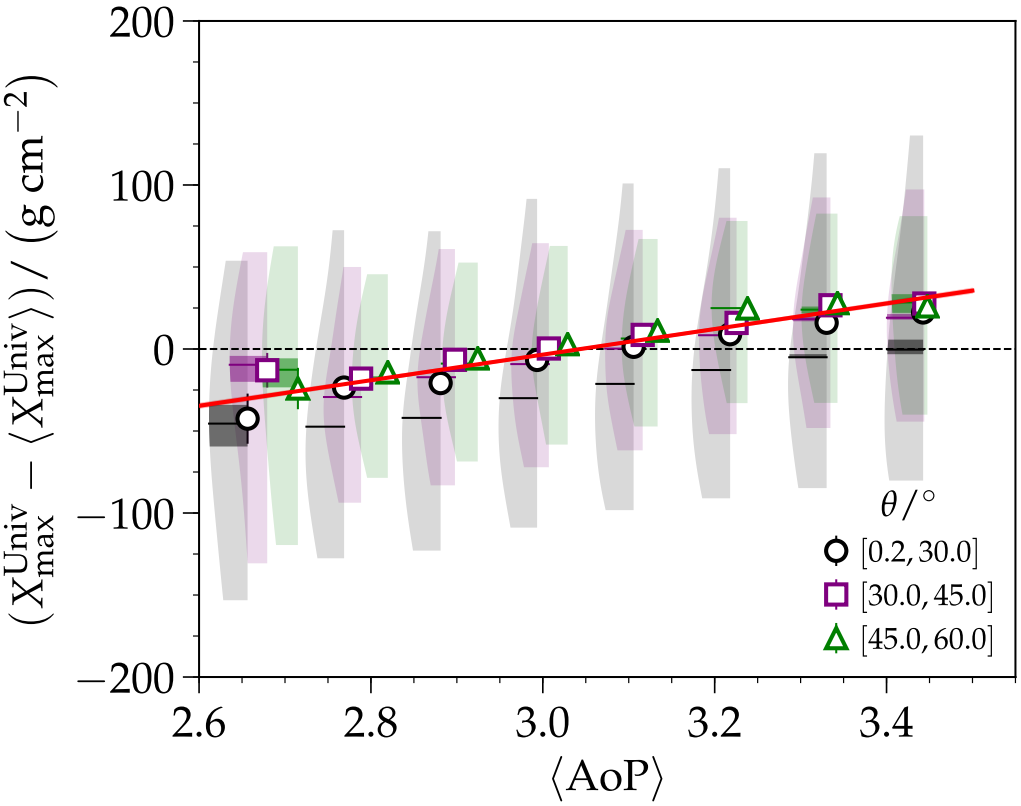

(c)

Figure D.38: The (a) bias and (b) resolution of the reconstructed depth of the shower maximum is determined for golden hybrid events. (c) The bias is shown with respect to the average area over peak. These biases are evaluated after correcting for the bias observed in simulations and the residual bias.

D.6 Global reconstruction with fixed axis

The reconstruction methods discussed throughout this work are detailed in Section 3.2.3. Out of the methods discussed, the constrained axis reconstruction has the highest average reconstruction efficiency while still including the correlations between the physics variables. In this universality reconstruction, the constrainment is such that the universality reconstructed axis must be within 1° of the SD-reconstructed shower axis, which has been found to be, on average, within 0.5° of the true axis. The angular constraint on the reconstructed axis may be increased or decreased. For this work, a special case of the constrained axis reconstruction —known as the fixed axis fit— is analyzed where the universality shower axis is fixed to the SD-reconstructed shower axis (e.g. constrainment of the difference in the axes is 0°.

The overall and zenith-dependent reconstruction efficiencies of the fixed axis method are given in Fig. D.39. Like the reconstruction efficiencies for the constrained axis fit (Fig. 3.25), more than 90 % of events are reconstructed with minimal outliers. At low energies, there is a drop in the efficiency that can be attributed to events with a zenith angle between 55° to 60°. Such events have strict timing constraints which prove challenging to fit. While the efficiencies of the constrained and fixed axis method look mostly similar, a detailed investigation at the highest energies indicates a slightly larger dependence on zenith angle at the highest energies for the fixed axis method.

As the simulation-based studies of the constrained and fixed axis methods use the true values for initial values, a study where the axis is set to the SD axis is performed (Appendix D.6.1). Finally, the results obtained with the constrained and fixed axis methods are compared (Appendix D.6.2).

D.6.1 Using SD axis vs MC axis

As discussed in Section 3.2.3, the initial reconstruction parameters for simulations come from the Monte Carlo values, whereas the initial values for data mostly come from the SD. It was shown using simulations that the angular resolution of the SD —when compared to the true values— has a range from 0.25° to 0.5°, which decreases with increasing zenith angle (Fig. 3.20). Moreover, the deviation of the SD axis to the true is not uniform or equally distributed among its components. In order to fairly assess the implementation of the constrained axis for data, a reconstruction was performed where the axis in simulations was fixed to the axis reconstructed by the SD. The reconstruction efficiencies and biases of the reconstruction[17] are presented in Fig. D.40. Overall, the reconstruction efficiency, bias, and resolution look similar to that of the fixed and constrained axis reconstructions.

In Fig. D.41, 50 471 non-saturated events are compared for a fixed reconstruction using the SD or MC axis. The reconstructed depth of the shower maximum and relative muon content are unbiased and do not exhibit further dependencies with respect to zenith angle. On average, the change in axis leads to a energy-independent resolution of 15 g cm^{-2} in X_{max} and 3 % in the relative difference of R_μ. While the observables might differ from event to event, both methods have nearly identical biases and resolutions when compared to the true values. Furthermore, the correlation between the reconstructed X_{max} and R_μ is unchanged. The difference between the reconstructed and true core position is given in Fig. D.42. The reconstructed core relative to the true core position is mostly unbiased with a mean deviation of 1.5 m. The 1 σ spread is larger for the modified reconstructions at $10^{18.5}$ eV, yet it is of the same order across all other energies. At small zenith angles, a selection bias

[17] The fixed axis reconstruction using the true axis is given in Fig. D.39.

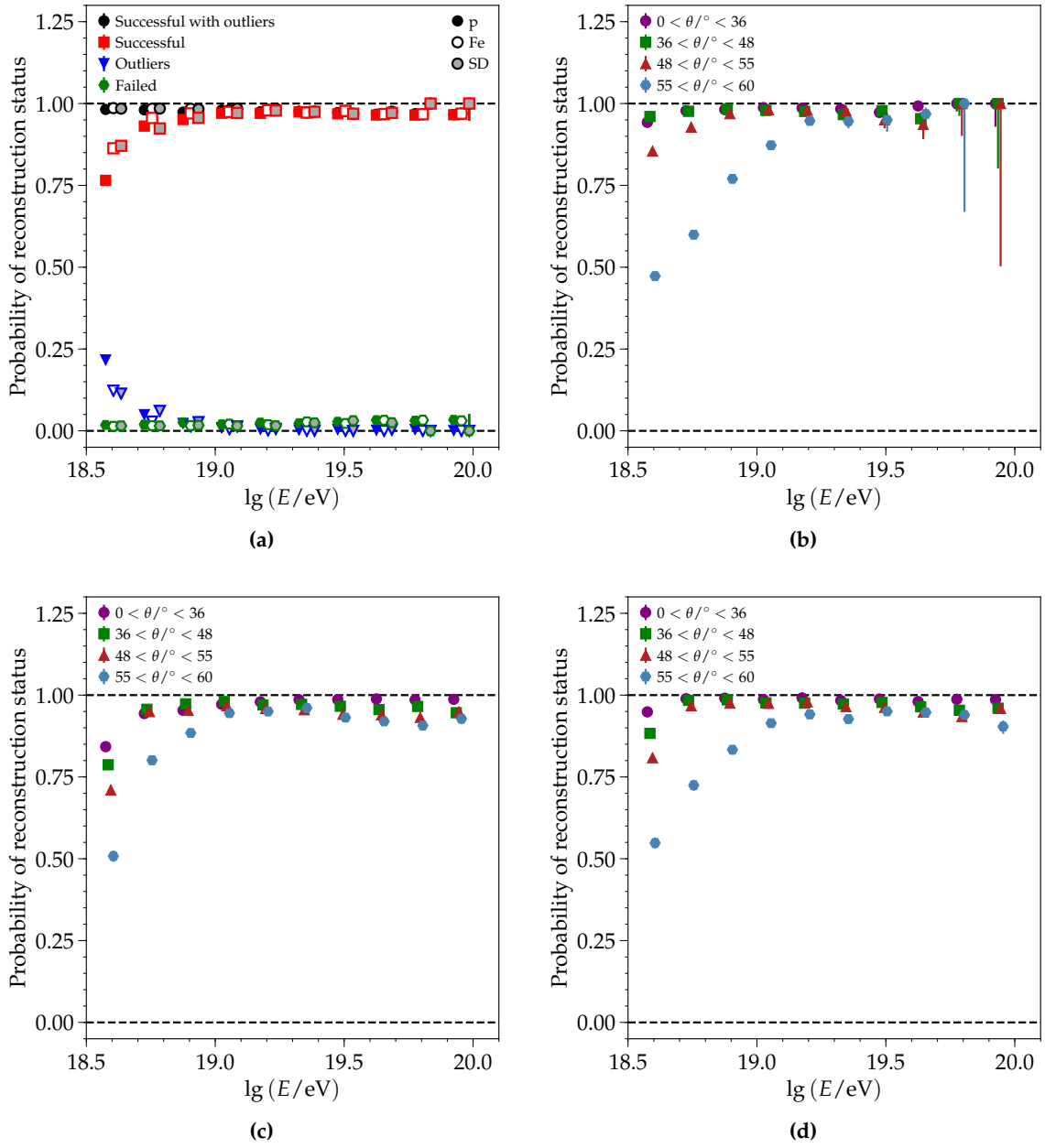

Figure D.39: Reconstruction efficiency of the fixed axis fit for non-saturated events with respect to energy. (a) The overall efficiency is shown for QGSJET-II.04 simulations from the Napoli library in comparison to SD data from 2004-2016. **Successful** reconstructed events are analyzed with respect to energy and zenith angle for (b) SD data and (c) proton and (d) iron simulations. In comparing the plots shown here to those of the constrained axis of Fig. 3.25, an overall similarity in the efficiencies may be observed. The efficiencies of simulations in the fixed axis method have a greater dependence with respect to increasing zenith angle that generally increases with respect to energy. However, in SD data, this separation is not clearly observed.

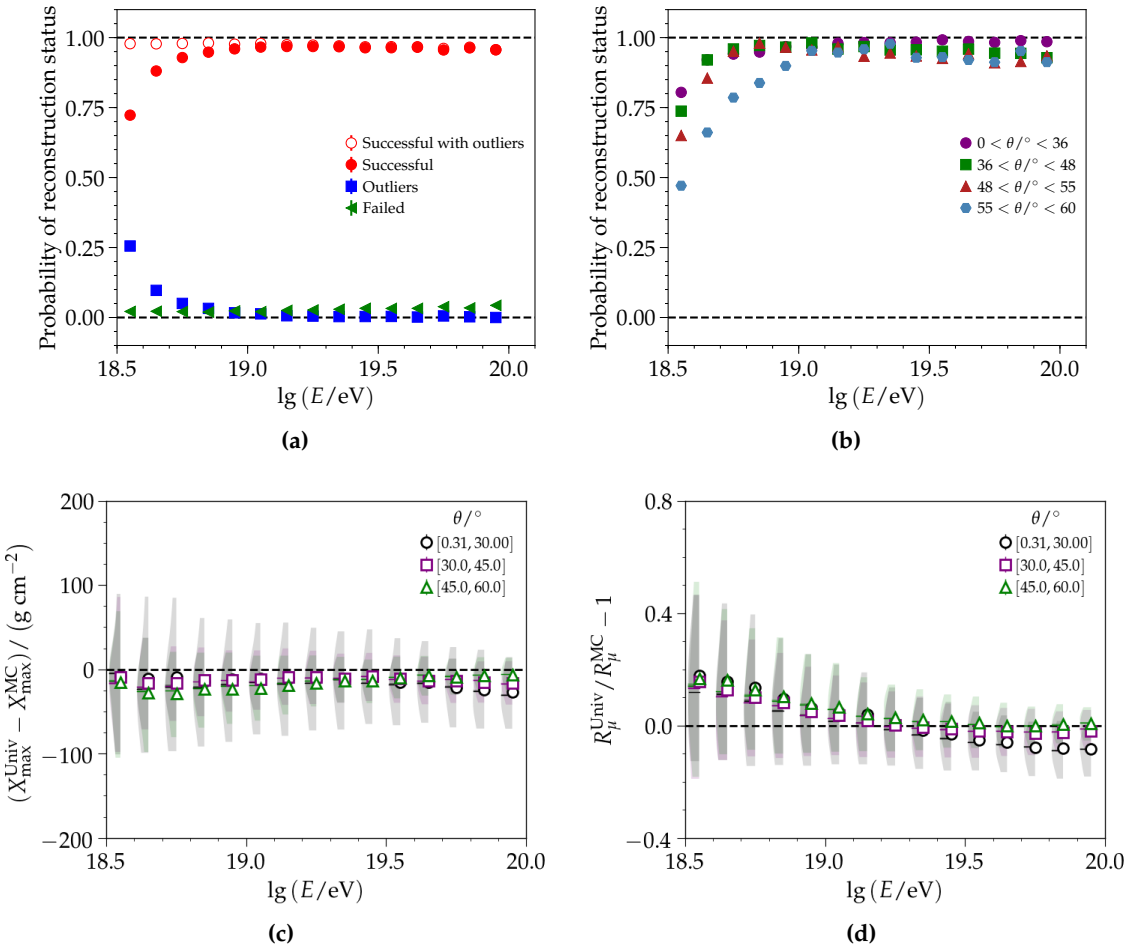

Figure D.40: QGSJET-II.04 proton-induced simulations of non-saturated events from the Napoli library reconstructed with a fixed SD axis. The (a) overall and (a) zenith-dependent, **successful** efficiencies. Difference in the reconstructed and true values of **successful** events for the (c) depth of the shower maximum and (d) relative muon content.

of the global reconstruction should be noted; for energies less than 10^{19} eV, events with a zenith angle less than 36° are increasingly more likely to be poorly reconstructed.

D.6.2 Comparison to constrained axis fit

Many of the figures included in this subsection are meant to be compared with those found in Section 4.2. The biases of the reconstructed observables are given in Fig. D.43 for the fixed axis fit. Like the constrained axis, the reconstructed depth of the shower maximum is biased by less than 30 g cm^{-2} above an energy of $10^{18.6}$ eV for zenith angles below 52.2°. At the highest energies, there is a bias — on order of 40 g cm^{-2}— for proton-induced showers which increases with decreasing zenith angle. This zenith-dependent bias is roughly twice as large as that found with the constrained axis reconstruction. Correspondingly, the zenith-dependent bias of the relative muon content is also more pronounced in the fixed axis reconstruction.

In Fig. D.44, the reconstructed results of the constrained and fixed axis fits are compared. Above an energy of $10^{19.0}$ eV, the spread of the bias of the constrained axis method is larger than that found with the fixed axis by around 5 g cm^{-2} to 10 g cm^{-2}, yet the average bias is smaller by around 5 g cm^{-2}. While this may not seem significant, when this taken into

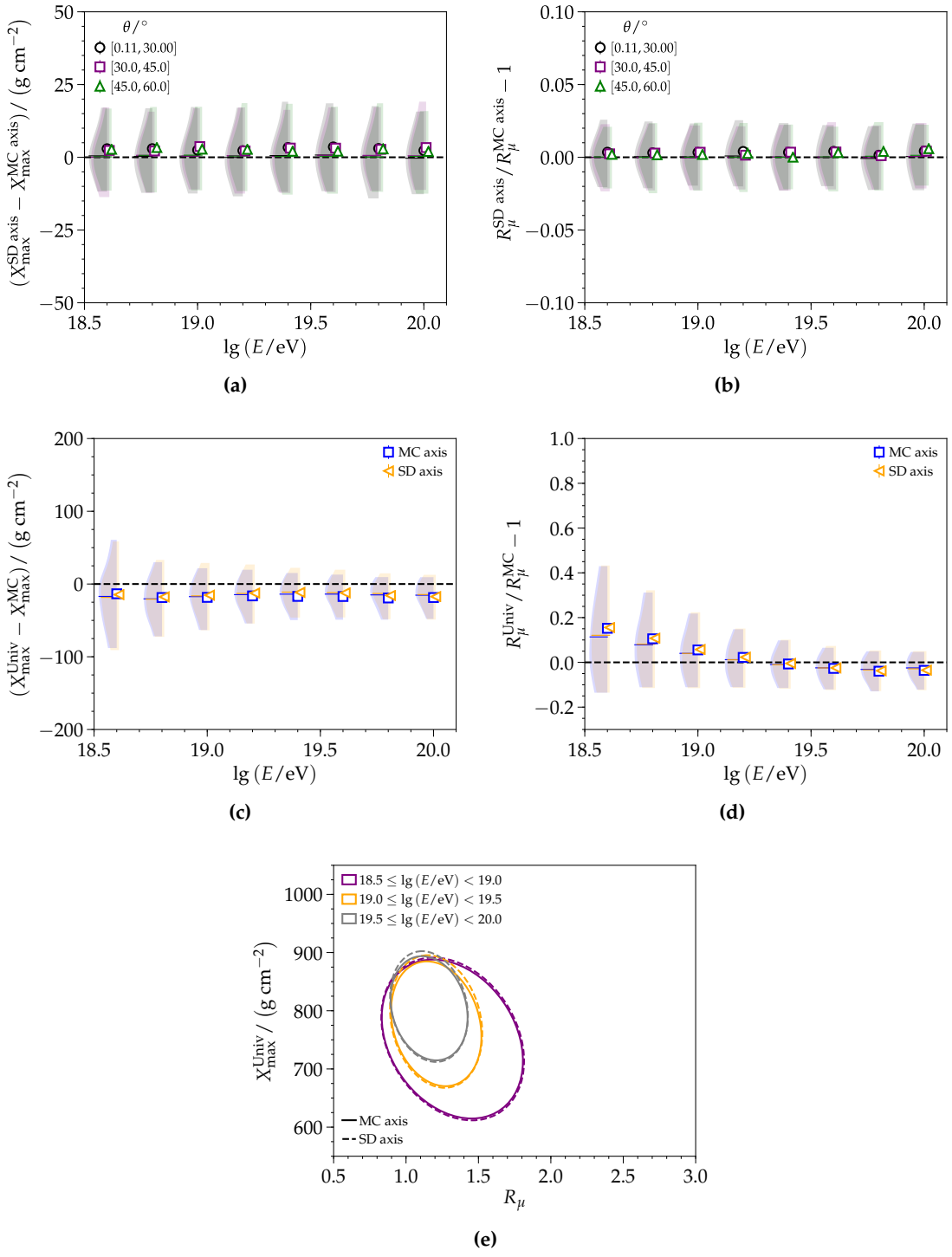

Figure D.41: QGSJET-II.04 proton-induced simulations of non-saturated events from the Napoli library reconstructed with a fixed SD axis and true axis (MC). Difference in the reconstructed values for the (a) depth of shower maximum and (b) relative muon content. (c), (d) Difference between the reconstructed and true values. (e) The correlation between the depth of the shower maximum and relative muon content is shown with 1 σ contours for various energy bins.

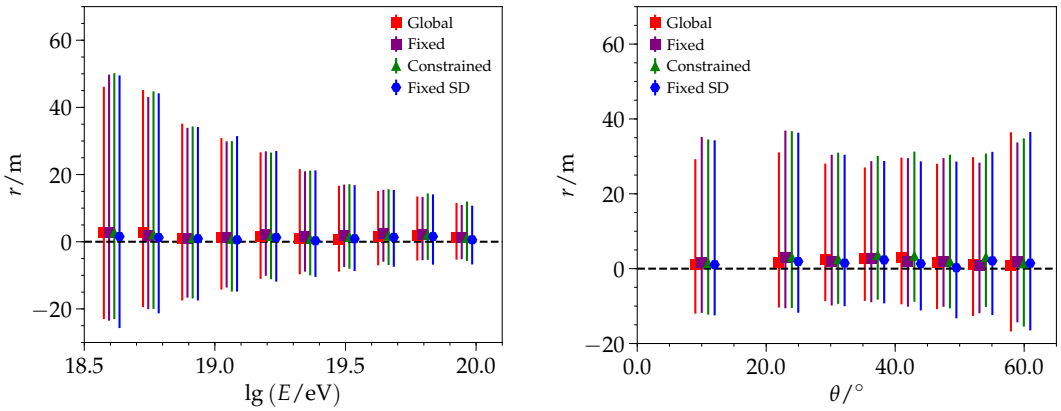

Figure D.42: QGSJET-II.04 proton-induced simulations of non-saturated events from the Napoli library reconstructed using the **global** method without modification, with a **fixed**/**constrained** true axis, and **fixed SD** axis.

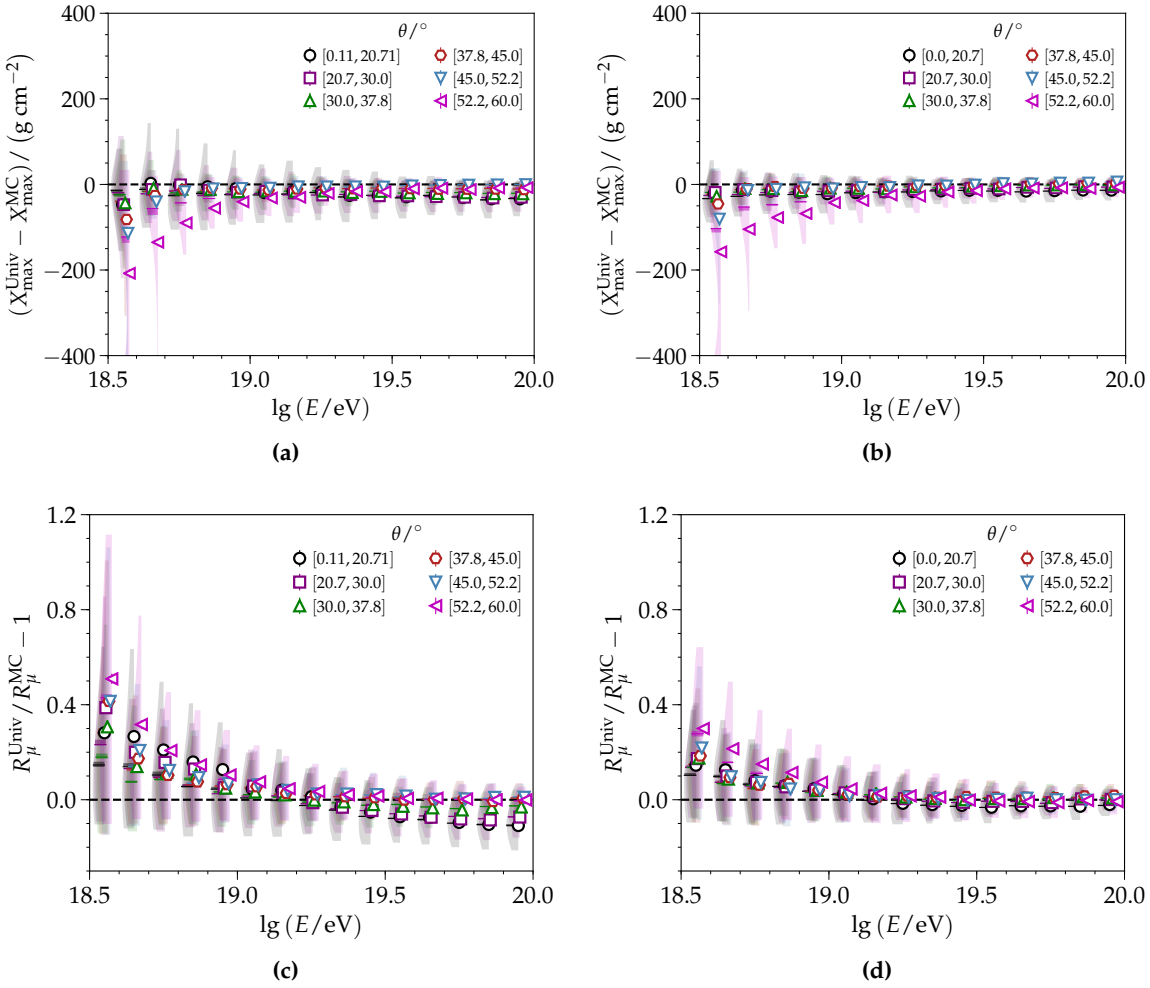

Figure D.43: QGSJET-II.04 (*left*) proton- and (*right*) iron-induced simulations from the Napoli library reconstructed with the fixed axis method. Only non-saturated events are considered with no further cuts applied. The bias of the reconstructed (*top*) depth of the shower maximum and (*bottom*) relative muon content are considered with respect to energy and zenith angle.

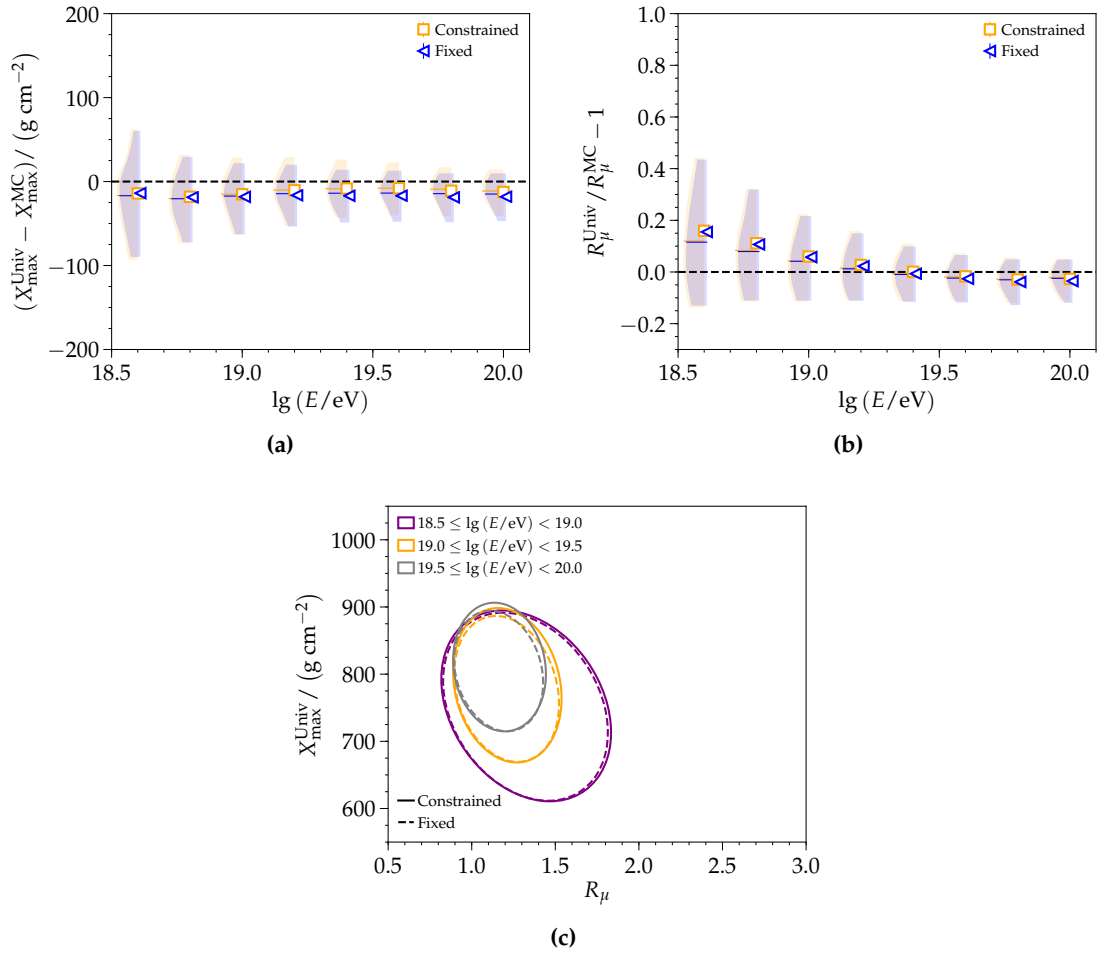

Figure D.44: Comparison of the reconstructed results of the constrained and fixed axis methods. Non-saturated events from QGSJET-II.04 proton-induced simulations are used. The difference in the reconstructed and true values for the (a) depth of the shower maximum and (b) relative muon content are compared for the two methods. (c) The correlation between the depth of the shower maximum and relative muon content is shown with $1\,\sigma$ contours for various energy bins.

account with the greater dependence on the zenith angle in the fixed axis fit, it is likely that a fiducial selection in zenith angle involving this method would reject more events than the selection performed for the constrained axis fit. A comparison of the correlation of the depth of the shower maximum and relative muon content indicates that the both methods contain the same correlations. As the constrained axis was shown to contain all correct physics correlations Section 4.1, such agreement indicates that the fixed axis fit also includes all physics correlations.

D.7 Addendum to mass composition

Each subsection contained in this section is a supplement to the section in Chapter 5 of which has a matching title.

D.7.1 Event selection and systematics

In Fig. D.45, the mean values after each selection or modification are made are compared to the original reconstructed values as a function of energy. In contrast to the study given in Fig. 5.1, this analysis shows how the overall mean is changed after all modifications are performed. As the selections are applied sequentially (in the order, given in the legend), the overall biases are given by the **Bias from** $\langle$**AoP**$\rangle$. Above an energy of $10^{19.3}$ eV, the bias correction from golden hybrids reduces the bias correction obtained from simulations to less than 15 g cm^{-2} and 2 % (based on Fig. D.45c).

Throughout this appendix, the residual bias of the reconstructed depth of the shower maximum (Fig. 4.6e and Fig. 4.6f) has been corrected for as a function of zenith angle and energy (Appendix D.5.2). Correspondingly, the data-based corrections were performed again (Appendix D.5.3). To carry on this analysis, the resulting systematics are given in Fig. D.46 and tabulated in Table D.6. The remaining zenith-dependent bias is estimated from Fig. D.33 to be at most 10 g cm^{-2}. By correcting for the residual bias in simulations, the change in the mean at the highest energies is reduced from around 15 g cm^{-2} (Fig. D.45) to 10 g cm^{-2}; this mean remains unchanged throughout the subsequent modifications. The additional systematics considered, as given in Fig. 5.2, are similar to what was shown before. For further information on how systematics are calculated and a discussion of them, see Section 5.1.

D.7.2 Average depth of the shower maximum

The first and second moment of the depth of the shower maximum are given in Fig. D.47 where the residual bias of X_{max} has been corrected for from parameterizations in simulations (Appendix D.5.2). The elongation rate is fit with a $\chi^2/n_{\mathrm{dof}} = 1.2$ was achieved with a fit to a broken line. The break point in energy is fit to $\lg(E_{\mathrm{ref}}/\mathrm{eV}) = 19.60\pm0.05$, which is indicated with a magenta hexagon. Below E_{ref}, the elongation rate $D_{10} = \frac{\mathrm{d}\langle X_{\mathrm{max}}\rangle}{\mathrm{d}\lg E}$ is[18]:

$$D_{10} = (25\pm1)\,\mathrm{g\,cm^{-2}}\,, \tag{D.15}$$

and above E_{ref}:

$$D_{10} = (118\pm35)\,\mathrm{g\,cm^{-2}}\,. \tag{D.16}$$

To better visualize the break in the plot, the model prior to the break is continued as a dashed line. The elongation rate below E_{ref} is in better agreement with the elongation rate (26 g cm^{-2}) found for the FD in Eq. (4.7) than the result obtained in Section 5.2.1 ((15$\pm$2) g cm^{-2}).

Because the spread of X_{max} is still correlated with zenith angle and energy, the fluctuations as a function of energy are nearly identical to the results presented in Fig. 5.6, and thus, it is not necessary to refit the fractional mass composition found in Fig. 5.12, as this will yield similar results. In order to improve the mass composition results presented in this work, further studies on the reconstruction procedure are warranted, as detailed at the end of Section 5.3.

[18]The intercept of the line is found to be (771$\pm$1) g cm^{-2}.

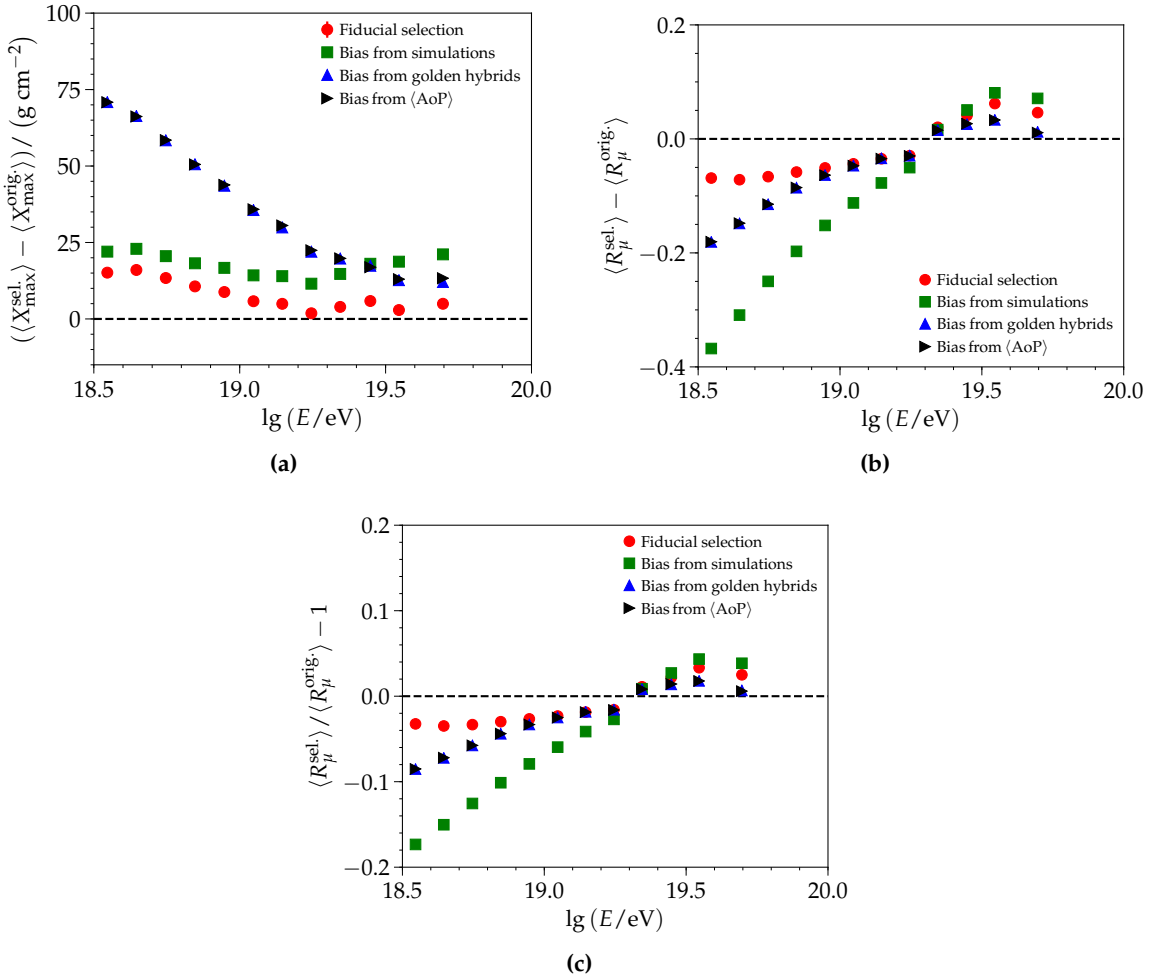

Figure D.45: The change in the mean reconstructed (a) depth of the shower maximum and (b) relative muon content compared to the mean values obtained after each selection is applied. (c) the relative difference in the mean is also considered for the relative muon content.

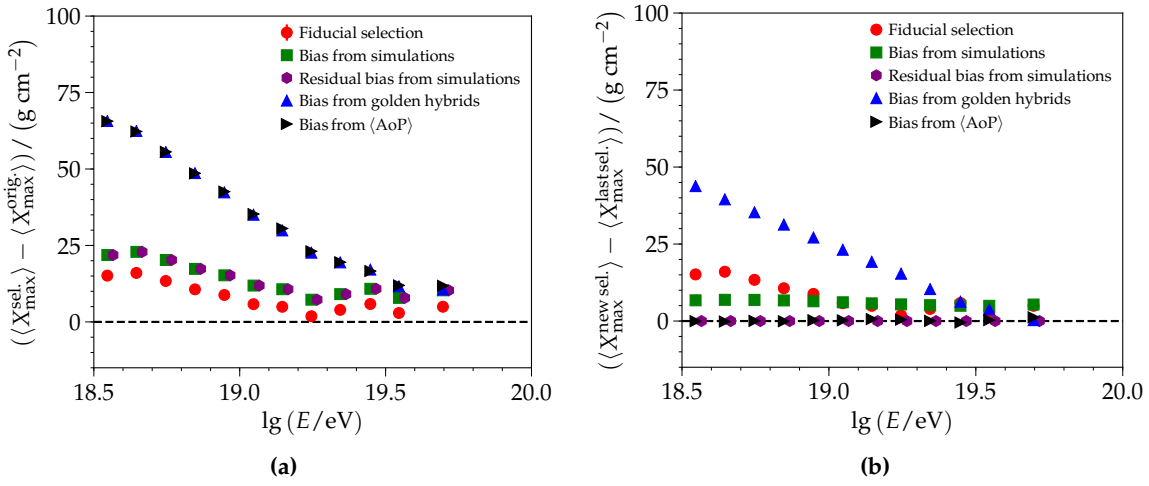

Figure D.46: The change in the mean reconstructed depth of the shower maximum compared to the mean values obtained (a) after each selection is applied to the original value (b) to the mean of the modification previously applied.

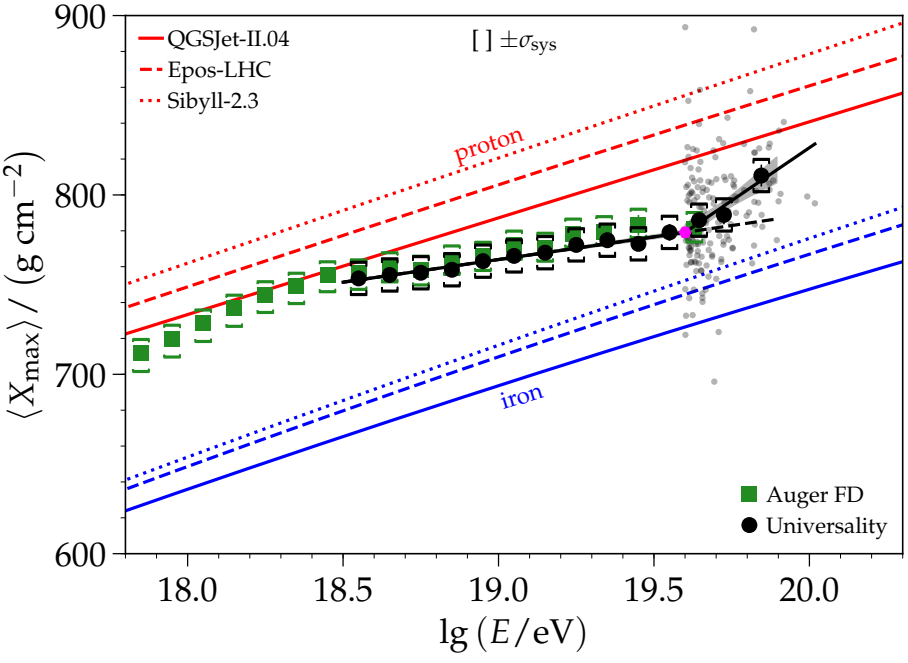

(a)

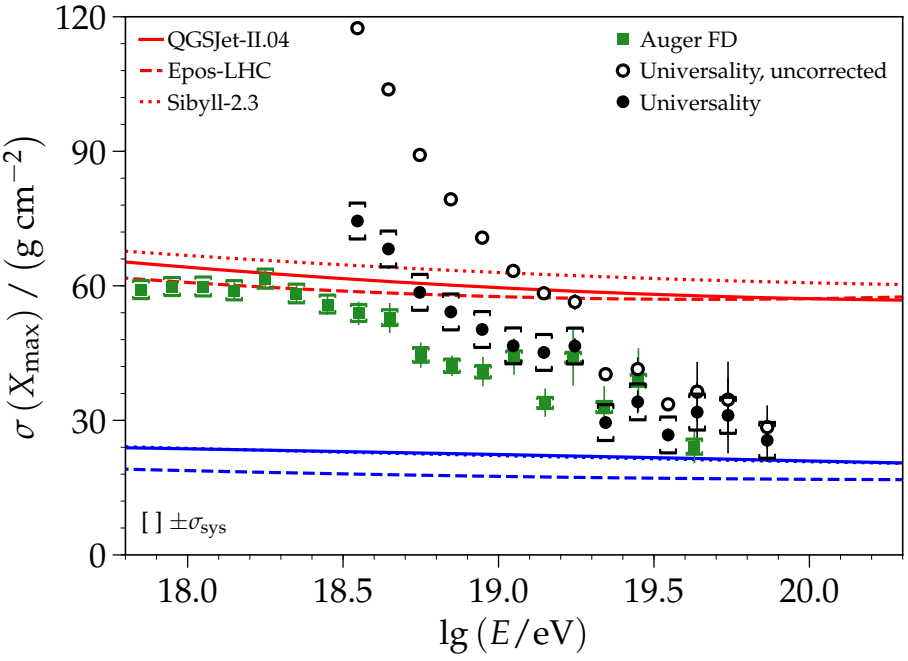

(b)

Figure D.47: (a) Profiles of the average reconstructed depth of the shower maximum with statistical and systematic uncertainties. Recent results as measured by the Auger FD are shown with the green rectangles ([104]). The elongation rate was fit with a broken line, as described in the text. (b) The uncorrected fluctuations —corresponding to the raw second moment of X_{max}— and values corrected with the detector resolution are shown as a function of energy.

Table D.6: Average systematic uncertainty for each selection and correction applied.

	X_{max} / g cm^{-2}
Fiducial selection	3.8
Bias from simulations	5.3
Remaining zenith bias	5.0
Total	8.2

D.7.3 Distribution-based analysis method

In Section 5.3, the changing fractional composition of ultra-high energy cosmic rays is determined using the distributions of the depth of the shower maximum in distinct energy bins. Nevertheless, in Fig. 1.4 and Fig. 1.2, the energy spectrum may also be decomposed into contributions from elemental groups. While this was not investigated in this work, the fractions derived in Section 5.3 may be multiplied with the measured energy spectrum of Auger [135] to observe the predicted fluxes, as is done in Fig. D.48. In future analyses, the universality-derived energy spectrum and depth of the shower maximum may be simultaneously fit with Monte Carlo templates or injection spectra[19].

[19]Such a method has been explored in [196] using a mixture of FD X_{max} data and the SD energy spectrum.

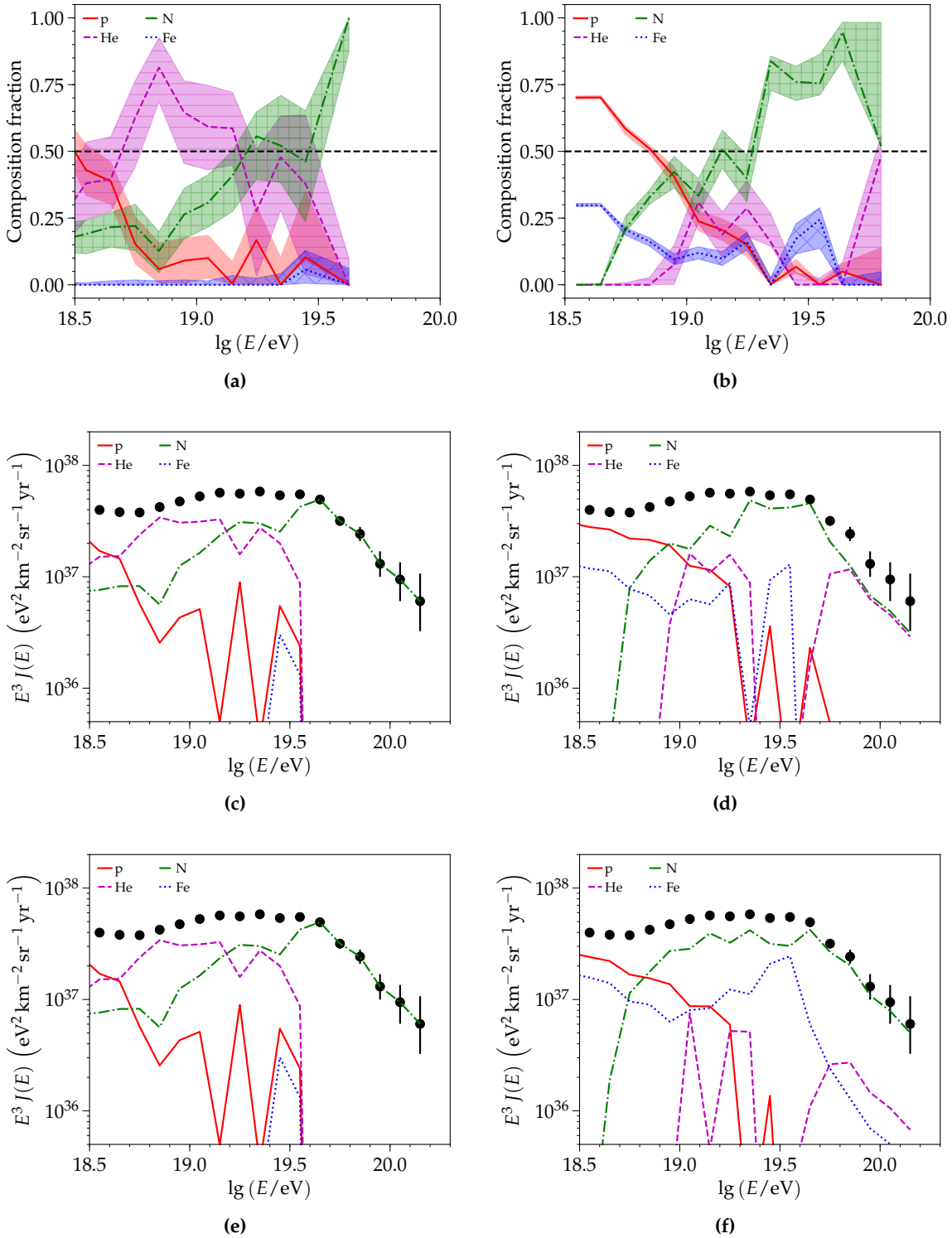

Figure D.48: Comparison of the predicted composition of the energy spectrum using (*left*) FD (values from [104]) and (*right*) SD-1500 data (this work). (*Top*) The fractional values (lines) and their statistical uncertainties (hatched areas) are shown for a proton-helium-nitrogen-iron mixture derived from EPOS-LHC simulations. Due to the large number of events, the statistical uncertainty is greatly reduced with SD-1500 data. The predicted decomposed energy spectra are given for (*middle*) EPOS-LHC and (*bottom*) SIBYLL-2.3. In both cases, the predicted spectra are not as smooth as would be expected from potential sources. Further improvement of the method developed in this work, as well as simultaneously fitting the composition and energy spectrum, should yield better, more constrained results.

APPENDIX E

Acknowledgments

Throughout the development of this work, many people have generously supported me. First and foremost, I would like to express my gratitude to Prof. Johannes Blümer and the *Karlsruhe School of Elementary Particle and Astroparticle Physics: Science and Technology* (KSETA) for making this research project possible. I am very thankful for the scientific opportunities that have been facilitated by KIT, particularly the visits to Argentina and other countries for workshops and Auger collaboration meetings.

My sincerest thanks goes to Prof. Ulrich Husemann for acting as my co-referee and for the extensive feedback he provided as the document entered its final stages. I want to thank my advisor Dr. Markus Roth for his constant support throughout these last four years. I hope that the further development of the analyses presented in this work will be successful and help in the determination of the mass composition and identification of cosmic accelerators.

To all my colleagues, thank you for the many interesting discussions, fun social outings, and your support over these years. Thank you to Sabine Bucher for everything that she does; life at the institute would not be possible without her steadfast efforts.

The most heartfelt thanks go to Alexander Schulz for proofreading this work, his unwavering support over the years, and the many fruitful discussions we have shared. Thanks to David Schmidt for his suggestions for this work and for convincing me to do a PhD Germany. To Darko Veberič, thank you for all the support that you provide to Auger via Offline. Without your debugging efforts, this thesis and several others would not contain as many results as they do. Thank you to Daniela Mockler and Sarah Mueller for being wonderful office mates. Finally, thank you to my family for their support over all of these years. Without your tutelage, I could not have reached my goals.

Bibliography

[1] V. F. Hess, Beobachtungen der durchdringenden Strahlung bei sieben Freiballonfahrten, Phys. Z. 13 (1912) 1084.

[2] A. D. Angelis, N. Giglietto, S. Stramaglia, Domenico Pacini, the forgotten pioneer of the discovery of cosmic rays (2010). arXiv:1002.2888.

[3] J. Clay, P. van Alphen, C. Hooft, Results of the Dutch Cosmic Ray Expedition 1933: II. The magnetic latitude effect of cosmic rays a magnetic longitude effect, Physica 1 (7–12) (1934) 829 – 838. doi:10.1016/S0031-8914(34)80277-7.

[4] J. Blümer, R. Engel, J. R. Hörandel, Cosmic Rays from the Knee to the Highest Energies (2009). arXiv:astro-ph/0904.0725.

[5] P. Auger, P. Ehrenfest, R. Maze, J. Daudin, R. A. Fréon, Extensive cosmic-ray showers, Rev. Mod. Phys. 11 (3-4) (1939) 288–291. doi:10.1103/RevModPhys.11.288.

[6] W. Heitler, The Quantum Theory of Radiation, 3rd Edition, Oxford University Press, Oxford, 1954.

[7] J. Matthews, A Heitler model of extensive air showers, Astropart. Phys. 22 (5-6) (2005) 387 – 397. doi:10.1016/j.astropartphys.2004.09.003.

[8] J. Linsley, Evidence for a Primary Cosmic-Ray Particle with Energy 10^{20} eV, Phys. Rev. Lett. 10 (4) (1963) 146–148. doi:10.1103/PhysRevLett.10.146.

[9] K. Greisen, End to the cosmic-ray spectrum?, Phys. Rev. Lett. 16 (17) (1966) 748–750. doi:10.1103/PhysRevLett.16.748.

[10] G. T. Zatsepin, V. A. Kuz'min, Upper Limit of the Spectrum of Cosmic Rays, JETP Lett. 4 (1966) 78 – 80.

[11] D. M. Edge *et al.* (Haverah Park Collab.), The cosmic ray spectrum at energies above 10^{17} eV, J. Phys. A 6 (1973) 1612 – 1634.

[12] High Resolution Fly's Eye Collab., Observation of the Ankle and Evidence for a High-Energy Break in the Cosmic Ray Spectrum, Phys. Lett. B 619: 271-280 (2005). arXiv:astro-ph/0501317, doi:10.1016/j.physletb.2005.05.064.

[13] P. Sokolsky (HiRes Collab.), Final Results from the High Resolution Fly's Eye (HiRes) Experiment (2010). arXiv:astro-ph/1010.2690.

[14] N. Sakaki (AGASA Collab.), Cosmic ray energy spectrum above 3×10^{18} eV observed with AGASA, in: Proc. 27th Int. Cosmic Ray Conf., Hamburg, Germany, 2001.

[15] A. Aab *et al.* (Pierre Auger Collab.), The Pierre Auger Observatory Upgrade - Preliminary Design Report (2016). arXiv:astro-ph.IM/1604.03637".

[16] M. Lemoine, G. Sigl, Physics and Astrophysics of Ultra-High-Energy Cosmic Rays, Springer Verlag, Berlin, 2001.

[17] A. Haungs *et al.*, KCDC — The KASCADE Cosmic-ray Data Centre, J. of Phys.: Conf. Series 632 (1) (2015) 012011.
URL http://stacks.iop.org/1742-6596/632/i=1/a=012011

[18] B. Rossi, K. Greisen, Cosmic-ray theory, Rev. Mod. Phys. 13 (1941) 240–309. doi:10.1103/RevModPhys.13.240.

[19] C. Meurer, J. Bluemer, R. Engel, A. Haungs, M. Roth, Muon production in extensive air showers and its relation to hadronic interactions, Czech. J. Phys. 56 (2006) A211. arXiv:astro-ph/0512536.

[20] D. Heck, G. Schatz, T. Thouw, J. Knapp, J. Capdevielle, CORSIKA: A Monte Carlo code to simulate extensive air showers, Forschungszentrum Karlsruhe Report FZKA (1998) 6019.

[21] A. Fasso *et al.*, The Physics models of FLUKA: Status and recent developments arXiv:hep-ph/0306267.

[22] H. Fesefeldt, The Simulation of Hadronic Showers: Physics and Applications, III. Physikalisches Institut, RWTH Aachen (1985).
URL http://cds.cern.ch/record/162911/files/CM-P00055931.pdf

[23] S. Ostapchenko, Monte Carlo treatment of hadronic interactions in enhanced Pomeron scheme: I. QGSJET-II model, Phys. Rev. D83 (2011) 014018. arXiv:1010.1869, doi:10.1103/PhysRevD.83.014018.

[24] T. Pierog, I. Karpenko, J. M. Katzy, E. Yatsenko, K. Werner, EPOS LHC: Test of collective hadronization with data measured at the CERN Large Hadron Collider, Phys. Rev. C 92 (2015) 034906. doi:10.1103/PhysRevC.92.034906.

[25] F. Riehn, H. P. Dembinski, R. Engel, A. Fedynitch, T. K. Gaisser, T. Stanev, The hadronic interaction model SIBYLL 2.3c and Feynman scaling (2017)arXiv:hep-ph/1709.07227.

[26] T. Antoni *et al.* (KASCADE Collab.), Muon density measurements with the KASCADE central detector, Astropart. Phys. 16 (4) (2002) 373 – 386. doi:10.1016/S0927-6505(01)00120-7.

[27] T. Antoni *et al.*, KASCADE measurements of energy spectra for elemental groups of cosmic rays: Results and open problems, Astropart. Phys. 24 (1-2) (2005) 1 – 25. doi:10.1016/j.astropartphys.2005.04.001.

[28] W. D. Apel *et al.* (KASCADE-Grande Collab.), Kneelike Structure in the Spectrum of the Heavy Component of Cosmic Rays Observed with KASCADE-Grande, Phys. Rev. Lett. 107 (2011) 171104. doi:10.1103/PhysRevLett.107.171104.

[29] V. Berezinsky, Transition from galactic to extragalactic cosmic rays, in: Proc. 30th Int. Cosmic Ray Conf., Mérida, Mexico, 2007. arXiv:astro-ph/0710.2750v2.

[30] R. Engel, Private communication about energy spectrum of cosmic rays (Sep. 2017).

[31] A. M. Hillas, Cosmic Rays: Recent Progress and some Current Questions, in: Conf. on Cosmology, Galaxy Formation and Astro-Particle Physics on the Pathway to the SKA address = Oxford, England, 2006. arXiv:astro-ph/0607109.

[32] M. Unger, G. R. Farrar, L. A. Anchordoqui, Origin of the ankle in the ultra-high energy cosmic ray spectrum and of the extragalactic protons below it, Phys. Rev. D 92 (12) (2015) 123001. arXiv:astro-ph.HE/1505.02153, doi:10.1103/PhysRevD.92.123001.

[33] A. Aab *et al.* (Pierre Auger Collab.), Depth of Maximum of Air-Shower Profiles at the Pierre Auger Observatory: Measurements at Energies above $10^{17.8}$ eV, Phys. Rev. D 90 (12) (2014) 122005. arXiv:astro-ph.HE/1409.4809, doi:10.1103/PhysRevD.90.122005.

[34] K.-H. Kampert, P. Tinyakov, Cosmic rays from the ankle to the cutoff, Comptes Rendus Physique 15 (2014) 318–328. arXiv:1405.0575, doi:10.1016/j.crhy.2014.04.006.

[35] A. Schulz (Pierre Auger Collab.), The measurement of the energy spectrum of cosmic rays above 0.3 EeV with the Pierre Auger Observatory, in: Proc. 33rd Int. Cosmic Ray Conf., Rio de Janeiro, Brazil, 2013. arXiv:astro-ph.HE/1307.5059.

[36] E. Kido and O. E. Kalashev (Telescope Array Collab.), Constraining UHECR source models by the TA SD energy spectrum, in: Proc. 33rd Int. Cosmic Ray Conf., Rio de Janeiro, Brazil, 2013. arXiv:astro-ph.HE/1310.6093.

[37] R. Aloisio, V. Berezinsky, P. Blasi, Ultra high energy cosmic rays: implications of Auger data for source spectra and chemical composition, JCAP 1410 (10) (2014) 020. arXiv:1312.7459, doi:10.1088/1475-7516/2014/10/020.

[38] R. Engel, D. Heck, T. Pierog, Extensive air showers and hadronic interactions at high energy, Ann. Rev. Nucl. Part. Sci. 61 (2011) 467–489. doi:10.1146/annurev.nucl.012809.104544.

[39] P. Abreu *et al.* (Pierre Auger Collab.), Interpretation of the Depths of Maximum of Extensive Air Showers Measured by the Pierre Auger Observatory, JCAP 1302 (2013) 026. arXiv:1301.6637, doi:10.1088/1475-7516/2013/02/026.

[40] R. U. Abbasi *et al.* (Pierre Auger Collab., Telescope Array Collab.), Pierre Auger Observatory and Telescope Array: Joint Contributions to the 34th International Cosmic Ray Conference (ICRC 2015), in: Proc. 34th Int. Cosmic Ray Conf., The Hague, The Netherlands, 2015. arXiv:astro-ph.HE/1511.02103.

[41] I. C. Mariş, J. Blümer, M. Roth, T. Schmidt, M. Unger, Comparison of Two Methods to Infer the Cosmic Ray Spectrum at Highest Energies, Auger internal note GAP-2007-044 (2007).

[42] J. W. Cronin, The highest-energy cosmic rays, Nuclear Physics B - Proceedings Supplements 138 (2005) 465 – 491. doi:http://dx.doi.org/10.1016/j.nuclphysbps.2004.11.107.

[43] A. Aab *et al.* (Pierre Auger Collab.), The Pierre Auger Cosmic Ray Observatory, Nucl. Instrum. Meth. A798 (2015) 172–213. arXiv:astro-ph.IM/1502.01323, doi:10.1016/j.nima.2015.06.058.

[44] Alan Coleman (Pierre Auger Collab.), The influence of weather effects on the reconstruction of extensive air showers at the Pierre Auger Observatory, in: Proc. 35th Int. Cosmic Ray Conf., Busan, South Korea, 2017. arXiv:1708.06592.

[45] D. Veberič, Private communication about current map for Pierre Auger Observatory (Jan. 2017).

[46] I. Allekotte *et al.* (Pierre Auger Collab.), The Surface Detector System of the Pierre Auger Observatory, Nucl. Instrum. Meth. A586 (2007) 409–420. arXiv:astro-ph/0712.2832, doi:10.1016/j.nima.2007.12.016.

[47] X. Bertou *et al.* (Pierre Auger Collab.), Calibration of the surface array of the Pierre Auger Observatory, Nucl. Instrum. Meth. A568 (2006) 839–846.

[48] D. Veberič (Pierre Auger Collab.), Estimation of Signal in Saturated Stations of the Pierre Auger Surface Detector, in: Proc. 33rd Int. Cosmic Ray Conf., Rio de Janeiro, Brazil, 2013. arXiv:astro-ph.HE/1307.5059.

[49] M. Aglietta, I. De Mitri, S. Maglio, S. Maldera, I. C. Maris, D. Martello, G. Navarra, M. Roth, Recovery of Saturated Signals of the Surface Detector, Auger internal note GAP-2008-30 (2008).

[50] I. C. Mariş, Measurement of the Ultra High Energy Cosmic Ray Flux using Data of the Pierre Auger Observatory, Auger internal note GAP-2008-026 (2008).

[51] J. Abraham *et al.* (Pierre Auger Collab.), The fluorescence detector of the Pierre Auger Observatory, Nucl. Instrum. Meth. A620 (2010) 227 – 251.

[52] J. F. Debatin, Investigation of optical properties of the fluorescence telescopes of the pierre auger observatory, Master's thesis, Karlsruhe Institute of Technology (2015).

[53] P. Abreu *et al.* (Pierre Auger Collab.), Description of Atmospheric Conditions at the Pierre Auger Observatory using the Global Data Assimilation System (GDAS), Astropart. Phys. 35 (2012) 591–607. arXiv:1201.2276, doi:10.1016/j.astropartphys.2011.12.002.

[54] P. Abreu *et al.* (Pierre Auger Collab.), The Rapid Atmospheric Monitoring System of the Pierre Auger Observatory, JINST 7 (2012) P09001. arXiv:1208.1675, doi:10.1088/1748-0221/7/09/P09001.

[55] D. Ravignani, A. D. Supanitsky, D. M. P. A. Collab.), Reconstruction of air shower muon densities using segmented counters with time resolution, Astropart. Phys. 82 (2016) 108–116. doi:10.1016/j.astropartphys.2016.06.001.

[56] A. Aab *et al.* (Pierre Auger Collab.), Muons in air showers at the Pierre Auger Observatory: Mean number in highly inclined events, Phys. Rev. D91 (3) (2015) 032003, [Erratum: Phys. Rev.D91,no.5,059901(2015)]. arXiv:1408.1421, doi:10.1103/PhysRevD.91.059901,10.1103/PhysRevD.91.032003.

[57] A. Aab *et al.* (Pierre Auger Collab.), Testing Hadronic Interactions at Ultrahigh Energies with Air Showers Measured by the Pierre Auger Observatory, Phys. Rev. Lett. 117 (2016) 192001. doi:10.1103/PhysRevLett.117.192001.

[58] A. Almela, Private communication regarding configuration of AMIGA (Oct. 2016).

[59] F. Suarez (Pierre Auger Collab.), The AMIGA muon detectors of the Pierre Auger Observatory, in: Proc. 33rd Int. Cosmic Ray Conf., Rio de Janeiro, Brazil, 2013. arXiv:astro-ph.HE/1307.5059.

[60] A. Aab (Pierre Auger Collab.), Prototype muon detectors for the AMIGA component of the Pierre Auger Observatory, JINST 11 (02) (2016) P02012. arXiv:physics.ins-det/1605.01625, doi:10.1088/1748-0221/11/02/P02012.

[61] H. Falcke *et al.*, (LOPES Collab.), Detection and imaging of atmospheric radio flashes from cosmic ray air showers, Nature 435 (7040) (2005) 313–316. doi:10.1038/nature03614.

[62] D. Ardouin *et al.*, Radioelectric field features of extensive air showers observed with CODALEMA, Astropart. Phys. 26 (2006) 341–350. arXiv:astro-ph/0608550, doi:10.1016/j.astropartphys.2006.07.002.

[63] F. G. Schröder, Radio detection of high-energy cosmic rays with the Auger Engineering Radio Array, Nucl. Instrum. Meth. A 824 (2016) 648 – 651. doi:http://dx.doi.org/10.1016/j.nima.2015.08.047.

[64] A. Aab *et al.* (Pierre Auger Collab.), Probing the radio emission from air showers with polarization measurements, Phys. Rev. D89 (2014) 052002. arXiv:1402.3677, doi:10.1103/PhysRevD.89.052002.

[65] A. Aab *et al.* (Pierre Auger Collab.), Energy Estimation of Cosmic Rays with the Engineering Radio Array of the Pierre Auger Observatory, Phys. Rev. D93 (12) (2016) 122005. arXiv:1508.04267, doi:10.1103/PhysRevD.93.122005.

[66] A. Aab *et al.* (Pierre Auger Collab.), Nanosecond-level time synchronization of autonomous radio detector stations for extensive air showers, JINST 11 (01) (2016) P01018. arXiv:1512.02216.

[67] S. Buitink (LOFAR Collab.), Shower Xmax determination based on LOFAR radio measurements, in: Proc. 33rd Int. Cosmic Ray Conf, Rio de Janeiro, Brazil, 2013.

[68] N. Barenthien *et al.*, Scintillator Surface Detectors of the Engineering Array: Production and Validation, Auger internal note GAP-2016-0840 (2016).

[69] I. Valino (Pierre Auger Collab.), The flux of ultra-high energy cosmic rays after ten years of operation of the Pierre Auger Observatory, in: Proc. 34th Int. Cosmic Ray Conf., The Hague, The Netherlands, 2015.

[70] J. Abraham *et al.* (Pierre Auger Collab.), Limit on the diffuse flux of ultrahigh energy tau neutrinos with the surface detector of the Pierre Auger Observatory, Phys. Rev. D 79 (10) (2009) 102001. doi:10.1103/PhysRevD.79.102001.

[71] J. Abraham *et al.* (Pierre Auger Collab.), Upper limit on the cosmic-ray photon fraction at EeV energies from the Pierre Auger Observatory, Astropart. Phys. 31 (6) (2009) 399 – 406. doi:10.1016/j.astropartphys.2009.04.003.

[72] J. Abraham *et al.* (Pierre Auger Collab.), Measurement of the energy spectrum of cosmic rays above 10^{18} eV using the Pierre Auger Observatory, Phys. Lett. B 685 (4-5) (2010) 239 – 246. doi:10.1016/j.physletb.2010.02.013.

[73] J. Abraham *et al.* (Pierre Auger Collab.), Measurement of the Depth of Maximum of Extensive Air Showers above 10^{18} eV, Phys. Rev. Lett. 104 (9) (2010) 091101. doi:10.1103/PhysRevLett.104.091101.

[74] P. Abreu *et al.* (Pierre Auger Collab.), A Search for Ultra-High Energy Neutrinos in Highly Inclined Events at the Pierre Auger Observatory, Phys. Rev. D84 (2011) 122005. arXiv:1202.1493, doi:10.1103/PhysRevD.85.029902,10.1103/PhysRevD.84.122005.

[75] P. Abreu *et al.* (Pierre Auger Collab.), The Lateral Trigger Probability function for the ultra-high energy cosmic ray showers detected by the Pierre Auger Observatory, Astropart. Phys. 35 (2011) 266–276. arXiv:1111.6645, doi:10.1016/j.astropartphys.2012.02.005,10.1016/j.astropartphys.2011.08.001.

[76] P. Abreu *et al.* (Pierre Auger Collab.), Anisotropy and chemical composition of ultra-high energy cosmic rays using arrival directions measured by the Pierre Auger Observatory, JCAP 1106 (2011) 022. arXiv:1106.3048, doi:10.1088/1475-7516/2011/06/022.

[77] P. Abreu *et al.* (Pierre Auger Collab.), The effect of the geomagnetic field on cosmic ray energy estimates and large scale anisotropy searches on data from the Pierre Auger Observatory, JCAP 1111 (2011) 022. arXiv:1111.7122, doi:10.1088/1475-7516/2011/11/022.

[78] P. Abreu *et al.* (Pierre Auger Collab.), Advanced functionality for radio analysis in the Offline software framework of the Pierre Auger Observatory, Nucl. Instrum. Meth. A635 (2011) 92–102. arXiv:1101.4473, doi:10.1016/j.nima.2011.01.049.

[79] P. Abreu *et al.* (Pierre Auger Collab.), Measurement of the Cosmic Ray Energy Spectrum Using Hybrid Events of the Pierre Auger Observatory, Eur. Phys. J. Plus 127 (2012) 87. arXiv:1208.6574, doi:10.1140/epjp/i2012-12087-9.

[80] P. Abreu *et al.* (Pierre Auger Collab.), A Search for Point Sources of EeV Neutrons, Astrophys. J. 760 (2012) 148. arXiv:1211.4901, doi:10.1088/0004-637X/760/2/148.

[81] P. Abreu *et al.* (Pierre Auger Collab.), Large scale distribution of arrival directions of cosmic rays detected above 10^{18} eV at the Pierre Auger Observatory, Astrophys. J. Suppl. 203 (2012) 34. arXiv:1210.3736, doi:10.1088/0067-0049/203/2/34.

[82] P. Abreu *et al.* (Pierre Auger Collab.), Results of a self-triggered prototype system for radio-detection of extensive air showers at the Pierre Auger Observatory, JINST 7 (2012) P11023. arXiv:1211.0572, doi:10.1088/1748-0221/7/11/P11023.

[83] P. Abreu *et al.* (Pierre Auger Collab.), Search for point-like sources of ultra-high energy neutrinos at the Pierre Auger Observatory and improved limit on the diffuse flux of tau neutrinos, Astrophys. J. 755 (2012) L4. arXiv:1210.3143, doi:10.1088/2041-8205/755/1/L4.

[84] P. Abreu *et al.* (Pierre Auger Collab.), Constraints on the origin of cosmic rays above 10^{18} eV from large scale anisotropy searches in data of the Pierre Auger Observatory, Astrophys. J. 762 (2012) L13. arXiv:1212.3083, doi:10.1088/2041-8205/762/1/L13.

[85] P. Abreu *et al.* (Pierre Auger Collab.), Antennas for the Detection of Radio Emission Pulses from Cosmic-Ray, JINST 7 (2012) P10011. arXiv:1209.3840, doi:10.1088/1748-0221/7/10/P10011.

[86] P. Abreu *et al.* (Pierre Auger Collab.), A search for anisotropy in the arrival directions of ultra high energy cosmic rays recorded at the Pierre Auger Observatory, JCAP (2012).

[87] P. Abreu *et al.* (Pierre Auger Collab.), Search for signatures of magnetically-induced alignment in the arrival directions measured by the Pierre Auger Observatory, Astropart. Phys. 35 (2012) 354–361. arXiv:1111.2472, doi:10.1016/j.astropartphys.2011.10.004.

[88] P. Abreu *et al.* (Pierre Auger Collab.), Ultrahigh Energy Neutrinos at the Pierre Auger Observatory, Adv. High Energy Phys. 2013 (2013) 708680. arXiv:1304.1630, doi:10.1155/2013/708680.

[89] P. Abreu *et al.* (Pierre Auger Collab.), Techniques for Measuring Aerosol Attenuation using the Central Laser Facility at the Pierre Auger Observatory, JINST 8 (2013) P04009. arXiv:1303.5576, doi:10.1088/1748-0221/8/04/P04009.

[90] P. Abreu *et al.* (Pierre Auger Collab.), Identifying Clouds over the Pierre Auger Observatory using Infrared Satellite Data, Astropart. Phys. 50-52 (2013) 92–101. arXiv:1310.1641, doi:10.1016/j.astropartphys.2013.09.004.

[91] P. Abreu *et al.* (Pierre Auger Collab.), Bounds on the density of sources of ultra-high energy cosmic rays from the Pierre Auger Observatory, JCAP 1305 (05) (2013) 009. arXiv:1305.1576, doi:10.1088/1475-7516/2013/05/009.

[92] A. Aab *et al.* (Pierre Auger Collab.), Origin of atmospheric aerosols at the Pierre Auger Observatory using studies of air mass trajectories in South America, Atmos. Res. 149 (2014) 120–135. arXiv:astro-ph.IM/1405.7551, doi:10.1016/j.atmosres.2014.05.021.

[93] A. Aab *et al.* (Pierre Auger Collab., Telescope Array Collab.), Searches for Large-Scale Anisotropy in the Arrival Directions of Cosmic Rays Detected above Energy of 10^{19} eV at the Pierre Auger Observatory and the Telescope Array, Astrophys. J. 794 (2) (2014) 172. arXiv:1409.3128, doi:10.1088/0004-637X/794/2/172.

[94] A. Aab *et al.* (Pierre Auger Collab.), Reconstruction of inclined air showers detected with the Pierre Auger Observatory, JCAP 1408 (08) (2014) 019. arXiv:1407.3214, doi:10.1088/1475-7516/2014/08/019.

[95] A. Aab *et al.* (Pierre Auger Collab.), Muons in air showers at the Pierre Auger Observatory: Measurement of atmospheric production depth, Phys. Rev. D90 (2014) 012012. arXiv:1407.5919, doi:10.1103/PhysRevD.90.012012,10.1103/PhysRevD.90.039904.

[96] A. Aab *et al.* (Pierre Auger Collab.), Search for patterns by combining cosmic-ray energy and arrival directions at the Pierre Auger Observatory, Eur. Phys. J. C75 (6) (2015) 269. arXiv:astro-ph.HE/1410.0515.

[97] A. Aab *et al.* (Pierre Auger Collab.), A Targeted Search for Point Sources of EeV Neutrons, Astrophys. J. 789 (2014) L34. arXiv:1406.4038, doi:10.1088/2041-8205/789/2/L34.

[98] A. Aab *et al.* (Pierre Auger Collab.), A search for point sources of EeV photons, Astrophys. J. 789 (2014) 160. arXiv:1406.2912, doi:10.1088/0004-637X/789/2/160.

[99] A. Aab *et al.* (Pierre Auger Collab.), Depth of Maximum of Air-Shower Profiles at the Pierre Auger Observatory: Composition Implications, Phys. Rev. D (2014)arXiv:astro-ph.HE/1409.5083.

[100] A. Aab *et al.* (Pierre Auger Collab.), Large Scale Distribution of Ultra High Energy Cosmic Rays Detected at the Pierre Auger Observatory With Zenith Angles up to 80 degrees, Astrophys. J. 802 (2) (2015) 111. arXiv:1411.6953, doi:10.1088/0004-637X/802/2/111.

[101] A. Aab *et al.* (Pierre Auger Collab.), Searches for Anisotropies in the Arrival Directions of the Highest Energy Cosmic Rays Detected by the Pierre Auger Observatory, Astrophys. J. 804 (1) (2015) 15. arXiv:1411.6111, doi:10.1088/0004-637X/804/1/15.

[102] A. Aab *et al.* (Pierre Auger Collab.), Search for patterns by combining cosmic-ray energy and arrival directions at the Pierre Auger Observatory, Eur. Phys. J. C75 (6) (2015) 269. arXiv:1410.0515, doi:10.1140/epjc/s10052-015-3471-0.

[103] A. Aab *et al.* (Pierre Auger Collab.), Improved limit to the diffuse flux of ultrahigh energy neutrinos from the Pierre Auger Observatory, Phys. Rev. D91 (9) (2015) 092008. arXiv:1504.05397, doi:10.1103/PhysRevD.91.092008.

[104] J. Bellido (Pierre Auger Collab.), Depth of maximum of air-shower profiles at the Pierre Auger Observatory: Measurements above $10^{17.2}$ eV and composition implications, in: Proc. 35th Int. Cosmic Ray Conf., Busan, South Korea, 2017. arXiv:1708.06592.

[105] D. Maurel, Mass composition of ultra-high energy cosmic rays based on air shower universality, Dissertation, Karlsruhe Institute of Technology (2013).

[106] M. Ave, I. Allekotte, X. Bertou, R. Engel, M. Roth, Preliminary results for the Xmax reconstruction using SD vertical events, Auger internal note GAP-2013-075 (2013).

[107] M. Ave, X. Bertou, R. Engel, D. Maurel, M. Roth, A. Schulz, (Energy,Nmu,Xmax) from the Bariloche reconstruction, Auger internal note GAP-2013-109 (2013).

[108] A. Schulz, Measurement of the Energy Spectrum and Mass Composition of Ultra-high Energy Cosmic Rays, Dissertation, Karlsruhe Institute of Technology (2016).

[109] S. Argirò, S. Barroso, J. Gonzalez, L. Nellen, T. Paul, T. Porter, L. P. Jr., M. Roth, R. Ulrich, D. Veberič, The Offline software framework of the Pierre Auger Observatory, Nucl. Instrum. Meth. A580 (2007) 1485–1496. doi:http://dx.doi.org/10.1016/j.nima.2007.07.010.

[110] D. Veberič, M. Roth, Offline reference manual: Sd reconstruction, Auger internal note GAP-2005-035, an updated version is shipped with the Offline software distribution (2005).

[111] P. Billoir, Proposition to improve the local trigger of the Surface Detector for low energy showers, Auger internal note GAP-2009-179 (2009).

[112] P. Billoir, P. Ghia, D. Nitz, R. Sato, First results of the ToTd trigger in the test hexagon, Auger internal note GAP-2011-032 (2011).

[113] L. M. Bueno, P. Billoir, I. C. Maris, Signal variance for the TOTd and MoPS triggers, Auger internal note GAP-2014-035 (2014).

[114] P. Ghia (Pierre Auger Collab.), Statistical and systematic uncertainties in the event reconstruction and S(1000) determination by the Pierre Auger surface detector, in: Proc. 29th Int. Cosmic Ray Conf., Tokyo, Japan, 2005.

[115] R. Hiller, M. Roth, An update on the signal accuracy using the infill array, Auger internal note GAP-2012-012 (2012).

[116] I. C. Mariş, M. Roth, T. Schmidt, A Phenomenological Method to Recover the Signal from Saturated Stations, Auger internal note GAP-2006-012 (2006).

[117] D. Newton, J. Knapp, A. A. Watson, The Optimum Distance at which to Determine the Size of a Giant Air Shower, Astropart. Phys. 26 (2007) 414–419.

[118] A. Schulz, Measurement of the Energy Spectrum of Cosmic Rays between 0.1 EeV and 30 EeV with the Infill Extension of the Surface Detector of the Pierre Auger Observatory, Master's thesis, Karlsruhe Institute of Technology (2012).

[119] A. Herve, Measurement of the Mass Composition of the Highest Energy Cosmic Rays with the Pierre Auger Observatory, Dissertation, University of Adelaide (2013).

[120] K. Kamata, J. Nishimura, The Lateral and the Angular Structure Functions of Electron Showers, Prog. Theoret. Phys. Suppl. 6 (1958) 93–155.

[121] K. Greisen, Progress in elementary particle and cosmic ray physics, Vol. 3, North-Holland Publishing, Amsterdam, 1956.

[122] D. Mockler, The first measurement of an energy spectrum at 0.1 EeV with the Surface Detector of the Pierre Auger Observatory, Master's thesis, Karlsruhe Institute of Technology (2014).

[123] I. Lhenry-Yvon, P. Ghia, The communications crisis in 2009: proposal for handling data between June and November, Auger internal note GAP-2010-020 (2010).

[124] D. Veberič, Private communication about Auger SD Reconstruction (Jan. 2017).

[125] S. Dagoret-Campagne, The central trigger user guide and reference manual, Auger internal note GAP-2004-020 (2004).

[126] J. Abraham *et al.* (Pierre Auger Collab.), Trigger and aperture of the surface detector array of the Pierre Auger Observatory, Nucl. Instrum. Meth. A613 (2010) 29–39.

[127] B. Keilhauer, Investigation of Atmospheric Effects on the Development of Extensive Air Showers and their Detection with the Pierre Auger Observatory, Dissertation, Karlsruhe University, Karlsruhe, Germany (2003).

[128] C. Bleve, Atmospheric effects on extensive air showers observed with the Surface Detector of the Pierre Auger Observatory, preprint submitted to Elsevier (12 2008).

[129] D. Harari, S. Mollerach, E. Roulet, On the implementation of the energy correction due to weather effects, Auger internal note GAP-2008-175 (2008).

[130] C. Bleve (Pierre Auger Collab.), Weather induced effects on extensive air showers observed with the surface detector of the Pierre Auger Observatory, in: 30th Proc. Int. Cosm. Ray Conf., Merida, Mexico, 2007.

[131] A. Remoto, S. Mollerach, E. Roulet, On the weather correction and energy calibration, Auger internal note GAP-2009-054 (2009).

[132] E. Roulet, I. Allekotte, D. Harari, S. Mollerach, On the Constant Intensity Cut and weather effects, Auger internal note GAP-2009-024 (2009).

[133] S. Mollerach, E. Roulet, O. Taborda, Revisiting the effects of weather on the air shower energy reconstruction, Auger internal note GAP-2014-047 (2014).

[134] S. Mollerach, E. Roulet, O. Taborda, Weather effects on the event rate of the Infill array, Auger internal note GAP-2014-105 (2014).

[135] F. Fenu (Pierre Auger Collab.), The cosmic ray energy spectrum measured using the Pierre Auger Observatory, in: Proc. 35th Int. Cosmic Ray Conf., Busan, South Korea, 2017. arXiv:1708.06592.

[136] V. Verzi (Pierre Auger Collab.), The Energy Scale of the Pierre Auger Observatory, in: Proc. 33rd Int. Cosmic Ray Conf., Rio de Janeiro, Brazil, 2013. arXiv:astro-ph.HE/1307.5059.

[137] Max Malacari (Pierre Auger Collab.), Improvements to aerosol attenuation measurements at the Pierre Auger Observatory, in: Proc. 35th Int. Cosmic Ray Conf., Busan, South Korea, 2017. arXiv:1708.06592.

[138] B. Gookin, Calibration of the Pierre Auger Fluorescence Detector and the Effect on Measurements, Dissertation, Colorado State University (2015).

[139] S. Y. BenZvi *et al.* (Pierre Auger Collab.), The LIDAR system of the Pierre Auger observatory, Nucl. Instrum. Meth. A574 (2007) 171–184. arXiv:astro-ph/0609063, doi:10.1016/j.nima.2007.01.094.

[140] A. Porcelli, Measurement of the Depth of Shower Maximum in the Transition Region between Galactic and Extragalactic Cosmic Rays with the Pierre Auger Observatory, Dissertation, Karlsruhe Institute of Technology (2014).

[141] H. Dembinski, T. Hebbeker, T. Schmidt, Determination of the energy calibration function and primary composition of very inclined showers, Auger internal note GAP-2009-048 (2009).

[142] H. Dembinski, M. Roth, A. Schulz, Energy calibration revisited: The simplified likelihood method, Auger internal note GAP-2012-090 (2012).

[143] H. Dembinski, B. Kégl, I. C. Mariş, M. Roth, D. Veberič, A likelihood method to cross-calibrate air-shower detectors (2015)arXiv:1503.09027.

[144] L. Cazon, R. Ulrich, The Non-Linearity Between $\langle \ln A \rangle$ and $\langle X_{\max} \rangle$ Induced by the Acceptance of Fluorescence Telescopes, Auger internal note GAP-2012-015 (2012).

[145] P. Lipari, The Concepts of 'Age' and 'Universality' in Cosmic Ray Showers, Phys. Rev. 79 (2008) 063001. arXiv:0809.0190.

[146] A. M. Hillas, Angular and energy distributions of charged particles in electron photon cascades in air, J. Phys. G8 (1982) 1461–1473. doi:10.1088/0305-4616/8/10/016.

[147] M. Giller, A. Kacperczyk, J. Malinowski, W. Tkaczyk, G. Wieczorek, Similarity of extensive air showers with respect to the shower age, J. Phys. G31 (2005) 947–958.

[148] F. Nerling, J. Blümer, R. Engel, M. Risse, Universality of electron distributions in high-energy air showers: Description of cherenkov light production, Astropart. Phys. 24 (2006) 421–437. arXiv:astro-ph/0506729.

[149] P. Lipari, Universality of cosmic ray shower development, Nucl. Phys. Proc. Suppl. 196 (2009) 309–318. doi:10.1016/j.nuclphysbps.2009.09.060.

[150] S. Lafebre, R. Engel, H. Falcke, J. Hörandel, T. Huege, J. Kuijpers, R. Ulrich, Universality of electron-positron distributions in extensive air showers, Astropart. Phys. 31 (2009) 243–254. arXiv:0902.0548.

[151] F. Schmidt, M. Ave, L. Cazon, A. C. P. A. Collab.), Applying extensive air shower universality to ground detector data, in: Proc. 30th Int. Cosmic Ray Conf., Mérida, Mexico, 2007.

[152] M. Ave, R. Engel, J. Gonzalez, D. Heck, T. Pierog, M. Roth, Extensive air shower universality of ground particle distributions, Proc. of 31st Int. Cosmic Ray Conf., Beijing (2011) #1025.

[153] D. Maurel, M. Roth, J. G. P. A. Collab.), Universality of the time structure of ground particle distributions and its application to the reconstruction of extensive air showers, in: Proc. 33rd Int. Cosmic Ray Conf., Rio de Janeiro, Brazil, 2013. arXiv:astro-ph.HE/1307.5059.

[154] M. Ave, M. Roth, A. Schulz (Pierre Auger Collab.), A universal description of temporal and lateral distributions of ground particles in extensive air showers, in: Proc. 34th Int. Cosmic Ray Conf., The Hague, The Netherlands, 2015.

[155] M. Ave, R. Engel, J. Gonzalez, D.Heck, D. Maurel, T. Pierog, M. Roth, Prediction of the tank response $S(r, \mathrm{DX}, E|\theta, \phi)$ from shower universality, Auger internal note GAP-2011-087 (2011).

[156] M. Ave, N. Busca, L. Cazon, F. Schmidt, T. Yamamoto, Can EPOS Reproduce the Auger SD and Hybrid Data?, Auger internal note GAP-2007-098 (2007).

[157] M. T. Dova, L. N. Epele, A. G. Mariazzi, The Effect of atmospheric attenuation on inclined cosmic ray air showers, Astropart. Phys. 18 (2003) 351–365. arXiv:astro-ph/0110237, doi:10.1016/S0927-6505(02)00150-0.

[158] M. Ave, Ground signal parameterization for water Cherenkov and scintillator detectors and performance of ground arrays that combine both techniques, Auger internal note GAP-2012-141 (2012).

[159] M. Ave, R. Engel, M. Roth, A. Schulz, A generalized description of the signal size in extensive air shower detectors and its applications, Astropart. Phys. 87 (2017) 23 – 39. doi:https://doi.org/10.1016/j.astropartphys.2016.11.008.

[160] D. Maurel, M. Ave, J. Gonzalez, M. Roth, Extended shower universality: A model of the time-dependent signal in water Cerenkov tanks, Auger internal note GAP-2013-022 (2013).

[161] M. Ave, X. Bertou, R. Engel, M. Roth, A model for the time-dependent signal in water Cherenkov detectors, Auger internal note GAP-2013-072 (2013).

[162] F. Schmidt, M. Ave, L. Cazon, A. S. Chou, A Model-Independent Method of Determining Energy Scale and Muon Number in Cosmic Ray Surface Detectors, Astropart. Phys. 29 (2008) 355–365. arXiv:0712.3750.

[163] M. Ave, M. Roth, A. Schulz, A generalized description of the time dependent signals in extensive air shower detectors and its applications, Astropart. Phys. 88 (2017) 46 – 59. doi:https://doi.org/10.1016/j.astropartphys.2017.01.003.

[164] D. Garcia-Gamez, L. Molina, The resampling algorithm in Offline: bias in the time of the particles injected in the surface detectors, Auger internal note GAP-2015-006 (2015).

[165] P. Billoir, A sampling procedure to regenerate particles in a ground detector from a 'thinned' air shower simulation output, Astropart. Phys. 30 (2008) 270–285. doi:10.1016/j.astropartphys.2008.10.002.

[166] M. Ave, R. Engel, J. Gonzalez, D. Maurel, M. Roth, Tabulated response of the Auger surface detector, Auger internal note GAP-2011-086 (2011).

[167] H. Dembinski, Measurement of the flux of ultra high energy cosmic rays using data from very inclined air showers at the Pierre Auger Observatory, Dissertation, RWTH Aachen University (2009).

[168] J. P. Roberts, G. R. Farrar, Another look at energy reconstruction systematics, Auger internal note GAP-2012-096 (2012).

[169] Eun-Joo Ahn (Pierre Auger Collab.), Inferences about the mass composition of cosmic rays from data on the depth of maximum at the Auger Observatory, in: Proc. 33rd Int. Cosmic Ray Conf., Rio de Janeiro, Brazil, 2013. arXiv:astro-ph.HE/1307.5059.

[170] M. D. Domenico, M. Settimo, S. Riggi, E. Bertin, Reinterpreting the development of extensive air showers initiated by nuclei and photons, J. Cosmol. Astropart. Phys. 2013 (07) (2013) 050. doi:10.1088/1475-7516/2013/07/050.

[171] Simon Blaess, https://www.auger.unam.mx/AugerWiki/XmaxHeatIcrc2017.

[172] NLopt - library for non-linear optimization, http://ab-initio.mit.edu/wiki/. URL http://ab-initio.mit.edu/wiki/index.php/NLopt_manual

[173] G. J. Feldman, R. D. Cousins, Unified approach to the classical statistical analysis of small signals, Phys. Rev. D 57 (1998) 3873 – 3889.

[174] W. A. Rolke, A. M. López, J. Conrad, Limits and confidence intervals in the presence of nuisance parameters, Nucl. Instrum. Methods Phys. Res., Sect. A 551 (2005) 494. doi:10.1016/j.nima.2005.05.068.

[175] Ariel Bridgeman (Pierre Auger Collab.), Shower universality reconstruction of data from the Pierre Auger Observatory and validations with hadronic interaction models, in: Proc. 35th Int. Cosmic Ray Conf., Busan, South Korea, 2017. arXiv:1708.06592.

[176] Scipy - A Python library for scientific calculations, http://www.scipy.org/.

[177] M. Rosenblatt, Remarks on some nonparametric estimates of a density function, Ann. Math. Statist. 27 (3) (1956) 832–837.

[178] S. Sheather, M. Jones, A reliable data-based bandwidth selection method for kernel density estimation, J. R. Statist. Soc. B 53 (3) (1991) 683 – 690.

[179] D. Ravignani, The formulas of the angular resolution, Auger internal note GAP-2017-003 (2017).

[180] Observer, https://web.ikp.kit.edu/augeroracle/doku.php?id=auger:observer, accessed: 2017-10-30.

[181] R. Bruijn, Private communication from [182] (Jun. 2011).

[182] P. S. Lucas, The $\langle\delta\rangle$ method: an estimator for the mass composition of ultra-high-energy cosmic rays, Dissertation, Universidad de Granada (2016).

[183] Sources of data: Napoli library, https://web.ikp.kit.edu/augeroracle/doku.php?id=auger:data#napoli_library, accessed: 2017-10-30.

[184] D. Heck, J. Knapp, J. Capdevielle, G. Schatz, T. Thouw, CORSIKA: A Monte Carlo Code to Simulate Extensive Air Showers, Report FZKA 6019, Karlsruhe (1998).

[185] T. Pierog, R. Engel, D. Heck, S. S. Ostapchenko, K. Werner, Latest Results of Air Shower Simulation Programs CORSIKA and CONEX, in: Proc. 30th Int. Cosmic Ray Conf., Mérida, Mexico, 2007. arXiv:astro-ph/0802.1262.

[186] D. Heck, T. Pierog, Extensive air shower simulation with CORSIKA: A user's guide, Institut für Kernphysik, Forschungszentrum Karlsruhe, Karlsruhe, Germany, guide for version 6.6 (2007).

[187] D. Heck, J. Knapp, Upgrade of the monte carlo code corsika to simulate extensive air showers with energies $> 10^{20}$ ev, Report FZKA 6097B, Karlsruhe (1998).

[188] M. Kobal, A thinning method using weight limitation for air-shower simulations, Astropart. Phys. 15 (2001) 259. doi:10.1016/S0927-6505(00)00158-4.

[189] P. Billoir, Does the resampling procedure induce distortions in the FADC traces of the Surface Detector?, Auger internal note GAP-2005-109 (2005).

[190] P. Billoir, Reconstruction of showers with the ground array: status of the "prototype" program, Auger internal note GAP-2000-025 (2000).

[191] M. Unger, Private communication about fiducial field of view for the simulated fluorescence detector (Sept. 2017).

[192] G. Anastasi, S. Petrera, F. Salamida, Trace fit in the Universality Reconstruction, Auger internal note GAP-2017-041 (2016).

[193] J. Beringer *et al.*, Particle Data Group, Review of Particle Physics, Phys. Rev. D 86 (2012) 010001. doi:10.1103/PhysRevD.86.010001.

[194] J. K. Lindsey, Parametric Statistical Inference, Oxford University Press, New York, 1996.

[195] G. Anastasi, S. Petrera, F. Salamida, Study of performances for the global Universality reconstruction, Presentation in Malargue Collab. Meeting Nov. 2017 (11 2017).

[196] D. Wittkowski (Pierre Auger Collab.), Reconstructed properties of the sources of UHECR and their dependence on the extragalactic magnetic field, in: Proc. 35th Int. Cosmic Ray Conf., Busan, South Korea, 2017. arXiv:1708.06592.

Erklärung

Karlsruhe, den 16.04.2018

Erklärung der selbständigen Anfertigung meiner Dissertationsschrift

Hiermit versichere ich, dass ich die Dissertationsschrift mit dem Titel

Determining the Mass Composition of Ultra-high Energy Cosmic Rays Using Air Shower Universality

selbständig und ohne unerlaubte fremde Hilfe verfasst habe. Dabei habe ich keine anderen, als die von mir angegebenen Hilfsmittel benutzt.

Ariel Bridgeman